Supporting Crewed Missions using LiAISON Navigation in the Earth-Moon System

by

Jason M. Leonard

B.S., Aerospace Engineering, Embry-Riddle Aeronautical University, 2009

M.S., Aerospace Engineering Sciences, University of Colorado Boulder, 2012

A thesis submitted to the

Faculty of the Graduate School of the

University of Colorado in partial fulfillment

of the requirements for the degree of

Doctor of Philosophy

Department of Aerospace Engineering Sciences

2015

This thesis entitled:
Supporting Crewed Missions using LiAISON Navigation in the Earth-Moon System
written by Jason M. Leonard
has been approved for the Department of Aerospace Engineering Sciences

George H. Born

Jeffrey S. Parker

Daniel J. Scheeres

Brandon A. Jones

Webster C. Cash

Date

The final copy of this thesis has been examined by the signatories, and we find that both the content and the form meet acceptable presentation standards of scholarly work in the above mentioned discipline.

Leonard, Jason M. (Ph.D., Aerospace Engineering Sciences)

Supporting Crewed Missions using LiAISON Navigation in the Earth-Moon System

Thesis directed by Prof. George H. Born

Crewed navigation in certain regions of the Earth-Moon system provides a unique challenge due to the unstable dynamics and observation geometry relative to standard Earth-based tracking systems. The focus of this thesis is to advance the understanding of navigation precision in the Earth-Moon system, analyzing the observability of navigation data types frequently used to navigate spacecraft, and to provide a better understanding of the influence of a crewed vehicle disturbance model for future manned missions in the Earth-Moon system.

In this research, a baseline for navigation performance of a spacecraft in a Lagrange point orbit in the Earth-Moon system is analyzed. Using operational ARTEMIS tracking data, an overlap analysis of the reconstructed ARTEMIS trajectory states is conducted. This analysis provides insight into the navigation precision of a spacecraft traversing a Lissajous orbit about the Earth-Moon L_1 point. While the ARTEMIS analysis provides insight into the navigation precision using ground based tracking methods, an examination of the benefits of introducing Linked Autonomous Interplanetary Satellite Orbit Navigation (LiAISON) is investigated. This examination provides insight into the benefits and disadvantages of LiAISON range and range-rate measurements for trajectories in the Earth-Moon system.

In addition to the characterization of navigation precision for spacecraft in the Earth-Moon system, an analysis of the uncertainty propagation for noisy crewed vehicles and quiet robotic spacecraft is given. Insight is provided on the characteristics of uncertainty propagation and how it is correlated to the instability of the Lagrange point orbit. A crewed vehicle disturbance model is provided based on either Gaussian or Poisson assumptions. The natural tendency for the uncertainty distribution in a Lagrange point orbit is to align with the unstable manifold after a certain period of propagation. This behavior is influenced directly by the unstable nature of the orbit itself.

This thesis then examines several different LiAISON mission configurations to determine the benefits and disadvantages for future crewed missions in the Earth-Moon system. The following LiAISON supplemented configurations are analyzed over a wide trade space to determine their feasibility: 1) Geosynchronous and Earth-Moon halo orbiters; 2) A crewed vehicle in an Earth-Moon L_2 halo orbit with a navigation satellite orbiting another Earth-Moon Lagrange point; 3) A navigation satellite in an Earth-Moon halo orbit tracking a crewed vehicle in low lunar orbit; 4) A crewed vehicle on a trans-lunar cruise being tracked by a navigation satellite in an Earth-Moon halo orbit.

Dedication

> We are like dwarfs sitting on the shoulders of giants. We see more, and things that are more distant, than they did, not because our sight is superior or because we are taller than they, but because they raise us up, and by their great stature add to ours.
>
> *John of Salisbury, 12th-century theologian*

To my parents,

for whom the foundation behind this thesis would never have been possible.

Acknowledgements

I would like to thank, first and foremost, my advisor Dr. George Born, for his extensive help and guidance throughout my graduate career. Without him, I would have never found my passion in spacecraft navigation and stochastic processes. His support and dry humor throughout the years has created a foundation of knowledge, confidence, and sanity which can be so easily lost in the pursuit of an advanced degree. I express my deepest appreciation for the environment he and his wife, Carol, have made for his students. I am indebted to you both.

I am also very grateful for the assistance and technical knowledge from Dr. Jeffrey Parker and Dr. Rodney Anderson who helped introduce me to my thesis topic. Without either of them, and the support from the Jet Propulsion Laboratory during the initial exploratory phase of this research, this thesis would not have been possible. Their guidance through the years has provided me the understanding and inspiration behind this work. I would also like to thank Dr. Brandon Jones for keeping a sound mind while I explored a multitude of topics during my graduate career. I will always be indebted to him for taking the time to teach and explain new material and concepts. I would also like to thank the other members of the committee, including Dr. Daniel Scheeres and Dr. Webster Cash.

To all of my friends at the Colorado Center for Astrodynamics Research, it has been a pleasure working with everyone over the past several years. I would specifically like to thank Ben Bradley for all of our technical discussions and collaboration over the years and for the mid-afternoon round of 9 to keep our sanity in check. To Bradley Cheetham, Eduardo Villalba, Steve Gehly, Ann Dietrich, and Juliana Feldhacker, there will never be a better work environment than the one they created.

May the fourth floor of CCAR forever be ours.

A portion of this work has been performed under the support of the NASA Space Technology Research Fellowship (NSTRF) under grant NNX13AL40H. I would like to sincerely thank this program for generosity in funding the latter years of my research and for the extensive support in molding this body of work through the experiences the program endows. To Dr. Russell Carpenter, my NSTRF mentor, I am extremely grateful for his assistance over the past several years formulating a direction for this work inline with NASA goals.

I would like to thank the JPL Center Innovation Fund (CIF) Program, sponsored by NASA Office of the Chief Technologist (OCT), which has supported this research. Portions of the research presented in this dissertation have been partially carried out at the Jet Propulsion Laboratory, California Institute of Technology, under a contract with the National Aeronautics and Space Administration. Government sponsorship acknowledged. I would also like to acknowledge NASA contract NAS5-02099 and V. Angelopoulos for use of data from the THEMIS Mission. Specifically: M. Bester and D. Cosgrove for the use of spacecraft tracking data.

Finally, I would like to expresses my deepest gratitude to my parents, brother, family and friends. Without your unconditional support over my academic career, I would not have been able to arrive at this point.

Contents

Chapter

1 Introduction 1

1.1 Background 1

1.2 Navigation in Libration Point Orbits 2

1.2.1 ISEE–3 3

1.2.2 SOHO 4

1.2.3 ACE 5

1.2.4 WMAP 6

1.2.5 Herschel and Planck 7

1.2.6 ARTEMIS 7

1.3 Crewed Navigation 8

1.4 Autonomous Navigation 9

1.5 Thesis Overview 11

1.6 Thesis Contributions 13

2 Dynamical Models 14

2.1 Two-Body Problem 14

2.2 Three-Body Problem 17

2.2.1 CRTBP 19

2.2.2 Periodic and Quasiperiodic Orbits 20

2.3 State Transition and Monodromy Matrix . . . 22
2.4 Stability . . . 23
2.5 Full Ephemeris . . . 23
2.6 Satellite State Dynamics . . . 25
2.6.1 Gravity . . . 26
2.6.2 Third-body perturbations . . . 27
2.6.3 SRP . . . 27

3 Orbit Determination Methods 29
3.1 Introduction . . . 29
3.2 Least Squares Estimators . . . 31
3.3 Batch Processor . . . 32
3.4 Sequential Processors . . . 34
3.4.1 Linearized Kalman Filter . . . 34
3.4.2 Extended Kalman Filter . . . 36
3.5 Cramér-Rao Lower Bound . . . 36
3.6 Process Noise and Stochastics . . . 37
3.6.1 Shaping Filter . . . 38
3.6.2 Stochastic Time Update . . . 39
3.6.3 Stochastic Processes . . . 41
3.7 Square Root Formulations . . . 45
3.7.1 UD Factorization . . . 46
3.7.2 SRIF . . . 49
3.8 Smoother . . . 51
3.9 Uncertainty Propagation . . . 51
3.10 Observability . . . 53
3.10.1 Linear Time-Invariant Systems . . . 54

3.10.2 Linear Time-Varying System . . . 56
3.10.3 Nonlinear System . . . 57
3.11 Measurement Types . . . 59
3.11.1 Instantaneous Range . . . 60
3.11.2 Instantaneous Range-rate . . . 61

4 Earth-Moon Libration Point Orbit Navigation: ARTEMIS Baseline 62
4.1 Introduction . . . 62
4.2 Technical Overview . . . 63
4.2.1 MONTE . . . 64
4.2.2 Tracking Data and File Formats . . . 64
4.2.3 Overlap Analysis . . . 65
4.2.4 Orbit Determination Set-up . . . 66
4.3 Overview of Initial Results . . . 69
4.4 Solar Coefficient Results . . . 74
4.5 Short-arc Overlaps . . . 76
4.6 Long-arc Overlaps . . . 77
4.7 Solutions Considering Maneuvers . . . 79
4.8 Summary and Future Work . . . 80

5 Linked, Autonomous, Interplanetary Satellite Orbit Navigation 81
5.1 Overview . . . 81
5.2 Observability . . . 83
5.2.1 Hamilton and Melbourne discussion . . . 84
5.2.2 Generalized Analytical Model . . . 89
5.2.3 Observation Effectiveness . . . 94
5.3 Observability and Rank Analysis . . . 100

6 Uncertainty propagation in Halo orbits 105

6.1 Halo Orbit Trajectory Stability . . . 105

6.2 Lyapunov Exponents . . . 107

6.2.1 Local Lyapunov Exponents . . . 107

6.3 CRTBP Simulations . . . 109

7 Crewed Vehicle Disturbance and Environment Modeling 114

7.1 Discrete Noise FLAK Modeling . . . 115

7.2 Discrete Poisson FLAK Modeling . . . 117

7.3 Uncertainty Mapping with FLAK . . . 121

7.4 Monte Carlo Analysis . . . 123

7.5 Full Simulation . . . 124

8 LiAISON Supporting Lagrange Point Orbits 128

8.1 GEO Navigation using LiAISON . . . 128

8.1.1 Models and Setup . . . 129

8.1.2 Navigation Simulation Results . . . 133

8.1.3 Conclusions . . . 144

8.2 LPO NavSat for Crewed Vehicle at L2 . . . 146

8.2.1 Models and Setup . . . 146

8.2.2 Navigation Simulation Results . . . 150

8.2.3 LiAISON Only . . . 154

8.2.4 Ground and LiAISON support . . . 157

8.2.5 Trade Study . . . 162

9 LiAISON Supporting Low Lunar Orbit 163

9.1 Mission Concept . . . 164

9.1.1 Orbits . . . 165

9.1.2 Tracking Data . . . 166
9.2 Simulations . . . 167
9.2.1 LiAISON Only . . . 168
9.2.2 Ground Only . . . 169
9.2.3 DSN with LiAISON . . . 171
9.3 L1 vs L2 NavSat Trade . . . 172
9.4 Variations in FLAK Level . . . 175
9.5 Conclusions . . . 175

10 LiAISON Supporting Trans-lunar Cruise 177
10.1 Mission Design . . . 178
10.1.1 Lunar L1 Halo Orbit . . . 178
10.1.2 Trans-lunar Cruise . . . 179
10.1.3 Ground Tracking Networks . . . 180
10.2 Navigation Performance Methods . . . 181
10.2.1 FLAK Model Used . . . 181
10.3 Trans-lunar Cruise Navigation Performance . . . 183
10.3.1 TLC with Standard FLAK Level . . . 183
10.3.2 Navigation Sensitivity to FLAK Level . . . 185
10.4 Conclusions . . . 186

11 Conclusions and Future Work 187
11.1 Conclusions . . . 187
11.2 Future Work . . . 189

Bibliography 191

Tables

Table

1.1 ISEE–3 Comparisons of Overlap Differences and Covariance Analysis [71]. 3

1.2 SOHO Definitive Overlap Comparisons [7]. 4

1.3 ACE Single Point Overlap Comparisons [7]. 5

1.4 WMAP Overlap Comparisons [7]. 6

4.1 Orbit determination filter uncertainties. 69

4.2 ARTEMIS SRP Specular Coefficient Change (NORMALIZED) 75

4.3 ARTEMIS SRP Diffuse Coefficient Change (NORMALIZED) 75

4.4 Maneuver Evaluation (Designed-Estimated) 79

7.1 FLAK Type and Strength of Unmodeled Acceleration [27, 28] 115

8.1 L_1 quasi-halo orbit parameters. 130

8.2 Summary of models used in the LiAISON simulations. 132

8.3 Orbit determination filter uncertainties. 134

8.4 The parameters used to define the errors in the tracking data. The bias added to each link and the white noise added to each observation are drawn from Gaussian distributions with zero mean and the given standard deviations. 148

8.5 The mean and 99% position uncertainty 3-σ values for the ground-only simulations of a crewed vehicle in an L_2 halo orbit after the simulation has reached a nearly steady state. 153

8.6 The mean and 99% position uncertainty 3-σ values for the LiAISON-only simulations, where the crewed vehicle is in a 10,000 km L_2 halo orbit and the NavSat is in one of many halo orbits as indicated. The results are shown after each simulation has reached a nearly steady state. 156

8.7 The navigation performance for the configuration that includes continuous LiAISON tracking between the crew at L_2 and the NavSat, as well as continuous DSN tracking of the NavSat; there is no ground tracking of the crewed vehicle. 159

8.8 The navigation performance for the configuration that includes continuous LiAISON tracking between the crew at L_2 and the NavSat, as well as continuous DSN tracking of both vehicles. 160

8.9 The navigation performance for the configuration that includes continuous LiAISON tracking between the crew at L_2 and the NavSat, as well as continuous ground tracking of both vehicles: DSN for the NavSat and IDAC4B for the crewed vehicle. . 161

8.10 Summary of the approximate position uncertainty levels observed in several different navigation configurations. FLAK and station keeping maneuvers are included. . . . 162

9.1 The parameters used to define the errors in the tracking data. The bias added to each link and the white noise added to each observation are drawn from Gaussian distributions with zero mean and the given standard deviations. The L_1 and L_2 orbiters have the same tracking data characteristics, indicated by **LPO**. 166

9.2 The 3σ position uncertainties observed in a system that includes the crewed low lunar orbiter and a lunar libration orbiter, being tracked by the three DSN stations and LiAISON. 172

9.3 Survey of LLO scenarios, including their definitions and resulting performance. . . . 174

10.1 Initial LEO parking orbit conditions for TLI. 179

10.2 Navigation performance initial uncertainties. 184

10.3 TLC navigation uncertainties. 185

Figures

Figure

1.1 ISEE-3 Trajectory [107]. 3

1.2 SOHO Trajectory [108]. 4

1.3 ACE Trajectory [15]. 5

1.4 WMAP Trajectory [109]. 6

1.5 Herschel and Planck Trajectory [30]. 7

1.6 ARTEMIS trajectory [106]. 8

2.1 Diagram of the Two-Body Problem [154]. 15

2.2 Diagram of the Three-Body Problem [154]. 17

2.3 Diagrams of the CRTBP: (a) CRTBP geometry with a rotating, nondimensional coordinate frame, and (b) the Lagrange points in the CRTBP. 19

2.4 Lyapunov orbits [119]. 21

2.5 Halo orbits [119]. 21

3.1 Auto-covariance functions for different instances of second-order GMP. 45

4.1 Schematic of 3-day and 7-day Overlaps. 65

4.2 ARTEMIS spacecraft shape models. 68

4.3 ARTEMIS-P2 trajectory from 19-NOV-2010 to 13-MAR-2011 displayed in the Earth-Moon rotating frame (Earth is in the -X axis with the Moon in the +X axis). The red dots represent the locations of Station Keeping Maneuvers that were performed. 70

4.4 Doppler post-fit residuals for entire timeframe under analysis for Goldstone (blue), Canberra (green), Madrid (red), Berkeley (grey). 71
4.5 Range post-fit residuals with range biases for entire timeframe under analysis for Goldstone (blue), Canberra (green), Madrid (red), Berkeley (grey). 71
4.6 Histogram of Doppler residuals by station. 72
4.7 Sping signature seen in Doppler residuals throughout the data arcs for 2 passes in different months. 73
4.8 Example of stochastics fit during a Long Arc: Z-axis is S/C-Moon line. 74
4.9 Short Arc Doppler tracking. 76
4.10 Short Arc Position Overlap Analysis. 77
4.11 Short Arc Velocity Overlap Analysis. 77
4.12 Long Arc Position Overlap Analysis. 78
4.13 Long Arc Velocity Overlap Analysis. 78

5.1 Observation geometry for truth model simulations for LiAISON and ground tracking. 83
5.2 Partial derivative of the solar gravitational acceleration of r with respect to r [114]. . 88
5.3 Partial derivative $\partial\ddot{r}_{rel}/\partial r$ with respect to L_2. 96
5.4 Partial derivative $\partial\ddot{r}_{rel}/\partial X$ with respect to L_2. 96
5.5 Partial derivative $\partial\ddot{r}_{rel}/\partial Y$ with respect to L_2. 96
5.6 Partial derivative $\partial\ddot{r}_{rel}/\partial r$ with respect to L_1. 98
5.7 Partial derivative $\partial\ddot{r}_{rel}/\partial X$ with respect to L_1. 98
5.8 Partial derivative $\partial\ddot{r}_{rel}/\partial Y$ with respect to L_1. 98
5.9 Partial derivative $\partial\ddot{r}_{rel}/\partial r$ with respect to Earth. 99
5.10 Partial derivative $\partial\ddot{r}_{rel}/\partial X$ with respect to Earth. 99
5.11 Partial derivative $\partial\ddot{r}_{rel}/\partial Y$ with respect to Earth. 99
5.12 Time to full numerical rank for L_1 Halo Orbits. 102
5.13 Time to full numerical rank for L_2 Halo Orbits. 103

6.1 Local Lyapunov Exponents variation over the orbit of various halo orbit sizes (orbit projections in black). 109

6.2 Surface comparing the size of the Covariance semi-major axis (km) compared to the size of the Halo orbit, the initial tau angle, and the angle between the unstable manifold direction and the maximum covariance. Integration time is equal for all cases. 111

6.3 Surface comparing the size of the Covariance semi-major axis compared to the size of the Halo orbit, the initial tau angle, and the time it takes for the angle between the unstable manifold direction and the maximum covariance to get to within 10 degrees. 112

6.4 Relationship between the LLE and the distance of the S/C to the Moon. 113

7.1 Surface comparing the size of the Covariance semi-major axis compared to the size of the Halo orbit, the initial tau angle, and the time it takes for the angle between the unstable manifold direction and the maximum covariance to get to within 10 degrees with discrete Poisson white noise. 122

7.2 Surface comparing the size of the Covariance semi-major axis compared to the size of the Halo orbit, the initial tau angle, and the time it takes for the angle between the unstable manifold direction and the maximum covariance to get to within 10 degrees with discrete Poisson white noise. 123

7.3 Position realizations for 500 Monte Carlo runs of a halo orbit perturbed by FLAK. . 124

7.4 Velocity realizations for 500 Monte Carlo runs of a halo orbit perturbed by FLAK. . 125

7.5 Doppler Residuals. 126

7.6 Range Residuals. 126

7.7 Stochastic Accelerations. 127

7.8 Crewed halo orbiter accuracy and uncertainty. 127

8.1 Satellite constellation geometry for truth model simulations for LiAISON and ground tracking viewed in the Earth-Moon rotating frame. 129

8.2 Range observations to the GEO and L_1 orbiter from LiAISON and ground station measurements. 132

8.3 Position accuracy and uncertainty for a GEO and L_1 orbiter tracked by ground networks twice a day for 3 hours. 135

8.4 Orbit determination accuracy and 3-sigma uncertainty for various amounts of LiAISON and ground station tracking. 137

8.5 Time history comparison of 3-sigma position uncertainty for various tracking schedules. 139

8.6 Position accuracy and uncertainty for LiAISON constellation for a tracking schedule with continuous LiAISON tracking and 3 hours of ground tracking followed by 72 hour observation gap (0,72). 140

8.7 Position accuracy and uncertainty for LiAISON constellation for a tracking schedule with 3 hours of LiAISON followed by 72 hour observation gap and continuous ground tracking (72,0). 141

8.8 Position accuracy and uncertainty for LiAISON constellation for a tracking schedule with 3 hours of LiAISON followed by 28 hour observation gap and 3 hours of ground tracking followed by 49 hour observation gap (28,49). 142

8.9 LiAISON L_1 and GEO measurement offset analysis. Solid lines represent 3D-RMS accuracy and dashed lines represent 3-sigma uncertainty. 144

8.10 An illustration of the orbits studied in this paper, viewed in the Earth-Moon rotating frame from above (left) and from the side (right). The orbits pulsate with the Moon's motion. The NavSat is only located in one orbit per scenario, though each of the locations is visualized. 147

8.11 An illustration of the schedule of tracking observations for the case of an L_1 halo orbiter. Not all observations are used in all scenarios. 149

8.12 Example observation errors applied to the DSN–Crew links. 149

8.13 The first 30 hours of simulated LiAISON tracking data errors. 150
8.14 The position uncertainty over time of both the NavSat and the crewed vehicle as they are each independently tracked by the three main DSN ground stations. No FLAK or LiAISON observations are included. 151
8.15 The position uncertainty components over time of both the NavSat and the crewed vehicle as they are each independently tracked by the three main DSN ground stations. No FLAK or LiAISON observations are included. 151
8.16 The velocity uncertainty components over time of both the NavSat and the crewed vehicle as they are each independently tracked by the three main DSN ground stations. No FLAK or LiAISON observations are included. 152
8.17 A comparison of the position uncertainty over time of the crewed L_2 vehicle as it is tracked by either the DSN or IDAC4B in the presence or not of FLAK. 153

9.1 The scenarios studied in this paper include a crewed spacecraft in low lunar orbit being tracked by the DSN from the Earth and from a navigation satellite located in orbit about the Earth-Moon L_1 (top) or L_2 (bottom) libration points. 164
9.2 LiAISON Configuration. 165
9.3 An illustration of the schedule of tracking observations for the case of an L_1 halo orbiter. Not all observations are used in all scenarios. 167
9.4 A compressed timeline, illustrating when each tracking option is in view. 168
9.5 The position 3σ uncertainty of the halo orbiter (top) and the crewed lunar orbiter (middle) while processing LiAISON-only observation data using very large *a priori* covariances. The FLAK time profile and availability of LiAISON data is shown at the bottom. 169

9.6 The position 3σ uncertainty of the halo orbiter (top) and the crewed lunar orbiter (middle) while processing ground-only observation data from the three DSN sites using very large *a priori* covariances. The FLAK time profile and availability of DSN tracking data is shown at the bottom. 170

9.7 The position 3σ uncertainty of the halo orbiter (top) and the crewed lunar orbiter (middle) while processing DSN and L_1 (left) / L_2 (right) LiAISON tracking data. . . 171

9.8 The 3σ position uncertainty of the crewed lunar orbiter for a variety of scenarios. The main shaded bars illustrate the mean 3σ position uncertainties over time for each scenario and the thin error bar extensions on top illustrate the 99th percentile of the 3σ position uncertainties over time. The scenarios are defined in Table 9.3. . . 173

9.9 The effect of changing the level of FLAK in the simulation. 175

10.1 LiAISON constellation for an EML-1 navigation satellite and a crewed spacecraft on TLC. The plots are visualized in the Earth-Moon rotating frame. 178

10.2 Locations of the DSN, IDAC4B, and Apollo tracking networks. The DSN network is common for all of the tracking networks and is denoted by green circles; the IDAC4B network is denoted by red squares, and the Apollo stations are given by yellow diamonds. 180

10.3 Time history of the position and velocity RSS navigation uncertainty for four different tracking architectures. 1) DSN only (blue), 2) IDAC4B only (red), 3) DSN and LiAISON (black), and 4) IDAC4B and LiAISON (green). 184

10.4 Navigation sensitivities due to FLAK levels. 1) DSN only (blue), 2) IDAC4B only (red), 3) DSN and LiAISON (black), and 4) IDAC4B and LiAISON (green). 185

Chapter 1

Introduction

1.1 Background

Recently, NASA has been considering new mission concepts to enable future lunar explorations. One of the concepts being analyzed is to send a crewed spacecraft on a trans-lunar cruise that flies past the Moon and then enters a libration point orbit (LPO) about the Earth-Moon L_2 (EML-2) point. Another concept is that of sending a mission to the Moon similar to that of the Apollo era missions. This would entail a crewed mission that goes into a low lunar orbit (LLO) that eventually descends to the Moon's surface. Other options do exist, such as a double-lunar swingby or going into orbit about the EML-1 point as opposed to EML-2.

There has been much debate over which Lagrange point has the most advantages for future missions. In many respects, both EML-1 and EML-2 offer similar advantages. Dynamically, these points are not that much different. Ref. [33] has shown that the stationkeeping budgets for a spacecraft in orbit about EML-1 and EML-2 are roughly the same. A big advantage of an outpost at these Lagrange points is that it requires a relatively low delta-V to move from one point to another as shown by NASA's ARTEMIS mission [5, 38, 145]. This implies that while a propulsive budget is important, it is not necessarily the decisive factor when determining which Lagrange point is optimal. Power generation for a spacecraft at either Lagrange point is straightforward and provides near continuous illumination when compared to a LLO.

One of the biggest differences when choosing which Lagrange point to visit is which side of the Moon one would like to look at. A spacecraft at EML-1 can mostly see the near side of the Moon

while a spacecraft at EML-2 can mostly view the far side. Much focus has been given for a mission to EML-2 to provide a sample return from the Moon's South Pole–Aitken basin. A cataclysmic asteroid impact is believed to have created what is known to be one of the largest, deepest, and oldest craters in the solar system thus exposing the inner layers of the Moon for analysis on the internal structure.

The concept of sending a crewed vehicle to EML-2 is also considered to be a waypoint mission on the road to human exploration of asteroids and Mars. A crewed mission to EML-2 would travel about 15% farther from Earth than any of the Apollo missions and spend nearly three times longer in deep space or more. Each flight to EML-2 would be at least 18 days in duration or as long as supplies last proving the life support systems and radiation shielding of the vehicle and test high speed reentry capabilities that are necessary for a return to Earth from the Moon or deep space.

A future mission to EML-2 is the next step in crewed exploration of our solar system. This thesis focuses on advancing the understanding of navigation challenges and possible solutions to make future missions to the Earth-Moon lagrange points a possibility. This first chapter will briefly introduce the necessary background to understand the current status of crewed navigation, navigation in LPOs, autonomous navigation, and a newer interplanetary autonomous navigation technique known as LiAISON (Linked Autonomous Interplanetary Satellite Orbit Navigation). The remainer of the thesis is outlined in Section 1.5.

1.2 Navigation in Libration Point Orbits

With the rise of LPOs for future science missions, it is necessary to understand the current navigation ability for this unique regime. LPOs are nothing like Low Earth Orbits (LEO) and interplanetary trajectories that are commonly supported by NASA centers. In this regime, the dynamics are slow and thus require an extensive amount of tracking data and time to obtain a quality state estimate. Most missions that have flown LPOs have used the DSN for tracking. The use of the Universal Space Network (USN) is a possibility to reduce strain on the DSN for future missions. The following summarizes past LPO missions and their navigation uncertainties.

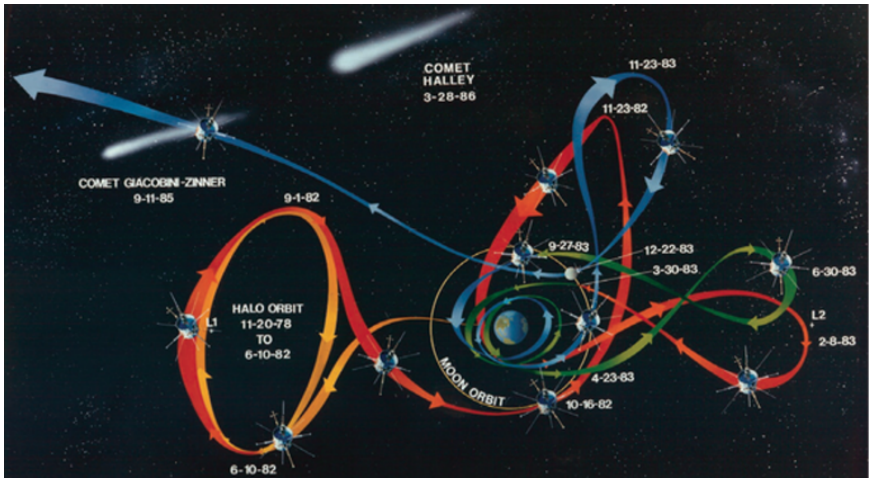

Figure 1.1: ISEE-3 Trajectory [107].

1.2.1 ISEE–3

The first LPO mission was the International Sun–Earth Explorer–3 (ISEE–3). ISEE–3 was a joint ESA and NASA mission to study the interaction between Earth's magnetic field and the solar wind. ISEE–3 entered it's Earth-Sun L_1 halo orbit on November 20, 1978 with a period of approximately 6 months and a Y-amplitude of almost 700,000 km [34]. ISEE–3 was tracked by NASA's S-band Tracking Data Network while it was in the halo orbit [71]. The tracking schedule was erratic with very short passes of roughly 5 minutes for each station [71]. Prior to launch, early covariance analysis showed that the optimum measurement batch tracking arc would be a length of about 21 days with station keeping maneuvers every 45 days allowing for a 7–day orbit determination (OD) overlap analysis [7]. Table 1.1 gives an overview of navigation overlap comparisons and covariance analysis for the ISEE–3 mission.

Table 1.1: ISEE–3 Comparisons of Overlap Differences and Covariance Analysis [71].

Period	Overlap Comparison (km)	Covariance Analysis (km)
A	8.1	6.0
B	9.0	5.5
C	3.6	5.4

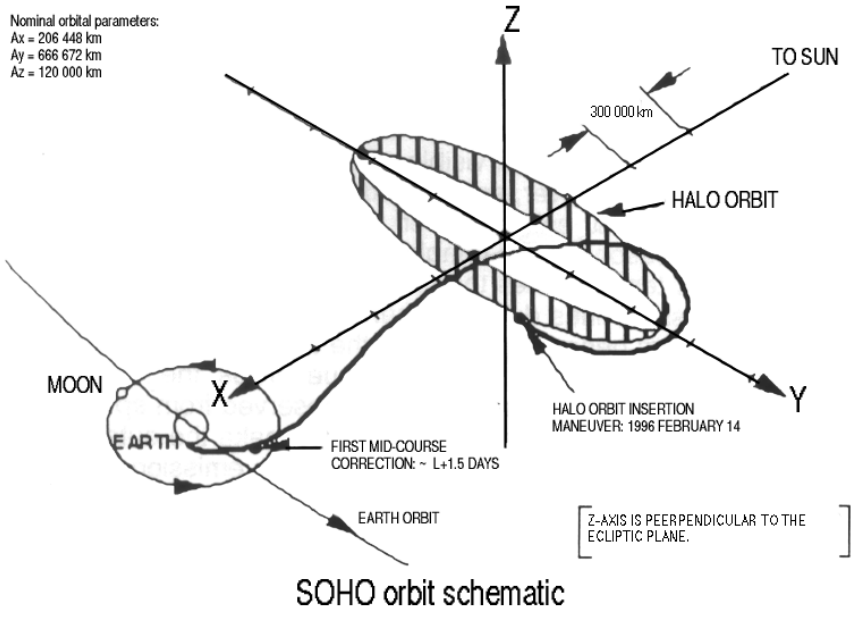

Figure 1.2: SOHO Trajectory [108].

1.2.2 SOHO

The Solar & Heliospheric Observatory (SOHO) is another joint ESA and NASA mission to study the Sun. SOHO entered a Earth-Sun L_1 halo orbit in March of 1996 with a Y-amplitude of approximately 670,000 km [7]. SOHO was also tracked by the DSN for approximately 5 hours a day. Pre-mission covariance analysis showed that the optimum arc length for a conservative tracking schedule of 1 hour per day would give orbital uncertainties of less than 9 km [70]. SOHO generally performed station keeping maneuvers every 8 to 12 weeks which was much longer than that of ISEE–3. SOHO's overlap requirements were 50 km in position RSS with actual overlap comparisons showing about 7 km in position RSS [7]. Most of the uncertainty for SOHO was in the cross-track direction with radial uncertainties of less than 1 km. Table 1.2 gives an overview of the radial, in-track, and cross-track overlap comparisons.

Table 1.2: SOHO Definitive Overlap Comparisons [7].

	RSS	Radial	In-track	Cross-track
Position (km)	7	1	2	7
Velocity (mm/s)	0.4	0.1	0.2	0.3

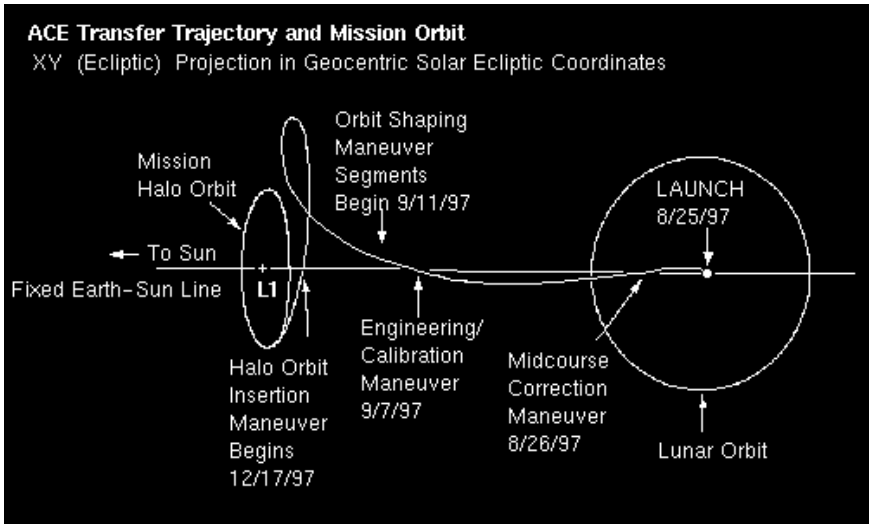

Figure 1.3: ACE Trajectory [15].

1.2.3 ACE

The Advanced Composition Explorer (ACE) was a NASA Explorer mission that arrived at the Earth-Sun L_1 point in December of 1997. ACE was inserted into a Lissajous orbit with a Y-amplitude of about 150,000 km. This orbit was significantly different than the halo orbits flown by ISEE–3 and SOHO. Due to the Lissajous orbit flown, the spacecraft would periodically move in front of the Sun as viewed from Earth requiring frequent station keeping maneuvers (as frequent as every 5 days) to maintain communication and sun-pointing angles. These maneuvers would force ACE navigators to use data arcs of 4 to 14 days and not the required 21 days for optimal OD uncertainty [7]. ACE also used the DSN with approximately 3.5 hour tracking passes per day. Due to the frequent attitude maneuvers, overlap analysis for ACE is not obtainable and thus only a single point overlap is possible at the time of the maneuver. Table 1.3 gives an overview of the single point overlap comparisons in the radial, in-track, and cross-track directions.

Table 1.3: ACE Single Point Overlap Comparisons [7].

	RSS	Radial	In-track	Cross-track
Position (km)	10	4	5	8
Velocity (mm/s)	1.2	0.9	0.1	0.9

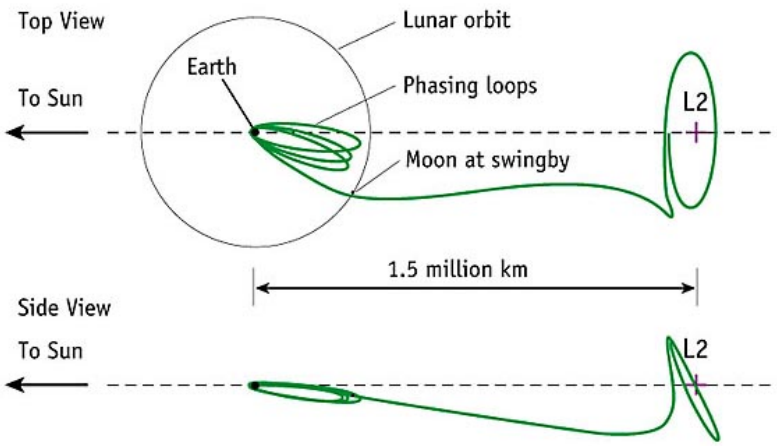

Figure 1.4: WMAP Trajectory [109].

1.2.4 WMAP

The Wilkinson Microwave Anisotropy Probe (WMAP) was a NASA mission to measure the microwave background radiation and arrived at the Earth-Sun L_2 point in October of 2001. WMAP was the first mission to orbit the Earth-Sun L_2 point in a Lissajous orbit. WMAP tracking data was the highest quality measurement data of any previous LPO mission and was tracked for at least 45 minutes every day. A huge benefit of WMAP's attitude requirements was that it produced a nearly constant cross-sectional area for solar radiation pressure estimation [7]. This allows for extended measurement arcs after maneuvers of 14 to 72 days. Table 1.4 gives an overview of overlap comparisons in the radial, in-track, and cross-track directions for 5-week and 9-week predictions.

Table 1.4: WMAP Overlap Comparisons [7].

	RSS	Radial	In-track	Cross-track
	5-Week Predictive Overlap			
Position (km)	2.0	0.3	1.4	2.0
Velocity (mm/s)	0.83	0.36	0.40	0.79
	9-Week Predictive Overlap			
Position (km)	6.7	6.2	2.3	1.8
Velocity (mm/s)	3.9	3.8	0.4	0.6

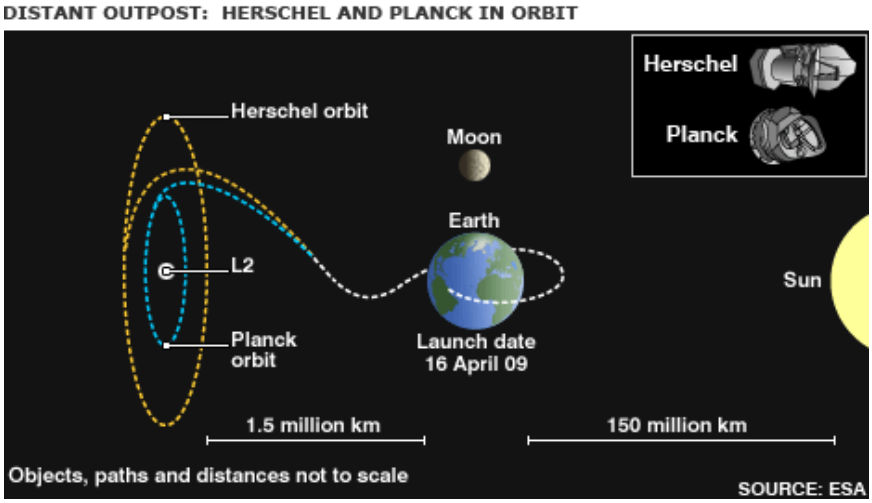

Figure 1.5: Herschel and Planck Trajectory [30].

1.2.5 Herschel and Planck

ESA launched the two spacecraft observatories Herschel and Planck on May 14, 2009 to Earth-Sun L_2 point. Herschel was injected into a quasi-halo orbit with a dimension of 750,000 km $\times$ 450,000 km [35]. Planck was injected into a Lissajous orbit with dimensions of 300,000 km $\times$ 300,000 km [35]. Tracking data for Herschel and Planck were obtained from stations located at New Norcia and Perth. Each OD solution was performed on a weekly basis using four weeks worth of data with 3 hours per day passes of two-way Doppler and 20 minute passes per day of two-way range. An assessment of the OD accuracy was conducted by comparing the overlapping results of successive OD solutions and comparing solutions with various data arc lengths. Reference [47] describes the overall OD performance to be better than 1 km in position and 1 cm/s in velocity for Planck with the EME2000 Z component containing the most error. Prediction accuracies for Planck were estimated to be 30 km in position and 5 cm/s in velocity after three weeks [47].

1.2.6 ARTEMIS

The ARTEMIS mission utilized two of the five THEMIS spacecraft after their primary mission was over to study the Moon and the lunar space environment. The two ARTEMIS spacecraft successfully demonstrated spacecraft operations in Earth-Moon LPOs as they traversed EML-1 and EML-2 [12, 163]. ARTEMIS tracking data was taken from the DSN, USN, and the Berkeley

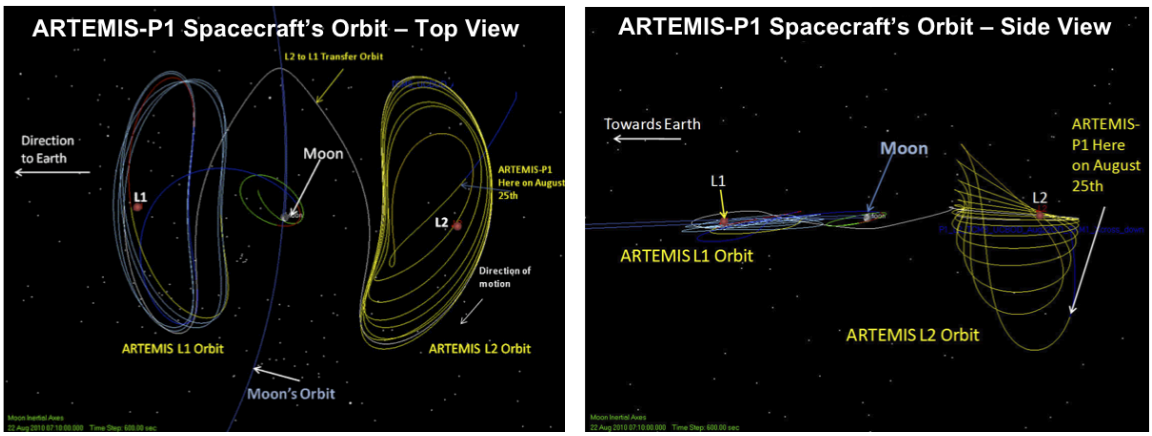

(a) Artemis top view (b) Artemis side view

Figure 1.6: ARTEMIS trajectory [106].

Ground Station (BGS) [38, 162]. Navigation data included two-way range and Doppler with a 3.5 hour tracking pass every other day from DSN, and two 45-minute passes from BGS every other day, and one 30-minute pass from the USN per week [162]. OD uncertainties for ARTEMIS were on the order of 100 meters in position and 1 mm/s in velocity [38, 145].

1.3 Crewed Navigation

Historically, crewed vehicles behave significantly different than that of a robotic spacecraft. While a robotic spacecraft is considered to be a quiet vehicle (performing maneuvers infrequently, passive thermal controls, minimal venting, etc.), crewed vehicles typically experience significant statistical accelerations that have unknown or poorly modeled characteristics. During the Apollo era, it was determined that significant deviations on the order of 500 m error in the trajectory over and hour occurred due to the activity of the crew and certain outgassing or maneuver events [25, 161].

The Apollo lunar missions required an extensive number of ground stations in order to obtain a reasonable state uncertainty. While the Deep Space Network (DSN) has been significantly advanced since the Apollo era and future spacecraft will be quieter in terms of unmodeled accelerations, three tracking stations alone are not sufficient to accurately estimate future crewed missions [26, 42]. One possible solution that has been put forth is that of introducing additional track-

ing stations culminating in the 4B integrated design and analysis cycle (IDAC4B) configuration [29]. The proposed IDAC4B configuration utilizes the three DSN stations and three other tracking stations located in the opposite hemisphere as receive only stations. While this configuration is enough to obtain uncertainties necessary for a crewed mission to the Moon, infrastructure costs are significantly increased due to the additional stations.

1.4 Autonomous Navigation

The purpose behind autonomous navigation is to provide a significant reduction in operations cost and increase mission performance by minimizing human interaction from the ground. When a spacecraft can be controlled to follow a chosen reference trajectory, ground operations can be significantly reduced and ground scheduling can become more predictable. One of the largest dependencies for a spacecraft on the ground is that of navigation. Navigation consists of collecting observations of the spacecraft and using these observation to estimate the current trajectory that the spacecraft is on and a course correction to place the spacecraft back onto a desirable trajectory. Orbit determination algorithms are used for estimating the current state of the spacecraft and maneuvers are used to correct errors in this state.

Autonomous OD is only possible if navigation can be done onboard without any intervention from the ground [18]. Therefore, for a spacecraft to be fully autonomous, all measurements used in the estimation process must be collected by only the spacecraft. There can be two generalized classes of autonomous OD techniques for spacecraft: Individual autonomy is when a single satellite can collect all necessary measurements; and Constellation autonomy exists when multiple spacecraft obtain and share information. There is also the possibility of a semiautonomous spacecraft that utilizes minimal interaction or dependence on Earth-based operations. Observations from GPS, DORIS, and TDRSS are considered semiautonomous due to their reliance on ground-based support.

There are several different measurement types that can be used to obtain an autonomous OD solution. These measurements can be scalar or angular in nature. Angular measurements generally give a direction of the spacecraft from some reference. Scalar measurements generally

give the distance to or speed of a reference. Autonomous spacecraft can utilize angular, scalar, or both measurement types to achieve a desired navigation solution.

Some of the earliest work in developing autonomous navigation systems was done using horizon scanners to detect Earth's horizon from space [18]. Landmark tracking is another method that utilizes knowledge of specific details of a body to obtain an angle measurement from that spot. Landmark tracking has been used successfully on NEAR [17, 98, 100] and Deep Impact [81, 95, 116]. Another method that has been proposed is to use a magnetometer to measure Earth's magnetic field [72, 127, 128, 139]. A more recent development is the use of X-ray pulsars, or XNAV, for navigation [8, 49, 138]. The use of multiple sensor types for navigation have also been investigated [129, 173, 174].

Through the use of satellite-to-satellite tracking (SST), new navigation techniques have revealed the ability to perform accurate absolute navigation of one or more satellites in a given constellation. Satellite navigation for low Earth orbit (LEO) has been revolutionized through the Global Positioning System (GPS) and the use of accurate atomic clocks for time keeping. Some of the successful aspects of GPS have been extended to a relatively new navigation technique known as LiAISON (Linked Autonomous Interplanetary Satellite Orbit Navigation) [58, 60]. LiAISON has the ability to extend some aspects of GPS to orbits in new regimes beyond LEO for which a minimum of two satellites in a LiAISON constellation are all that is necessary to perform absolute autonomous navigation.

LiAISON navigation typically involves two or more satellites collecting relative tracking data to determine the absolute positions and velocities of each vehicle in space over time. In most applications, relative measurements only permit a system of vehicles to determine their relative states. For instance, any normal constellation of Earth orbiters could rotate the entire constellation about the Earth and achieve the same relative tracking measurements. LiAISON navigation works because the spacecraft constellation is in an asymmetric gravity field: one that involves both the Earth and the Moon. A time-series of satellite-to-satellite measurements in such a system is unique and fixed to the positions of the Earth and Moon. Therefore, LiAISON navigation results in the

determination of both satellites' absolute trajectories using relative measurements. The LiAISON navigation technique has been shown to be very beneficial when applied to the navigation of lunar satellites, including low lunar orbiters and lunar libration orbiters [52, 56–58, 60–62, 155]. Chapter 5 will provide a more in depth discussion and analysis of LiAISON.

1.5 Thesis Overview

This first chapter provides the necessary background and history of research and operations conducted crewed navigation, navigation in LPOs, autonomous navigation, and LiAISON. The overview of operational mission navigation abilities is necessary to provide a baseline for what is possible with ground-only tracking data types. While a majority of these missions have been flown around the Sun-Earth libration points, their experiences are directly applicable to the Earth-Moon system. LEO crewed navigation has become commonplace with the introduction of GPS. The only experiences relatable to the work conducted in this thesis arise from the Apollo program experiences. Finally, an overview of autonomous navigation techniques was given to provide the necessary background in the current status of this field.

Chapter 2 describes the dynamical models used throughout this dissertation. These include such topics as the Circular Restricted Three Body Problem (CRTBP), periodic and quasiperiodic orbits, the state transition and monodromy matrices, stability, and satellite dynamics in the JPL full ephemeris model.

Chapter 3 provides an in-depth discussion on modern orbit determination techniques for navigation and analysis. The original forms of the least-squares batch processor and sequential Kalman filters are presented for completeness. An overview of the Cramér-Rao lower bound is provided to acquaint the reader with a technique not commonly used in the spacecraft navigation industry. A detailed description of stochastic processes and shaping filters is provided necessary to understand the implementation of compound stochastic processes. A survey of observability techniques is provided with a focus on linear system analysis. Finally, an overview of the measurement types utilized in this work is provided.

Chapter 4 presents research providing a baseline navigation ability for ground tracking using the operational ARTEMIS spacecraft tracking data. This chapter provides the necessary understanding of the difficulties and precision of navigation solutions for spacecraft traversing the Earth-Moon system being tracked by the current ground network. An overlap analysis is provided for insight into the precision of navigation solutions and the required amount of data to provide that precision. A detailed analysis of solar radiation pressure effects and maneuver estimation errors is also provided.

Chapter 5 discusses the background of LiAISON navigation in more detail. It also provides a discussion on the observability of LiAISON analyzing the information content of the radiometric range and range-rate data types. Section 5.2.3 provides an in-depth analysis of the observation effectiveness of Doppler type measurements in the Earth-Moon system, systematically mapping out regions where these observation types have limited ranging information. Finally, Section 5.3 analyzes the observability of LiAISON using numerical rank analysis techniques and observability criterium outlined in previous chapters.

Chapter 6 and 7 investigates the uncertainty propagation and their properties associated with spacecraft in halo orbits. Utilizing local Lyapunov exponents, an analysis of the local stability is provided relating to the orientation of the uncertainty when propagated. This analysis is then extended through the addition of a crewed vehicle disturbance and environment model. A similar analysis is conducted to provide insight into the effects the stochastic modeling of crewed behavior has on the uncertainty distribution when propagated in a halo orbit. A Monte Carlo analysis is provided to show that the uncertainty propagation remains in the linear regime for the timeframes of importance in this work.

Chapters 8 through 10 analyze several scenarios relevant for crewed exploration in the Earth-Moon system. Chapter 8 analyzes the capabilities of LiAISON supporting missions in Lagrange point orbits themselves. A focus on trade studies for GEO/TDRSS navigation types as well as libration point orbiters around EML-1 and EML-2. Chapter 9 focuses on crewed mission in low lunar orbit supported with LiAISON with a trade study for placing a navigation satellite at EML-1

or EML-2. Chapter 10 provides insight into the capabilities of LiAISON supplemented navigation for a crewed vehicle on a trans-lunar cruise. Each of these chapters provides a trade study to compare the capabilities of LiAISON when used as a supplemental navigation data type for ground based tracking networks.

Finally, Chapter 11 summarizes this thesis and the contributions it makes in the field of navigation. A suggestion of future topics and research is provided that would compliment this body of work.

Significant portions of this thesis have been pulled from publications and conference papers by the author. This includes text and figures generated for publication and presented at conference proceedings used in whole or modified to fit this thesis. Portions of Section 2.6 are from [85]. Chapter 3 has contributions from [86] and [83]. Chapter 4 has reproduction of figures and significant contributions from [84]. Section 5.1 is modified from [85]. Chapters 6 and 7 are pulled from [88]. Chapter 8 has signifiant portions from both [85] and [121]. Chapter 9 reproduces images from [122]. Finally, Chapter 10 stems from [87].

1.6 Thesis Contributions

The primary contributions of this dissertation are listed below. The final chapter of this thesis discusses the contributions in more detail as well as the conclusions drawn from this work.

- Post-processing and in depth analysis of ARTEMIS navigation solutions, precision, and techniques.
- Development of observability and information content for LiAISON constellations.
- Analysis of uncertainty propagation and influences of local stability in a halo orbit.
- Development of discrete compound Poisson noise process for crew disturbance modeling.
- Navigation performance trade study analysis of crewed vehicles in halo orbits, low lunar orbits, and trans-lunar cruise trajectories.

Chapter 2

Dynamical Models

The studies conducted in this work use several different dynamical models to represent a spacecraft's physical interaction with the Earth-Moon environment. The three most important models used in the following studies are the Two-Body Model, the Circular Restricted Three-Body model, and the Full Ephemeris approximation of the Solar System. The Two-Body model is typically used when the spacecraft is near a central body with no other significant celestial body perturbing the trajectory. The Three-Body model is often used when there is a significant celestial body perturbing a spacecraft. This model is often used in the Earth-Moon system as well as the Sun-Earth system. There are a variety of simplifications to the Three-Body model, but a common one is the Circular Restricted Three-body Problem (CRTBP). This model assumes that both of the perturbing bodies orbit in a perfectly circular fashion. The Full Ephemeris model uses precise positions of the celestial bodies to model the perturbations on a spacecraft.

2.1 Two-Body Problem

There has been a long history of description and analysis concerning the motion of two bodies orbiting each other, where each is a massive spherically-symmetric body that can be represented as a point mass. While there have been numerous treatise on the two-body problem in the field of orbital mechanics, the information here is presented in brevity. Newton developed his universal law of gravitation, formulated in Philosophiæ Naturalis Principia Mathematica [111], in 1687. An excerpt from Proposition 75, Theorem 35, describing the universal law of gravitation:

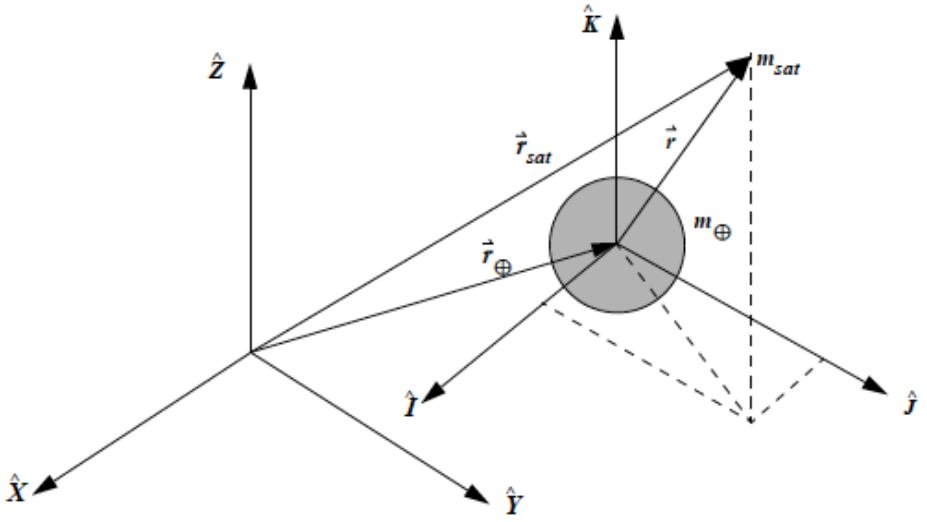

Figure 2.1: Diagram of the Two-Body Problem [154].

> *Every point mass attracts every single other point mass by a force pointing along the line intersecting both points. The force is proportional to the product of the two masses and inversely proportional to the square of the distance between them.*[111]

The modern day equation that describes this relationship is given by

$$\vec{F}_g = -\frac{Gm_1m_2}{r^3}\vec{r}, \tag{2.1}$$

where $\vec{F}_g$ is the gravitational force, G is the universal gravitational constant, m_1 and m_2 are the masses of the two bodies, and $\vec{r}$ is the vector from one body to the other. The fraction $\vec{r}/r$ denotes the unit vector pointing from one body to the other for a cartesian description of the gravitational force.

Figure 2.1 is a diagram of the Two-Body Problem with the defined position vectors $\vec{r}_sat$, $\vec{r}_1$ and $\vec{r}$. These vectors are expressed in an inertial cartesian coordinate system allowing one to differentiate the vector equations without the need to take the derivatives of the coordinate system itself. The vector of most importance is that of the relative position vector between the main perturbing body m_1 and the satellite m_2. This vector is expressed as

$$\vec{r}_{1,sat} = \vec{r}_{sat} - \vec{r}_1. \tag{2.2}$$

Due the the use of an inertial coordinate system, this position vector can be differentiated twice to give the second derivative describing the acceleration of the spacecraft relative to the main perturbing body, where

$$\ddot{\vec{r}}_{1,sat} = \ddot{\vec{r}}_{sat} - \ddot{\vec{r}}_1. \tag{2.3}$$

Using Newton's second law combined with the universal law of gravitation allows us to derive the inertial forces acting upon each body. Solving for the relative acceleration vector $\ddot{\vec{r}}$ one gets

$$\ddot{\vec{r}} = -\frac{G(m_1 + m_2)}{r^3}\vec{r}. \tag{2.4}$$

If the secondary mass of the satellite $m_2 << m_1$ then we can simplify this equation and use what is known as the gravitational constant μ, where $\mu = Gm_1$. Thus the simplified acceleration of the spacecraft relative to the main perturbing body is

$$\ddot{\vec{r}} = -\frac{GM}{r^3}\vec{r}. \tag{2.5}$$

It is important to clarify the assumptions that govern the derivation of the two-body problem so that one may understand their limitations during implementation to approximate a real-world system. The following are the assumptions that went into the derivation of the two-body problem:

- The coordinate system used for the derivation of the equations of motion is that of an idealized inertial reference frame.
- The mass of the satellite is infinitesimal when compared to that of the main perturbing body.
- The bodies of the main perturbing body and that of the satellite are assumed to be spherically symmetric with a uniform density. This allows for the simplification and assumption that these bodies act as a point mass.
- There are no other external forces acting upon the system.

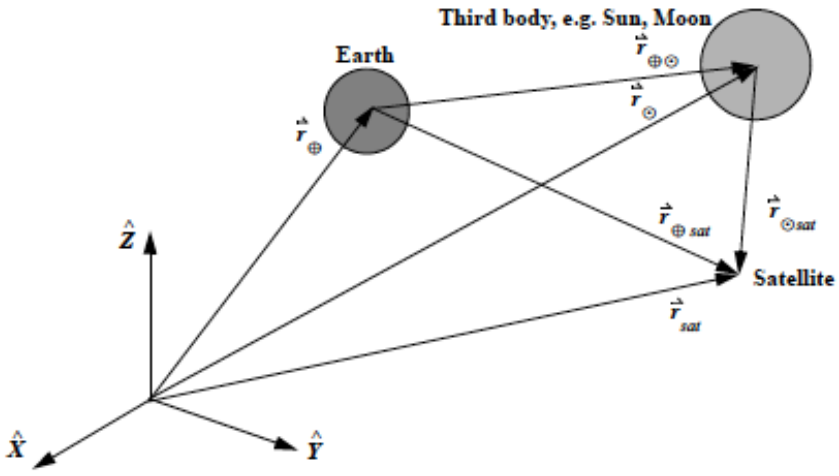

Figure 2.2: Diagram of the Three-Body Problem [154].

2.2 Three-Body Problem

A natural extension of the Two-Body problem where you only have one main perturbing body and a satellite is that of the Three-Body problem where a secondary perturbing body is introduced. There are several systems in our solar system that can be modeled as a Three-Body system, but the one mainly used in this work is that of the Earth-Moon system. While Earth is the significant perturbing body, the Moon exhibits a non-negligible force on spacecraft in orbits within the Earth-Moon system, particularly those that are not in low Earth orbit or low Lunar orbit. The introduction of a third body adds another force upon the infinitesimal spacecraft mass and can be derived in a similar manner as the Two-Body problem. Figure 2.2 gives a representation of the relevant position vectors and bodies necessary to describe the equations of motion of the spacecraft within this system.

Since there is more than one perturbing body acting upon the spacecraft, we need to take into account multiple forces acting upon the spacecraft. For this, Newton's second law is used to sum up the forces such that

$$\sum \vec{F} = \frac{d(m\vec{v})}{dt} = m\vec{a}, \tag{2.6}$$

where m is the mass of the satellite and $\vec{a}$ is the acceleration that the satellite experiences due to

the perturbing bodies. Form Figure 2.2 we can see that the vector from the main perturbing body (Earth) to the satellite can be defined by

$$\vec{r}_{1,sat} = \vec{r}_{sat} - \vec{r}_1, \tag{2.7}$$

where $\vec{r}_{sat}$ is the inertial vector of the satellite and $\vec{r}_1$ is the inertial vector of the main perturbing body. Since we have defined this to be in an inertial coordinate system, we can take the second derivative such that

$$\ddot{\vec{r}}_{1,sat} = \ddot{\vec{r}}_{sat} - \ddot{\vec{r}}_1. \tag{2.8}$$

This provides us with a description of the relative motion that the satellite will experience relative to the main perturbing body. Using Newton's second law as well as his law of universal gravitation, we can write the relative motion equations as follows

$$\sum \vec{F} = m_1 \ddot{\vec{r}} = -\frac{Gm_1 m_2}{r_{12}^3}\vec{r}_{12} - \frac{Gm_1 m_3}{r_{13}^3}\vec{r}_{13}. \tag{2.9}$$

This equation can be further simplified such that

$$\ddot{\vec{r}}_{1,sat} = -\frac{G(m_1 + m_{sat})}{r_{1,sat}^3}\vec{r}_{1,sat} + Gm_2\left(\frac{\vec{r}_{sat,2}}{r_{sat,2}^3} - \frac{\vec{r}_{1,2}}{r_{1,2}^3}\right). \tag{2.10}$$

This now expresses the satellite's motion relative to a main perturbing body as influenced by another significant perturbing body. Inspection of the equation will show that the left portion is simply the solution to the Two-Body problem. However, the introduction of another body has modified this acceleration both directly and indirectly. The direct effect is an acceleration from the secondary perturbing body acting upon the satellite itself. The indirect effect comes from the secondary perturbing body accelerating the main perturbing body. Nearly all of the time, the spacecraft mass m_{sat} is neglected and the combination of $\mu_i = Gm_i$ is used as defined in the Two-Body problem.

2.2.1 CRTBP

The research conducted in this thesis relies on the use of the Circular Restricted Three-body Problem (CRTBP) and full ephemeris models of the solar system. The CRTBP is a decent approximation of the dynamics of the Earth-Moon system. Slight variations in the Moon's orbit about the Earth cause the dynamics of the CRTBP and the full ephemeris to differ. In this work both models are used extensively, however, the CRTBP provides a basic understanding of the complex dynamics experienced by a spacecraft in an orbit about a Lagrange point. With this understanding, trajectories designed in the CRTBP can thus be translated into the more realistic full ephemeris model.

In the CRTBP model, there are two massive bodies orbiting their mutual barycenter with the third body being a massless spacecraft. The model assumes that both massive bodies orbit in the same plane and are perfectly circular. The spacecraft experiences forces due to the gravitational influence of both massive bodies simultaneously. Figure 2.3(a) depicts the geometry of the CRTBP. The primary body has a mass given by m_1 and the less massive secondary body has a mass given m_2 where the three-body gravitation parameter μ is defined by

$$\mu = \frac{m_2}{m_1 + m_2}. \tag{2.11}$$

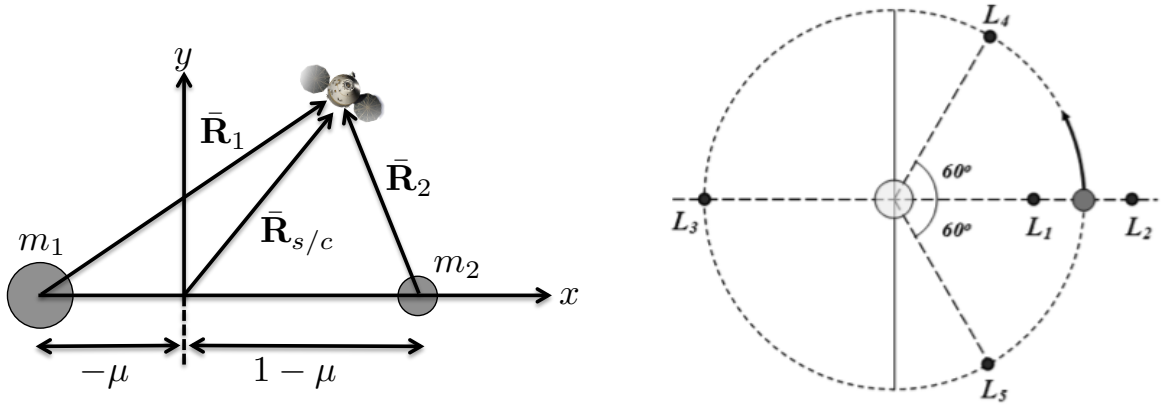

(a) CRTBP

(b) Lagrange Points

Figure 2.3: Diagrams of the CRTBP: (a) CRTBP geometry with a rotating, nondimensional coordinate frame, and (b) the Lagrange points in the CRTBP.

The mass of the primary body m_1 is nondimensionalized such that it has a mass of $1-\mu$ and the secondary body has a mass of μ. A nondimensional length unit (LU) is defined to be the distance between the two primaries. The time unit for the system (TU) is defined such that the secondary orbits the primary in 2π TU. The equations of motion for the CRTBP are given by

$$\ddot{x} - 2\dot{y} = x - (1-\mu)\frac{x+\mu}{R_1^3} - \mu\frac{x+\mu-1}{R_2^3}, \tag{2.12}$$

$$\ddot{y} + 2\dot{x} = \left(1 - \frac{1-\mu}{R_1^3} - \frac{\mu}{R_2^3}\right) y, \tag{2.13}$$

$$\ddot{z} = \left(\frac{\mu-1}{R_1^3} - \frac{\mu}{R_2^3}\right) z, \tag{2.14}$$

where $R_1 = \sqrt{(x+\mu)^2 + y^2 + z^2}$ and $R_2 = \sqrt{(x+\mu-1)^2 + y^2 + z^2}$.

From this, five equilibrium points can be obtained in the rotating CRTBP frame. These are specific locations where the gravitational acceleration is balanced by the centripetal acceleration. These points are known as Lagrange points and are shown in Figure 2.3(b). A satellite placed on one of these points with zero velocity will remain there. The three collinear Lagrange points, L_1, L_2, and L_3 are unstable equilibrium points.

2.2.2 Periodic and Quasiperiodic Orbits

A plethora of three-body orbits exist in the CRTBP [13]. This dissertation focuses on orbits that remain in the vicinity of the Lagrange points, known as LPOs. Two of the many three-body orbits that are of most concern for this work are the Lissajous and Halo orbits. For a spacecraft orbiting a Lagrange point, there exists analytic expressions describing the trajectory that show periodic motion in the orbit plane of the primary and secondary masses. There also exists periodic motion in the out-of-plane direction [130]. One of the solutions to these expressions is an orbit that traces out a Lissajous figure whose class of orbits are known as Lissajous orbits [66]. Ref. [131] developed up to a fourth order analytic expansion of the motion of a satellite in a Lissajous orbit. The position and velocity of the orbit can be computed once an amplitude of the x-y plane oscillation and out-of-plane oscillation is chosen.

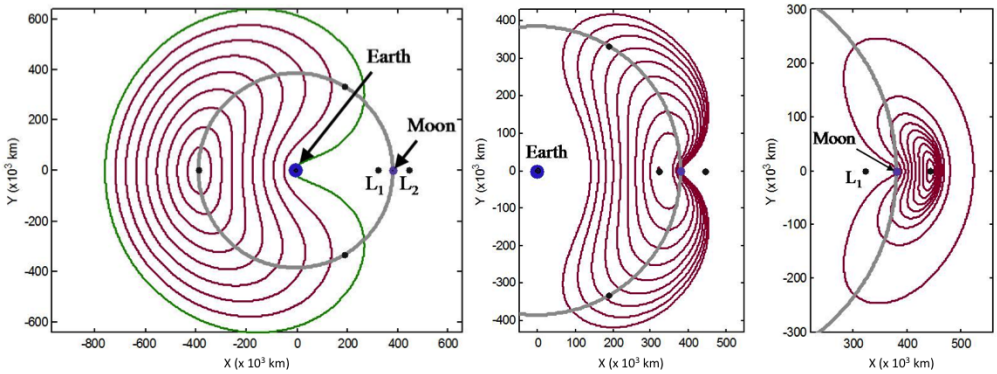

Figure 2.4: Lyapunov orbits [119].

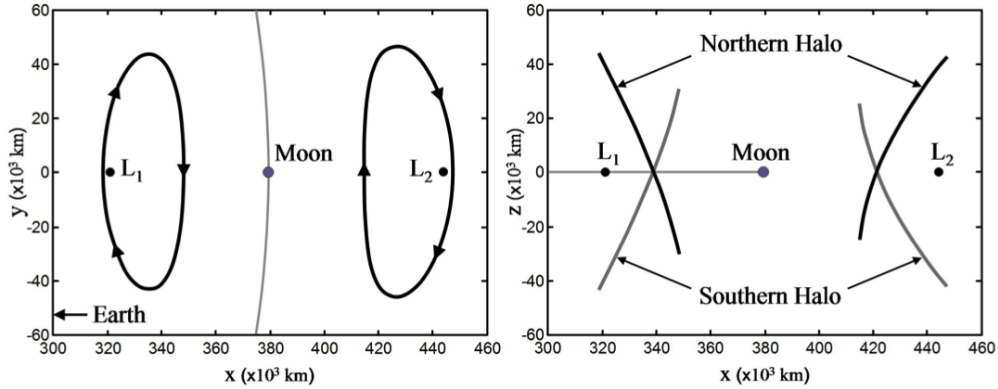

Figure 2.5: Halo orbits [119].

If the libration point orbit amplitudes are chosen to be large enough, the frequencies of the two oscillations can match forming a periodic orbit known as the halo orbit. Ref. [32] provides an analytical solution for halo orbits in the Earth-Moon system while Ref. [130] provides a third order analytic solution applicable to any three-body system. Halo orbits can also be found through numerical methods utilizing a guess of the initial state at the x-z plane with a y velocity only. The orbit is then integrated until the next x-z plane crossing using the state transition matrix to differentially correct the initial state until there is zero velocity in the x and z direction making the plane crossing perpendicular. This process is repeated iteratively until a solution is converged upon [65]. The introduction of a phase angle τ is a convenient way to define where a spacecraft is located in the halo orbit. A phase angle of zero indicates when the spacecraft is located at the intersection of the x-z plane traveling in the y direction. The phase angle increases in the direction of motion such that

$$\tau(t) = 2\pi \frac{t - t_0}{p}, \tag{2.15}$$

where $t - t_0$ is the time since the x-z plane intersection and p is the orbital period.

2.3 State Transition and Monodromy Matrix

The state transition matrix $\Phi(t, t_0)$ is used to determine the relationship between state errors $\delta\mathbf{x}$ at a specific time t to the state errors $\delta\mathbf{x}_0$ at an initial time t_0. The state transition matrix gives an indication as to how initial errors propagate along the nominal trajectory over a specific period of time. The state transition matrix can be compute using analytical, numerical integration techniques, or by finite differencing. In general, the state transition matrix for a given state

$$\mathbf{X} = \begin{bmatrix} \mathbf{r}^{\mathrm{T}}, & \dot{\mathbf{r}}^{\mathrm{T}} \end{bmatrix}^{\mathrm{T}} \tag{2.16}$$

can be formed by the partial derivatives of the state with respect to the initial state such that

$$\Phi(t, t_0) = \frac{\partial \mathbf{X}(t)}{\partial \mathbf{X}(t_0)}. \tag{2.17}$$

The initial conditions for the state transition matrix are thus $\Phi(t_0, t_0) = I$ where I is the identity matrix. The state transition matrix can be solved using the following relationship where

$$\dot{\Phi}(t, t_0) = A(t)\Phi(t, t_0), \tag{2.18}$$

where $A(t)$ is the Jacobian matrix of the state $\mathbf{X}$ at time t and is computed as

$$A(t) = \frac{\partial \dot{\mathbf{X}}(t)}{\partial \mathbf{X}(t)}. \tag{2.19}$$

The monodromy matrix exists for any periodic orbit and is defined as the state transition matrix that describes a perturbation over exactly one orbital period P such that

$$M = \Phi(t_0 + P, t_0). \tag{2.20}$$

The matrix M contains information describing the particles path across every region that it traverses in the orbit.

2.4 Stability

In general, the stability of an orbit that is periodic can be determined through analysis of the eigenvalues of it's monodromy matrix. The monodromy matrix is the state transition matrix propagated along the trajectory for a full orbit and provides information on how slight deviations in the state variables propagates along the trajectory. If the initial state of a spacecraft on an unstable orbit is perturbed, the perturbed trajectory will deviate from the original trajectory exponentially. From analyzing the eigenvalues of the monodromy matrix, one can determine the stability of a periodic orbit from it's eigenvalues.

The eigenvalues of a periodic orbit in the CRTBP are the roots of the characteristic equation with each having a characteristic exponent, α, where the eigenvalues are given by $\lambda = e^{\alpha T}$. For Keplerian orbits, there exists three pairs of eigenvalues equal to one. For this case, a perturbation in the initial state neither grows nor decays exponentially after a full orbit. CRTBP periodic orbit eigenvalues can have eigenvalue pairs that include real values not equal to one and possible complex number pairs. In general, if a periodic orbit's monodromy matrix has eigenvalues outside of the range $[-1, 1]$ then that orbit is asymptotically unstable. Typically, if the eigenvalues are between $(-1, 1)$ then the orbit is stable, however, in the CRTBP the orbit is only stable if every eigenvalue pair is complex with the real part between $(-1, 1)$.

2.5 Full Ephemeris

The final model used in this body of work is that of the Full Ephemeris. The Two-Body and Three-Body models have been previously described and provide simplified understanding of the motion of a spacecraft under the influence of one or two main bodies. The next logical step is to consider N-bodies where there are no constraints on their locations like the CRTBP imposes. While the N-body problem can be expressed in simplified terms using unperturbed conic orbits, the next step taken in this work is to model the solar system with a detailed and accurate ephemeris provided by the Jet Propulsion Laboratory. These ephemerides provide precise positions and velocities of

all of the major solar system bodies.

The ephemerides provided by JPL have been used to support a variety of spacecraft missions for several decades now. These ephemerides have become the de facto source for precise states of celestial bodies in our solar system for applications that require the highest accuracy. Several versions of the ephemerides have existed over the past few decades with one of the earliest and widely used JPL ephemerides being DE200/LE200. This set was used widely between the 1980s to the early 2000s. Most commonly, it was used to describe the tabulated planetary positions in *The Astronomical Almanac* [1, 97, 142]. This work uses one of the more recent releases known as DE405 which replaced DE200 as the ephemeris used in *The Astronomical Almanac* since 2003 [2]. More recently, DE421 and DE430 have been released, with DE430 being the most up-to-date release.

The JPL ephemerides are numerically integrated solutions to the solar systems N-body problem. They are typically integrated in a solar system barycentric frame of reference with the time system being barycentric dynamical time (TDB). The equations of motion range from point mass forces due to the planetary bodies themselves, to relativistic effects, and mass distributions to represent asteroids. These integrations are fit to observations to produce the highest accuracy possible [141]. The integrations are typically valid for centuries with DE200 ranging from December 9, 1599 to March 31, 2169 and DE405 ranging from December 9, 1599 to February 20, 2201.

The position and velocity vectors obtained from the JPL ephemerides are referred to the solar system barycenter and are represented in the ICRF reference frame. They are distributed as a series of Chebyshev coefficients to evaluate the position and velocity vectors of any of the major planets. The ephemerides also provide rotational data for the Moon describing it's body-fixed orientation relative to the ICRF reference frame. The position of a body can be interpolated using the following Chebyshev polynomial interpolation:

$$R_i(t) = \sum_{k=0}^{n} a_k T_k(t) \tag{2.21}$$

where $T_k(t)$ is the Chebyshev polynomial of the first kind with corresponding coefficient a_k that

are given in the ephemeris file. The velocity can be obtained by simply taking the derivative of the Chebyshev polynomial such that

$$V_i(t) = \sum_{k=0}^{n} a_k k T_{k-1}(t), \tag{2.22}$$

where $kT_{k-1}(t)$ is the derivative of $T_k(t)$. The Chebyshev polynomial can be computed in a recursive form such that

$$T_0(t) = 1, \tag{2.23}$$

$$T_1(t) = t, \tag{2.24}$$

$$T_{k+1}(t) = 2tT_k(t) - T_{k-1}(t). \tag{2.25}$$

Another important aspect of the JPL ephemerides is that they are normalized over time such that $-1 \leq t \leq 1$ for any give set of Chebyshev coefficients. Each set of coefficients have a valid time interval at which they are valid for. In order to normalize the requested time, the following equation can be used

$$t = \frac{JD - JD_0}{\Delta T} - 1, \tag{2.26}$$

where JD is the requested time that is on the interval $JD_0 \leq JD \leq JD_f$ and ΔT is simply $JD_f - JD_0$.

2.6 Satellite State Dynamics

In this work, an attempt is made at estimating the state of two satellites, their solar radiation pressure (SRP) coefficients, and associated biases in the measurement equations. A simplified state vector is used that contains both satellites' positions and velocities as well as the constant terms

previously mentioned as given in Eq. 2.27. The range bias term $\boldsymbol{\rho}_{\text{bias}}$ does not affect the satellite state dynamics but is part of the estimated state and is used in the filter and measurement equations.

$$\mathbf{X} = \begin{bmatrix} \mathbf{r}_1^{\mathrm{T}} & \mathbf{v}_1^{\mathrm{T}} & \mathbf{r}_2^{\mathrm{T}} & \mathbf{v}_2^{\mathrm{T}} & \delta C_{R,1} & \delta C_{R,2} & \mathbf{w}_1^{\mathrm{T}} & \mathbf{w}_2^{\mathrm{T}} & \boldsymbol{\rho}_{\text{bias}}^{\mathrm{T}} \end{bmatrix}^{\mathrm{T}}. \tag{2.27}$$

The first four elements of the state vector are the position and velocities (both vectors have a dimension of 3) of the two spacecraft in the Geocentric Celestial Reference Frame (GCRF). The remaining elements of the state vector are deviations from *a priori* values of the SRP reflectivity coefficients, empirical acceleration vectors for both satellites (each vector has a dimension of 3), and the range biases being estimated for each observation link (a total of 5 in this work).

The time evolution of the state vector $\mathbf{X}$ is given by a system of nonlinear first order differential equations. In this work, the time evolutions of the position and velocity vectors of a spacecraft are given the following dynamics:

$$\begin{bmatrix} \dot{\mathbf{r}}_i \\ \dot{\mathbf{v}}_i \end{bmatrix} = \begin{bmatrix} \mathbf{v}_i \\ \mathbf{a}_g(t, \mathbf{r}_i) + \mathbf{a}_{SRP}(t, \mathbf{r}_i) + \mathbf{a}_{n\text{-}body}(\mathbf{r}_i, \mathbf{r}_{\oplus 3}) + [\gamma]_{RTN}^{\mathrm{T}} \mathbf{w}_i \end{bmatrix}, \tag{2.28}$$

where $\mathbf{a}_g(t, \mathbf{r})$ is the gravitational accelerations due to two-body and Earth's non-spherical body. In addition to the gravitational acceleration, SRP $\mathbf{a}_{SRP}(t, \mathbf{r}_i)$, n-body perturbations $\mathbf{a}_{n\text{-}body}(\mathbf{r}_i, \mathbf{r}_{\oplus 3})$, and empirical accelerations $\mathbf{w}_i$, are acting upon the spacecraft.

2.6.1 Gravity

The Earth's gravitational potential including the two-body term is commonly given in terms of spherical harmonics as

$$U(x, y, z) = \frac{\mu}{r} \left[1 + \sum_{l=2}^{\infty} \sum_{m=0}^{l} \left(\frac{R}{r} \right)^l P_{l,m}(\sin \phi_{\text{gc}}) \left\{ C_{l,m} \cos(m\lambda) + S_{l,m} \sin(m\lambda) \right\} \right]. \tag{2.29}$$

The normalized Cartesian spherical harmonic model is used in this work for the calculation of local gravitational acceleration [48]. The normalized Cartesian model does not rely on spherical coordinates and does not contain any singularities as seen in the classical formulation. The acceleration vector from spherical harmonics is given in International Terrestrial Reference Frame (ITRF) and must be rotated back to GCRF. The conversion from the Earth-centered, Earth-fixed reference frame to the Earth-centered inertial reference frame is computed through the 1976 IAU Precession, 1980 IAU Nutation (no IERS corrections are used), Earth rotation parameters, and polar motion [101].

2.6.2 Third-body perturbations

In addition to the central body non-spherical gravitational acceleration, the gravitation effects of multiple bodies (n-body) are determined. This can include extra perturbations due to the Sun, Moon, or other planets in the solar system. The acceleration $\mathbf{a}_{n\text{-}body,i}$ due to the gravitational attraction of body k of the n-bodies is given by

$$\mathbf{a}_{n\text{-}body,k} = -\mu_k \left[\frac{\mathbf{r}_{k,sat}}{r^3_{k,sat}} + \frac{\mathbf{r}_{\oplus,k}}{r^3_{\oplus,k}} \right], \tag{2.30}$$

where μ_k is the gravitational parameter of the k^{th} body, $\mathbf{r}_{k,sat}$ is the vector from the k^{th} body to the satellite, and $\mathbf{r}_{\oplus,k}$ is the vector from the central body to the k^{th} body. The position of celestial bodies is computed from the JPL DE 405 ephemerides [63, 141].

2.6.3 SRP

The solar radiation pressure model used is based on a constant area, constant reflectance model. The shadow model used determines an approximate value of the percentage of the Sun's face that is visible from the spacecraft location. The radii of the bodies used in the shadow model are taken from the JPL DE405 (Ref. [141] and [63]) ephemeris, and the solar radiation pressure is adjusted based on the distance from the sun. The acceleration due to SRP is given by

$$\mathbf{a}_{SRP} = P_{SRP} C_R \frac{A_\odot}{m} \frac{\mathbf{r}_{\odot sat}}{|\mathbf{r}_{\odot sat}|}, \tag{2.31}$$

where C_R is the reflectivity of the spacecraft, $A_\odot$ is the cross-sectional area of the spacecraft facing the Sun, m is the mass of the spacecraft, $\mathbf{r}_{\odot sat}$ is the vector from the center of the Sun to the spacecraft, and P_{SRP} is the solar radiation pressure of the Sun. The value used for P_{SRP} is about 4.5298×10^{-6} Pa at one AU. The variation in P_{SRP} for various distances from the sun is calculated by

$$P_{SRP} = P_{SRP,AU} \frac{(149,597,870\ km)^2}{|\mathbf{r}_{\odot sat}|^2}. \tag{2.32}$$

Chapter 3

Orbit Determination Methods

3.1 Introduction

Estimation theory is derived from the field of statistics primarily dealing with the estimation of parameters that are based on a set a measured or empirical data. These measurements and underlying physics can have a random component affecting the underlying physical setup. This ultimately affects the distribution of those measured values necessary to describe the physical phenomena that one is trying to understand. An estimator is a mathematical tool that is commonly used to approximate the underlying physics and unknowns using measurements.

In this sense, a statistical parameter estimator for orbital systems attempts to determine the most probable estimate of a spacecraft's state at some epoch. The state of the system is governed by dynamics that can be modeled to a certainty accuracy level based on previous observations or the solar system by astronomers and mathematicians over the past centuries. For the satellite orbit estimation, there is generally an abundance of measurements available when compared to the parameters being estimated, thus the system that is being estimated is generally an over-determined problem. In most cases an L_2-norm estimator is the desired solution technique commonly employed.

The state of a dynamical system refers to all of the parameters required to predict the motion of an object in that system. In the case of this work, the object is typically a satellite under the influence of the gravitational effects of the celestial bodies, as well as radiation pressure from the sun, and non-spherical gravitational effects of the bodies. These are not the only physical parameters that govern the motion of a satellite, however, they are some of the most significant for

the Earth-Moon system being explored.

A satellite state can range from simply the position and velocity at an epoch of the satellite to physical parameters that describe the shape of the satellite, as well as parameters that govern the physical properties of celestial bodies. This set of parameters can then be broken up into dynamical and measurement model parameters. Dynamical parameters refer to those parameters that only affect the physical motion and forces acting upon the satellite. Measurement model parameters are those that govern the behavior and physics of the measurement itself. Both of these types of parameters are estimated in the orbit determination process.

The orbit determination process is typically as follows. At some initial epoch, the state of the spacecraft is integrated using a set of dynamical equations forward or backwards in time to generate a predicted ephemeris. This initial state is technically never known and is generally a best guess based on a variety of initial orbit determination procedures. Once the predicted ephemeris is integrated, predicted measurements are computed to mimic what the real measurements will be. These two sets of measurements, observed and computed, are then compared to generate residuals, These residuals are just the differences between the observed and computed measurements. The predicted values will differ from the observed values for several reasons. Some of the possible reasons are outlined as follows:

- Errors introduced into the observed measurement due to equipment.
- Unmodeled error sources in the observed values.
- Approximations or assumptions made on the physical model used to generate the predicted ephemeris.
- Errors in the computational process used to generate the solution.
- Numerical errors due to compute precision.

A solution to the state is generated in a statistical sense using some type of L_2-norm estimator. The estimator generates an uncertainty based on processing all of the measurements and relates

it to the estimated state at the initial epoch. If there is structure in the residuals, typically the estimator is iterated to reduce the spread in the residuals until a solution is converged upon. The optimality of this solution is defined in a statistical sense and the techniques used to obtain it can vary widely.

There can be an infinite amount or combination of parameters that can be estimated. However, in order for a parameter to be estimable it must have an explicit or implicit dependence on the satellite dynamics or measurement model. Even if one has a set of parameters that govern either the dynamics or measurements, it is also possible that the parameters can be correlated and thus an estimate of each parameter is not possible since they cannot be separated in an estimation sense. In the field of orbit determination, it is generally a poor choice to estimate any set of parameters that are a linear combination of each other. A common issue involves the estimation of parameters governing the solar radiation pressure or drag forces on a spacecraft. Both governing dynamics depend on a combination of three parameters: mass, area, and a varying environmental property (solar radiation flux for SRP and atmospheric density for Drag). In the basic equations, these three parameters are linear combinations and thus cannot be separable in most cases. This generally leads to poor conditioning of the covariance matrix describing the uncertainty and correlations of the parameters.

3.2 Least Squares Estimators

An L_2-norm estimator, or least squares estimator, is the most common type of estimation theory used in orbit determination. The least squares estimator attempts to solve the estimation problem by minimizing the sum of the squares of the observation residuals. This is done by using the following cost function

$$J(\mathbf{x}) = \frac{1}{2}\boldsymbol{\epsilon}^{\mathrm{T}}\boldsymbol{\epsilon}, \tag{3.1}$$

where $\mathbf{x}$ is the estimated state and $\boldsymbol{\epsilon}$ is the measurement errors. A measurement system is thus

described as

$$\mathbf{y} = \mathbf{H}\mathbf{x} + \boldsymbol{\epsilon}, \tag{3.2}$$

where $\mathbf{y}$ are the observed values and $\mathbf{H}$ is the measurement mapping matrix that relates the state to a specific epoch. Thus, the cost function attempts to minimize the sum of the squares of the observation errors. Substituting in the equation for the measurement system the cost function can be expressed by

$$J(\mathbf{x}) = \sum_{i=1}^{l} \frac{1}{2}(\mathbf{y}_i - \mathbf{H}_i\mathbf{x})^{\mathrm{T}}(\mathbf{y}_i - \mathbf{H}_i\mathbf{x}). \tag{3.3}$$

Finding the minima of this equation is trivial yet a certain condition arises that imposes the fact that $\mathbf{H}^{\mathrm{T}}\mathbf{H}$ must be positive definite implying that $\mathbf{H}$ must be full rank. This is an important condition that describes the observability of the system and must be taken note of. The solution for this least squares estimate is given by

$$\hat{\mathbf{x}} = (\mathbf{H}^{\mathrm{T}}\mathbf{H})^{-1}\mathbf{H}^{\mathrm{T}}\mathbf{y}. \tag{3.4}$$

This expression is the well known solution for the least squares problem given a set of linear observation state relationship $\mathbf{y} = \mathbf{H}\mathbf{x} + \boldsymbol{\epsilon}$.

3.3 Batch Processor

The batch processor is used when it is desired to obtain an estimate of the state deviation vector $\mathbf{x}_0$ at some reference time, t_0. If we are given a set of initial conditions $\mathbf{X}_0^*(t_0)$, an *a priori* estimate $\bar{\mathbf{x}}_0$ and its associated error variance-covariance matrix, $\bar{\mathbf{P}}_0$, the normal equation form of $\hat{\mathbf{x}}_0$ derived from the minimum variance estimate with *a priori* information can be used to obtain the best estimate of $\mathbf{x}_0$. Utilizing a set of observations, the normal equation for $\hat{\mathbf{x}}_0$ is given by

$$\left(\mathbf{H}^{\mathrm{T}}\mathbf{R}^{-1}\mathbf{H} + \bar{\mathbf{P}}_0^{-1}\right)\hat{\mathbf{x}}_0 = \mathbf{H}^{\mathrm{T}}\mathbf{R}^{-1}\mathbf{y} + \bar{\mathbf{P}}_0^{-1}\bar{\mathbf{x}}_0. \tag{3.5}$$

The matrices $\mathbf{H}^{\mathrm{T}}\mathbf{R}^{-1}\mathbf{H}$ and $\mathbf{H}^{\mathrm{T}}\mathbf{R}^{-1}\mathbf{y}$ must be accumulated for use in the batch processor. If the observations at any given time are uncorrelated then $\mathbf{R}$ is a block diagonal matrix, these matrices can be accumulated as follows:

$$\mathbf{H}^{\mathrm{T}}\mathbf{R}^{-1}\mathbf{H} = \sum_{i=1}^{l} \left[\tilde{\mathbf{H}}\Phi(t_i, t_0)\right]^{\mathrm{T}} \mathbf{R}_i^{-1}\tilde{\mathbf{H}}_i\Phi(t_i, t_0), \tag{3.6}$$

$$\mathbf{H}^{\mathrm{T}}\mathbf{R}^{-1}\mathbf{y} = \sum_{i=1}^{l} \left[\tilde{\mathbf{H}}_i\Phi(t_i, t_0)\right]^{\mathrm{T}} \mathbf{R}_i^{-1}\mathbf{y}_i, \tag{3.7}$$

where Φ is the state transition matrix and is obtained by integrating

$$\dot{\Phi}(t, t_k) = \mathbf{A}(t)\Phi(t, t_k), \tag{3.8}$$

subject to the initial conditions

$$\Phi(t_k, t_k) = \mathbf{I}, \tag{3.9}$$

along with the reference trajectory $\mathbf{X}^*(t)$. The matrix $\mathbf{A}(t)$ is evaluated along the reference trajectory $\mathbf{X}^*(t)$ and is given by

$$\mathbf{A}(t) = \frac{\partial F(\boldsymbol{X}^*, t)}{\partial \boldsymbol{X}}, \tag{3.10}$$

where $F(\mathbf{X}^*, t)$ is the time derivative of the state vector $\mathbf{X}(t)$. The observation-state mapping matrix is thus given by

$$\tilde{\mathbf{H}}_i = \frac{\partial G(\boldsymbol{X}_i^*, t_i)}{\partial \boldsymbol{X}}, \tag{3.11}$$

where $G(\mathbf{X}^*, t)$ are the observation-state relationships evaluated on the reference trajectory. The variance-covariance matrix $\mathbf{P}_0$ can be obtained by inverting the information matrix Λ_0

$$\mathbf{P}_0 = \Lambda_0^{-1} = (\mathbf{H}^{\mathrm{T}}\mathbf{R}^{-1}\mathbf{H} + \bar{\mathbf{P}}_0^{-1})^{-1}. \tag{3.12}$$

3.4 Sequential Processors

3.4.1 Linearized Kalman Filter

An alternative to the batch processor in which the observations are processed when they are obtained is known as the sequential estimation algorithm or conventional Kalman filter. This algorithm is derived from the batch algorithm in a sequential manner. The dynamic model and observation model are respectively

$$\dot{\mathbf{X}}(t) = \mathbf{F}(\mathbf{X}, t), \tag{3.13}$$

$$\mathbf{Y}(t) = \mathbf{G}(\mathbf{X}, t). \tag{3.14}$$

These models are then linearized about their reference trajectory (denoted with a *) by

$$\dot{\mathbf{x}}(t) = \mathbf{A}(t)\mathbf{x}(t) + \mathbf{B}(t)\mathbf{n}(t), \tag{3.15}$$

$$\mathbf{y}(t) = \tilde{\mathbf{H}}(t)\mathbf{x}(t) + \boldsymbol{\epsilon}(t), \tag{3.16}$$

where $\mathbf{x}(t) = \mathbf{X}^*(t) - \mathbf{X}(t)$ and $\dot{\mathbf{x}}(t) = \dot{\mathbf{X}}^*(t) - \dot{\mathbf{X}}(t)$. Here, $\mathbf{n}(t)$ and $\boldsymbol{\epsilon}(t)$ are the dynamic and observation noise, respectively, and $\mathbf{B}(t)$ is the process noise mapping matrix.

An estimate $\hat{\mathbf{x}}_j$ and a covariance matrix $\mathbf{P}_j$ can be propagated forward in time t_k by

$$\bar{\mathbf{x}}_k = \Phi(t_k, t_j)\hat{\mathbf{x}}_j, \tag{3.17}$$

$$\bar{\mathbf{P}}_k = \Phi(t_k, t_j)\mathbf{P}_j\Phi^{\mathrm{T}}(t_k, t_j). \tag{3.18}$$

Assuming that an observation $\mathbf{y}_k$ exists at time t_k

$$\mathbf{y}_k = \tilde{\mathbf{H}}_k\mathbf{x}_k + \boldsymbol{\epsilon}_k. \tag{3.19}$$

The best estimate of $\mathbf{x}_k$ can be obtained by

$$\hat{\mathbf{x}}_k = \left(\tilde{\mathbf{H}}_k^{\mathrm{T}}\mathbf{R}_k^{-1}\tilde{\mathbf{H}}_k + \bar{\mathbf{P}}_k^{-1}\right)^{-1}\left(\tilde{\mathbf{H}}_k^{\mathrm{T}}\mathbf{R}_k^{-1}\mathbf{y}_k + \bar{\mathbf{P}}_k^{-1}\bar{\mathbf{x}}_k\right). \tag{3.20}$$

Similar to the batch processor, the variance-covariance matrix $\mathbf{P}_k$ at time t_k is obtained by

$$\mathbf{P}_k = \left(\tilde{\mathbf{H}}_k^{\mathrm{T}}\mathbf{R}_k^{-1}\tilde{\mathbf{H}}_k + \bar{\mathbf{P}}_k^{-1}\right)^{-1}, \tag{3.21}$$

which can be re-written as

$$\mathbf{P}_k = \bar{\mathbf{P}}_k - \bar{\mathbf{P}}_k\tilde{\mathbf{H}}_k^{\mathrm{T}}\left[\tilde{\mathbf{H}}_k\bar{\mathbf{P}}_k\tilde{\mathbf{H}}_k^{\mathrm{T}} + \mathbf{R}_k\right]^{-1}\tilde{\mathbf{H}}_k\bar{\mathbf{P}}_k. \tag{3.22}$$

The Kalman gain is then defined by

$$\mathbf{K}_k = \bar{\mathbf{P}}_k\tilde{\mathbf{H}}_k^{\mathrm{T}}\left[\tilde{\mathbf{H}}_k\bar{\mathbf{P}}_k\tilde{\mathbf{H}}_k^{\mathrm{T}} + \mathbf{R}_k\right]^{-1}. \tag{3.23}$$

Equation 3.22 can then be simplified to

$$\mathbf{P}_k = \left[\mathbf{I} - \mathbf{K}_k\tilde{\mathbf{H}}_k\right]\bar{\mathbf{P}}_k. \tag{3.24}$$

Substituting Eq. 3.21 into Eq. 3.20 and the derived $\mathbf{P}_k$ matrix and Kalman gain $\mathbf{K}_k$, the best estimate of the state deviation vector $\hat{\mathbf{x}}_k$ at time t_k is given by

$$\hat{\mathbf{x}} = \bar{\mathbf{x}}_k + \mathbf{K}_k[\mathbf{y}_k - \tilde{\mathbf{H}}_k\bar{\mathbf{x}}_k]. \tag{3.25}$$

In order to prevent $\mathbf{P}_k$ from losing its symmetric positive definite condition, the Joseph computation was introduced and is given by

$$\mathbf{P}_k = (\mathbf{I} - \mathbf{K}_k\tilde{\mathbf{H}}_k)\bar{\mathbf{P}}_k(\mathbf{I} - \mathbf{K}_k\tilde{\mathbf{H}}_k)^{\mathrm{T}} + \mathbf{K}_k\mathbf{R}_k\mathbf{K}_k^{\mathrm{T}}. \tag{3.26}$$

This formulation of $\mathbf{P}_k$ will always yield in a symmetric matrix but it may lose its positive definite condition for poorly observed systems.

3.4.2 Extended Kalman Filter

The extended sequential estimation algorithm was introduced in order to minimize the effects of nonlinearities in the conventional Kalman filter due to neglecting higher order terms in the linearization process. The main differences between the extended Kalman filter and the conventional one is that the reference trajectory $\mathbf{X}_k^*$ is updated after each observation is processed in order give the best estimate of the true trajectory. The reference trajectory $\mathbf{X}_k^*$ for the extended Kalman filter at some time t_k is given by

$$(\mathbf{X}_k^*)_{new} = \hat{\mathbf{X}}_k = \mathbf{X}_k^* + \hat{\mathbf{x}}_k. \tag{3.27}$$

Utilizing this updated reference trajectory in the conventional Kalman filter leads to $\hat{\mathbf{x}}_k = 0$ and thus $\bar{\mathbf{x}}_{k+1} = 0$. The reference trajectory and state transition matrix are then reinitialized and integrated from t_k to t_{k+1}. With $\hat{\mathbf{x}}_k = 0$, Eq. 3.25 is reduced to

$$\hat{\mathbf{x}}_{k+1} = \mathbf{K}_{k+1}\mathbf{y}_{k+1}. \tag{3.28}$$

3.5 Cramér-Rao Lower Bound

In the realm of orbit determination, there are many sequential estimation algorithms used to estimate the state and uncertainty of a spacecraft. These applications generally require the estimation of unknown deterministic variables from a set of discrete nonlinear observations. Most practical estimation methods are not capable of estimating the optimal solution in such a way that it approaches the estimation error lower bound. The Cramér-Rao inequality is a very powerful tool that is used to estimate filter performance [75, 149]. The Cramér-Rao lower bound (CRLB) can be calculated for any nonlinear system in which the truth trajectory is known and gives a limit on the best performance any nonlinear estimator can achieve. If $\mathbf{P}_k$ is the estimation error covariance matrix corresponding to any unbiased estimator of a set of unknown states, and $\mathbf{P}_k^*$ is the CRLB, then the inequality exists

$$\mathbf{P}_k \geq \mathbf{P}_k^* \equiv \mathbf{J}_k^{-1}, \tag{3.29}$$

such that $\mathbf{J}_k$ is the Fisher information matrix at time t_k. It has been shown that the extended Kalman filter covariance propagation equations linearized about the true trajectory correspond to the CRLB for a continuous-time nonlinear deterministic system with discrete nonlinear measurements [149]. Thus the recursive relationship for the Fisher information matrix is obtained by solving

$$\mathbf{J}_k = \Big(\mathbf{\Phi}(t_k, t_{k-1})\mathbf{J}_{k-1}^{-1}\mathbf{\Phi}(t_k, t_{k-1})^{\mathrm{T}}\Big)^{-1} + \tilde{\mathbf{H}}_k^{\mathrm{T}}\mathbf{R}_k^{-1}\tilde{\mathbf{H}}_k, \tag{3.30}$$

where $\mathbf{R}_k$ is the observation weighting matrix. This recursion process is initialized by setting the initial Fisher information matrix $\mathbf{J}_0 = \mathbf{P}_0^{-1}$. This formulation works well for cases that do not have process noise. However, for the covariance study performed in this work, an additive noise is necessary. Thus Eq. 3.29 is modified to include process noise and takes the form

$$\begin{aligned} \mathbf{J}_k &= \mathbf{Q}_{k-1}^{-1} + \tilde{\mathbf{H}}_k^{\mathrm{T}}\mathbf{R}_k^{-1}\tilde{\mathbf{H}}_k \\ &- \mathbf{Q}_{k-1}^{-1}\mathbf{\Phi}(t_k, t_{k-1})\Big(\mathbf{J}_{k-1} + \mathbf{\Phi}(t_k, t_{k-1})\mathbf{Q}_{k-1}^{-1}\mathbf{\Phi}(t_k, t_{k-1})^{\mathrm{T}}\Big)^{-1}\mathbf{\Phi}(t_k, t_{k-1})^{\mathrm{T}}\mathbf{Q}_{k-1}^{-1}, \end{aligned} \tag{3.31}$$

where $\mathbf{Q}$ is the process noise covariance. For this study, $\mathbf{Q}$ is computed such that

$$\mathbf{Q}_k = \mathbf{\Gamma}(t_k, t_{k-1})\mathbf{q}\mathbf{\Gamma}(t_k, t_{k-1})^{\mathrm{T}}. \tag{3.32}$$

3.6 Process Noise and Stochastics

Empirical acceleration estimation methods are more commonly known as reduced dynamic modeling (RDM) [102, 169]. Several methods exist to estimate these un-modeled accelerations. One such method attempts to estimate periodic accelerations with trigonometric coefficients at fixed frequencies [90, 93]. Another, called dynamic model compensation (DMC), utilizes an exponentially

time-correlated system noise process, known as a first-order Gauss-Markov process (GMP1) [10, 104, 148]. A third option lies in physically-based auto-covariance models describing errors of commission and omission in gravity [165–168]. A fourth variant exists in batch estimation, where piecewise-constant time-dependent accelerations can be included as unknown parameters [9]. Reference [110] developed an approach for estimating the colored noise parameters in the orbit determination process for correlation functions of gravity disturbing forces.

3.6.1 Shaping Filter

There are many cases in which a commonly employed white Gaussian noise model does not describe the system dynamic noise adequately. It would be more desirable to have a model that could match the empirical auto-covariance or power spectral density data of an observed system, and then generate a stochastic mathematical model to reproduce the empirical characteristics. If an observed set of data were samples of a stationary Gaussian process with known auto-covariance (or power spectral density), then a linear time-invariant system, or shaping filter, driven by white Gaussian noise, could provide such a model [96]. Moreover, it is often the case that only the first and second order statistics are known, for which a Gaussian process with the same first and second order statistics can be generated by a shaping filter.

The system dynamics were previously defined by Eq. (3.15) and Eq. (3.16) where the observation noise $\boldsymbol{\epsilon}(t)$ is postulated uncorrelated and the dynamic noise $\mathbf{n}(t)$ is a non-white, time-correlated, dynamic Gaussian noise. The latter is obtained by passing a white Gaussian noise, $\mathbf{w}(t)$, through a shaping filter defined by

$$\dot{\mathbf{x}}_{\mathrm{s}}(t) = \mathbf{A}_{\mathrm{s}}(t)\mathbf{x}_{\mathrm{s}}(t) + \mathbf{B}_{\mathrm{s}}(t)\mathbf{w}(t), \tag{3.33}$$

$$\mathbf{y}_{\mathrm{s}}(t) = \tilde{\mathbf{H}}_{\mathrm{s}}(t)\mathbf{x}_{\mathrm{s}}(t), \tag{3.34}$$

where the shaping filter output, $\mathbf{y}_{\mathrm{s}}(t) = \mathbf{n}(t)$, is used to drive the system defined by Eq. (3.15). An augmented state vector $\mathbf{x}_{\mathrm{a}}(t)$ is then defined through

$$\mathbf{x}_{\mathrm{a}}(t) = \begin{bmatrix} \mathbf{x}(t) \\ \mathbf{x}_{\mathrm{s}}(t) \end{bmatrix}, \tag{3.35}$$

where the augmented state equation is given by

$$\begin{bmatrix} \dot{\mathbf{x}}(t) \\ \dot{\mathbf{x}}_{\mathrm{s}}(t) \end{bmatrix} = \begin{bmatrix} \mathbf{A}(t) & \mathbf{B}(t)\tilde{\mathbf{H}}_{\mathrm{s}}(t) \\ \mathbf{0} & \mathbf{A}_{\mathrm{s}}(t) \end{bmatrix} \begin{bmatrix} \mathbf{x}(t) \\ \mathbf{x}_{\mathrm{s}}(t) \end{bmatrix} + \begin{bmatrix} \mathbf{0} \\ \mathbf{B}_{\mathrm{s}}(t) \end{bmatrix} \mathbf{w}(t), \tag{3.36}$$

or

$$\dot{\mathbf{x}}_{\mathrm{a}}(t) = \mathbf{A}_{\mathrm{a}}(t)\mathbf{x}_{\mathrm{a}}(t) + \mathbf{B}_{\mathrm{a}}(t)\mathbf{w}(t), \tag{3.37}$$

and its associated output equation

$$\begin{aligned} \mathbf{y}_{\mathrm{a}}(t) &= \begin{bmatrix} \tilde{\mathbf{H}}(t) & \mathbf{0} \end{bmatrix} \begin{bmatrix} \mathbf{x}(t) \\ \mathbf{x}_{\mathrm{s}}(t) \end{bmatrix} + \boldsymbol{\epsilon}(t), \\ &= \tilde{\mathbf{H}}_{\mathrm{a}}(t) \quad \mathbf{x}_{\mathrm{a}}(t) + \boldsymbol{\epsilon}(t). \end{aligned} \tag{3.38}$$

3.6.2 Stochastic Time Update

The previous section developed a set of equations for a linear stochastic system driven by white noise and defined by Eq. (3.37). It is possible to interpret it as a linear stochastic differential equation of the form

$$\mathrm{d}\mathbf{x}_{\mathrm{a}}(t) = \mathbf{A}_{\mathrm{a}}(t)\mathbf{x}_{\mathrm{a}}(t)\mathrm{d}t + \mathbf{B}_{\mathrm{a}}(t)\mathrm{d}\mathbf{w}(t), \tag{3.39}$$

whose solution is

$$\mathbf{x}_{\mathrm{a}}(t) = \Phi_{\mathrm{a}}(t, t_0)\mathbf{x}_{\mathrm{a}}(t_0) + \int_{t_0}^{t} \Phi_{\mathrm{a}}(t, t')\mathbf{B}_{\mathrm{a}}(t')\mathrm{d}\mathbf{w}(t'), \tag{3.40}$$

where $\Phi_{\mathrm{a}}(t, t_0) = \partial \mathbf{X}_{\mathrm{a}}(t)/\partial \mathbf{X}_{\mathrm{a}}(t_0)$ and the statistical expectation $\mathrm{E}\{\mathbf{x}_{\mathrm{a}}(t)\} = 0$. Also, the stochastic integral of the white Gaussian noise process is implicitly independent of $\mathbf{x}_{\mathrm{a}}(t)$ and therefore,

$$\mathrm{E}\left\{ \left[\int_{t_0}^{t} \Phi_{\mathrm{a}}(t, t')\mathbf{B}_{\mathrm{a}}(t')\mathrm{d}\mathbf{w}(t') \right] [\mathbf{x}_{\mathrm{a}}(t)] \right\} = 0, \tag{3.41}$$

thus the time update for the state $\mathbf{x}_{\mathrm{a}}(t)$ is not affected and is simply $\mathbf{x}_{\mathrm{a}}(t) = \Phi_{\mathrm{a}}(t, t_0)\mathbf{x}_{\mathrm{a}}(t_0)$. However, the variance-covariance matrix of $\mathbf{x}_{\mathrm{a}}(t)$ is affected and has the form

$$\bar{\mathbf{P}}_{\mathrm{a}}(t) = \Phi_{\mathrm{a}}(t, t_0)\mathbf{P}_{\mathrm{a}}(t_0)\Phi_{\mathrm{a}}^{\mathrm{T}}(t, t_0) + \int_{t_0}^{t} \Phi_{\mathrm{a}}(t, t')\mathbf{B}_{\mathrm{a}}(t')\mathbf{Q}_{\mathrm{a}}(t')\mathbf{B}_{\mathrm{a}}^{\mathrm{T}}(t')\Phi_{\mathrm{a}}^{\mathrm{T}}(t, t')\mathrm{d}t', \tag{3.42}$$

$$\dot{\bar{\mathbf{P}}}_{\mathrm{a}}(t) = \mathbf{A}_{\mathrm{a}}(t)\bar{\mathbf{P}}_{\mathrm{a}}(t) + \bar{\mathbf{P}}_{\mathrm{a}}(t)\mathbf{A}_{\mathrm{a}}^{\mathrm{T}}(t) + \mathbf{B}_{\mathrm{a}}(t)\mathbf{Q}_{\mathrm{a}}(t)\mathbf{B}_{\mathrm{a}}^{\mathrm{T}}(t). \tag{3.43}$$

This relationship allows for a time-varying system model and non-white, time-correlated, dynamic Gaussian noise model to be evaluated. Two possible methods of solution exist for non-trivial dynamics: numerical integration of Eq. (3.43); or a discrete case for time-invariant or slowly varying system models based on Eq. (3.42). For the derivation of the discrete case Reference [96] is closely followed:

$$\bar{\mathbf{P}}_{\mathrm{a}}(t) = \Phi_{\mathrm{a}}(t, t_0)\mathbf{P}_{\mathrm{a}}(t_0)\Phi_{\mathrm{a}}^{\mathrm{T}}(t, t_0) + \mathbf{B}_{\mathrm{d}}(t_0)\mathbf{Q}_{\mathrm{d}}(t_0)\mathbf{B}_{\mathrm{d}}^{\mathrm{T}}(t_0), \tag{3.44}$$

where the subscript "d" denotes the discrete case to distinguish it from the instantaneous case previously presented. If the system model natural transients are time-invariant or slowly varying when compared to the observation samples, then a first order approximation can be used, where

$$\Phi_{\mathrm{a}}(t, t_0) = \mathbf{I} - \mathbf{A}_{\mathrm{a}}(t_0) \times (t - t_0), \tag{3.45}$$

$$\mathbf{Q}_{\mathrm{d}}(t_0) = \mathbf{B}_{\mathrm{a}}(t_0)\mathbf{Q}_{\mathrm{a}}(t_0)\mathbf{B}_{\mathrm{a}}^{\mathrm{T}}(t_0) \times (t - t_0). \tag{3.46}$$

The time-updated state covariance matrix can be obtained two different ways. The first is numerical integration of Eq. (3.43). The other is for the discrete case given in Eq. (3.44) where the covariance matrix can be broken up into two terms: $\bar{\mathbf{P}}_{\mathrm{a}} = \bar{\mathbf{P}}'_{\mathrm{a}} + \bar{\mathbf{P}}''_{\mathrm{a}}$; the first term is simply $\bar{\mathbf{P}}'_{\mathrm{a}} = \Phi_{\mathrm{a}}\mathbf{P}_{\mathrm{a}}\Phi_{\mathrm{a}}^{\mathrm{T}}$; and the second term:

$$\bar{\mathbf{P}}''_{\mathrm{a}} = \mathbf{B}_{\mathrm{d}}(t_0)\mathbf{Q}_{\mathrm{d}}(t_0)\mathbf{B}_{\mathrm{d}}^{\mathrm{T}}(t_0) = \mathbf{B}_{\mathrm{d}}(t_0)\left[\mathbf{B}_{\mathrm{a}}(t_0)\mathbf{Q}_{\mathrm{a}}(t_0)\mathbf{B}_{\mathrm{a}}^{\mathrm{T}}(t_0) \times (t - t_0)\right]\mathbf{B}_{\mathrm{d}}^{\mathrm{T}}(t_0). \tag{3.47}$$

Some simplifications for this case can be made as discussed in Reference [96] in which one can postulate that $\mathbf{B}_{\mathrm{d}} = \mathbf{I}$, $\mathbf{Q}_{\mathrm{a}} = \mathbf{I}$. It must be emphasized that Eq. (3.47) is a first order approximation and is only valid if the system model is time-invariant or slowly varying. If the system is not time-invariant or slowly varying an analytical solution or numerical integration of Eq. (3.43) is necessary. It may also be necessary to obtain an analytical solution or numerical integration of Eq. (3.43) if one is making future predictions in which time-lags are considerably large.

3.6.3 Stochastic Processes

A random variable is any variable whose value can be described by an associated probability and are thus subject to variations of chance. There are two main types of random variables that are used in this work: discrete and continuous. A discrete random variable is one in which a specified finite list of possible values with a probability mass function are characteristic to a certain probability distribution. A continuous random variable is one whose value is characterized by a probability density function that describes possible outcomes of random events. The most common model used in this work is that of the normal or Gaussian distribution. The Gaussian probability density function can be described by

$$f(x) = \frac{1}{2\pi|P|} e^{-\frac{1}{2}(x-\mu)' P^{-1}(x-\mu)} \tag{3.48}$$

where μ is the mean values of x and P is the variance-covariance matrix describing the correlation between different components of x. A Gaussian distribution can be completely characterized by the mean and covariance and is generally expressed as

$$x \sim N(\mu, P) \tag{3.49}$$

If the covariance P is diagonal with no off-diagonal terms, it is easy to generate random realizations. If, however, there do exist off-diagonal terms (which is the case for nearly all applications in this work) it is necessary to decompose the covariance matrix such that

$$P = \bar{S}\bar{S}^{\mathrm{T}} \tag{3.50}$$

where $\bar{S}$ is the upper triangular square root of P and is known as the Cholesky factor. If a set of Gaussian-distributed random variables of the same dimension x are zero mean and unit variance, where

$$y \sim N(0, I) \tag{3.51}$$

then realizations of x with proper correlations given in P can be generated by

$$x = \bar{S}y. \tag{3.52}$$

The following sections will outline several different methods of modeling random processes within the filter framework used throughout this work. Both continuous and discrete derivations of several random processes is derived and the relationship between each process is explained. All of the models below will use a simplified linear process to describe the random processes' behavior and characteristics over time. The three main processes presented in this section are that of a Gaussian white noise process driving velocity and acceleration, a first order Gauss-Markov process driving an acceleration state, and a second order Gauss-Markov process driving an acceleration state.

3.6.3.1 White Noise Processes

Pure white noise is defined by a GMP0 whose auto-covariance function is represented by

$$\Psi_{nn}(\tau) = \sigma^2\delta(\tau), \tag{3.53}$$

where σ^2 is the noise variance corresponding to $\tau = 0$ and δ is the Dirac delta function.

3.6.3.2 Gauss-Markov Processes

A Gauss-Markov random process is a Markov random process with restriction that the probability $p[x(t)]$ and the conditional probability $p[x(t)/x(t+\tau)]$, where $\tau = \Delta t$, are Gaussian density functions for all times t and $t+\tau$ over the interval $t_0 \rightarrow t_f$ [14]. In terms of filter theory, a zeroth-, first-, and second-order process (GMP0, GMP1, GMP2) augment the state vector with zero, one, or two parameters, respectively, per spatial dimension [113]. For any scalar process zero-mean noise the auto-covariance is defined as

$$\Psi_{nn}(\tau) = \mathrm{E}\{n(t)n(t+\tau)\}; \tag{3.54}$$

3.6.3.3 First Order Gauss-Markov Processes

GMP1 is also defined by the first-order Langevin equation of the form[1]

$$\dot{n}(t) = -\lambda n(t) + w(t), \tag{3.55}$$

$$\mathrm{E}\{w(t)\} = 0, \quad \mathrm{E}\{w(t)w(t+\tau)\} = Q\delta(\tau). \tag{3.56}$$

GMP1 is defined by an exponentially correlated function with a correlation time T, where $\lambda = 1/T$, and an auto-covariance

$$\Psi_{nn}(\tau) = \sigma^2 e^{-\lambda\tau}. \tag{3.57}$$

[1] It must be made aware that Q in Eq. (3.56) and q in Eq. (3.59) are the strengths of a white noise process but may have different units and are thus defined differently. Also σ^2 in Eq. (3.53) $\neq Q$ or q but can also be defined as the strength of a white noise process for GMP0.

3.6.3.4 Second Order Gauss-Markov Processes

The second-order Gauss-Markov process is defined by an autonomous second-order dynamical system with a white noise forcing function of the type:[2]

$$\begin{bmatrix} \dot{x}_1 \\ \dot{x}_2 \end{bmatrix} = \begin{bmatrix} 0 & 1 \\ -\omega_n^2 & -2\zeta\omega_n \end{bmatrix} \begin{bmatrix} x_1 \\ x_2 \end{bmatrix} + \begin{bmatrix} 0 \\ c \end{bmatrix} w(t), \tag{3.58}$$

$$\mathrm{E}\{w(t)\} = 0, \quad \mathrm{E}\{w(t)w(t+\tau)\} = q\delta(\tau), \tag{3.59}$$

where ω_n, ζ, and c are constants.[3] The strength of the white noise process is generally taken to be $q = 1$ and can be increased to add more noise. The state transition matrix for Eq. (3.58) is easily obtained:

$$\Phi_s(t) = e^{-\zeta\omega_n t} \begin{bmatrix} \cos\beta t + \dfrac{\zeta\omega_n}{\beta}\sin\beta t & \dfrac{1}{\beta}\sin\beta t \\ -\dfrac{\omega_n^2}{\beta}\sin\beta t & \cos\beta t - \dfrac{\zeta\omega_n}{\beta}\sin\beta t \end{bmatrix}, \tag{3.60}$$

where, $\beta = \omega_n\sqrt{1-\zeta^2}$. From Eq. (3.42) with $\mathbf{B}_\mathrm{s} = [\ 0,\ c\ ]^\mathrm{T}$, the auto-covariance function for a GMP2 is given by [14, 157]

$$\Psi_{nn}(\tau) = \sigma^2 e^{-\zeta\omega_n|\tau|}\left\{\cos\beta|\tau| + \frac{\zeta\omega_n}{\beta}\sin\beta|\tau|\right\}, \tag{3.61}$$

where $\sigma^2 = qc^2/4\omega_n^3\zeta$. This formula will always be written for the under-damped case; for the aperiodic case let $\beta \to 0$ and for the over-damped case set $\beta = \mathrm{i}\beta$ [157].

Figure 3.1 illustrates the versatility of the GMP2 auto-covariance function as see in Eq. (3.61). From GMP2, one can obtain GMP0, GMP1 and a pure sinusoid by altering the coefficients ω_n, and ζ. For example, if $\zeta = 1$, it degenerates into GMP1 with a pure exponential decay. On the other extreme, $\zeta = 0$ leads to a pure sinusoidal oscillation. The frequencies are governed by ω_n and if $\zeta = 1$ with $\omega_n \to \infty$, approaching the solution of GMP0.

[2] Notice that Reference [113] followed Reference [96], yet here Reference [14] and Reference [157] are followed; these two are not exactly equivalent especially in Eq. (3.58), (3.61), and (3.47). Furthermore, there was a typo in Reference [113], Eq. (16): where it is b, but should be c.

[3] In Reference [113], $\omega_n = \omega$ and c is a variable different than the constant defined here.

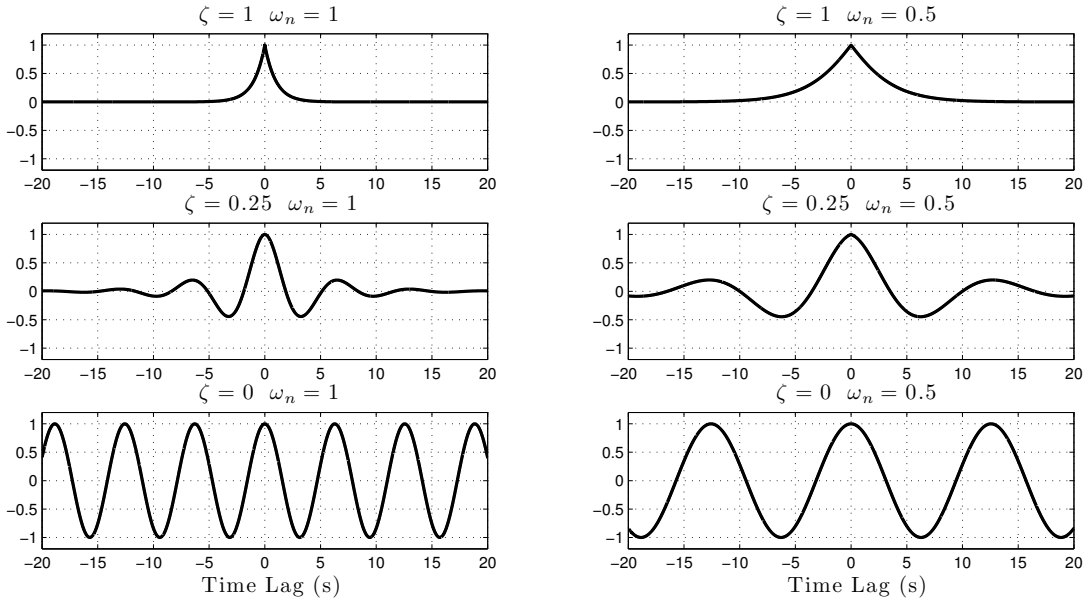

Figure 3.1: Auto-covariance functions for different instances of second-order GMP.

3.7 Square Root Formulations

The previous sections have outline estimation algorithms for a Batch Least Squares and sequential data processing for orbit determination used in this work. There are two common issues associated with these types of estimation algorithms that hinder their general implementation. The primary issue with sequential estimators is their ability to diverge. Divergence is a phenomenon that occurs when the estimated state departs in an unbounded manner for the actual values. Two of the main causes for divergence arise from inaccuracies in the physics used to describe the system. This can either be in the dynamical integration or in the model used to relate the observations to the state. To alleviate the first issue of inaccuracies in the dynamical model, process noise is introduced to mask errors in the dynamical model and an iteration scheme over the observations has been introduced to reduce the linearization errors in the nonlinear observation calculation. This was addressed in the previous sections discussing stochastic processes and process noise. The second factor, and the focus of this section, is that of divergence due to errors in the measurement update equations in which the covariance matrix becomes nonpositive definite. The cause of this stems from numerical precision of math computations and to reduce or eliminate this error the

problem must be reformulated.

The most common method to eliminate the errors introduced into the covariance update is through the use of square root covariance matrix implementations. If one uses the square root of the covariance matrix for the mathematical filter algorithms, one can insure that the covariance matrix maintains its positive definiteness during the time and measurement updates. In the general sense, the covariance matrix can be expressed as

$$P = WW^{\mathrm{T}}, \tag{3.62}$$

where W is the square root matrix of P. This formulation ensures that the covariance matrix P will never be nonpositive definite even if numerical precision roundoff errors occur. The following will discuss two common methods that have been implemented in this work to model the sequential Kalman filter algorithm as a square root filter.

3.7.1 UD Factorization

One of the most common square root free implementations is known as the U-D covariance factorization developed by Bierman and Thornton [10, 150]. UD factorization has the following relationship

$$P = UDU^{\mathrm{T}}, \tag{3.63}$$

where P is the positive definite symmetric covariance matrix, U is the upper triangular matrix with diagonals of ones, and D is a diagonal matrix whose off-diagonal elements are zeros. Factorization methods to transform the covariance to the UDU^{T} system and the UDU^{T} system to the covariance are given in Bierman [10].

3.7.1.1 Time Update

The state update of the time update sequence of the sequential Kalman filter is unaltered from the implementation derived in the previous section. For the UD factorization, only the covariance

matrix is modified. The sequential Kalman filter has a time update for the covariance matrix of the following form

$$\bar{P}_{k+1} = \Phi(t_{k+1}, t_k) P_k \Phi^{\mathrm{T}}(t_{k+1}, t_k) + \Gamma(t_{k+1}, t_k) Q_k \Gamma^{\mathrm{T}}(t_{k+1}, t_k). \tag{3.64}$$

This can be modified using the UD factorization of P_k and Q_k such that

$$\bar{P}_{k+1} = \Phi(t_{k+1}, t_k) U_k D_k U_k^{\mathrm{T}} \Phi^{\mathrm{T}}(t_{k+1}, t_k) + \Gamma(t_{k+1}, t_k) U_k^q D_k^q U_k^q \Gamma^{\mathrm{T}}(t_{k+1}, t_k). \tag{3.65}$$

The most common procedure for obtaining $\bar{P} = UDU^{\mathrm{T}}$, where the bar denotes time update values, is through the Gram-Schmidt procedure [10]. The problem (dropping the subscripts $k+1$ and k for brevity) can be formulated as

$$\bar{P} = [\Phi U,\ \Gamma U^q]\, \mathrm{Diag}\,(D,\ D^q)\, [\Phi U,\ \Gamma U^q]^{\mathrm{T}}\,, \tag{3.66}$$

which can be reformulated as

$$\bar{P} = W D' W^{\mathrm{T}}, \tag{3.67}$$

where

$$W = \left[\Phi U \,\vdots\, \Gamma U^q\right], \tag{3.68}$$

and

$$D' = \begin{bmatrix} D & \mathbf{0} \\ \mathbf{0} & D^q \end{bmatrix}. \tag{3.69}$$

The Gram-Schmidt orthogonalization can then take place in order to compute the necessary matrices to obtain $\bar{P}$. This completes the time update sequence of the UD factorization of the covariance matrix.

3.7.1.2 Measurement Update

Similar to the previous section on the UD factorized time update, it is necessary to describe the *a posteriori* covariance matrix in the form $P = UDU^{\mathrm{T}}$. The same conditions apply that U is an upper triangular matrix and D is a diagonal matrix. The general form of the covariance measurement update is given by

$$P = [I - KH]\,\bar{P}. \tag{3.70}$$

For simplification, a single scalar observation is assumed such that P can be expressed by

$$UDU^{\mathrm{T}} = \bar{U}\bar{D}\bar{U}^{\mathrm{T}} - \bar{U}\bar{D}\bar{U}^{\mathrm{T}}H^{\mathrm{T}}yH\bar{U}\bar{D}\bar{U}^{\mathrm{T}}, \tag{3.71}$$

where $\bar{P} = \bar{U}\bar{D}\bar{U}^{\mathrm{T}}$ and y is the scalar observation. Since

$$y = (H\bar{P}H^{\mathrm{T}} + R)^{-1} = (H\bar{U}\bar{D}\bar{U}^{\mathrm{T}}H^{\mathrm{T}} + R)^{-1}, \tag{3.72}$$

the equation for the covariance P can be rewritten as follows

$$UDU^{\mathrm{T}} = \bar{U}\left[\bar{D} - \bar{D}\bar{U}H^{\mathrm{T}}yH\bar{U}\bar{D}\right]\bar{U}^{\mathrm{T}}. \tag{3.73}$$

This can be further simplified using the substitution $V = \bar{D}\bar{U}^{\mathrm{T}}H^{\mathrm{T}}$ so that the covariance is expressed by

$$P = UDU^{\mathrm{T}} = \bar{U}\left[\bar{D} - VyV^{\mathrm{T}}\right]\bar{U}^{\mathrm{T}}. \tag{3.74}$$

If one computes the factorized values U' and D' the covariance can be derived as

$$P = UDU^{\mathrm{T}} = \bar{U}U'D'U'^{\mathrm{T}}\bar{U}^{\mathrm{T}}. \tag{3.75}$$

Since the $\bar{U}$ and U' are both upper triangular their product $\bar{U}U'$ will also be upper triangular, thus P now takes the form of $P = UDU^{\mathrm{T}}$. This can be factorized using any method of choice, but

the Gram-Schmidt method described earlier can also be employed here. This completes the UD factorized filter implementation of a sequential Kalman filter.

3.7.2 SRIF

As described previously, a reformulation of the original sequential conventional Kalman filter is necessary for the computational procedure to minimize the effects of numerical instabilities in matrix inversions. The UD factorized method is one such approach, however, the other most common method is that of a square-root information filter (SRIF) [10, 99, 126]. The complete implementation used in this study is that of an Extended Kalman version of the SRIF with measurement iteration known as the Iterated Extended Kalman Square-Root Information Filter (IEK-SRIF). The original SRIF derivation follows in a similar fashion, however, additional focus is added on the measurement iteration scheme and state estimate update.

The Extended Kalman filter in SRIF form uses the information equation in order to store the state estimate and covariance. The *a posteriori* state information equation that is used with the SRIF takes the form

$$\hat{\boldsymbol{R}}_k(\mathbf{X}_k - \hat{\mathbf{X}}_k) = -\boldsymbol{\nu}_k, \tag{3.76}$$

where $\hat{\mathbf{X}}_k$ is the *a posteriori* state estimate at time t_k, $\boldsymbol{\nu}_k$ is the discrete-time zero-mean Gaussian white-noise with an identity covariance matrix, and $\hat{\boldsymbol{R}}_k$ is the the upper-triangular square-root information matrix of $\hat{\mathbf{X}}_k$. The estimation error covariance for $\hat{\mathbf{X}}_k$ is $\hat{\boldsymbol{P}}_k = \boldsymbol{R}_k^{-1}\boldsymbol{R}_k^{-\mathrm{T}}$. The time update in SRIF form is thus

$$\bar{T}_k \begin{bmatrix} \boldsymbol{R}_u & \mathbf{0} \\ -\tilde{\boldsymbol{R}}_k\boldsymbol{\Gamma}(t_k, t_{k-1}) & \tilde{\boldsymbol{R}}_k \end{bmatrix} \Rightarrow \begin{bmatrix} \bar{\boldsymbol{R}}_{u_k} & \bar{\boldsymbol{R}}_{ux_k} \\ \mathbf{0} & \bar{\boldsymbol{R}}_k \end{bmatrix}, \tag{3.77}$$

where $\tilde{\boldsymbol{R}}_k = \hat{\boldsymbol{R}}_{k-1}\boldsymbol{\Phi}^{-1}(t_k, t_{k-1})$ and $\bar{T}_k$ is the application of an orthogonal transformation that eliminates the explicit dependence of the state on the previous noise. An orthogonal reflection, such as the Householder transformation, is used for the orthogonal transformations. The inclusion

of process noise is given by the process noise transition matrix $\mathbf{\Gamma}(t_k, t_{k-1})$. With this transformation, the solution to the time update in SRIF form is given by

$$\begin{bmatrix} \bar{\boldsymbol{R}}_{u_k} & \bar{\boldsymbol{R}}_{ux_k} \\ \mathbf{0} & \bar{\boldsymbol{R}}_k \end{bmatrix} \begin{bmatrix} \mathbf{u}_{k-1} \\ \mathbf{X}_k - \bar{\mathbf{X}}_k \end{bmatrix} = - \begin{bmatrix} \boldsymbol{\nu}_{uk} \\ \boldsymbol{\nu}_k \end{bmatrix}. \tag{3.78}$$

The *a priori* values of the state can then be determined. Once this is accomplished, the measurement update in SRIF form is given by

$$\hat{T}_k \begin{bmatrix} \bar{\boldsymbol{R}}_k & \mathbf{0} \\ \tilde{\mathbf{H}}_k & \boldsymbol{y}_k \end{bmatrix} \Rightarrow \begin{bmatrix} \hat{\boldsymbol{R}}_k & \hat{\mathbf{b}}_k \\ 0 & \mathbf{e}_k \end{bmatrix}, \tag{3.79}$$

where $\tilde{\mathbf{H}}_k = [\tilde{\mathbf{H}}_{\mathbf{X},k} \quad \tilde{\mathbf{H}}_{\mathbf{w},k}]$ and $\boldsymbol{y}_k$ is the nonlinear measurement deviation. From this transformation, an optimal *a posteriori* estimate of the state deviation can be obtained by

$$\delta\mathbf{x}_k = \hat{\boldsymbol{R}}_k^{-1} \hat{\mathbf{b}}_k \tag{3.80}$$

where $\delta\mathbf{x}_k = \mathbf{X}_k - \bar{\mathbf{X}}_k$. The *a posteriori* state estimate can then be computed by adding the *a posteriori* deviation to the *a priori* state estimate as

$$\hat{\mathbf{X}}_k = \bar{\mathbf{X}}_k + \delta\mathbf{x}_k \tag{3.81}$$

The nonlinearities in the measurement equation can be removed by an iteration over the measurement deviation. This is done by a relinearization about the most current best estimate of the state and iterating until convergence [41, 68]. The iteration scheme used is given by

$$\boldsymbol{y}_k = \boldsymbol{Y}_k - \boldsymbol{h}(\boldsymbol{\eta}_i, t_k) - \tilde{H}_k \left[\bar{\mathbf{X}}_k - \boldsymbol{\eta}_i\right]. \qquad i = 1, \ldots, l \tag{3.82}$$

The substitution of Eq. 3.82 back into Eq. 3.79 and solving for Eq. 3.81, where the solution of Eq. 3.81 is given by $\boldsymbol{\eta}_{i+1} = \hat{\mathbf{X}}_{k,i+1}$. The iteration is initiated by $\boldsymbol{\eta}_1 = \bar{\mathbf{X}}_k$ and is terminated when the difference between two consecutive iterations is less than a specified tolerance. The final solution after convergence is given by $\hat{\mathbf{X}}_k = \boldsymbol{\eta}_l$. This procedure has been designed to reduced the

errors induced by measurement linearities and does not directly improve the reference trajectory on the interval $[t_k, t_{k+1})$. The improvement in the reference trajectory occurs over the interval of $[t_{k+1}, t_{k+2})$.

3.8 Smoother

While the sequential filter processors are exceptional for real-time data processing, there is a limited capability when attempting to get the best estimate using all of the processed data. In order to alleviate this issue, a filter smoother operation is typically used. The filter smoother process is extremely beneficial for obtaining estimates of a state at an initial epoch and estimates of stochastic processes that have happened over the data arc. If there is not stochastic process in the filtering algorithm, a smoothed sequential estimator will produce the same results as a batch least squares estimator previously defined. The batch algorithm, as written, does not handle the addition of process noise or stochastic processes easily. For this reason, it is common practice to use a smoothed sequential processor. The smoothing algorithms used in this work can be found in [148] and [10].

3.9 Uncertainty Propagation

Several methods have been proposed to achieve more accurate uncertainty propagation for the nonlinear regime of orbital mechanics. Junkins *et al.* have shown that the uncertainty of a satellite does not remain Gaussian for long integration times or when the satellite is in certain LEO orbits that experience highly nonlinear dynamics [73]. It has been commonplace for spacecraft navigation and uncertainty propagation to use a linearization of the dynamics [68, 101, 148]. This method's linear propagation of the uncertainty through the state transition matrix is appropriate for dense observations when propagation times are small and the nonlinearities are not significant from measurement to measurement. However, for the realm of interplanetary navigation when observations can be taken in sparse intervals, long propagation times are necessary and the linear propagation through the state transition matrix fails to obtain an appropriate approximation of

the uncertainty. There has been significant research in the realm of nonlinear propagation of uncertainty of orbital motion. Such methods include, but are not limited to, state transition tensors [6, 40, 41, 118, 158], Gaussian mixture models [46, 64], polynomial chaos [69], and Monte Carlo approximations of the propagation uncertainty [133, 134]. All of these methods have been shown to be possible solutions to the problem of uncertainty propagation in the orbital regime but there are limitations based on their theory and integration into current orbit determination methods.

A major difficulty in uncertainty propagation stems from the solution of the nonlinear stochastic differential equations that must be solved for. All of the aforementioned methods attempt to solve these stochastic differential equations through various means. Polynomial Chaos expansion (PCE) methods are used to approximate a solution to a stochastic differential equation. The fundamental basis of Polynomial Chaos (PC) is that any random process can be approximated by a weighted sum of multivariate orthogonal polynomials of the random independent variables [159]. Polynomial chaos methods have deep roots in the study of uncertainties in structural mechanics, fluid mechanics, and vibrations [43, 44, 170, 171]. Depending on the method used, the propagation of uncertainty can be obtained through the use of Galerkin projection or through use of numerical evaluation of the PC expansion through deterministic or random sampling [105]. An intrusive approach allows for the direct PC representation to be found through a reformulation of the original model. A non-intrusive method treats the original deterministic model as a black box but may require extra computations to obtain an accurate PC representation of the original model.

The first application of non-intrusive PC to orbital mechanics has only recently been employed [69]. Jones *et al.* demonstrated the use of PC to approximate the solution of a stochastic ordinary differential equation that governs orbital mechanics. The use of PC expansions were considered for two types of orbits, Sun-synchronous and Molniya. A comparison of multiple coordinate systems was conducted and compared to determine which coordinate system utilizes the least PC expansions to accurately estimate the uncertainty propagation. Jones *et al.* also investigate the use of PC for more complicated dynamical models including the two-body problem, gravity perturbations,

atmospheric drag, solar radiation pressure, and third-body effects. For the cases examined by Jones *et al.*, improvements in the orbit state uncertainty propagation were obtained through PCE-based methods when compared to linear uncertainty propagation and the unscented transformation methods [69].

3.10 Observability

Any system is observable if the state being investigated at any specific instant in time can be uniquely determined given a finite sequence of its outputs. In principle, for an mth-order dynamical system that is being investigated, the m physical state variables should all be measured to have a complete description of the system under examination. However, in most situations, the measured quantities do not explicitly relate to all state variables at that specific instance in time. Therefore, it is common to reconstruct a phase space from a time series of measurements by using a time delay or time derivative coordinates. Thus, the reconstructed trajectory has the same properties as the trajectory from the original phase space. As an example, a dynamical system that contains a state of several constant but unknown quantities can be estimated given a sufficient number of measurements with arbitrarily small uncertainty [74].

Observability can be extended to linear systems as well as nonlinear systems. For time-invariant linear systems, observability can be measured by employing test such as the rank of the Gramian matrix [80, 96] or the Popov–Belevitch–Hautus (PBH) test [132]. If one is investigating a linearized nonlinear system (as is the case for OD) the PBH test cannot be used. The use of the rank criterium of the Gramian matrix, which does not rely on time invariance, often becomes intractable when extended from 2-D to 3-D [4].

An alternative to these linearized methods is that of the observability rank condition extended to nonlinear systems based on Lie derivatives [55]. The use of Lie derivatives to examine observability in nonlinear systems has a foundation in robotics [4, 11, 82, 94]. These methods have also more recently been applied to astrodynamics and attitude observability analysis [129, 143, 173]. The following sections will explore the concepts behind these three tests for observability.

3.10.1 Linear Time-Invariant Systems

One of the most common and well known measures of observability stems for a linear time-invariant system. Consider the following time-invariant linear system

$$\mathbf{x}_{k+1} = \mathbf{\Phi}\mathbf{x}_k \tag{3.83}$$

$$\mathbf{z}_k = \mathbf{H}\mathbf{x}_k \tag{3.84}$$

where $\mathbf{\Phi}$ is a constant state mapping matrix, $\mathbf{H}$ is a $m \times n$ constant measurement mapping matrix, $\mathbf{x}_k$ is the $n \times 1$ state at time t_k and $\mathbf{z}_k$ is the $m \times 1$ set of linear measurements at time t_k. From this, a series of measurements can be obtained such that

$$\begin{array}{rcccl} \mathbf{z}_k & = & \mathbf{H}\mathbf{x}_k & = & \mathbf{H}\mathbf{x}_k, \\ \mathbf{z}_{k+1} & = & \mathbf{H}\mathbf{x}_{k+1} & = & \mathbf{H}\mathbf{\Phi}\mathbf{x}_k, \\ \mathbf{z}_{k+2} & = & \mathbf{H}\mathbf{x}_{k+2} & = & \mathbf{H}\mathbf{\Phi}^2\mathbf{x}_k, \\ & \vdots & & \vdots & \\ \mathbf{z}_d & = & \mathbf{H}\mathbf{x}_d & = & \mathbf{H}\mathbf{\Phi}^{d-1}\mathbf{x}_k. \end{array} \tag{3.85}$$

Rewriting this equation into a compact form yields

$$\boldsymbol{\zeta} = \mathbf{\Psi}\mathbf{x}_k, \tag{3.86}$$

where $\boldsymbol{\zeta}$ and $\mathbf{\Psi}$ are defined as

$$\boldsymbol{\zeta} = \begin{bmatrix} \mathbf{z}_k \\ \mathbf{z}_{k+1} \\ \mathbf{z}_{k+2} \\ \vdots \\ \mathbf{z}_d \end{bmatrix}_{dm \times 1} \quad \text{and} \quad \mathbf{\Psi} = \begin{bmatrix} \mathbf{H} \\ \mathbf{H}\mathbf{\Phi} \\ \mathbf{H}\mathbf{\Phi}^2 \\ \vdots \\ \mathbf{H}\mathbf{\Phi}^{d-1} \end{bmatrix}_{dm \times n} \tag{3.87}$$

For the limiting case where $m = 1$, the inverse of $\mathbf{\Psi}$ must exist. The matrix $\mathbf{\Psi}$ can be used for the unweighted least squares solution

$$\mathbf{x}_k = \left(\mathbf{\Psi}^{\mathrm{T}}\mathbf{\Psi}\right)^{-1}\mathbf{\Psi}^{\mathrm{T}}\boldsymbol{\zeta}. \tag{3.88}$$

If $\mathbf{\Psi}$ is not a square matrix, then for $\mathbf{x}$ to be uniquely determined the inverse of the Gramian matrix $\mathbf{\Psi}^{\mathrm{T}}\mathbf{\Psi}$ must exist. If the matrix is invertible, then it is said to be full rank as well. If the Gramian matrix is full rank, then $\mathbf{\Psi}$ must also be full rank.

This measure of observability implies that a systems is either observable or not based on whether or not the measurement mapping or Gramian matrix are full rank. If the rank is less than n, this method does provide some insight into the total number of linear combinations of the state that are observable. Some limitations of this method are that it does not provide any insight into the rank based on previous measures, comparing observability when the rank is constant, or a measure of the degree of observability.

These concepts can also be extended to an n^{th} order linear time-invariant system expressed as

$$\dot{\mathbf{x}} = \mathbf{A}\mathbf{x} \tag{3.89}$$

$$\mathbf{z} = \mathbf{H}\mathbf{x}. \tag{3.90}$$

This results in the commonly used LTI observability matrix $\mathcal{O}$ where

$$\mathcal{O} = \begin{bmatrix} \mathbf{H} \\ \mathbf{HF} \\ \mathbf{HF}^2 \\ \vdots \\ \mathbf{HF}^{d-1} \end{bmatrix}_{dm\times n} \tag{3.91}$$

where n is the number of states and m is the length of the measurement vector $\mathbf{z}$. Similar to the previous discussion, $\mathcal{O}$ must be full rank for the system to be observable. The LTI observability condition is defined to be locally observable if, and only if, $\det\left(\mathcal{O}^{\mathrm{T}}\mathcal{O}\right)^{1/2} \neq 0$.

Even though a majority of systems examined in astrodynamics and all of the systems examined in this work are not linear or time-invariant, the definition of $\mathbf{A}$ and $\mathbf{H}$ allows for the evaluation of observability along a nominal or reference trajectory at a specific instance in time providing useful insight into the local observability of the system. This technique does not provide any information on the build-up of observability due to measurement processing over the course of a trajectory.

3.10.2 Linear Time-Varying System

One of the primary shortcomings of the LTI observability analysis is the inability to provide insight into the accumulation of observability due to measurement processing. This is due to the fact that $\mathbf{\Phi}$, $\mathbf{A}$, and $\mathbf{H}$ are assumed to be time-invariant matrices. If we expand this analysis to a time-varying system such that $\mathbf{\Phi} = \mathbf{\Phi}(t_{k+1}, t_k)$ and $\mathbf{H} = \mathbf{H}(t_k)$, then for a series of measurements

$$\begin{aligned}
\mathbf{z}_k &= \mathbf{H}(t_k)\mathbf{x}_k &&= \mathbf{H}(t_k)\mathbf{x}_k, \\
\mathbf{z}_{k+1} &= \mathbf{H}(t_{k+1})\mathbf{x}_{k+1} &&= \mathbf{H}(t_{k+1})\mathbf{\Phi}(t_{k+1}, t_k)\mathbf{x}_k, \\
\mathbf{z}_{k+2} &= \mathbf{H}(t_{k+2})\mathbf{x}_{k+2} &&= \mathbf{H}(t_{k+2})\mathbf{\Phi}(t_{k+2}, t_k)\mathbf{x}_k, \\
&\vdots &&\vdots \\
\mathbf{z}_d &= \mathbf{H}(t_d)\mathbf{x}_d &&= \mathbf{H}(t_d)\mathbf{\Phi}(t_d, t_k)\mathbf{x}_k.
\end{aligned} \tag{3.92}$$

Rewriting this similar to before one can obtain the time varying matrices

$$\boldsymbol{\zeta}(t_k) = \mathbf{\Psi}(t_k)\mathbf{x}_k \tag{3.93}$$

where $\boldsymbol{\zeta}$ and $\mathbf{\Psi}$ are defined as

$$\boldsymbol{\zeta}(t_d) = \begin{bmatrix} \mathbf{z}(t_k) \\ \mathbf{z}(t_{k+1}) \\ \mathbf{z}(t_{k+2}) \\ \vdots \\ \mathbf{z}(t_d) \end{bmatrix}_{dm\times 1} \quad \text{and} \quad \boldsymbol{\Psi}(t_d) = \begin{bmatrix} \mathbf{H}(t_k) \\ \mathbf{H}(t_{k+1})\boldsymbol{\Phi}(t_{k+1}, t_k) \\ \mathbf{H}(t_{k+2})\boldsymbol{\Phi}(t_{k+2}, t_k) \\ \vdots \\ \mathbf{H}(t_d)\boldsymbol{\Phi}(t_d, t_k) \end{bmatrix}_{dm\times n} \tag{3.94}$$

For the system to be observable, it is necessary for the Gramian matrix to be full rank. For a discrete-time system commonly employed in this work, the Gramian matrix can be written in the following form

$$\mathcal{M}(t_d) = \boldsymbol{\Psi}^{\mathrm{T}}(t_d)\boldsymbol{\Psi}(t_d) = \sum_{k=1}^{d} \boldsymbol{\Phi}(t_k, t_1)\mathbf{H}^{\mathrm{T}}(t_k)\mathbf{H}(t_k)\boldsymbol{\Phi}(t_k, t_1) \tag{3.95}$$

The Gramian matrix can also be written in recursive form such that

$$\mathcal{M}(t_k) = \mathcal{M}(t_{k-1}) + \boldsymbol{\Phi}^{\mathrm{T}}(t_k, t_1)\mathbf{H}^{\mathrm{T}}(t_k)\mathbf{H}(t_k)\boldsymbol{\Phi}(t_k, t_1) \tag{3.96}$$

with the initial condition $\mathcal{M}(t_1) = 0$. In order for the system to be observable, a set of minimal measurements d must be processed before $\mathcal{M}(t_n)$ can be full rank. This provides insight into the number of measurements required for the system to be observable. Once the Gramian matrix becomes full rank after processing a limited set of measurements, each additional measurement processed will make the Gramian matrix determinant more positive and remain full rank.

3.10.3 Nonlinear System

In addition to linear systems, observability techniques have also been extended to a set of nonlinear systems typically of the form

$$\dot{\mathbf{x}} = \mathbf{f}(\mathbf{x}) \tag{3.97}$$

$$\mathbf{z} = \mathbf{h}(\mathbf{x}) \tag{3.98}$$

which describes nearly all systems defined in this body of work. For nonlinear systems, the establishment of observability is difficult to achieve. In general, observability must be tested numerically for complex systems and depends greatly on the number of measurements, their frequency, geometry and accuracy or uncertainty. A method of controllability and observability was introduced for nonlinear systems by Ref [55]. In generally, a set of points in a state space are defined to be indistinguishable if the two trajectories have identical outputs. It is possible to define local weak observability through a test using linear operators such as Lie differentiation. The Lie derivatives are defined for $\mathbf{f}(\mathbf{x})$ and $\mathbf{h}(\mathbf{x})$ such that

$$L_f\mathbf{h}(\mathbf{x}) = \frac{\partial \mathbf{h}}{\mathbf{x}}\mathbf{f}(\mathbf{x}) \tag{3.99}$$

If $\mathbf{h}$ is differntiable k times along the direction of $\mathbf{f}$, then the notation for the k^{th} Lie derivative is defined as

$$L_f^k\mathbf{h}(\mathbf{x}) = \frac{\partial\left(L_f^{k-1}\mathbf{h}\right)}{\partial \mathbf{x}}\mathbf{f}(\mathbf{x}) \tag{3.100}$$

where $L_f^0\mathbf{h}(\mathbf{x}) = \mathbf{h}(\mathbf{x})$.

Local observability can be determined through the following observability matrix of Lie derivatives.

$$\mathcal{O} = \begin{bmatrix} \dfrac{\partial \mathbf{h}}{\partial \mathbf{x}} \\ \dfrac{L_f \partial \mathbf{h}}{\partial \mathbf{x}} \\ \vdots \\ \dfrac{L_f^{n-2} \partial \mathbf{h}}{\partial \mathbf{x}} \\ \dfrac{L_f^{n-1} \partial \mathbf{h}}{\partial \mathbf{x}} \end{bmatrix} \tag{3.101}$$

Similar to the linear methods, if the observability matrix $\mathcal{O}$ is full rank, then it is said that the system is locally weakly observable. The benefit of this method, is that at any time along the

trajectory, the observability can be determined by examining the rank of $\mathcal{O}$ computed at that location. Global observability is extremely difficult to define for nonlinear systems. One technique has been used in which the observability matrix $\mathcal{O}$ is accumulated along the trajectory and examined at the final time [172].

The observability matrix $\mathcal{O}$ can be examined for degrees of observability using the eigenvalues and eigenvectors of $\mathcal{O}^{\mathrm{T}}\mathcal{O}$. The magnitude of the eigenvalues give an indication as to the strength of observability while the ratio of the largest eigenvalue to the smallest eigenvalue give an indication as to the overall observability of the system. The eigenvectors of $\mathcal{O}^{\mathrm{T}}\mathcal{O}$ provide information as to which combination of state variables gives the most observable quantity, while the state variable corresponding to the largest eigenvalue describes the most observable state parameter. While this method is directly applicable to the nonlinear systems commonly described in astrodynamics, utilization of Lie derivatives to define observability becomes extremely cumbersome for complex dynamics and measurement types. Automatic differentiation can alleviate complex derivatives, however, the accuracy of numerical derivatives is limited.

3.11 Measurement Types

Several measurement types are used throughout this work with various levels of fidelity. Geometric or instantaneous range and range-rate are typically used to define ranging and Doppler data for initial feasibility studies. More complex measurement types such as DSN Two-way range and Doppler are used for real data processing and high fidelity simulations. The use of instantaneous measurements allow for an immediate understanding of the information contained within the measurement and an intuitive understanding of their partial derivatives. While high fidelity models used in processing DSN differ in implementation, the end result of processing the measurements provide similar information obtained from the instantaneous version of the measurement. The following sections outline the observation and observation partials for both instantaneous and DSN range and Doppler measurements.

3.11.1 Instantaneous Range

Geometric range is defined as the instantaneous geometric distance between two participants. If the position vectors have a common center, then the instantaneous range measurement can be described by

$$\rho = |\mathbf{r}_2 - \mathbf{r}_1| + \rho_{bias} + \rho_{noise} \tag{3.102}$$

where $\mathbf{r}_2$ is the position vector of participant 2, $\mathbf{r}_1$ is the position vector of participant 1, ρ_{bias} is the measurement range bias, and ρ_{noise} is a Gaussian noise applied to the range when measurements are simulated.

The geometric range partial derivatives with respect to the two participants position and velocity are easily obtained and provided as follows

$$\frac{\partial \rho}{\partial \mathbf{r}_1} = -\hat{\rho}^{\mathrm{T}} \tag{3.103}$$

$$\frac{\partial \rho}{\partial \mathbf{v}_1} = \mathbf{0}_{1\times 3} \tag{3.104}$$

$$\frac{\partial \rho}{\partial \mathbf{r}_2} = \hat{\rho}^{\mathrm{T}} \tag{3.105}$$

$$\frac{\partial \rho}{\partial \mathbf{v}_2} = \mathbf{0}_{1\times 3} \tag{3.106}$$

where

$$\hat{\boldsymbol{\rho}} = \frac{\mathbf{r}_2 - \mathbf{r}_1}{|\mathbf{r}_2 - \mathbf{r}_1|} \tag{3.107}$$

The partial derivative of the range bias is simply

$$\frac{\partial \rho}{\partial \rho_{bias}} = 1 \tag{3.108}$$

3.11.2 Instantaneous Range-rate

Geometric range-rate is defined as the instantaneous relative velocity between two participants. If the state vectors have a common center, then the instantaneous range-rate measurement can be described by

$$\dot{\rho} = \dot{\boldsymbol{\rho}}^{\mathrm{T}}\hat{\boldsymbol{\rho}} + \dot{\rho}_{bias} + \dot{\rho}_{noise} \tag{3.109}$$

where $\dot{\boldsymbol{\rho}}$ is the relative velocity vector, $\hat{\boldsymbol{\rho}}$ is the relative position vector, $\dot{\rho}_{bias}$ is the measurement range-rate bias, and $\dot{\rho}_{noise}$ is a Gaussian noise applied to the range-rate when measurements are simulated. The relative velocity vector is defined by

$$\dot{\boldsymbol{\rho}} = \dot{\mathbf{r}}_2 - \dot{\mathbf{r}}_1. \tag{3.110}$$

The geometric range-rate partial derivatives with respect to the two participants position and velocity are easily obtained and provided as follows

$$\frac{\partial\dot{\rho}}{\partial\mathbf{r}_1} = -\frac{\dot{\boldsymbol{\rho}}}{\rho}\left(\mathbf{I}_{3\times3} - \hat{\boldsymbol{\rho}}\hat{\boldsymbol{\rho}}^{\mathrm{T}}\right) \tag{3.111}$$

$$\frac{\partial\dot{\rho}}{\partial\mathbf{v}_1} = -\hat{\rho}^{\mathrm{T}} \tag{3.112}$$

$$\frac{\partial\dot{\rho}}{\partial\mathbf{r}_2} = \frac{\dot{\boldsymbol{\rho}}}{\rho}\left(\mathbf{I}_{3\times3} - \hat{\boldsymbol{\rho}}\hat{\boldsymbol{\rho}}^{\mathrm{T}}\right) \tag{3.113}$$

$$\frac{\partial\dot{\rho}}{\partial\mathbf{v}_2} = \hat{\rho}^{\mathrm{T}} \tag{3.114}$$

where

$$\hat{\boldsymbol{\rho}} = \frac{\mathbf{r}_2 - \mathbf{r}_1}{|\mathbf{r}_2 - \mathbf{r}_1|} \tag{3.115}$$

The partial derivative of the range bias is simply

$$\frac{\partial\rho}{\partial\rho_{bias}} = 1 \tag{3.116}$$

Chapter 4

Earth-Moon Libration Point Orbit Navigation: ARTEMIS Baseline

4.1 Introduction

Orbits of spacecraft in the Earth-Moon three-body regime provide particular benefits for a variety of science and exploration missions. The focus of ongoing work which will be discussed in this paper is to better understand the dynamic environment and operational constraints of spacecraft in this orbital regime. The specific focus of this work is libration point orbits (LPOs) about the Earth-Moon co-linear L_1 and L_2 points. These orbits are unstable and thus require frequent station-keeping maneuvers to remain in the region. These station-keeping maneuvers are a primary driver of operational utility and previous studies have estimated the total cost of station-keeping to vary from approximately 1-4 m/s/yr to more than 50 m/s/yr. The former figure is based on orbit determination accuracy better than 10 meters [61] and the latter is based on dynamics including modeling and maneuver errors [37]. This paper will discuss work that seeks to improve the navigation solutions of missions in Earth-Moon LPOs. Improved navigation solutions are expected to have a direct impact on both the total delta-v required for these missions as well as the tracking and staffing requirements during orbital operations.

To obtain these operational improvements, raw tracking data from the **A**cceleration, **R**econnection, **T**urbulence and **E**lectrodynamics of the **M**oons **I**nteraction with the **S**un (ARTEMIS) mission is used to evaluate sources of navigational errors. The ARTEMIS mission is unique in that it was the first mission to ever maintain LPOs in the Earth-Moon system. The ARTEMIS mission utilized two spacecraft from the **T**ime **H**istory of **E**vents and **M**acroscale **I**nteractions during **S**ubstorms

(THEMIS) mission constellation and employed a highly efficient orbital transfer to relocate these spacecraft from high Earth orbits to the Moon [5, 12, 164]. These two spacecraft are operationally referred to as P1 and P2. This naming convention will be maintained in this paper. The spacecraft designated P1 maintained LPO from approximately August 25^{th} 2010 until June 6^{th} 2011 while P2 maintained LPO from approximately October 20^{th} 2010 until June 10^{th} 2011. The station-keeping budget for ARTEMIS was approximately 15 m/s for each spacecraft during the planned $\sim$6 month L_1/L_2 orbit maintenance portion of the mission. The magnitude of these station keeping maneuvers is driven primarily by the accuracy of navigation solutions and maneuver execution errors.

The primary motivation of this and future work is to evaluate the raw data from the ARTEMIS mission to develop a body of knowledge relevant to navigating spacecraft in Earth-Moon LPOs. This body of knowledge seeks to improve the operational efficacy of future missions planning to utilize this environment for space science and exploration. The work presented here is based on evaluating raw data from the P2 spacecraft.

This paper specifically will review the processes used to evaluate the raw operational data, discuss results of processing the data in between maneuvers, review solutions generated from processing data over maneuvers, and demonstrate preliminary results for increased fidelity estimates of solar coefficients. These results will be evaluated using overlap comparisons to draw conclusions on the precision of orbit solutions.

4.2 Technical Overview

Previously, simulated data was evaluated to better understand the navigation environment in LPO regions. This simulated data used spacecraft parameters and mission information meant to relate to the ARTEMIS operational mission. Upon completion of this preliminary work using simulated data, the research moved to look at what information could be derived from the raw operational data during the LPO mission phase.

Processing raw tracking data required significant new development work to establish the functionality in software tools at the Colorado Center for Astrodynamics Research capable of gen-

erating and evaluating navigation solutions. The following sub-sections will provide a a high level overview of select development activities.

4.2.1 MONTE

The **M**ission analysis and **O**perational **N**avigation **T**oolkit **E**nvironment (MONTE) software was developed at NASA's Jet Propulsion Laboratory (JPL) to replace legacy navigation software DPTRAJ/ODP [144]. MONTE was developed to help support trajectory and navigation analysis and design for spacecraft missions. The MONTE software provides a set of functions that enable the design, estimation, and control of spacecraft trajectories. MONTE relies heavily on object-oriented programming, thus allowing a user to construct object instances with callable functions.

The general form of MONTE's discrete-time kalman filter can be found in Bierman [10]. The estimated state vector can be separated into three categories: estimated parameters, stochastic parameters, and consider parameters. The estimated parameters include both dynamic and bias parameters whose covariance can be affected by the state transition matrix time updates but are not affected by any process noise or stochastics directly. Stochastic parameters are those parameters that can change over a time interval due to a discrete noise process. These discrete-time process noise stochastic parameters are applied at regular intervals, known as batches. Consider parameters have uncertainties that are fed into the estimation process and affect the consider covariance values but their values are not estimated and have no influence on the estimated parameters [148].

4.2.2 Tracking Data and File Formats

Observation data for the ARTEMIS mission is primarily S-band radiometric tracking data from several ground stations. The ARTEMIS tracking data comes from three primary ground-based tracking networks which include the Deep Space Network (DSN), the Universal Space Network (USN) and the Berkeley Ground Station (BGS). DSN tracking data was supplied in TRK-2-34 format and then converted to a Universal Tracking Data Format (UTDF) format with both Doppler and Range measurements. The Doppler measurements were compressed to 60 second count data.

BGS supplied Doppler tracking in UTDF format with primarily 10 second count data and some high-density data with 0.1 second count intervals. BGS does supply Range measurements. However, due to the link margin at BGS, Range data is generally not reliable. The USN tracking data was also in UTDF format with both Range and Doppler measurements with a count time of 5 seconds. This data was similarly compressed to 60 second count data and for the purposes of the solutions in this paper was not included in the filter runs.

4.2.3 Overlap Analysis

Comparing outputs from the navigation filter and generating reliable estimates for uncertainty and quality of solutions is a challenge with operational data. To evaluate the precision, or consistency, of orbit solutions generated with the raw tracking data for this work, overlap analyses were conducted [135, 140]. These overlap analyses were able to provide insight into the solutions being generated and provide a metric for evaluating the performance of the navigation filter.

The various approaches to processing the data necessitated two overlap strategies. A short-arc overlap was conducted to evaluate the navigation solutions between maneuvers. These solutions begin immediately after a station-keeping maneuver and end immediately before the next station-keeping maneuver. Once the ability to filter over and estimate maneuvers was demonstrated, a subsequent overlap approach which considered orbit solutions spanning over maneuvers was employed. In this analysis, these overlap studies are considered long-arc overlaps and generally consider periods spanning two station-keeping maneuvers. Fig. 4.1 gives a simple schematic of the overlap strategy used in this paper.

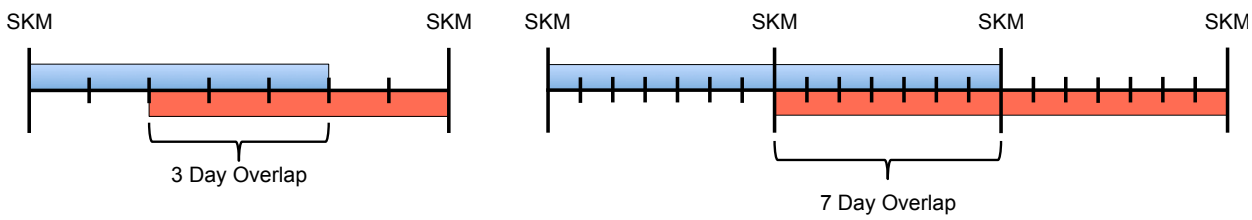

Figure 4.1: Schematic of 3-day and 7-day Overlaps.

4.2.4 Orbit Determination Set-up

The orbit determination procedure used to process the ARTEMIS tracking data and generate reliable solution estimates is an intricate process. There are several pre-processing stages that must be completed before any estimation can take place. The first pre-processing step was the conversion of ARTEMIS tracking data from UTDF format to a format that MONTE can read. Tracking data for the DSN, BGS, and USN from 2010 and 2011 were converted to a MONTE readable measurement format for both Two-way ranging and Two-way Doppler measurements. Due to run-time concerns and the dense Doppler tracking, all Doppler measurements were then compressed to a 60 second count time. This compression drastically reduced the noise level of the BGS Doppler measurements.

A major source of error for radiometric ground measurements is due to the propagation delay of a radio signal caused by the troposphere and ionosphere. The accuracy of radiometric ranging is greatly affected by the residual errors in modeling signal propagation delay through the troposphere and stratosphere. The main modeling method used in this work to mitigate the effects of the tropospheric delay rely on measurements of the zenith dry and wet delays at the ground station. These zenith delays are then mapped using the Niell mapping function [112]. A seasonal model for each ground station complex is obtained from monthly averages of zenith delay [31]. A 10^{th} order polynomial is then fit to 3 days worth of zenith delays that deviate from the seasonal model for the duration of the mission. The dispersive effects of the ionosphere on radio signal propagation are generally accounted for by a linear combination of observations with multiple frequencies. However, standard interplanetary navigation utilizes a single frequency that must be corrected as much as possible for the total ionospheric delay. The first order ionospheric delay terms contribute to 99.9% of the total ionospheric delay [124]. The first order ionospheric delay depends only on the Slant Total Electron Content (STEC). For this analysis, global Vertical Total Electron Content (VTEC) maps were obtained from the International GNSS Service (IGS) that were then interpolated spatially and through time [136]. A thin shell spherical layer mapping model

is then used to convert the interpolated VTEC values into the necessary STEC. An ionospheric delay is then calculated for each ground station based on the ground stations position and the position of the spacecraft. The total ionospheric delay during an observation pass is fit to a 10^{th} order polynomial and applied to the observations during the filtering process.

The next part of the OD procedure was the determination and initialization of dynamic models to use in the trajectory propagation and estimation. The main perturbing dynamics that are included in this analysis are that of gravity, solar radiation pressure, and random acceleration perturbations. The JPL planetary ephemeris DE421 is used for the positions of the celestial bodies [36]. The three main celestial bodies perturbing the ARTMEIS-P2 trajectory are that of the Earth, Moon, and Sun. The Earth was considered to be the main perturbing body with third-body gravitational perturbations evaluated from the Moon, Sun, and remaining planets. The Earth's non-spherical gravity was modeled using GGM02C with a 16x16 spherical harmonic representation [147]. The Moon's non-spherical gravity was modeled using the GRAIL derived GL0660B model with a 16x16 spherical harmonic representation [76]. The Earth's body-fixed orientation is represented by ITRF standards with Earth Orientation Parameter (EOP) updates. The Moon's body-fixed orientation is represented by the lunar librations present in the DE421 ephemeris.

Solar radiation pressure is included with a solar constant of 1366 W/m^2 at 1 AU. The spacecraft is modeled with a cylinder as the spacecraft bus, a one-sided top and bottom plate, a cylindrical antenna boom, and a cylindrical axial boom. The actual ARTEMIS spacecraft has a square bus with rectangular side plates as seen in Fig. 4.2(a). The shape model used in this analysis can be seen in Fig. 4.2(b). A cylindrical bus shape was chosen for this analysis since the ARTEMIS spacecraft has a spin rate of roughly 20 RPM throughout the mission. It was assumed that this spin rate with rectangular plates would average out the SRP effects similar to that of a cylinder with the same cross-sectional area.

The ARTEMIS spacecraft is spin-stabilized with it's body-fixed frame spin-axis pointed towards the south celestial pole. The attitude of the spacecraft was frequently estimated during the mission and was generally kept to within a few degrees of the south celestial pole [54, 92]. A time

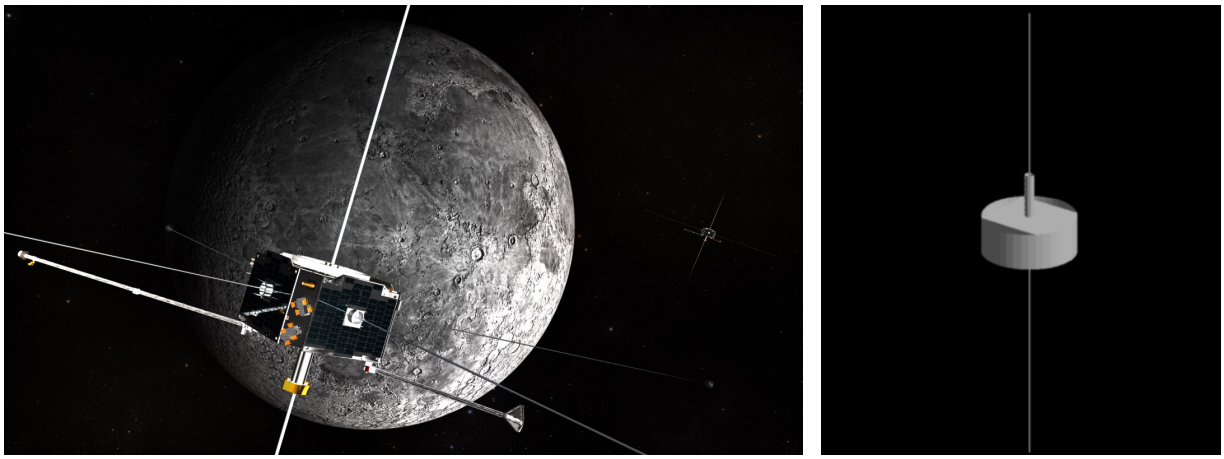

(a) Actual ARTEMIS shape [106] (b) Our Model

Figure 4.2: ARTEMIS spacecraft shape models.

history of the spacecraft's attitude has been implemented in our simulations in order to determine the area necessary for SRP calculations.

Throughout the mission, station-keeping maneuvers and small attitude burns were executed. Station-keeping maneuvers were generally on the order of less than a m/s in total imparted delta-V [91, 117]. It was assumed that the attitude burns that were executed were small and on the order of a mm/s or less. A time history of both station-keeping maneuvers and small attitude burns were also implemented in this analysis. While sufficient details for the station-keeping maneuvers (execution time and designed delta-V) are known, only the attitude maneuver execution time is known. Therefore, all initial estimates of these maneuvers are set to be 0.0 mm/s.

Once all of the models necessary to represent the mission were implemented, the orbit determination filter was initialized. In this work, a multitude of parameters are estimated. In general, every navigation solution estimated the spacecraft's position and velocity, an SRP scale factor, stochastic accelerations, station-keeping maneuvers, attitude maneuvers, and per-pass range biases. In certain cases, the specular and diffuse coefficients of the cylindrical bus, top plate, and bottom plate of the spacecraft model were estimated. Every navigation solution had errors in media calibrations (tropospheric and ionospheric delays), EOPs, and station locations as considered states. A list of the *a priori* uncertainties for the estimated and consider parameters, as well as

Table 4.1: Orbit determination filter uncertainties.

Estimation Parameters	*a priori* uncertainty (1-sigma)
Spacecraft position	100 km
Spacecraft velocity	1 m/s
SRP Coefficient	10%
Spacecraft Reflectivity Coefficients	
Specular	0.1
Diffuse	0.1
Empirical Accelerations	
Radial	5e-12 km/s^2
Transverse	5e-12 km/s^2
Normal	5e-12 km/s^2
Station Keeping Maneuvers	
X, Y, Z	10.0 mm/s
Start Time	10.0 s
Attitude Maneuvers	
X, Y, Z	1.0 mm/s
Start Time	10.0 s
DSN per-pass range bias	5 m
DSN measurements	
Range	2 m
Doppler	0.1 mm/s
Berkeley measurements	
Range	N/A
Doppler	2 mm/s
Consider Parameters	
Media Calibrations	
Earth Orientation Parameters	
DSN Station Locations	

observables, is given in Table 4.1. The measurement weighting was updated with the standard deviation of the postfit residuals after each filter iteration until convergence. For the cases presented in this work, 10 iterations of the filter were performed.

4.3 Overview of Initial Results

Given the approaches and spacecraft parameters discussed in the previous section, initial results processing the raw tracking data were generated for short arcs of less than 7 days commensurate with that performed by the operations team. The time period under examination begins on November 19, 2010 and goes until March 14, 2011. Fig. 4.3 shows the ARTEMIS-P2 trajectory

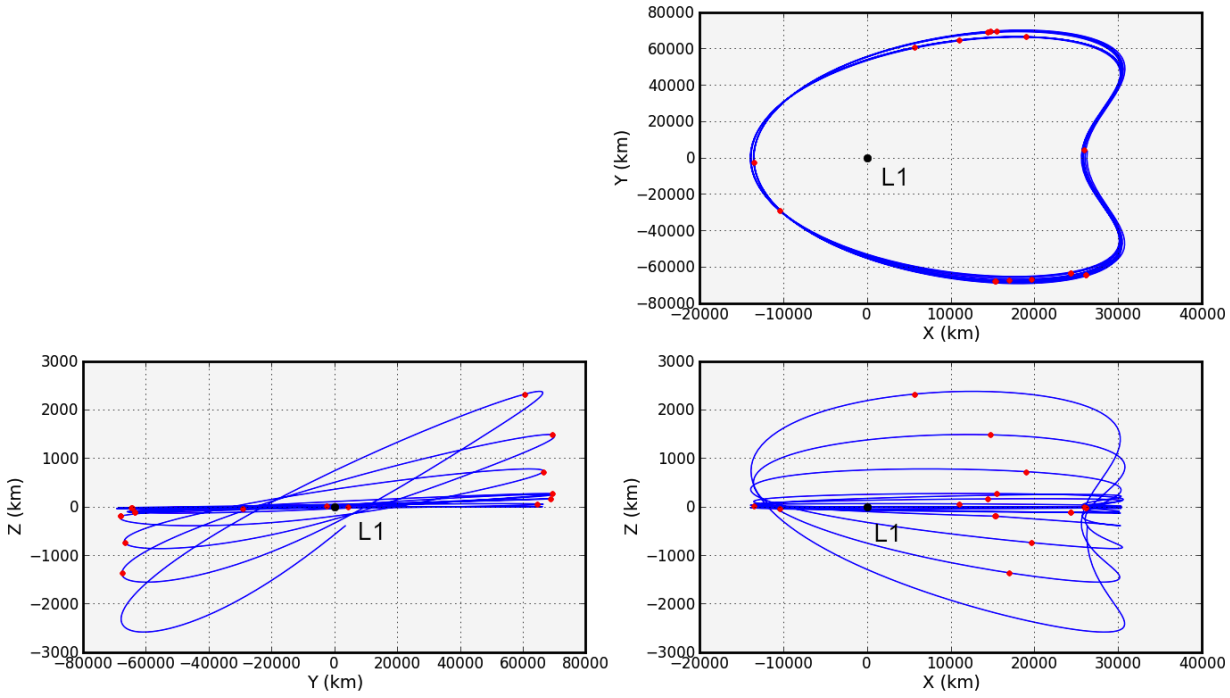

Figure 4.3: ARTEMIS-P2 trajectory from 19-NOV-2010 to 13-MAR-2011 displayed in the Earth-Moon rotating frame (Earth is in the -X axis with the Moon in the +X axis). The red dots represent the locations of Station Keeping Maneuvers that were performed.

that was under evaluation in this work. This period was chosen for analysis due to the fact that there was relatively low solar activity during this time-frame. The initial goal of this analysis was to obtain a detailed estimate of the spacecraft SRP parameters for use in later analyses.

Both short 7-day arcs and long 14-day arcs were evaluated over the 4 month time period of concern. Initial results spanning this time frame estimated position, velocity, SRP scale factor, and stochastic accelerations. The post-fit Doppler residuals for the 4 month time-span from the 14-day arc solutions are shown in Fig. 4.4. For reference, 1 mm/s corresponds to approximately 15.3 mHz. As expected the Berkeley Doppler data were considerably noisier than the DSN Doppler data. In addition, the tracking arc duration for Berkeley was considerably less than the DSN. In all of the following filter solutions, the data were weighted according to their post-fit residual standard deviations. Fig. 4.5 shows the post-fit range residuals for the DSN stations with their estimated per-pass range biases. Range data were weighted at a minimum of 2 m for the following filter solutions with an initial per-pass range bias uncertainty of 5 m. For reference, approximately 7 range units (RU) is 1 m.

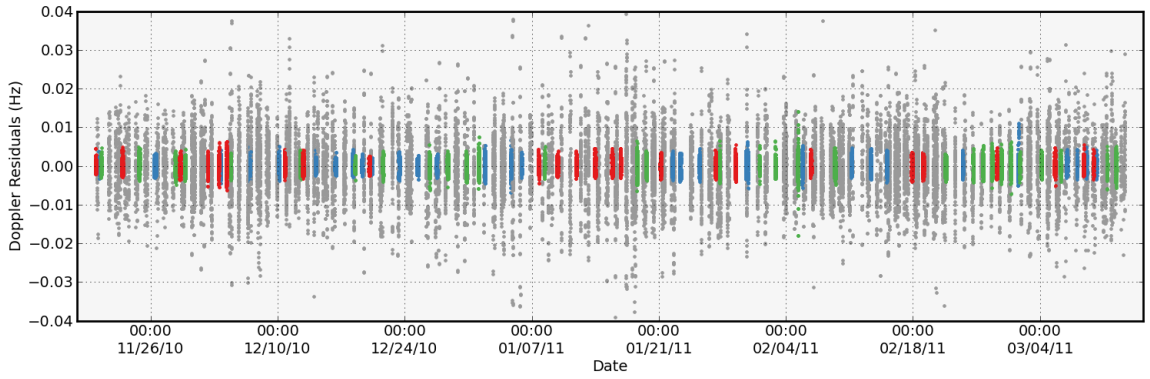

Figure 4.4: Doppler post-fit residuals for entire timeframe under analysis for Goldstone (blue), Canberra (green), Madrid (red), Berkeley (grey).

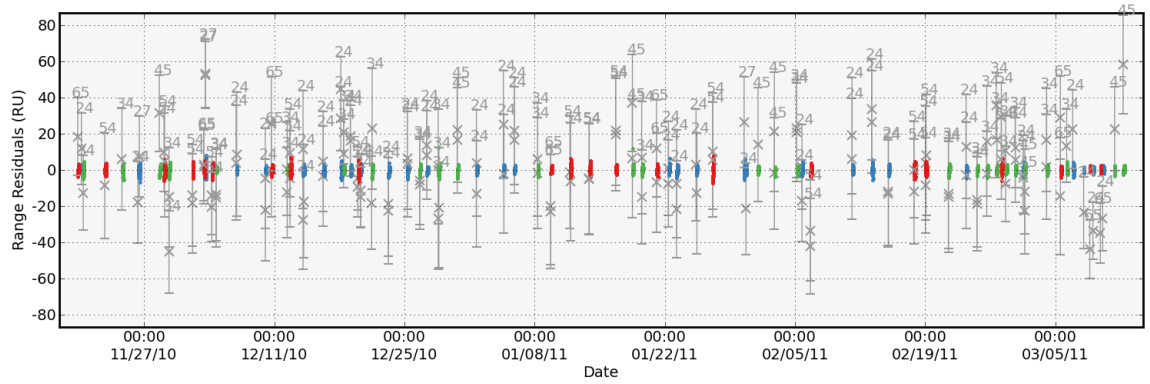

Figure 4.5: Range post-fit residuals with range biases for entire timeframe under analysis for Goldstone (blue), Canberra (green), Madrid (red), Berkeley (grey).

As a test to see if the post-fit residuals were Gaussian noise, a histogram of all post-fit residuals by station was examined. Fig. 4.6 shows the distribution of post-fit residuals for the Doppler measurements by station for the entire analysis period. On average, the Berkeley ground station (BRKS) had a Doppler residual of roughly 8 mHz with the DSN stations 1.8 mHz. While BRKS seems Gaussian, the other DSN stations do not. Fig. 4.6 shows an increased prominence of Doppler residuals for the DSN ground stations. It was also noticed on certain passes that the residuals seemed to have a sometimes periodic or bounded structure at a few mHz. This periodic or bounded behavior in the post-fit Doppler residuals is persistent throughout the entire data arc.

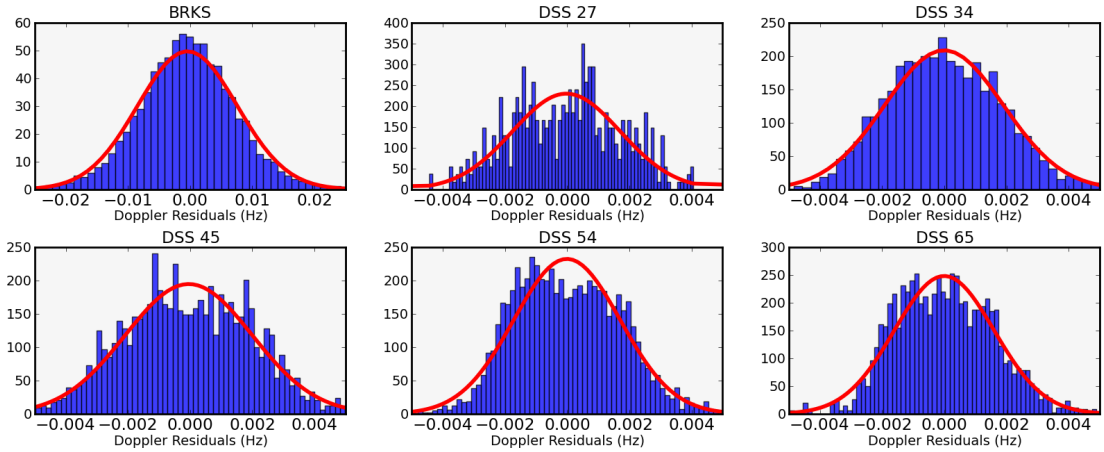

Figure 4.6: Histogram of Doppler residuals by station.

After a quick FFT analysis of the 60 sec count Doppler data for a subset of data arcs, a periodic structure was noticeable. It was determined that this signature is most likely due to a slight offset between the spin axis and the antenna which resulted in a slight modulation in the Doppler data. Fig. 4.7 shows two DSN Doppler passes during the time period under analysis. Fig. 4.7(b) clearly has a defined structure to it due to the spin rate of the spacecraft. Since this is 60 sec count Doppler, the signal is significantly aliased. In certain cases, the Doppler residuals appeared to have slight precession and nutation as well. In order to confirm that this signature is due to the spinning spacecraft, an FFT analysis was performed on dense BRKS Doppler data. The dense BRKS Doppler data is given at sparse times throughout the beginning of the analysis period at a rate of 10Hz. The FFT resulted in a peak frequency that was identical to the spin rate determined from telemetry at that time. Even though the 10Hz BRKS Doppler data is incredibly noisy, a frequency can still be determined. The estimation of the spin state and removal of the spin signature from the Doppler measurements was not performed in this analysis. Instead, the DSN Doppler measurements were de-weighted accordingly. The periodic structure being noticeable at the 2 to 4 mHz level is commensurate with the expected uncertainty of the DSN Doppler data.

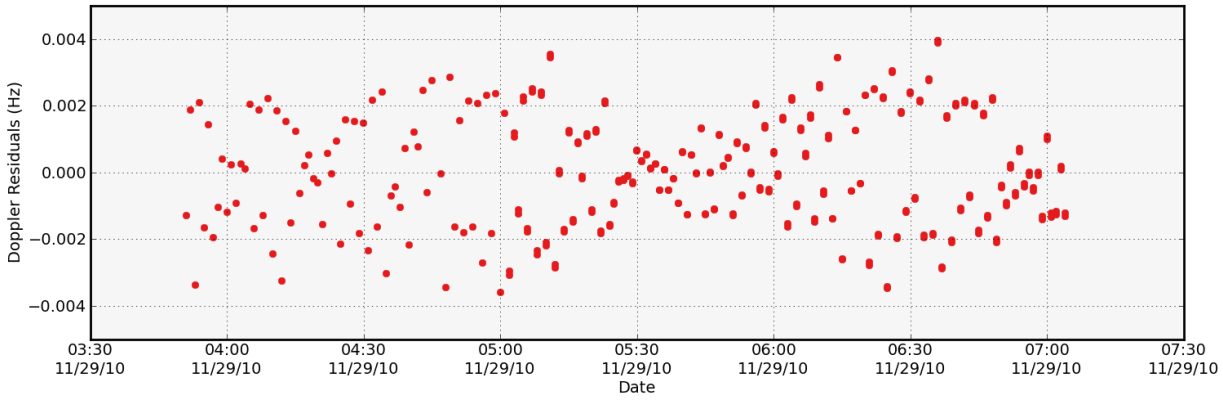

(a) Spin signature seen in November

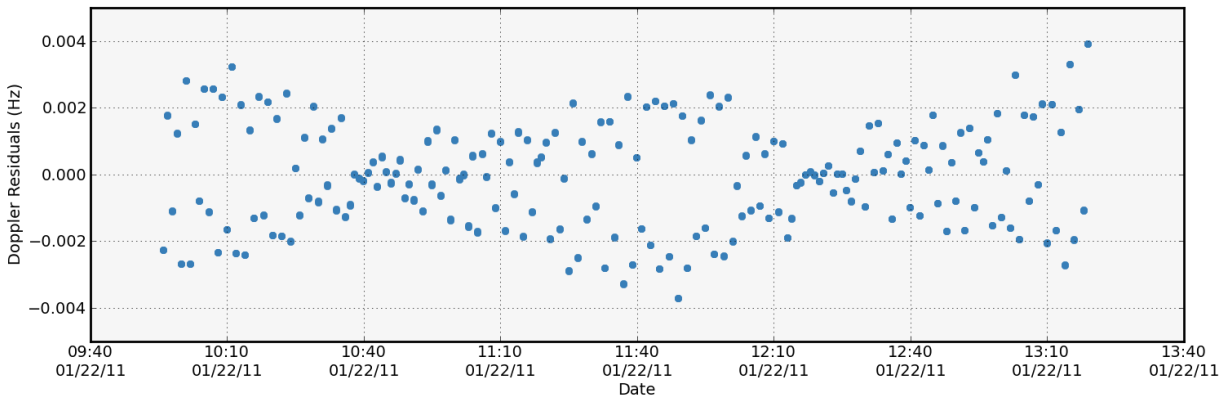

(b) Spin signature seen in January

Figure 4.7: Sping signature seen in Doppler residuals throughout the data arcs for 2 passes in different months.

A benefit of using a sequential filter to estimate the spacecraft state is that the estimation of stochastic accelerations can be included. The process of adding stochastic accelerations to a batch estimator, although it can be done, is quite difficult. The idea behind stochastic acceleration estimation is to pick up any unmodeled perturbations that the dynamics are not accounting for. Ideally, one would like the stochastics to be zero mean with slight deviations throughout the trajectory. There are cases where certain parameters, like an increase in solar irradiance causing an increase SRP force, cannot be modeled. In these cases, stochastic acceleration estimation is desired. Fig. 4.8 shows the estimated white-noise stochastic accelerations over a 14 day data arc. Though there are slight variations in the stochastic accelerations, they remain close to zero.

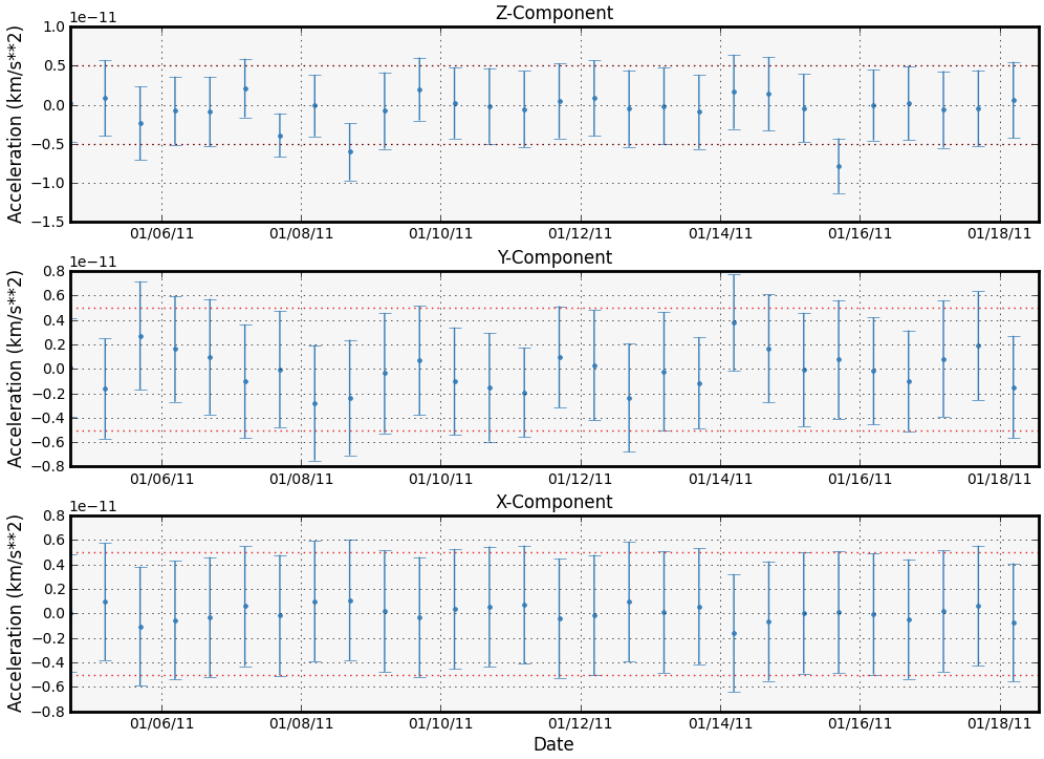

Figure 4.8: Example of stochastics fit during a Long Arc: Z-axis is S/C-Moon line.

4.4 Solar Coefficient Results

In an effort to increase the fidelity of the spacecraft model used in this analysis, specific focus was placed on estimating the spacecraft parameters that impact the effect of solar radiation pressure on the evolution of the trajectory. Gravitational perturbations are well defined and straightforward to implement with a high degree of fidelity. Solar perturbations on the other hand are susceptible to variations in spacecraft characteristics, attitude, and solar activity. A detailed model of the spacecraft shape was used in the analysis presented in this paper. The model used is represented by the shape model shown in Fig. 4.2(b) in a previous section. In order to increase the fidelity of the spacecraft parameters that are effected by SRP, seven 14-day arcs were used to estimate the specular and diffuse coefficients for the spacecraft cylindrical bus, top plate, and bottom plat. The spacecraft shape and area parameters were kept constant throughout the filter runs. The attitude of the spacecraft shape model was updated regularly when attitude maneuvers were known to be

Table 4.2: ARTEMIS SRP Specular Coefficient Change (NORMALIZED)

	Bus Cylinder	Bus Top Plate	Bus Bottom Plate
Arc 1	0.9099	N/A	1.0337
Arc 2	0.9449	0.9717	0.9663
Arc 3	0.9704	0.9783	N/A
Arc 4	1.0309	1.0057	N/A
Arc 5	0.9575	1.0267	N/A
Arc 6	1.0070	1.0364	N/A
Arc 7	1.1793	0.9811	N/A
Average	1.0000	1.0000	1.0000

Table 4.3: ARTEMIS SRP Diffuse Coefficient Change (NORMALIZED)

	Bus Cylinder	Bus Top Plate	Bus Bottom Plate
Arc 1	0.8576	N/A	1.0025
Arc 2	0.8833	0.9993	0.9975
Arc 3	0.9263	0.9982	N/A
Arc 4	1.0591	1.0005	N/A
Arc 5	0.9788	1.0074	N/A
Arc 6	1.0499	1.0050	N/A
Arc 7	1.2450	0.9895	N/A
Average	1.0000	1.0000	1.0000

performed. The filter solutions were iterated until there was very little change in the specular and diffuse coefficients. The purpose of this analysis was to determine an average solution to the spacecraft parameters for future use in data arcs. Tab. 4.2 gives the normalized values of the specular coefficients for the three spacecraft shapes being estimated. The values are normalized based on the average value of all seven data arcs. Tab. 4.3 gives the normalized values of the diffuse coefficients for the three spacecraft shapes being estimated. Out of all of the parameters being estimated, the diffuse coefficient for the bus cylinder was the most difficult to converge on. All of the other specular and diffuse coefficients settled onto nominal values.

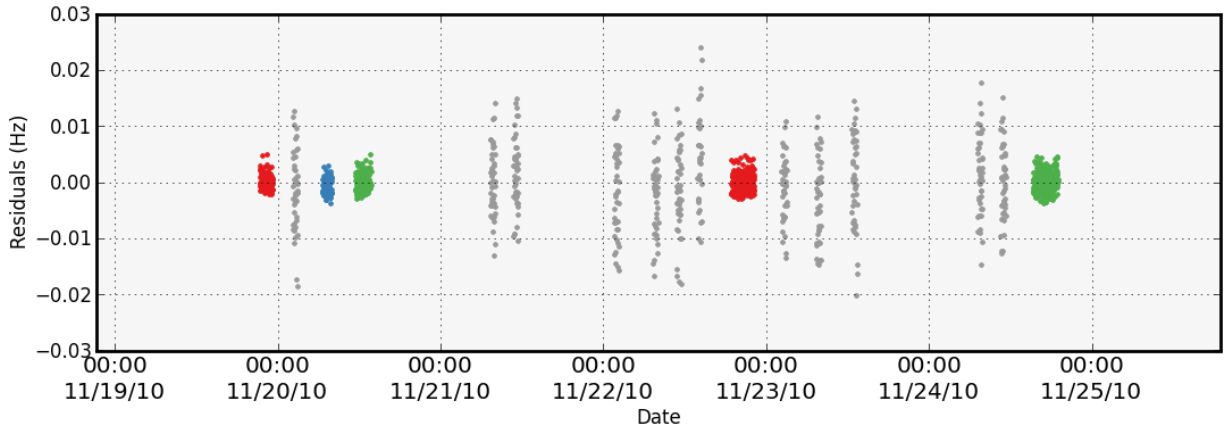

Figure 4.9: Short Arc Doppler tracking.

4.5 Short-arc Overlaps

The overlap strategy that was used in this section was that of generating solutions using 5 days worth of tracking data immediately after a station keeping maneuver and compare this to solutions where the epoch began 5 days before the next station keeping maneuver. Nominally, this produced an overlap of about 3 days where the typical duration between station keeping maneuvers was a week. A key consideration for these short-arc evaluations was whether the filter would be able to converge in enough time to perform meaningful comparisons between station-keeping maneuvers. The tracking data available are relatively sparse as shown in Fig. 4.9. Typically, 5 DSN passes were performed for each short-arc overlap analysis. The number of BRKS Doppler passes was usually 10 or more. Five days of tracking allowed for the initial position uncertainty to come down to 500 m or less in each coordinate with solutions converging after a few iterations.

Given these conditions, evaluation of the precision of the orbit solutions was possible during these short-arc periods. Fig. 4.10 and Fig. 4.11 demonstrate the precision as evidenced by short-arc overlap analyses described previously. Fig. 4.10 shows the position Radial, In-track, Cross-track, and 3D-RMS overlap precision for the short-arc analysis. The average short-arc overlap position errors are 15 $\pm$ 8 m Radial, 183 $\pm$ 146 m In-track, and 416 $\pm$ 247 m Cross-track. The average short-arc overlap velocity errors are 0.263 $\pm$ 0.182 mm/sec Radial, 1.427 $\pm$ 1.516 mm/sec In-track, and 2.825 $\pm$ 1.730 mm/sec Cross-track.

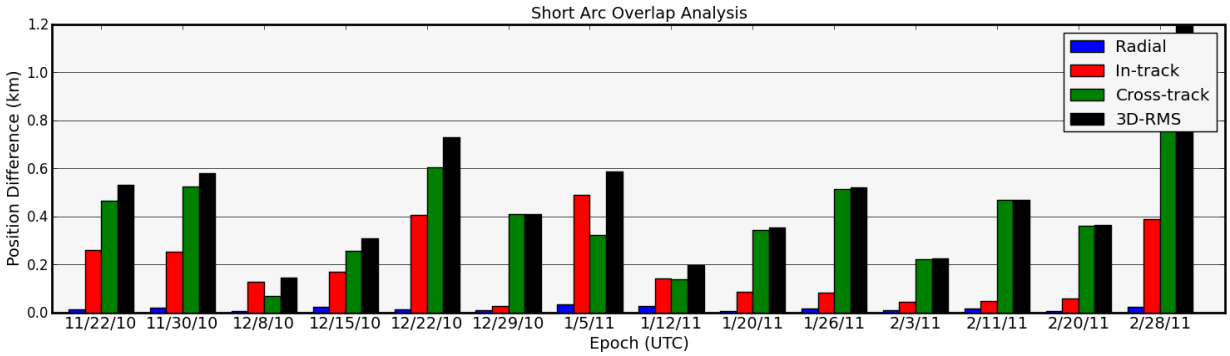

Figure 4.10: Short Arc Position Overlap Analysis.

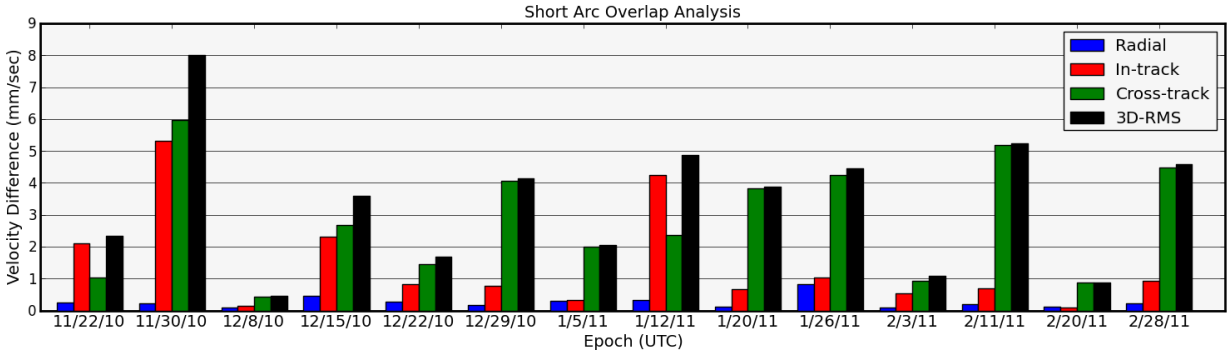

Figure 4.11: Short Arc Velocity Overlap Analysis.

The evaluations in this section and the subsequent section were estimated with an initial state derived from the spacecraft ephemeris which was subsequently perturbed.

4.6 Long-arc Overlaps

The short-arc overlap analysis contained data arcs and filter solutions that did not go over maneuvers and thus did not estimate station keeping maneuvers. The overlap strategy used in this section was to start a data arc just after a station keeping maneuver and estimate over a single station keeping maneuver with the data cut off just prior to the next station keeping maneuver. A second overlap was initialized just after the estimated station keeping maneuver in the preceding data arc and continued over the next maneuver ending just prior another maneuver. This left about a 7 day overlap to compare the two solutions which generally spanned 14 days. There was

significantly more tracking data during the long arcs than the short arcs. Fig. 4.12 and Fig. 4.13 demonstrate the precision as evidenced by long-arc overlap analyses described previously. Fig. 4.12 shows the position Radial, In-track, Cross-track, and 3D-RMS overlap precision for the short-arc analysis. The average long-arc overlap position errors are 5 ± 4 m Radial, 66 ± 50 m In-track, and 102 ± 53 m Cross-track. The average long-arc overlap velocity errors are 0.062 ± 0.048 mm/sec Radial, 0.283 ± 0.221 mm/sec In-track, and 0.687 ± 0.048 mm/sec Cross-track.

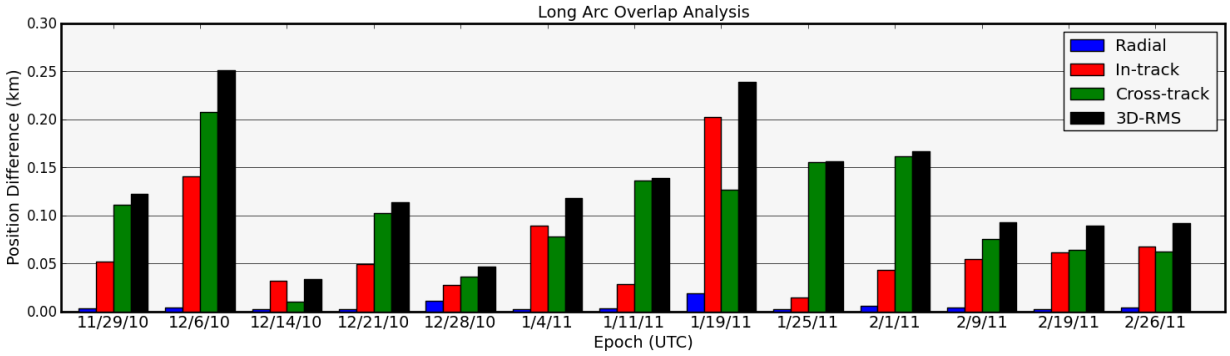

Figure 4.12: Long Arc Position Overlap Analysis.

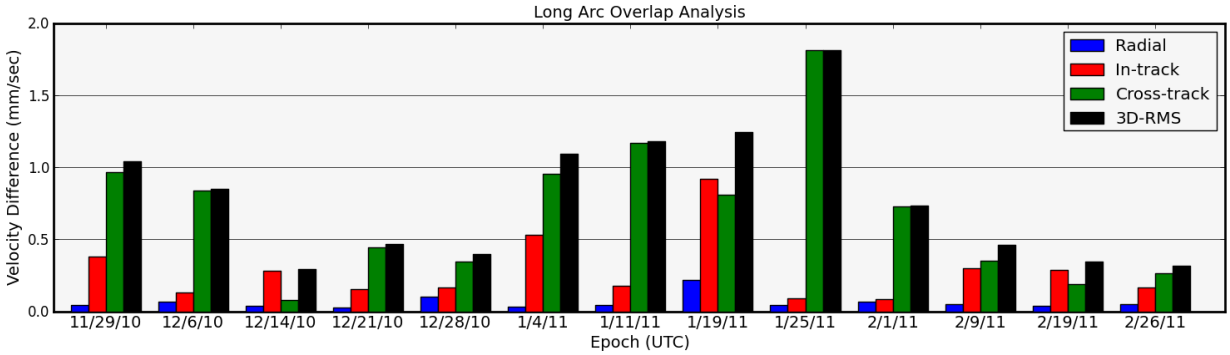

Figure 4.13: Long Arc Velocity Overlap Analysis.

4.7 Solutions Considering Maneuvers

As noted in the previous section, the sequential filter set-up enabled for solutions to span station-keeping maneuvers. In solving for filter runs that span maneuvers, the filter is able to obtain an estimate of the maneuver. The results discussed in this section were estimated from the filter given an *a priori* estimate of the timing of the maneuvers and no *a priori* information about the magnitude or direction of the maneuvers.

For this evaluation, 17 station-keeping maneuvers were estimated spanning a time frame from November 2010 and March 2011 for the P2 spacecraft. The estimated maneuvers were compared to the maneuvers designed by the mission team at Goddard Space Flight Center. These designed maneuvers do not include variations in the maneuver magnitude or direction caused by translation of the original design, done in AGI Satellite Tool Kit, into the maneuver commands constrained by the spacecraft performance constraints. The data used to generate the comparisons shown in Tab. 4.4 were derived by comparing the magnitude and the directional components of the maneuvers as designed and as estimated. The directional components are defined in the True of Date reference frame. The level of fidelity in the estimated solution as a result of the improved solar coefficients and the long data arcs enabled this evaluation.

Using a different method that leveraged differences in spacecraft state from propagated solutions, Woodard et al. performed a similar evaluation and obtained results of similar magnitude.[162] This data shows that, in general, the the magnitude and x-component of the maneuvers were accurately executed and estimated whereas the y-components and z-components were seen have larger variations between what was estimated and what was designed.

Table 4.4: Maneuver Evaluation (Designed-Estimated)

	Mag. (mm/s)	Mag. (%)	X (mm/s)	X (%)	Y (mm/s)	Y (%)	Z (mm/s)	Z (%)
Average	1.98	1.49	0.93	1.78	3.39	9.43	2.94	48.23
Median	0.71	0.58	0.61	1.10	1.98	5.69	1.78	6.51
Max	19.0	7.28	3.78	6.98	20.7	31.86	12.7	451.03
Min	0.10	0.03	0.21	0.06	0.06	0.30	0.25	1.22

4.8 Summary and Future Work

The work completed to date has demonstrated an ability to post-process raw tracking data from the ARTEMIS mission during the LPO phase of the mission. The navigation solutions generated are able to resolve spacecraft spin signatures which suggests the filter is fitting the Doppler data well. Analysis was performed to obtain accurate solar radiation pressure estimates for the P2 spacecraft which was subsequently used in the analysis and was shown to be relatively consistent over the arcs evaluated. Overlap analyses demonstrated precision of the orbit solution to be 128 $\pm$ 62 m for position 3D-RMS and 0.788 $\pm$ 0.448 mm/s for velocity 3D-RMS. The ability to filter over and subsequently estimate maneuvers was leveraged to compare designed and estimated station-keeping maneuver solutions. These differences were observed to be small, as a percentage of the total maneuver, in magnitude and the True of Date x-components of the maneuvers. The True of Date y-components and z-components were observed to have higher variations which could be caused by poor maneuver performance in those directions or poor observability of those directions within the navigation solutions.

During this work it was observed that the attitude maneuvers performed by the spacecraft had a noticeable impact on the solution fit and precision. Preliminary results suggest that this impact is on the order of hundreds of meters in position when comparing solutions with and without these attitude maneuvers modeled. Future work will evaluate this initial observation.

Additional work will investigate the overall data-set including evaluation with respect to attitude maneuvers, investigation of additional arcs of data, identification of filter or model parameters that yield improved solutions in terms of lower uncertainty and higher precision. This work will seek to systematically identify unmodeled accelerations observed in the stochastics of the solutions present here. This identification has the potential to increase the fidelity of the dynamics and thus increase the accuracy and convergence speed of future solutions. Future analysis will also evaluate data from the P1 spacecraft. This additional data-set is expected to provide valuable insight on the effect of spacecraft parameters on the navigation solution since both spacecraft are identical.

Chapter 5

Linked, Autonomous, Interplanetary Satellite Orbit Navigation

5.1 Overview

Autonomous SST relies on an ability to estimate the absolute positions of a spacecraft without the use of ground station observations. To do so, the size, shape, and orientation of the satellite's orbit must be observable from the measurements available between the linked spacecraft. The observability of the system depends on the existence of a unique observation time-series. The determining factor in whether a unique trajectory can exist, and thus whether LiAISON is possible, is the acceleration function acting on the orbiter. No unique SST time series can exist in a symmetric acceleration field, one in which the function and its time derivative are spherically symmetric. Even in regions with desired asymmetric perturbations, uncertainties in the force model and observation noise can counteract these effects in the accelerations and prevent SST orbit determination [56]. As a result, the asymmetric acceleration effects must be great enough to outweigh the uncertainties and force model inaccuracies that arise.

Acceleration functions with sufficient asymmetry for LiAISON are provided by three-body systems that give rise to libration point orbits (LPOs). The third-body perturbation of the Moon is sufficient to provide the asymmetry necessary for locally unique trajectories to exist. Due to the effects of the gravitational forces of the Moon and Earth, lunar LPOs can only have one orientation with respect to this system. EML-1 and EML-2 LPOs are specifically well suited for LiAISON because they are locally unique and reside in regions where the asymmetry of the accelerations is strong. Under these conditions a spacecraft at one of these Lagrange points can uniquely and

absolutely determine the state of a second satellite using crosslink range measurements without ground-based observations.

Several papers have demonstrated the benefits of LiAISON navigation applied to satellite constellations at the Moon. This effort has been motivated by NASA's aim to develop a permanent presence at the Moon. Hill et al. explored the cases of 2–4 satellites placed in combinations of low lunar orbits and libration orbits about EML-1 and/or EML-2 points[56, 57, 60, 61]. A potential mission was examined in detail, including only two satellites: one in a 100-km polar orbit about the Moon and the other in a libration orbit about the EML-1 point [61]. The results demonstrated that satellites may be navigated at the Moon using realistic constraints and achieve uncertainties on the order of 100 meters or less for halo orbiters and 10 meters or less for low lunar orbiters. Any ground tracking passes would only improve the solutions.

In order to make an accurate analysis of a LiAISON navigation solution between an EML-1 and GEO constellation, an understanding of current navigation accuracies for both regimes is necessary. For the GEO regime, most commercial operators track GEO satellites to within a kilometer in position. More stringent requirements are necessary for the TDRSS system. A position navigation accuracy of better than 100 meters is required, though in practice position navigation solutions tend to be accurate to within 30 meters [156]. Sabol has shown that range-only observations can be used to perform orbit determination to within 30 meters in position for GEO satellites by using several different tracking stations [135]. Moreau et al. have shown that one could track GPS signals from GEO for a position accuracy of about 15 meters [103]. Tombasco showed that optical tracking could reduce the uncertainty of a GEO orbit to within 10 meters [151].

The ARTEMIS (Acceleration, Reconnection, Turbulence and Electrodynamics of the Moon's Interaction with the Sun) mission was the first mission to demonstrate the navigation of satellites in lunar LPOs [12, 163]. The primary measurement type for this mission was radiometric tracking data from the Deep Space Network (DSN), the Universal Space Network (USN), and the Berkeley Ground Station (BGS) [38, 162]. The DSN navigation data used for the ARTEMIS mission was range and Doppler measurements with a tracking pass schedule of 3.5 hours of data every other day

making an attempt to alternate stations from the northern and southern hemispheres. Navigation solutions were obtained for each satellite on the order of 100 meters in position and approximately 1 mm/s in velocity.

The effectiveness of LiAISON is evaluated using orbit determination solely composed of range and range-rate measurements between two participating spacecraft. A dedicated navigation satellite anywhere near the Moon has an advantage over ground stations for tracking GEO satellites using radiometric data. While most satellites are only visible from ground stations at certain times, including those orbiting around the EML-1 point, a link between a GEO and the EML-1 satellite has nearly continuous visibility. Figure 5.1 demonstrates the near continuous dynamic range measurements between an example GEO satellite and a satellite traversing an LPO about the EML-1 point versus the range of a GEO orbit tracked by a ground station. One can see clear signals in the data that may be used to lock onto the position and velocity of both satellites.

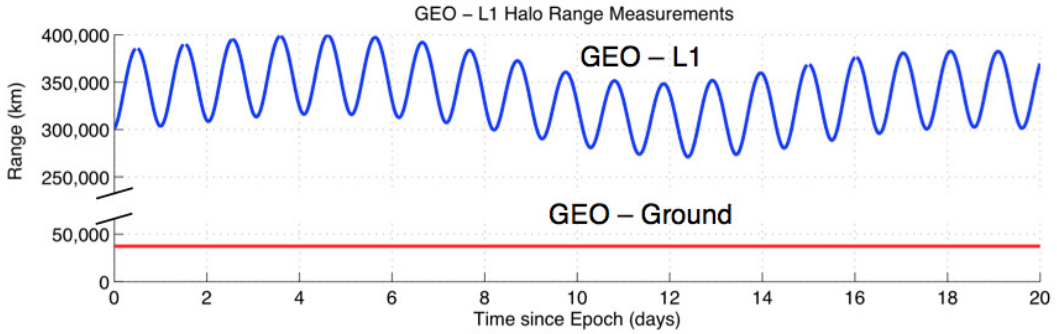

Figure 5.1: Observation geometry for truth model simulations for LiAISON and ground tracking.

5.2 Observability

The observability of LiAISON was first explored by Hill [56]. The approach taken in Hill's work was to investigate the information matrix to determine the amount of information contained for the position of a spacecraft at a specific time. The eigenvalues of the information matrix can be used to express a degree of information contained within the measurement itself. The value of the

eigenvalue of the information matrix represents the degree to which that observation influences the information. The eigenvector corresponding to that eigenvector provides insight on the direction to which that information is applied.

Hill determined some relationships of observability for Halo-Halo orbit constellations as well as Halo-LLO constellations. When the information matrix is expressed as

$$\Lambda = \sum_{i=1}^{l} H_i^{\mathrm{T}} W H_i \tag{5.1}$$

the effectiveness of observation i at t_i can be determined such that

$$\delta\Lambda(t_i) = H_i^{\mathrm{T}} W H_i. \tag{5.2}$$

The information contained within that observation can be obtained by computing the square root of the maximum eigenvalue of $\delta\Lambda(t_i)$. This measure gives some understanding of the information contained within a single measurement mapped back to the initial epoch t_0. Hill describes an exponentially increasing observation information as the time since the epoch increases. It is also pointed out that there to exist periods where the observation information decreases significantly suggesting portions of a Halo orbit where the geometry and natural dynamics when mapped back to the epoch have no influence on the initial state of the trajectory.

5.2.1 Hamilton and Melbourne discussion

Determination of the information content of radiometric signals for near-Earth, lunar trajectories, and interplanetary trajectories has been studied extensively over the past century [20, 53, 114]. For ranging data of near-Earth and lunar trajectories, Earth-based tracking relies on the rotation rate of the Earth to provide position parallax to obtain angular information of the trajectories. While ranging data alone provides the distance to the spacecraft, the parallax of the measurements over time give valuable information on the right ascension and declination of the orbit. A first order approximation of the topocentric range measurement commonly employed by the DSN can

be expressed as [20]

$$\rho \approx r - [r_s \cos\delta \cos(\phi - \alpha) + z_s \sin\delta] \tag{5.3}$$

where r is the geocentric range, δ is the declination, α is the right ascension, and ϕ is the longitude. This equation has been linearized for small quantities r_s/r and z_s/r. It shows immediately that angular information can be obtained as the station rotates. If a spacecraft is infinitely far away from the ground station and has infinitesimal velocity, a single pass of ranging data provides only position information. In addition, for spacecraft at low declinations, the information content of ranging data is limited [20**?**].

Not as well known are the benefits of the velocity parallax of Doppler tracking data providing angular information of a interplanetary spacecraft. The stations velocity about the geocenter impresses a sinusoidal signal upon Doppler tracking data whose amplitude and phase can be used to obtain angular position information. The velocity parallax for ground station Doppler data was first examined by [89] and later developed more by [53]. Since then considerable analysis have been done on the information content of Doppler tracking data for spacecraft at interplanetary distances [20, 53, 114]. The original analysis by Hamilton and Melbourne provided a 3 parameter first-order approximation of the geocentric range-rate of a spacecraft such that

$$\dot{\rho} = a + b\sin\omega_e t + c\cos\omega_e t \tag{5.4}$$

where

$$a = \dot{r}, \tag{5.5}$$

$$b = r_s \omega_e \cos\delta, \tag{5.6}$$

$$c = r_s \omega_e \cos\delta \Delta\alpha, \tag{5.7}$$

where $\Delta\alpha$ is the difference between the prime meridian at t_0 and the right ascension of the spacecraft. This formulation can be shown to provide geocentric range-rate information as well as right ascension and declination information over the course of a single tracking pass. If the tracking pass is symmetric about t_0 such, the half-width of the pass can be defined to describe the duration of the tracking arc. The maximum likelihood estimates of the 3 parameters a, b, and c can be determined analytically and show a strong correlation between [53]. The static doppler model from [53] can be used to determine the information content of a single pass of doppler assuming that the half-width of the pass is 90 degrees (meaning that the tracking data is taken from horizon to horizon). Using these assumptions, the covariance of the estimates of $\dot{r}$, δ, and α with respect to the coefficients a, b, and c is given by

$$\Lambda = \frac{\sigma_{\dot{\rho}}^2}{N(\pi^2-8)} \begin{bmatrix} \pi & 0 & \dfrac{4}{r_s\omega_e \cos\delta} \\ 0 & \dfrac{2(\pi^2-8)}{\pi r_s^2 \omega_e^2 \sin^2\delta} & 0 \\ \dfrac{4}{r_s\omega_e\cos\delta} & 0 & \dfrac{2\pi}{r_s^2\omega_e^2\cos^2\delta} \end{bmatrix} \tag{5.8}$$

Immediately, one notices a high correlation between the estimate of $\dot{\rho}$ and α. In addition, small declinations produce large uncertainties for δ.

Curkendall and McReynolds introduced a 6-parameter model describing the time history of a doppler measurement to first-order [20]. The 3-parameter static doppler model is extended by assuming that the quantities for $\dot{r}$, α, and δ can be expanded as

$$\begin{aligned} \dot{r}(t) &= \dot{r}(t_0) + \ddot{r}(t_0)\Delta t \\ \alpha(t) &= \alpha(t_0) + \dot{\alpha}(t_0)\Delta t \\ \delta(t) &= \delta(t_0) + \dot{\delta}(t_0)\Delta t \end{aligned} \tag{5.9}$$

The new 6-parameter doppler model is thus

$$\dot{\rho} = a + b\sin\tau + c\cos\tau + dt + e\tau\sin\tau + f\tau\cos\tau \tag{5.10}$$

where,

$$\begin{aligned} d &= a_g + r(\alpha^2 \cos^2\delta + \delta^2) \\ e &= -r_s \frac{\dot{\delta}}{r} \sin\delta \\ f &= -r_s \dot{\alpha} \cos\delta \\ \tau &= \omega_e t \end{aligned} \tag{5.11}$$

Similar to the 3-parameter model, the data partial matrix can be formed such that

$$\begin{aligned} A &= \frac{\partial(a,\ b,\ c,\ d,\ e,\ f)}{\partial(r,\ \delta,\ \alpha,\ \dot{r},\ \dot{\delta},\ \dot{\alpha})} \\ &= \begin{bmatrix} 0 & 0 & 0 & 1 & 0 & 0 \\ 0 & r_s\omega_e \sin\delta & 0 & 0 & 0 & 0 \\ 0 & 0 & -r_s\omega_e \cos\delta & 0 & 0 & 0 \\ \xi/\omega_e & \zeta/\omega_e & (\partial a_g/\partial\alpha)/\omega_e & 0 & 2r\dot{\delta}/\omega_e & 2r\dot{\alpha}\cos^2\delta/\omega_e \\ 0 & -r_s\dot{\delta}\cos\delta & -r_s\dot{\alpha}\cos\delta & 0 & -r_s\sin\delta & 0 \\ 0 & r_s\dot{\alpha}\cos\delta & r_s\dot{\delta}\cos\delta & 0 & 0 & -r_s\cos\delta \end{bmatrix} \end{aligned} \tag{5.12}$$

where,

$$\begin{aligned} \xi &= \frac{\partial a_g}{\partial r} + \dot{\alpha}^2 \cos^2\delta + \dot{\delta}^2, \\ \zeta &= \frac{\partial a_g}{\partial \delta} - 2r\dot{\alpha}^2 \cos\delta \sin\delta. \end{aligned} \tag{5.13}$$

The information matrix J can be formed where $J = A^{\mathrm{T}} W A$ and the covariance matrix is just $\Lambda = J^{-1}$. By investigating the the covariance matrix for small $\dot{\alpha}\cos\delta$ and $\dot{\delta}$, the following relations of the uncertainties hold true

$$\begin{aligned} \sigma_r &= \omega_e \sigma_d / \xi, \\ \sigma_\delta &= \sigma_b / (r_s \omega_e \sin\delta), \\ \sigma_\alpha &= \sigma_c / (r_s \omega_e \cos\delta), \\ \sigma_{\dot{r}} &= \sigma_a, \\ \sigma_{\dot{\delta}} &= \sigma_e / (r_s \sin\delta), \\ \sigma_{\dot{\alpha}} &= \sigma_f / (r_s \cos\delta), \end{aligned} \tag{5.14}$$

By inspection, the determination of the geocentric radial velocity $\dot{r}$ is directly related to the uncertainty in the a parameter. In addition, determination of δ and $\dot{\delta}$ is poor for low declinations. It

has been observed that the range component r is the most accurately observed position component using Doppler measurements. However, in some cases the geocentric range is the least observable position component.

The dominant term that determines whether or not range is observable stems from the partials of the solar gravity with respect to range. Figure 5.2 maps solar gravity partials with respect to range ($\partial a_g/\partial r$) for the region between 0.5 AU and 1.5 AU. The partial derivative is large when the Earth-spacecraf-sun angle is near 180° and near zero when the Earth-spacecraf-sun angle is near 55° or 125°. Reference [20] and [114] show that the determination of range for trajectories in this region is highly correlated to the solar gravity partials with respect to range ($\partial a_g/\partial r$). In addition, the determination of the cross velocity is coupled with the strength of information in the f term implying that the addition of range data significantly improves the determination of $\dot{\alpha}$.

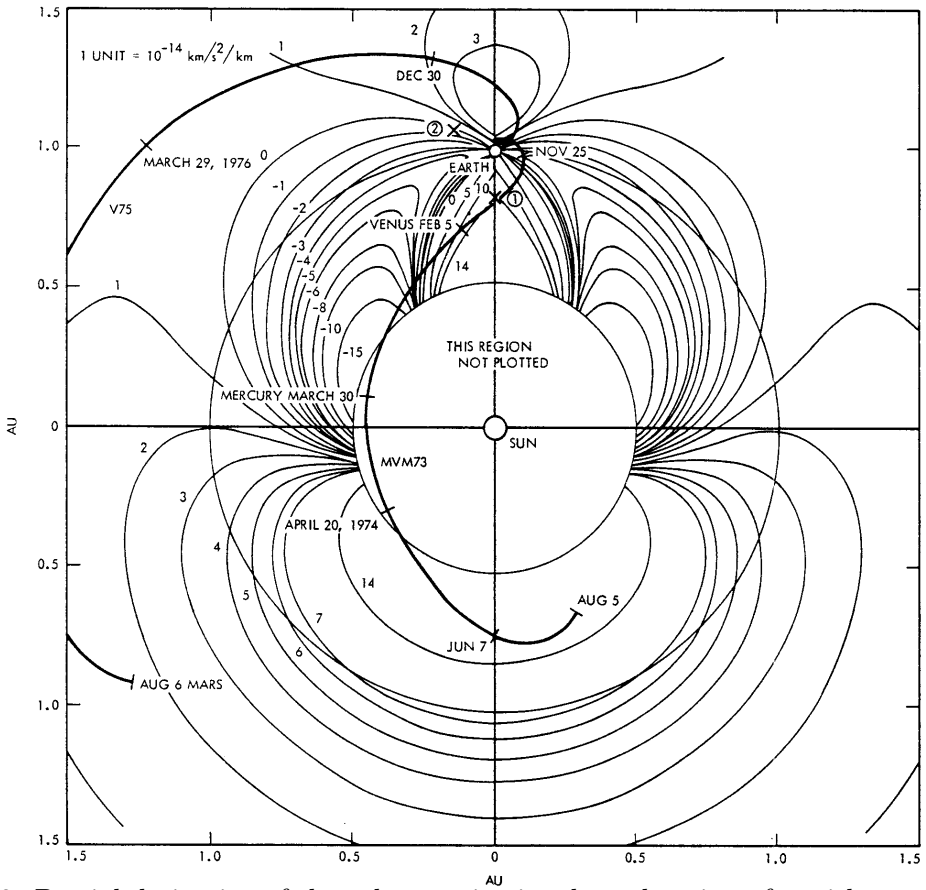

Figure 5.2: Partial derivative of the solar gravitational acceleration of r with respect to r [114].

5.2.2 Generalized Analytical Model

The previously described 3-, and 6-parameter range and Doppler models provide insight into the information content of a single pass of tracking data from an Earth based ground station. To this point, the observability of a LiAISON measurement has only notionally been investigated using observability techniques on a limited scale [56]. A simplified observation model a LiAISON measurement could provide insight into the information content contained within that measurement. The following sections uses a first-order approximation to a Halo orbit using a Richardson-Cary approximation. It is assumed that the tracking spacecraft is distant and not moving a significant amount over the course of the tracking arc. This assumption, however, breaks down for most spacecraft under the influence of the Earth-Moon system. The purpose of this analysis is to examine the parts of the observable that govern purely geometric information content, and the information gleaned from the dynamics of the environment. An approach similar to that taken in [53] is used to define the basic geometry of the problem. This is then extended notionally to a more dynamic system with numerical results.

5.2.2.1 First-Order Static Range Model in Rotating Frame

Richardson describes an analytical form for periodic orbits in the CRTBP for both first and third-order approximations [130, 131]. The expressions given in [130] are approximations of the periodic orbit reference to one of the libration points in the synodic frame of the primary and secondary. The parameter γ_L defines the distance from the libration point to the secondary body. If the equations of motion of the CRTBP are linearized, an analytical expression for the trajectory of a periodic orbit about a libration point can be determined. This work uses only the first order terms from the Richardson third-order approximation of the periodic orbit about a libration point, which are written by

$$x_s = a_{21}A_x^2 + a_{22}A_z^2 - A_x \cos\tau \tag{5.15}$$

$$y_s = -kA_x \sin\tau \tag{5.16}$$

$$z_s = A_z \cos\tau \tag{5.17}$$

where $\tau = \lambda t + \phi$. In general, the motion of the spacecraft is described by six variables: the amplitudes of the in-plane and out-of-plane motion A_x and A_z respectively, the frequency of the in-plane and out-of-plane motion λ (the original derivation has λ and ν, however, these frequencies are equal for a halo orbit used in this analysis), the orbit phase angle ϕ, and the coefficients a_{21} and a_{22}. The coefficients a_21 and a_22 are retained from the third-order approximation to better describe the first-order motion in the x-direction due to the amplitudes A_x and A_z.

The range between a spacecraft in a halo orbit and a very distant spacecraft can be expressed by

$$\rho^2 = r^2 + r_s^2 - 2xx_s - 2yy_s - 2zz_s \tag{5.18}$$

where the subscript s denotes the "station", or the libration point orbiter, and the other cartesian components represent the distant spacecraft. This equation can be linearized about the origin where $x_s = y_s = z_s = 0$ since the assumption is that $x_s \ll 0$, $y_s \ll 0$ and $z_s \ll 0$. Thus, the first order approximation of the range linearized about the libration point is described by

$$\rho = \rho|_0 + \left.\frac{\partial\rho}{\partial x_s}\right|_0 x_s + \left.\frac{\partial\rho}{\partial y_s}\right|_0 y_s + \left.\frac{\partial\rho}{\partial z_s}\right|_0 z_s \tag{5.19}$$

Assuming the distant spacecraft is static in the rotating frame, one can obtain the following first-order approximation of the range linearized about the libration point.

$$\rho = a + b\cos\tau + c\sin\tau \tag{5.20}$$

$$a = r - (a_{21}A_x^2 + a_{22}A_z^2)\frac{x}{r} \tag{5.21}$$

$$b = A_x \frac{x}{r} - A_z \frac{z}{r} \tag{5.22}$$

$$c = kA_x \frac{y}{r} \tag{5.23}$$

Some important simplifications can be made by converting from cartesian coordinates to spherical coordinates. The following expressions are used to define the right ascension and declination of the distant spacecraft relative to the libration point.

$$\frac{x}{r} = \cos\delta\cos\alpha, \quad \frac{y}{r} = \cos\delta\sin\alpha, \quad \frac{z}{r} = \sin\delta \tag{5.24}$$

Substituting these equations into the first-order cartesian range equation, one gets a spherical representation such that

$$a = r - (a_{21}A_x^2 + a_{22}A_z^2)\cos\delta\cos\alpha \tag{5.25}$$

$$b = A_x\cos\delta\cos\alpha - A_z\sin\delta \tag{5.26}$$

$$c = kA_x\cos\delta\sin\alpha \tag{5.27}$$

Similar to the approach taken in [53], an investigation of the partial derivatives of this measurement approximation are in order to understand where the information in the spacecraft state is coming from. The following are the partial derivatives of the range equation with respect to the spherical position states r, α, and δ.

$$\frac{\partial\rho}{\partial r} = 1 \tag{5.28}$$

$$\frac{\partial\rho}{\partial\alpha} = (a_{21}A_x^2 + a_{22}A_z^2)\cos\delta\sin\alpha - (A_x\cos\delta\sin\alpha)\cos\tau + (kA_x\cos\delta\cos\alpha)\sin\tau \tag{5.29}$$

$$\frac{\partial \rho}{\partial \delta} = (a_{21}A_x^2 + a_{22}A_z^2)\sin\delta\cos\alpha - (A_x\sin\delta\cos\alpha - A_z\cos\delta)\cos\tau - (kA_x\sin\delta\sin\alpha)\sin\tau \quad (5.30)$$

Immediately, one notices the complexity of the partials when compared to the results in [53] for the geocentric range measurement information content. Similarly, as expected, the range from the libration point is determined directly, while the determination of the right ascension and declination are coupled with the halo orbit amplitudes.

5.2.2.2 First-Order Static Range-rate Model in Rotating Frame

The first-order static range to a distant spacecraft from a libration point orbiter was found to be expressed by

$$\rho = a + b\cos\tau + c\sin\tau \quad (5.31)$$

From this expression, an approximation to the range-rate of a distant spacecraft can be determined. Using the chain rule and taking the time derivative of the first-order range equation, the range-rate can be expressed by

$$\dot{\rho} = \frac{da}{dt} + \frac{db}{dt}\cos\tau + b\frac{d}{dt}(\cos\tau) + \frac{dc}{dt}\sin\tau + c\frac{d}{dt}(\sin\tau) \quad (5.32)$$

where,

$$\frac{da}{dt} = \dot{r} \quad (5.33)$$

$$\frac{db}{dt} = 0 \quad (5.34)$$

$$\frac{dc}{dt} = 0 \quad (5.35)$$

$$\frac{d}{dt}\left(\cos\tau\right) = -\lambda\omega\sin\tau \tag{5.36}$$

$$\frac{d}{dt}\left(\sin\tau\right) = \lambda\omega\cos\tau \tag{5.37}$$

Thus, the simplified first-order range-rate observation model is simply

$$\dot{\rho} = \dot{r} - \lambda\omega b\sin\tau + \lambda\omega c\cos\tau \tag{5.38}$$

Similar to the approach taken in [53], an investigation of the partial derivatives of this measurement approximation are in order to understand where the information in the spacecraft state is coming from. The following are the partial derivatives of the range-rate with respect to the spherical position states r, α, and δ.

$$\frac{\partial\dot{\rho}}{\partial\dot{r}} = 1 \tag{5.39}$$

$$\frac{\partial\dot{\rho}}{\partial\alpha} = \lambda\omega\left(kA_x\cos\delta\cos\alpha\right)\cos\tau + \lambda\omega\left(A_x\cos\delta\sin\alpha\right)\sin\tau \tag{5.40}$$

$$\frac{\partial\dot{\rho}}{\partial\delta} = \lambda\omega\left(A_x\sin\delta\cos\alpha - A_z\cos\delta\right)\sin\tau - \lambda\omega\left(kA_x\sin\delta\sin\alpha\right)\cos\tau \tag{5.41}$$

5.2.2.3 Non-static interpretation

While the previous first-order range and range-rate measurement models provide some insight into the geometrical information content, the approximation is limited due to the environment in which a spacecraft traverses the Earth-Moon system. If one extends this analysis similar to that of [20] and [114] for the 6-parameter model, similarities begin to appear. Examination of the first-order range and range-rate models show a similar structure to the observable namely they can be expressed by three parameters a, b, and c such that

$$\rho = a + b\cos\tau + c\sin\tau \tag{5.42}$$

and,

$$\dot{\rho} = a' + b'\cos\tau + c'\sin\tau \tag{5.43}$$

To first order, the non-static spacecraft's motion can be approximated by

$$\begin{aligned} \dot{r}(t) &= \dot{r}(t_0) + \ddot{r}(t_0)\Delta t \\ \alpha(t) &= \alpha(t_0) + \dot{\alpha}(t_0)\Delta t \\ \delta(t) &= \delta(t_0) + \dot{\delta}(t_0)\Delta t \end{aligned} \tag{5.44}$$

With these assumptions, the range-rate model now has the familiar 6-parameter expression

$$\dot{\rho} = a' + b'\cos\tau + c'\sin\tau + d't + e'\tau\cos\tau + f'\tau\sin\tau \tag{5.45}$$

While the parameters a', b', c', e', and f' give information directly on the spherical cartesian elements $\dot{r}$, α, δ, $\dot{\alpha}$, and $\dot{\delta}$, only the parameter d' gives range information r. The determination of the range from range-rate measurements is thus reliant on the partial derivatives of the relative acceleration over time. It is this partial derivative that drives the full state determination for a spacecraft using LiAISON range-rate measurements.

5.2.3 Observation Effectiveness

Figures 5.3 through 5.11 map out the partial derivatives of the relative acceleration between a point in the Earth-Moon system to that of either the Earth, L_1 point or L_2 point. The contours are computed in the inertial frame at a specific instance in time. Only the cartesian X and Y coordinates are varied keeping the Z component constant with a value of 0 km. The map of the partial derivatives are rotated such that the Earth and Moon lie along the X axis. The libration points, L_1 and L_2 are plotted for convenience. The purpose of these curves is to give an inclination as

to the complexity of the environment a spacecraft traverses in the Earth-Moon system. The previous sections have shown that these relative acceleration partial derivatives govern the information obtained for positioning when range-rate or Doppler data is collected. Figures 5.3 through 5.11 are similar to Figure 5.2 from [114] in which only the sun is the perturbing body with partial derivatives computed relative to the Earth. However, the inclusion of the acceleration due to the Moon significantly perturbs the relative acceleration partials near the Moon and the interaction with the partials due to the acceleration of the Earth.

Figures 5.3 through 5.5 show the contours of the partial derivatives of the inertial acceleration relative to the L_2 libration point with respect to the distance R from the libration point, the cartesian X, and the cartesian Y coordinates in the inertial frame where the Earth and Moon lie along the X-axis at the instance the map was created. These curves are relatively constant in time with respect to the Earth and Moon. A slight variation is due to the eccentricity of the Moon's orbit relative to Earth. This variation, however, does not alter the contour map significantly. Intuitively, the partial derivative strength varies significantly near a primary body and diminishes the further away the spacecraft is to that body. There should exist locations where these partial derivatives are zero with respect to X, Y, and R. Investigating Figures 5.3 through 5.5 show that there are several regions where the partials derivatives are zero or very near zero, indicating locations where Doppler data would give significantly reduced information on the range of the spacecraft. Figure 5.3 has zero partial curves leaving the Earth roughly along the $\pm$ Y-axis. Figure 5.4 also has a similar zero curve in this region for the partial derivatives with respect to the X coordinate. Figure 5.5 shows the partials with respect to the Y coordinate. Naturally, there is a zero curve along the X-axis. However, there is also a zero partials curve emanating from point between the Earth and the Moon. All of these partials contain a zero curve emanating form the Moon. The enhanced image to the right is a zoomed in contour near the Moon and libration points. One can clearly see the region in which the partial derivatives vary significantly with the zero curve as well. If a navigation satellite at L_2 was tracking a spacecraft traversing these low partial derivative curves, the position information contained within the range-rate data would be severely limited.

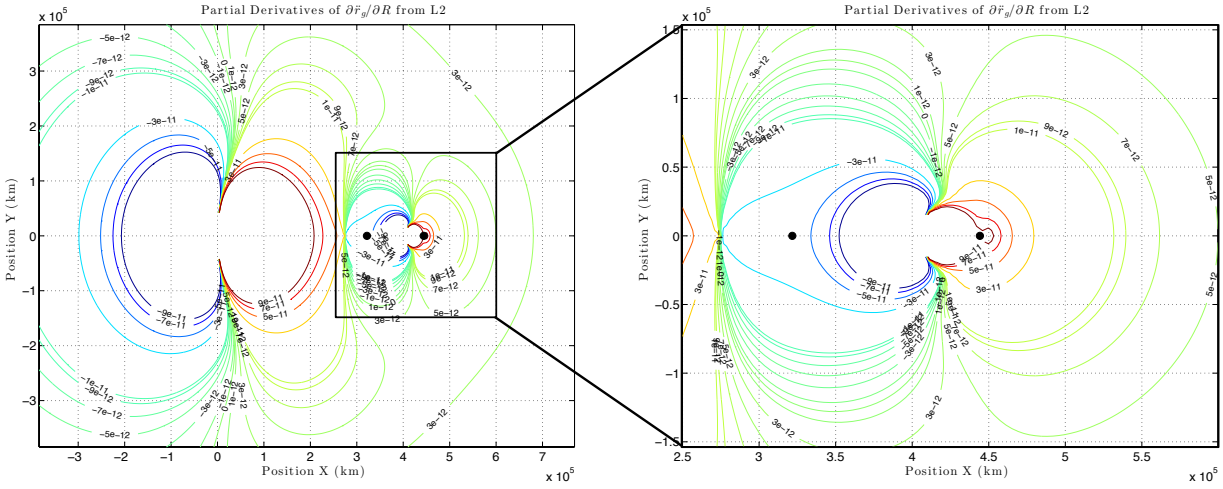

Figure 5.3: Partial derivative $\partial\ddot{r}_{rel}/\partial r$ with respect to L_2.

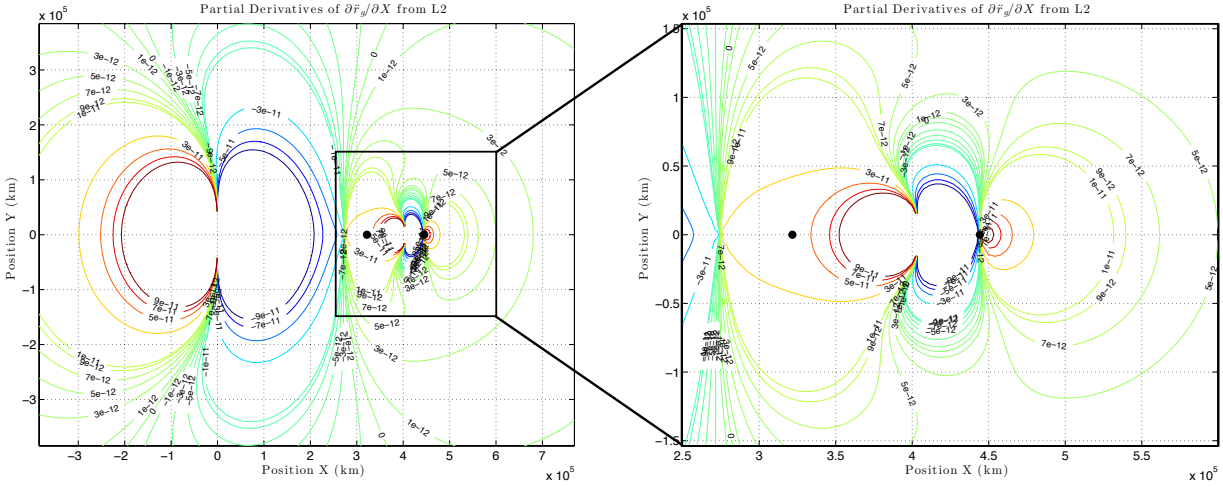

Figure 5.4: Partial derivative $\partial\ddot{r}_{rel}/\partial X$ with respect to L_2.

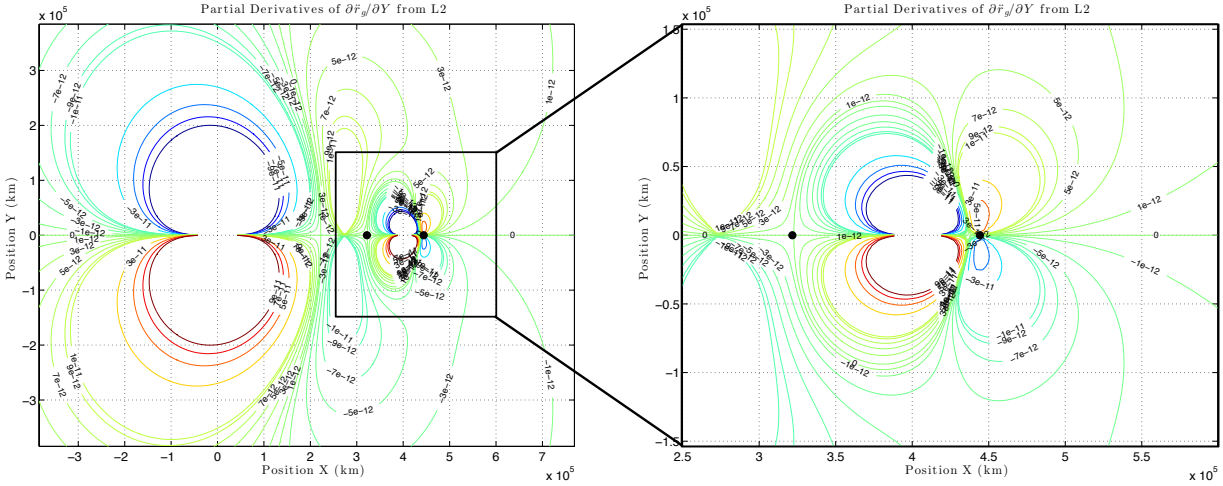

Figure 5.5: Partial derivative $\partial\ddot{r}_{rel}/\partial Y$ with respect to L_2.

Figures 5.6 through 5.8 show the contours of the partial derivatives of the inertial acceleration relative to the L_1 libration point with respect to the distance R from the libration point, the cartesian X, and the cartesian Y coordinates in the inertial frame where the Earth and Moon lie along the X-axis at the instance the map was created. Similar to the partial derivative contours relative to L_2, these curves do not vary significantly at different times due to the eccentricity of the moon. Investigating Figures 5.6 through 5.8 show that there are several regions where the partials derivatives are zero or very near zero, indicating locations where Doppler data would give significantly reduced information on the range of the spacecraft. Similar to Figure 5.3, Figure 5.6 has zero partial curves leaving the Earth roughly along the $\pm$ Y-axis. Figure 5.7 has a similar zero curve in this region for the partial derivatives with respect to the X coordinate. Figure 5.8 shows the partials with respect to the Y coordinate. Similar to Figure 5.5, there exists a zero curve along the X-axis as well as a zero partials curve emanating from a point between the Earth and Moon. The enhanced image to the right is a zoomed in contour near the Moon and libration points. One can clearly see the region in which the partial derivatives vary significantly with the zero curve as well. If a navigation satellite at L_1 was tracking a spacecraft traversing these low partial derivative curves, the position information contained within the range-rate data would be severely limited.

Figures 5.9 through 5.11 are the partial derivative contours relative to the Earth for completeness. These curves provide the relative acceleration partial derivatives to the center of the Earth to represent a tracking station on the surface. Figure 5.9 shows that the range partials are always strong except for a region near the moon in which the partial derivatives have a zero curve. In this region, there should be limited information on the range of the spacecraft from the Earth. Figure 5.10 has a zero curve along the Y-axis as expected with a region between L_1 and the Moon where a zero partials curve exists. Figure 5.11 has a zero curve along the X-axis as expected with a zero curve encompassing the L_1 point.

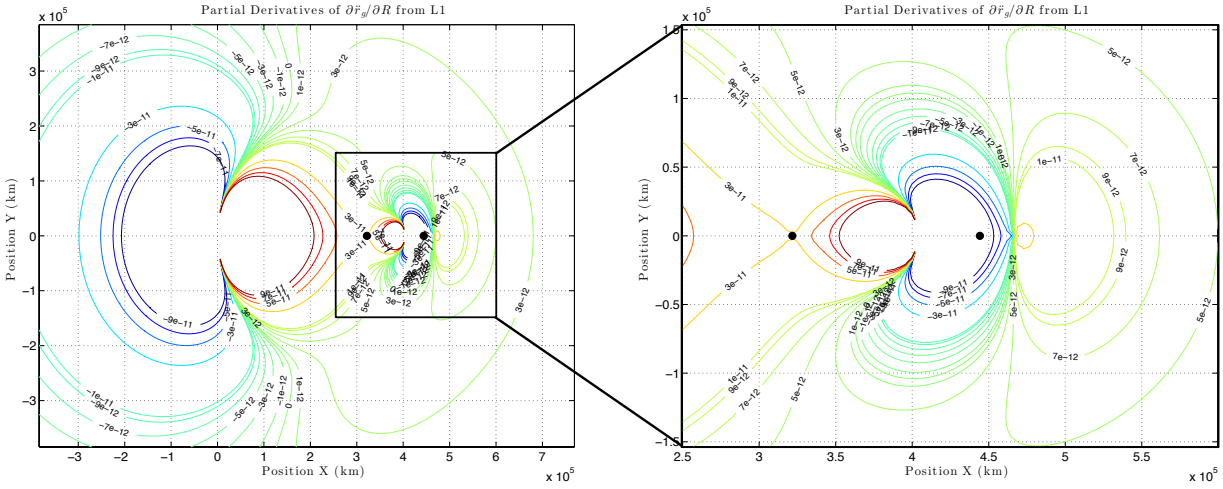

Figure 5.6: Partial derivative $\partial\ddot{r}_{rel}/\partial r$ with respect to L_1.

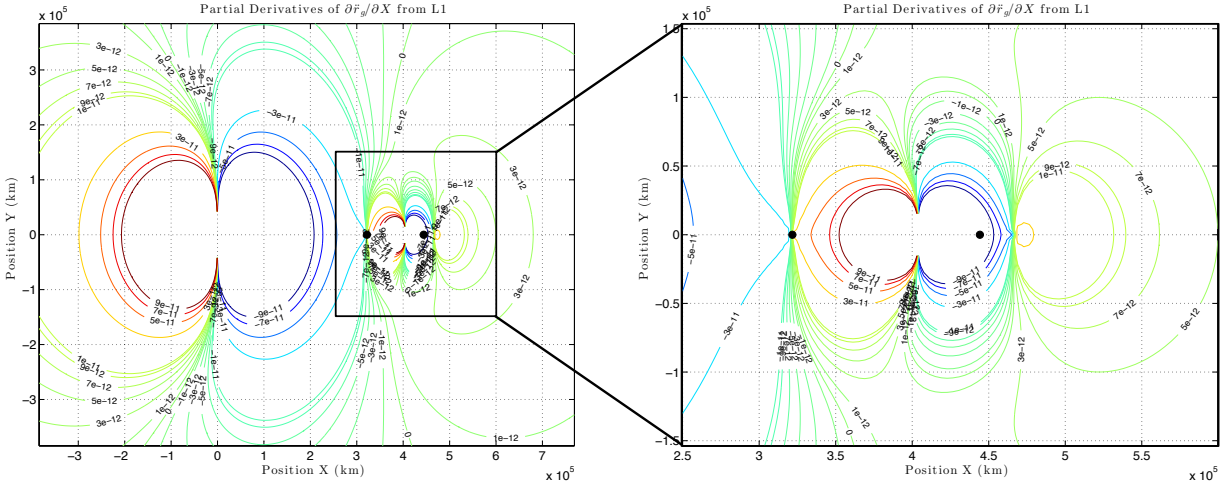

Figure 5.7: Partial derivative $\partial\ddot{r}_{rel}/\partial X$ with respect to L_1.

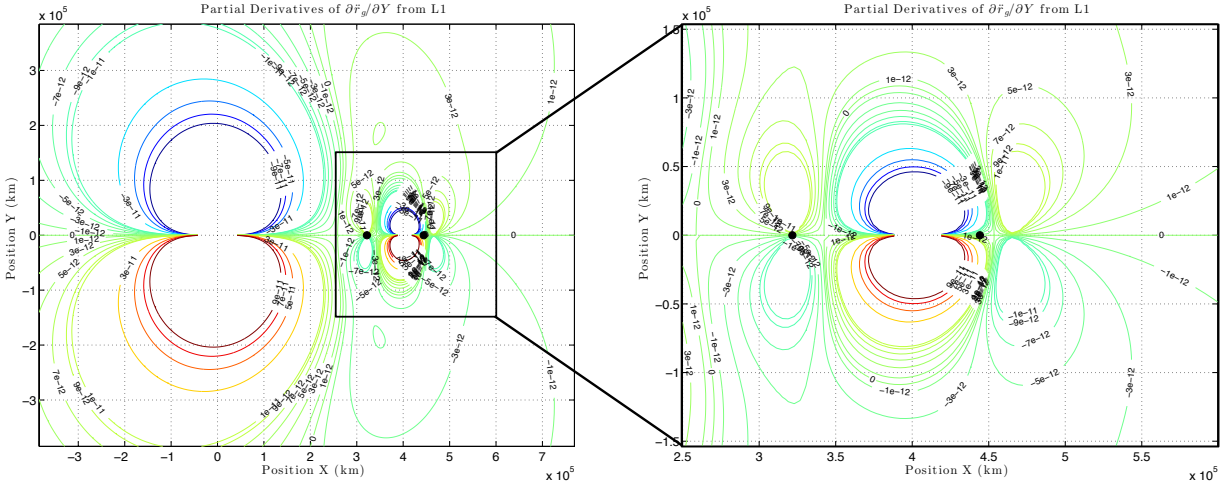

Figure 5.8: Partial derivative $\partial\ddot{r}_{rel}/\partial Y$ with respect to L_1.

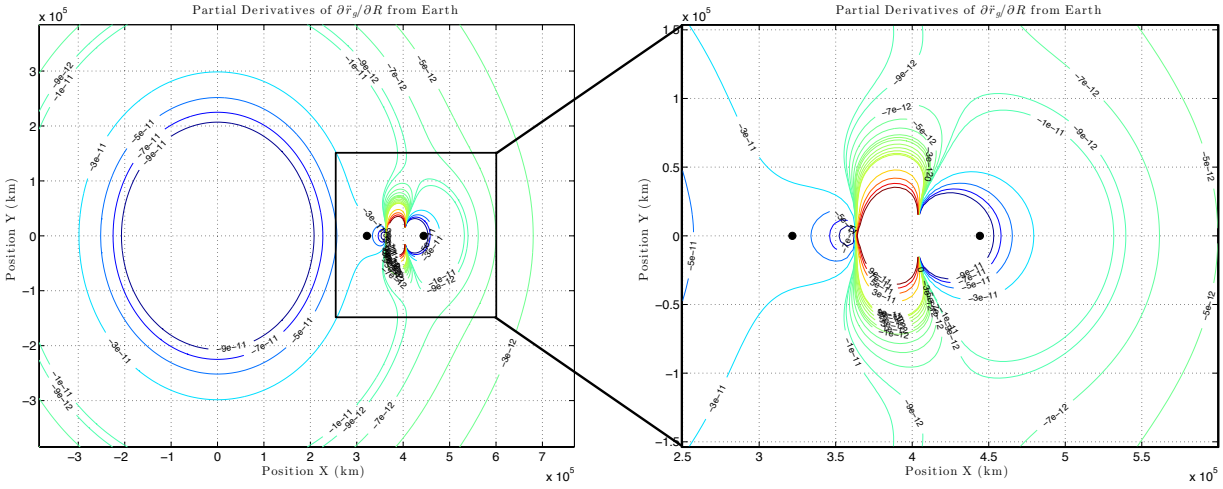

Figure 5.9: Partial derivative $\partial\ddot{r}_{rel}/\partial r$ with respect to Earth.

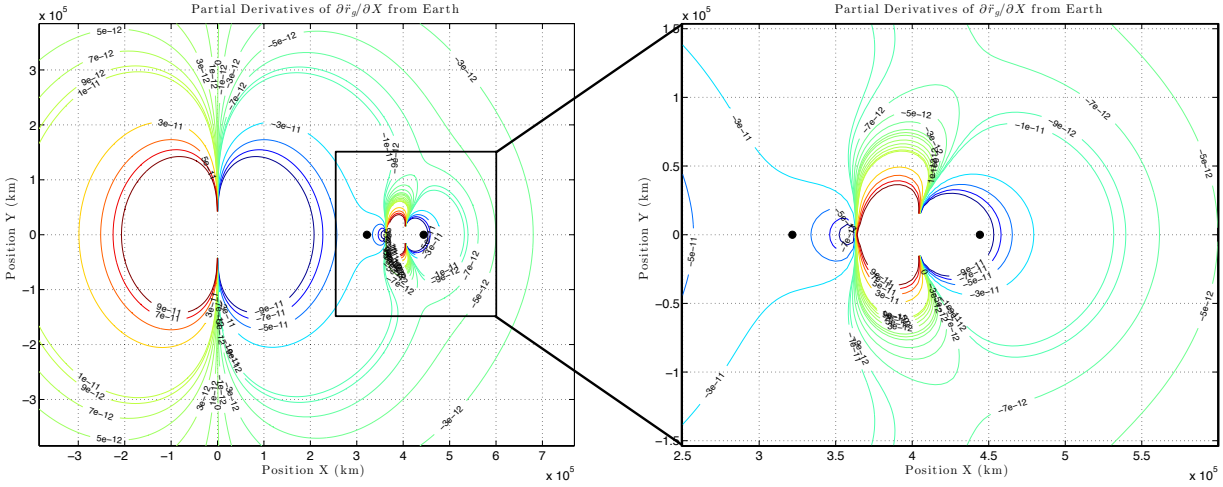

Figure 5.10: Partial derivative $\partial\ddot{r}_{rel}/\partial X$ with respect to Earth.

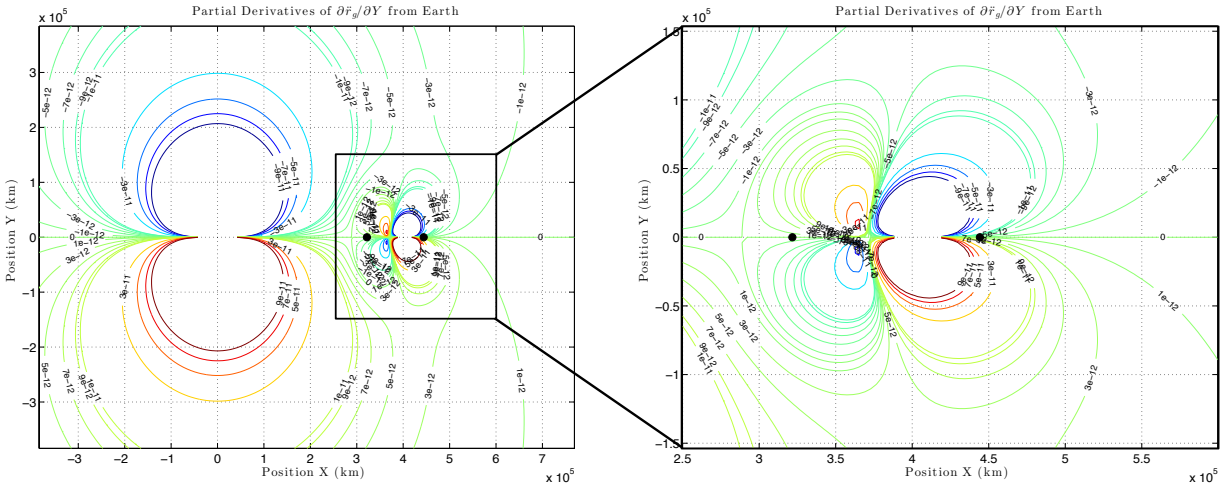

Figure 5.11: Partial derivative $\partial\ddot{r}_{rel}/\partial Y$ with respect to Earth.

5.3 Observability and Rank Analysis

Previous sections have outlined what is meant by observability of a system and the methods necessary to compute the observability of that system. If a system is assumed to follow the data equation $\mathbf{y} = \mathbf{H}\mathbf{x} + \boldsymbol{\epsilon}$, then it is common to say that the matrix $\mathbf{H}$ must be full rank for the system to be observable. This defines the theoretical observability which can be measure by any of the following methods:

(1) The rank of $\mathbf{H}_{m\times n}$ must be n.

(2) $\mathbf{H}$ must have n nonzero singular values.

(3) The eigenvalues of $\mathbf{H}^{\mathrm{T}}\mathbf{H}$ must be greater than zero.

(4) The determinant of $\mathbf{H}^{\mathrm{T}}\mathbf{H}$ must be greater than zero.

(5) $\mathbf{H}^{\mathrm{T}}\mathbf{H}$ must be a positive definite matrix.

(6) $\mathbf{H}^{\mathrm{T}}\mathbf{H}$ must be able to be uniquely factored as a lower or upper triangular matrix where the diagonals of the triangular matrix are nonzero.

While these conditions describe the theoretical observability, numerical errors may allow for one of these tests to fail even when $\mathbf{H}$ is full rank. Conversely, numerical errors may even allow for these conditions to pass when the system is not observable. This implies that numerical observability and theoretical observability, while attempting to define the same thing, may differ.

A common method to determine numerical observability is that of the condition number of the matrix $\mathbf{H}$. The condition number of $\mathbf{H}$ can be computed as follows

$$\kappa_p(\mathbf{H}) = \|\mathbf{H}\|_p \|\mathbf{H}^{-1}\|_p \tag{5.46}$$

where $\|\dots\|_p$ is the corresponding l_p matrix norm of $\mathbf{H}$. The condition number is considered "scale free" since it is unaffected by any scaling of $\mathbf{H}$ such that $\kappa_p(\alpha\mathbf{H}) = \kappa_p(\mathbf{H})$. It can be shown that relative errors in the least-squares solution and the condition number are affected by the scaling

of $\mathbf{H}$ columns [45]. However, when the elements of $\mathbf{x}$ are adjusted such that the magnitude of $\mathbf{y}$ is unchanged, then the errors associated with the least-squares solution are thus their unscaled values.

Often, the condition numbers $\kappa_p(\mathbf{H})$ are used to determine the observability of the system. The relative magnitudes of the largest and smallest singular values can also be used to determine whether specific states or combinations of states are observable. A significant problem stems from this analysis which was eluded to in the previous paragraph. The fundamental problem with this approach is that the singular values of $\mathbf{H}$ are inherently properties of the matrix, thus they do not take into account any relative magnitudes of states, measurements, and noise. This is a common problem in the field of orbit determination in which a multitude of square-root free filters have been designed to alleviate these types of issues.

Reference [45] has shown that prior to using singular values for observability criterium, both the rows and columns of $\mathbf{H}$ should be scaled. Similar to whitening the observations with their noise values, the data equation $\mathbf{y} = \mathbf{H}\mathbf{x} + \boldsymbol{\epsilon}$ should be normalized such that all measurements have the same error variance. This normalizes the rows of the data equation. In order to normalize the columns for observability analysis, the contribution of each state variable x_i should be approximately equal. This is accomplished by normalizing the columns of $\mathbf{H}$ such that

$$(\mathbf{R}^{-1/2}\mathbf{y}) = (\mathbf{R}^{-1/2}\mathbf{H}\mathbf{D}^{-1})(\mathbf{D}\mathbf{x}) + (\mathbf{R}^{-1/2}\boldsymbol{\epsilon}) \tag{5.47}$$

where $\mathbf{R}$ is the measurement weighting matrix (usually diagonal), $\mathbf{R}^{1/2}$ is the square-root factor of $\mathbf{R}$, and $\mathbf{D}$ is a diagonal $n \times n$ matrix whose elements are the l_2-norm of the corresponding columns of $\mathbf{H}$. Thus the new scaled data equation can be expressed by

$$\mathbf{H}' = \mathbf{R}^{-1/2}\mathbf{H}\mathbf{D}^{-1} \tag{5.48}$$

Now the resultant vector of $\mathbf{D}\mathbf{x}$ is a scaled version of $\mathbf{x}$. This new scaled measurement matrix $\mathbf{H}'$ can be used in an SVD analysis for observability while maintaining the numerical precision necessary for large variations in the state variables and observation noise. The singular values of $\mathbf{H}'$ give an indication as to the numerical rank of the system. If the difference between the largest

and smallest singular values is numerically insignificant, then the conclusion can be drawn that the system is not observable.

Using the linear time-varying observability analysis introduced in Section 3.10.2 and Equation 5.48 to normalize the observability gramian, several Halo orbits with varying z-axis amplitudes between 8,000 and 40,000 km were analyzed. The assumption in this observability analysis is that two spacecraft in the same size Halo orbit are performing LiAISON with an initial separation between the two spacecraft is $\Delta\tau = 90°$. Both range and range-rate observations are collected over the course of the orbit. Once the LiAISON configuration reaches full rank (rank 12 for position and

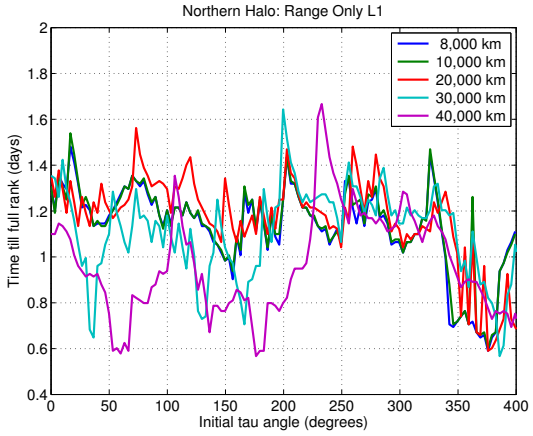

(a) L_1 Northern Range Only

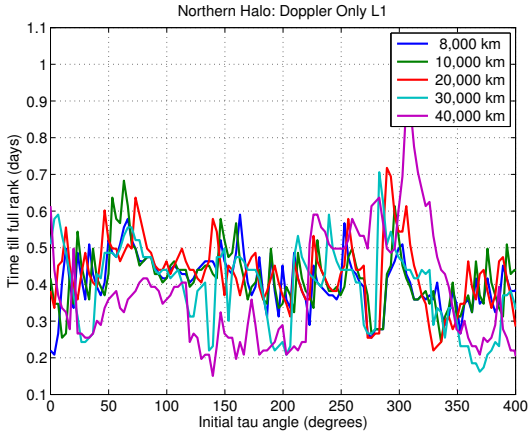

(b) L_1 Northern Doppler Only

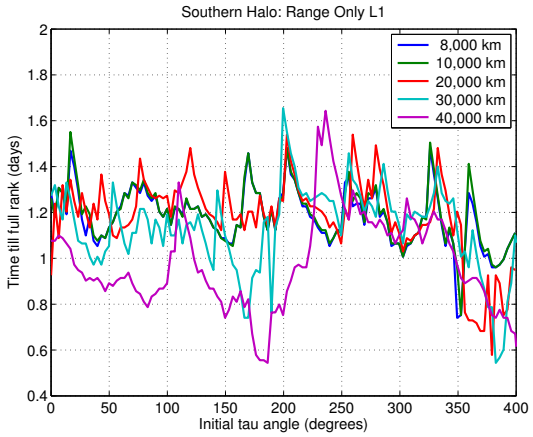

(c) L_1 Southern Range Only

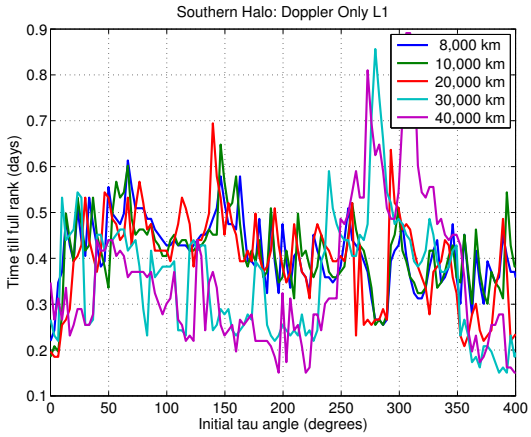

(d) L_1 Southern Doppler Only

Figure 5.12: Time to full numerical rank for L_1 Halo Orbits.

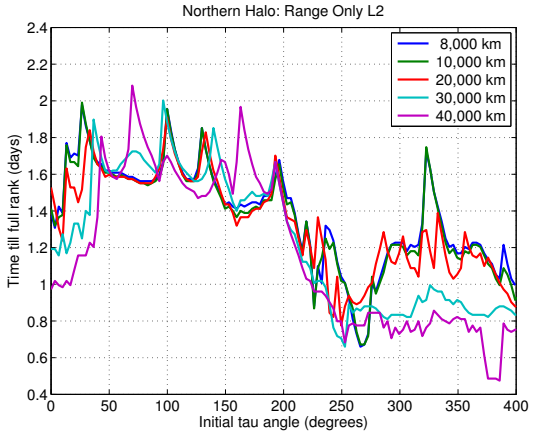

(a) L_2 Northern Range Only

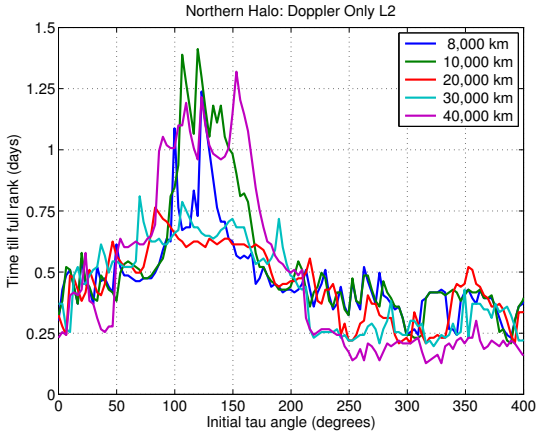

(b) L_2 Northern Doppler Only

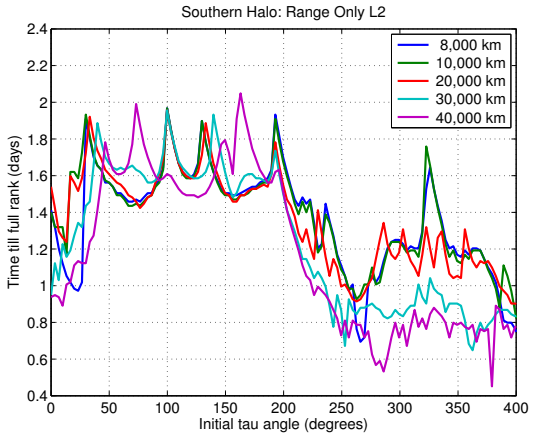

(c) L_2 Southern Range Only

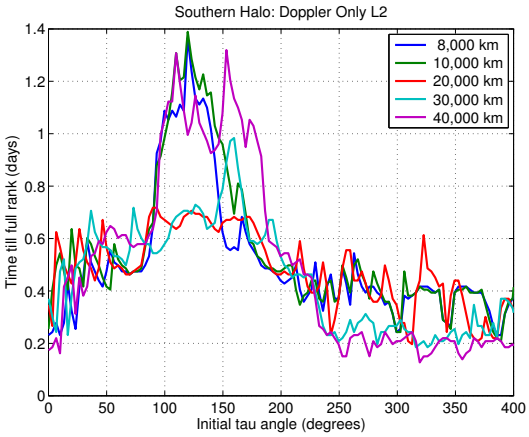

(d) L_2 Southern Doppler Only

Figure 5.13: Time to full numerical rank for L_2 Halo Orbits.

velocity of both spacecraft), the time it took to reach full rank is saved and then both initial halo orbit states are reinitialized 0.01° in their initial τ values until the whole periodic orbit is traversed.

Figure 5.12 displays the time it takes for range or Doppler observables only to reach full rank for this LiAISON configuration in orbit about L_1. It must be noted that if the formulation derived in Equation 5.48 is not used, neither observables allow for the system to reach full rank. Figure 5.12(a) displays the range only observable for northern L_1 Halo orbiters while Figure 5.12(c) displays the same for southern L_1 Halo orbiters. Figure 5.12(b) displays the Doppler only observable for northern L_1 Halo orbiters while Figure 5.12(d) displays the same for southern L_1 Halo orbiters.

There is no dependence on the size of the Halo orbit chosen concerning the time it takes to become observable for either northern or southern L_1 orbiters in this configuration. It takes about 1.2 days for the system to become full rank if ranging data only is used and about 0.45 days if Doppler only data is used.

Figure 5.13 displays the time it takes for range or Doppler observables only to reach full rank for this LiAISON configuration in orbit about L_2. Again, neither system reaches full rank unless the normalized observability matrix is used. Figure 5.13(a) displays the range only observable for northern L_2 Halo orbiters while Figure 5.13(c) displays the same for southern L_2 Halo orbiters. Figure 5.13(b) displays the Doppler only observable for northern L_2 Halo orbiters while Figure 5.13(d) displays the same for southern L_2 Halo orbiters. Figure 5.13 shows that there is little dependence on the size of the Halo orbit, however, the initial location in the Halo orbit does matter. This is contrary to the results in the L_1 case of Figure 5.12. For the first half of the orbit $\tau = 0^\circ - -180^\circ$, the average time to full rank for ranging data is about 1.6 days. However, this is reduced to about 1 day during the second half of the orbit. The Doppler analysis has similar results where the first half of the orbit takes longer to become full rank.

Chapter 6

Uncertainty propagation in Halo orbits

6.1 Halo Orbit Trajectory Stability

For uncertainty mapping and navigation of a crewed mission in a LPO, it is important to understand the trajectory characteristics for time periods that are less than that of the period for periodic and quasi-periodic orbits in the three-body problem. The navigation of crewed missions in this regime require a better understanding of how the dynamics and uncertainty naturally evolve over periods between measurement updates and uncertainty mapping after tracking data for maneuver design. There are several scenarios that can take place for crewed navigation, however the most likely scenario is that there will be continuous tracking from ground stations and with a possibility of gaps in the tracking of only a few hours. Once the tracking has stopped, the solution estimate and it's uncertainty must be propagated for hours to days into the future to determine if a maneuver is necessary to return to the nominal trajectory. This requires knowledge of how the dynamics will influence the uncertainty behavior over time. Scheeres et al. looked at the use of Lyapunov characteristic exponents (LCEs) to better understand how the frequency of measurements might influence navigation uncertainties for a Sun-Earth LPO [137]. Anderson et al. examined the use of local Lyapunov exponents as and indicator of the effects that perturbations and maneuvers have on unstable three-body trajectories over specific periods of time [3]. They showed that the local Lyapunov exponents correspond well with locations where perturbations caused the greatest deviation from the nominal trajectory and that maneuver ΔV to return to the nominal trajectory also had a relationship with the local Lyapunov exponent. These methods help to better under-

stand how the local stability characteristics of an unstable orbit impact the dynamics over short periods of time.

In general, the local stability characteristics of an orbit can be defined using the state transition matrix (STM) that is evaluated along the trajectory. The STM is computed by integrating the variational equations along a given trajectory. The STM is used to map deviations from an initial epoch over a finite time span using linearized methods and is defined by

$$\mathbf{\Phi}(t, t_0) = \frac{\partial \mathbf{X}(t)}{\partial \mathbf{X}(t_0)}. \tag{6.1}$$

The state transition matrix is obtained by integrating

$$\dot{\Phi}(t, t_0) = \mathbf{A}(t)\Phi(t, t_0) \tag{6.2}$$

subject to the initial conditions $\Phi(t_0, t_0) = \mathbf{I}$ along with the given trajectory $\mathbf{X}(t)$. The Jacobian matrix $\mathbf{A}(t)$ is evaluated along the trajectory $\mathbf{X}(t)$ as well and is given by

$$\mathbf{A}(t) = \frac{\partial F(\boldsymbol{X}, t)}{\partial \boldsymbol{X}}, \tag{6.3}$$

where $F(\mathbf{X}, t)$ is the time derivative of the state vector $\mathbf{X}(t)$. The STM is thus implicitly a function of the initial state $\mathbf{X}(t_0)$ as well as the initial and final time (t_0 and t). An STM initialized and computed at different starting locations along an orbit will have varying local stability characteristics. It has been shown that an STM computed over an orbital period becomes independent of the initial time and state according to Floquet Theory [16]. An STM computed over an orbital period is often referred to as the monodromy map or Monodromy Matrix [119, 146].

The stability characteristics of the STM can be examined through its eigenvalues and eigenvectors.

6.2 Lyapunov Exponents

Lyapunov exponents give an indication as to the rate of divergence of nearby trajectories and has been a key component for unstable and chaotic dynamical systems. In general, if a system is unstable, any two trajectories that start out close to each other will separate exponentially with time giving an indication of the attainable size of a given accessible state space. The sensitivity to initial conditions for a general case can be quantified by

$$||\delta x(t)|| \approx e^{\lambda t}||\delta x(t_0)|| \tag{6.4}$$

where λ is the mean rate of separation between the trajectories and is known as the leading Lyapunov exponent. If one takes the time to infinity then the Lyapunov exponent is a global measure of the divergence rate of nearby trajectories.

6.2.1 Local Lyapunov Exponents

Consider the dynamical system of dimension n that has variables $x_i (1 \leq i \leq n)$. This dynamical system can be defined by a set of nonlinear ordinary differential equations of the form:

$$\dot{\mathbf{x}}(t) = f(\mathbf{x}, t) \tag{6.5}$$

where $\mathbf{x}$ is a vector $(x_1, x_2, \ldots, x_n)^{\mathrm{T}}$ and $\dot{\mathbf{x}}$ is the time derivative of that vector. A solution of Eq. 6.5 defines the reference solution or reference trajectory.

If a small perturbation $\delta\mathbf{x}(t_0)$ is applied at some initial time $t = t_0$, then the time evolution of that small perturbation obeys a tangent linear equation given by:

$$\delta\dot{\mathbf{x}} = \mathbf{A}(t)\delta\mathbf{x}(t) \tag{6.6}$$

where $\mathbf{A}(t)$ is the Jacobian matrix of f at $\mathbf{x}(t)$ and $A_{ij} = \partial f_i/\partial x_j$. Integrating Eq. 6.6 from $t = [t_0, t_0 + \Delta t)$ one obtains

$$\delta\mathbf{x}(t_0 + \Delta t) = \mathbf{\Phi}(t_0 + \Delta t, t_0)\delta\mathbf{x}(t_0) \tag{6.7}$$

where the matrix Φ depends on the reference solution $\mathbf{x}(t)$.

If one considers the ordinary linear stability of a stationary solution $\mathbf{x}_0$ with the time variation of an infinitesimal perturbation described by Eq. 6.6 with a constant $A(t)$, then the stability of the solution can be investigated by examining the eigenvalues and eigenvectors of the matrix $A(t)$. In general, these eigenvalues are complex quantities and the eigenvectors are not orthogonal.

If the system is nonlinear, the Lyapunov stability of the dynamical system can be analyzed for almost every initial condition $\mathbf{x}(t_0)$ that contains a set of vectors $\{\xi_i(\mathbf{x}(t_0))\}(1 \leq i \leq n)$ such that

$$\lambda_i = \lim_{x\to\pm\infty} \frac{1}{|\tau|}\ln||\Phi(\mathbf{x_0}, \tau)\xi_i(\mathbf{x}(t_0))|| \tag{6.8}$$

where λ_i are known as the Lyapunov exponents. The Oseledec theorem implies that nearby trajectories that are perturbed by a small amount will separate at a rate of $e^{\lambda_i t}$ [115].

From Goldhirsch et al. one can define the quantity $e^{2\lambda_i(\mathbf{x}(t_0),\tau)\tau}$ as the ith largest eigenvalue of $\Phi^T(\mathbf{x}(t_0), \tau)\Phi(\mathbf{x}(t_0), \tau)$ and $\xi_i(\mathbf{x}(t_0), \tau)$ as the corresponding eigenvector, then

$$e^{\lambda_i(\mathbf{x}(t_0),\tau)\tau} = ||\Phi(\mathbf{x_0}, \tau)\xi_i(\mathbf{x}(t_0))|| \tag{6.9}$$

or,

$$\lambda_i(\mathbf{x}(t_0), \tau) = \frac{1}{\tau}||\Phi(\mathbf{x_0}, \tau)\xi_i(\mathbf{x}(t_0))|| \tag{6.10}$$

where $||\cdot||$ denotes the L_2 norm. Eq. 6.10 thus defines the finite-time or local Lyapunov exponent, λ_i and the finite-time or local Lyapunov vector ξ_i, over a finite time interval τ. A positive value for λ indicates the the reference solution is locally unstable in the Lyapunov sense at $\mathbf{x}(t_0)$ over the time interval τ.

6.3 CRTBP Simulations

Using the ideas of local Lyapunov exponents presented in the previous section, and analysis of the stability of various Halo orbits in the Circular Restricted Three Body Problem (CRTBP) was conducted. Local Lyapunov exponents were calculated along several CRTBP halo orbits with z-axis amplitudes ranging from 8,000 km to 40,000 km. These halo orbits traverse the 1st Earth-Moon Lagrange point (EML-1). Figure 6.1 shows an isometric view of the local Lyapunov exponents calculated as a surface for several different halo orbit sizes. The projections of the plot indicate the motion of the halo orbit in the X–Y, X–Z, and Y–Z planes. The colormap gives an indication of the strength of the calculated local Lyapunov exponents. One can see that for all halo orbits, the local Lyapunov exponent increases when the spacecraft approaches the moon. For smaller halo orbits. the local Lyapunov exponent is larger when the spacecraft is at apolune when compared to larger halo orbits. In addition, the larger z-axis amplitude halo orbits have a wider range of values for the local Lyapunov exponents with the perilune value being larger than smaller z-axis amplitude halo orbits.

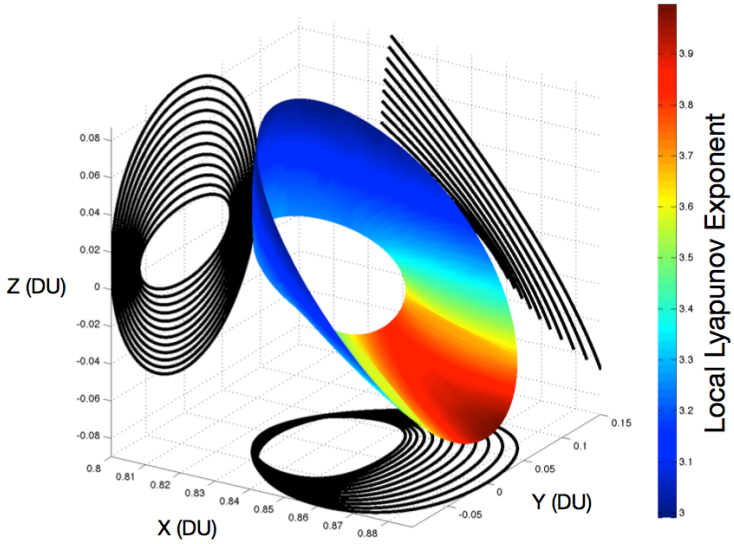

Figure 6.1: Local Lyapunov Exponents variation over the orbit of various halo orbit sizes (orbit projections in black).

This analysis gives an indication as to where in an EML-1 halo orbit one would expect small perturbations to influence the trajectory more than other locations. The rate at which an small perturbation grows exponentially is smaller during apolune and increases significantly when a spacecraft is at perilune. Thus one would expect a small perturbation to influence the reference trajectory more near perilune than at apolune.

With a better understanding of how the location of a small perturbation influences the trajectory, it was necessary to analyze how this behavior can affect the uncertainty distribution of the trajectory. To do this, each specific z-axis amplitude halo orbit was broken up into various segments based on the phase angle, τ. The phase angle of a halo orbit can be calculated based on it's orbital period p such that

$$\tau = \frac{t - t_0}{p} 2\pi \tag{6.11}$$

where the quantity $(t - t_0)$ is the time since the last X–Z plane crossing (at $\tau = 0$). The quantity τ ranges from 0 to 360 degrees where 0 degrees is located at apolune for this case and 180 degrees is located at perilune. The trajectory segments are broken up into increments every 10 degrees in τ. At that point, a spherical Gaussian covariance of 100 m in each direction and 1 mm/s in each direction is applied. The covariance is then mapped forward using linear methods and the STM. The trajectory and uncertainty are mapped forward in time to 2.5 days past epoch. At the end of the mapping several parameters are investigated. The main parameters of interest are the angle between the maximum uncertainty direction of the mapped covariance matrix and the unstable manifold as well as the size of the maximum uncertainty direction of the mapped covariance matrix.

Scheeres et al. showed that the mapped covariance matrix tends to stretch and align itself with the unstable manifold direction when no measurements are processed [137]. This analysis investigates how the covariance matrix is affected based on it's initial position in the halo orbit. Figure 6.2 indicates how the initial covariance is affected over the 2.5 day propagation. Figure 6.2(a)

shows the time history evolution of the angle between the maximum uncertainty direction and the unstable manifold as well as the size of the semi-major axis of the uncertainty for an 8,000 km z-axis amplitude halo orbit. The initial covariance is misaligned with the unstable manifold by roughly 80 degrees for all cases. As the trajectory and uncertainty are propagated, the covariance starts to align itself with the unstable manifold and by after 2 days of propagation, the maximum uncertainty direction is within 10 degrees of the unstable manifold direction. Figure 6.2(a) shows that there are regions where the semi-major axis of the covariance matrix is stretched significantly more than other areas. After 2.5 days of propagation, the semi-major axis has stretched significantly more for orbits with an initial τ angle of about 120-150 degrees. This plot indicates that the size of the semi-major axis of the covariance matrix tends to stretch more for τ angles that are near perilune.

Figure 6.2(b) shows the angle between the maximum uncertainty direction and the unstable manifold as well as the size of the covariance semi-major axis after 2.5 days of integration for various halo orbit z-axis amplitudes and initial τ angles. Several features are noticeable from this analysis. There exists ridges where the angle between the maximum uncertainty direction and

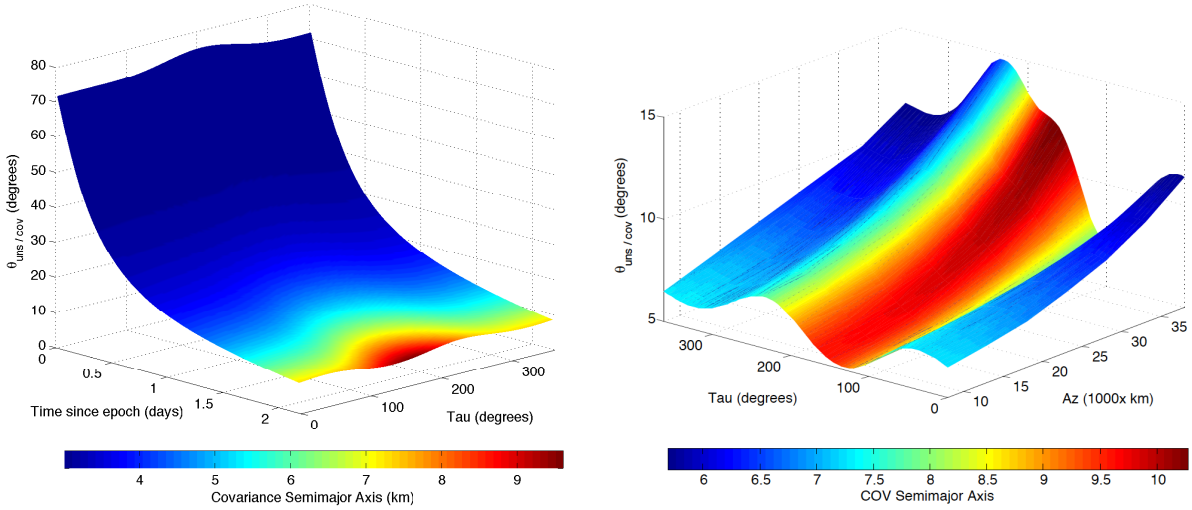

(a) LLE Time History Evolution

(b) LLE Characteristics

Figure 6.2: Surface comparing the size of the Covariance semi-major axis (km) compared to the size of the Halo orbit, the initial tau angle, and the angle between the unstable manifold direction and the maximum covariance. Integration time is equal for all cases.

the unstable manifold reach a minimum. This ridge occurs for orbits with an initial τ value of around 120 degrees and again occurs for regions near perilune. For all z-axis amplitude halo orbits this ridge exists. Larger z-axis amplitude halo orbits in general do not align to within 10 degrees between the maximum uncertainty direction and the unstable manifold given the same amount of propagation time. These larger orbits also tend to have a more dynamic range in the magnitude of the stretching of the covariance semi-major axis for various τ values when compared to the smaller halo orbits.

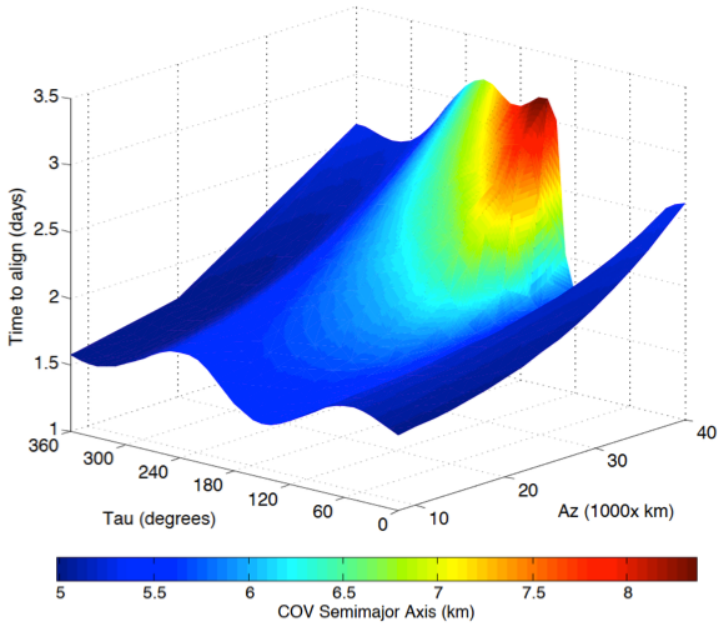

Figure 6.3: Surface comparing the size of the Covariance semi-major axis compared to the size of the Halo orbit, the initial tau angle, and the time it takes for the angle between the unstable manifold direction and the maximum covariance to get to within 10 degrees.

The previous analysis looked at the relationship between the unstable manifold and maximum uncertainty direction angle behaved as well as the stretching of the covariance semi-major axis. This analysis used a propagation time of 2.5 days for all cases. For larger halo orbits, this propagation time of 2.5 days did not allow all of the trajectories to have the angle between the two vectors to align to within 10 degrees. Figure 6.3 is a similar surface plot however the time that it takes for the two vectors to align to within 10 degrees is plotted on the z-axis. This shows that for larger

amplitude halo orbits, it can take up to two days longer for the two vectors to align to within 10 degrees.

Finally, the relationship between the local Lyapunov exponent and the distance to the moon was examined. Figure 6.4 shows the relationship between the computed local Lyapunov exponent and the distance that the spacecraft is away from the Moon. Once can see that the strength of the local Lyapunov exponent increases significantly when approaching perilune and drops off towards apolune. While the relationship is not linear, there is an obvious trend with the local Lyapunov exponent actually increasing slightly near apolune.

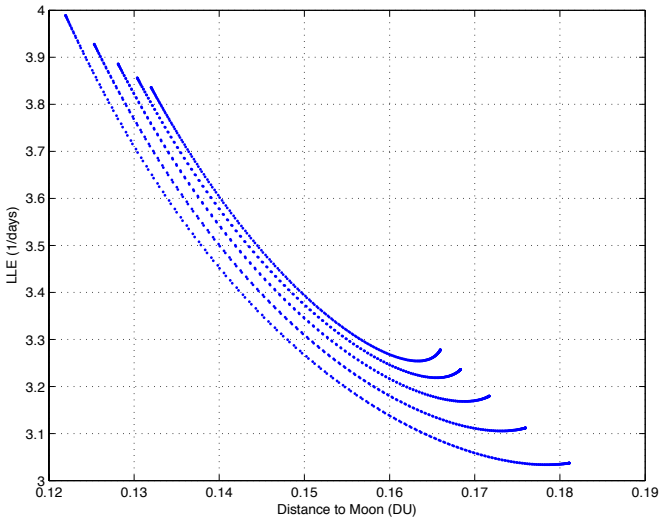

Figure 6.4: Relationship between the LLE and the distance of the S/C to the Moon.

Chapter 7

Crewed Vehicle Disturbance and Environment Modeling

For a spacecraft in cislunar space there are three main types of unmodeled accelerations that occur: gravitational perturbations, miss-modeled solar radiation pressure, and propulsive events. Previous crewed spacecraft, such as Apollo, have experienced significant trajectory perturbations due to propulsive events that are no well-modeled originating from activities that are attributed to the crew on board. It is expected that during future crewed missions these same disturbances will occur and significantly perturb the designed reference trajectory. These activities and small perturbations are known as FLAK (un**F**ortunate **L**ack of **A**cceleration **K**nowledge) and can include a variety of sources.

The main source of experience with FLAK comes from the Apollo missions. Apollo navigators observed that when crewed spacecraft was in lunar orbit that the spacecrafts position uncertainty would grow by approximately 500 meters in an hour when there was no tracking. The frequency of attitude maneuvers and life support system made fitting tracking residuals difficult. While some of the uncertainty noticed during Apollo can be attributed to errors in the lunar gravity field, perturbations due to the crew's activities and attitude maneuvers are expected to remain in future missions.

The propulsive events of concern in this work originate from thruster errors and the spacecrafts ECLSS (Environmental Control and Life Support System). Thruster errors in this analysis include attitude deadbanding maneuvers as well as attitude slewing maneuvers. ECLSS propulsive events include Pressure Swing Adsorption (PSA) (CO2 venting), ammonia sublimator venting, and

waste water venting events. D'Souza et al. have recently released expected errors due to these types of propulsive events [27, 28]. Table 7.1 outlines the frequency of events as well as their strength in terms of a white noise acceleration model. The attitude dead-banding maneuver errors are based on a 24-jet ESA-SM configuration with a 0.028 sec on-time. These events are expected to occur approximately once every 30 minutes. The expected total ΔV imparted by this type of event is 3.54×10^{-4} m/sec. The second major attitude related maneuver error source comes from attitude slewing maneuvers. This work assumes that there is one attitude slew maneuver every 3.2 hours resulting in a ΔV of 1.035×10^{-2} m/sec. PSA puffs are the most frequent propulsive event due to the ECLSS. These events are expected to occur every 6-10 minutes with a quiescent period during crew sleep periods. The PSA system can also be commanded to perform a complete desaturation maneuver allowing for 40-60 minute delay in the next event. The resulting ΔV from these events is roughly 3.83×10^{-4} m/sec. The last FLAK source modeled in this work from the ECLSS comes from the ammonia sublimator vents which occurs for 0.5 hours near the moon resulting in a total ΔV of 0.266 m/sec to 0.652 m/sec depending on the configuration.

Table 7.1: FLAK Type and Strength of Unmodeled Acceleration [27, 28]

Type of Noise	Assumptions	Strength (m^2/s^3)
Attitude Deadbanding	Jet firing every 30 minutes	2.313×10^{-11}
Attitude Slewing	50 attitude events	3.098×10^{-9}
Attitude Slewing	25 attitude events	1.601×10^{-9}
PSA Vents	Every 6-10 minutes	4.095×10^{-10}
Ammonia Sublimator	In Lunar Vicinity (0.5 hour)	CM/SM: 1.310×10^{-5}
Ammonia Sublimator	0.5 hour prior to EI	CM Only: 7.877×10^{-5}

7.1 Discrete Noise FLAK Modeling

Currently, the model most often used in determining the effects of FLAK disturbances on orbit uncertainty is based on a discrete uncorrelated white noise model that drives the acceleration state. This simplistic FLAK model has been used to determine the desired strength of FLAK. Commonly, it is assumed that this type of stochastic acceleration process will impart a 500 m (1-σ)

spherical position uncertainty over the course of an hour. A linear discrete model for this type of system in one dimension is given by

$$\begin{bmatrix} x_{k+1} \\ v_{k+1} \\ a_{k+1} \end{bmatrix} = \begin{bmatrix} 1 & \Delta t & \Delta t^2/2 \\ 0 & 1 & \Delta t \\ 0 & 0 & 0 \end{bmatrix} \begin{bmatrix} x_k \\ v_k \\ a_k \end{bmatrix} + \begin{bmatrix} 0 \\ 0 \\ 1 \end{bmatrix} u_k, \tag{7.1}$$

where $\Delta t = t_{k+1} - t_k$ and u_k is the discrete Gaussian white noise process such that the statistics are $E[u_k] = 0$ and $E[u_j u_k] = q\delta_{i,k}$ where $\delta_{i,k}$ is the Kronecker delta function. The state transition matrix and the process noise mapping matrix for one dimension of this linear system is defined as

$$\Phi(t_{k+1}, t_k) = \begin{bmatrix} 1 & \Delta t \\ 0 & 1 \end{bmatrix}, \quad \text{and} \quad \Gamma(t_{k+1}, t_k) = \begin{bmatrix} \frac{\Delta t^2}{2} \\ \Delta t \end{bmatrix}. \tag{7.2}$$

This type of method can be assumed if the natural dynamics do not change significantly over a short duration of time. In order to determine the strength of the process noise q one needs to know the desired covariance P_k at some time t_k. Ely et al. shows that if one assumes that the initial covariance P_0 is zero such that only the process noise used, the covariance P_k can be calculated as [29]

$$\mathbf{P}_k = q \begin{bmatrix} \frac{4n^3 - 3n^2 + 2n}{12} \Delta t^4 & \frac{n^2}{2} \Delta t^3 \\ \frac{n^2}{2} \Delta t^3 & n \Delta t^2 \end{bmatrix}. \tag{7.3}$$

A unique consequence of this derivation allows for more than one variation while achieving the same results such that the total propagation time $T = n\Delta t$. This shows that the same propagation time can result in different step sizes Δt and produce different values for P_k. Thus, the process noise strength q must be computed in conjunction with the selection of a step size Δt.

If one assumes that Δt is small and thus n is very large, the covariance can be simplified and approximated by

$$\mathbf{P}_k \approx q \begin{bmatrix} \frac{n^3}{3}\Delta t^4 & \frac{n^2}{2}\Delta t^3 \\ \frac{n^2}{2}\Delta t^3 & n\Delta t^2 \end{bmatrix}. \tag{7.4}$$

This result is the same as that found in Reference [25] and similar to that in Reference [23].

7.2 Discrete Poisson FLAK Modeling

There are many cases of engineering interest that use stochastic processes to model certain phenomena. The simplest form is that of a linear system driven by a normal white noise input thus drastically simplifying the analysis of the systems response. The first solution to this type of problem was given by Uhlenbeck and Ornstein [153]. The previous section describes a FLAK model that is based on a discrete Gaussian random sequence that drives the spacecrafts uncorrelated acceleration state. This type of model assumes that over a discrete time step, the acceleration is a white noise process that can be simulated as a normally distributed random draw that acts as a piecewise constant.

The fields of mechanical and structural systems have used these types of methods to describe stochastic loading [67, 78, 79]. In order to better define the mechanisms through which these disturbances occur, the use of Poisson white noise has become prominent. A Poisson white noise process can be viewed as a sequence of independent random pulses with exponential interarrival times. Poisson processes have been used to model several different types of random pulses in engineering such as traffic loading on bridges, forces acting on airplanes, seismic ground accelerations, wind gusts, as well as others [67, 78, 79, 152]. A linear system driven by a Poisson white noise is also known as a filtered Poisson process and it's theory has been examined [21–24].

A Poisson white noise process is a natural extension of the concept of a normal white noise process. It is a non-normal delta correlated process that idealizes the stochastic process of a series of impulses occurring at random times with a random strength over a specified time period. The Poisson white noise delta-correlated process can thus be defined by

$$u_k = \sum_{i=1}^{N(t)} a_i \delta(t - t_i), \tag{7.5}$$

where $N(t)$ is a homogenous counting Poisson process describing the number of impulses $\delta(t - t_i)$ that occur at random Poisson distributed times t_i over the interval $[0, t]$. The variable a_i is an identically distributed random variable which is mutually independent and independent of the Poisson random time t_i. The cummulants of $u_k(t_1)$, $u_i(t_2)$, ..., $u_i(t_k)$ define the correlations of u_k and are given by

$$R^{(r)}(t_1, t_2, \ldots, t_3) = \lambda E[a^r]\delta(t_2 - t_1)\delta(t_3 - t_1)\cdots\delta(t_k - t_1), \tag{7.6}$$

where λ is the Poisson distribution rate parameter that defines the mean arrival rate of the pulses over a unit of time. Several pieces of work have shown that the Poisson white noise model driving a linear system results in a covariance of similar form to that of the discrete white noise process. For a discrete Poisson white noise process, the covariance matrix can simply be represented by

$$P(t) = \Phi(t, t_o)P_o\Phi^{\mathrm{T}}(t, t_o) + Q_\pi(t). \tag{7.7}$$

If one assumes a a one-dimensional rectilinear system model similar to the one used in the previous discrete white noise case, the equations of motion are governed by the following:

$$\dot{x}(t) = Ax(t) + Bu(t), \tag{7.8}$$

where

$$x = \begin{bmatrix} r \\ v \end{bmatrix}, A = \begin{bmatrix} 0 & 1 \\ 0 & 0 \end{bmatrix}, \text{ and } B = \begin{bmatrix} 0 \\ 1 \end{bmatrix}. \tag{7.9}$$

The solution to this linear dynamics problem is commonly known and is given by

$$x(t) = \Phi(t, t_o)x_o + \int_{t_o}^{t} \Phi(t, \tau)Bu(\tau)d\tau, \tag{7.10}$$

where B is simply the white noise mapping matrix which is assumed to be constant here but is not always the case. This model assumes that the position and velocity are represented by x and u is the input (for this case, it is assumed to be white noise).

Thus, the impulse response at some future time t given the initial conditions ($x_o = 0, u(t) = u_k\delta(t - t_k)$) is

$$x(t) = \Phi(t, t_k)Bu_k = \begin{bmatrix} t - t_k \\ 1 \end{bmatrix} u_k = \Gamma(t, t_k)u_k. \tag{7.11}$$

With the response written in this form, it is clear that the units of u_k are units of velocity.

Now if one supposes that

$$x(t) = \Phi(t, t_o)x_o + \pi(t) \tag{7.12}$$

where the process noise term $\pi(t)$ can be defined by

$$\pi(t) = \sum_{k=1}^{n(t)} \Gamma(t, t_k)u_k, \tag{7.13}$$

with the statistics $u_k \sim N(0, q\delta_{jk})$ and $n(t) \sim P(\lambda(t - t_o))$, then the velocity impulses are uncorrelated in time, and normally distributed with zero mean and variance q, and the number of impulses in the interval $[t_o, t]$ is Poisson-distributed with rate parameter $\lambda(t - t_o)$.

Grigoriu shows that random processes such as $\pi(t)$ have a mean [50]

$$E\left[\pi(t)\right] = \lambda \int_{t_o}^{t} \Gamma(t, \tau) \left\langle u_\tau \right\rangle d\tau = 0 \tag{7.14}$$

and covariance, where $\Delta t = t - t_o$,

$$E\left[\pi(t)\pi(t)'\right] = Q_\pi(t) = \lambda \int_{t_o}^{t} \Gamma(t, \tau) \left\langle u_\tau u_\tau' \right\rangle \Gamma(t, \tau)' d\tau. \tag{7.15}$$

Carrying out the integration results in a covariance matrix that is similar to that of the discrete white noise process and is given as

$$Q_\pi(t) = q\lambda \begin{pmatrix} \Delta t^3/3 & \Delta t^2/2 \\ \Delta t^2/2 & \Delta t \end{pmatrix}. \tag{7.16}$$

It must be noted that the time difference defined by Δt in $Q_\pi(t)$ is the total elapsed time and not a simulation time step similar to that derived in the discrete white noise case. Thus, $Q_\pi(t)$ does not depend on the choice of time step whereas the discrete white noise process model does. Also, note that were it not for the presence of the rate parameter λ, the covariance would be identical to the covariance for a continuous white noise input process.

Now, with $x_o \sim N(0, P_o)$, the mean and covariance of the position and velocity are as follows:

$$E\left[x(t)\right] = 0 \tag{7.17}$$

and

$$E\left[x(t)x(t)'\right] = P(t) = \Phi(t, t_o)P_o\Phi^{\mathrm{T}}(t, t_o) + Q_\pi(t). \tag{7.18}$$

Thus, the covariance of the linear system driven by a train of Gaussian-distributed impulses whose arrival times follow a Poisson distribution is the same as the covariance of the same system driven by a continuous white noise input process, except for the scaling of the process noise covariance by the Poisson process rate parameter.

In order to simulate realizations, one must divide the simulation time interval $[t_o, t]$ into intervals of arbitrary length $[h_1, h_2, ..., h_K]$. There is no direct need for these intervals to be of the same length. Then, over each interval h_k, a realization is generated from a Poisson random number, n_k, using the rate parameter λh_k. Next, generate n_k realizations of the a normally distributed random number with mean zero and variance q. These represent the velocity impulses u_k that have been realized during the interval h_k. The realization of the compound Poisson/Gaussian noise sample for the increment h_i is then

$$\pi(h_k) = \sum_{k=1}^{n_k} \Gamma(t, t_k) u_k \tag{7.19}$$

and the realization of the state at then end of the interval h_k may then be found from the recursion

$$x(t_{k-1} + h_k) = \Phi(t_{k-1} + h_k, t_{k-1}) x(t_{k-1}) + \pi(h_k). \tag{7.20}$$

Note that if more than one event occurs within an interval, this approach treats all of the events as if they had occurred simultaneously at the beginning of the interval. This violates the Poisson model, which assumes non-simultaneous events. To avoid this problem, note that the arrival times of the events will be exponentially distributed, and the average wait time between events will be $1/\lambda$. Grigoriu et al. provides a Poisson random number generator that also returns the arrival times [51].

7.3 Uncertainty Mapping with FLAK

Earlier in this work, the effects of the local instability in the orbit was characterized using local Lyapunov exponents. This analysis involved the natural dynamic uncertainty mapping in the CRTBP using the state transition matrix to identify properties that are of concern for future mission designers. While this analysis showed that there were locations in the halo orbit where one would expect the orbits instability to stretch the uncertainty along the unstable direction, it did not give any insight into how additional process noise would influence these properties. This section aims to help quantify how the discrete Poisson white noise model influences the natural uncertainty mapping strength and orientation over a specific time span.

Given an initial uncertainty of 1 km in position and 1 mm/s in velocity, the evolution of the covariance matrix was analyzed for various halo orbit sizes and initial τ angles. Figure 7.1 shows the relationship between the halo orbit z amplitude, A_z, the initial covariance location τ and the final angle between the unstable manifold and the maximum uncertainty direction, $\theta_{uns/cov}$, as well as the size of the covariance semi-major axis. Similar to Figure 6.2 we can see that there exists

a location where the covariance is stretched significantly. This occurs in the same region as the natural mapping without process noise for propagations that begin with an initial τ value of ~ 120 degrees. Similar to before, the smaller amplitude halo orbits experience less variation in the angle between the unstable manifold and the maximum uncertainty direction as well as the stretching of the covariance matrix. Larger amplitude halo orbits experience the inverse affect where there is a larger variation in the angle between the two directions as well as a significant difference in the amount of stretching that occurs for the halo orbiter.

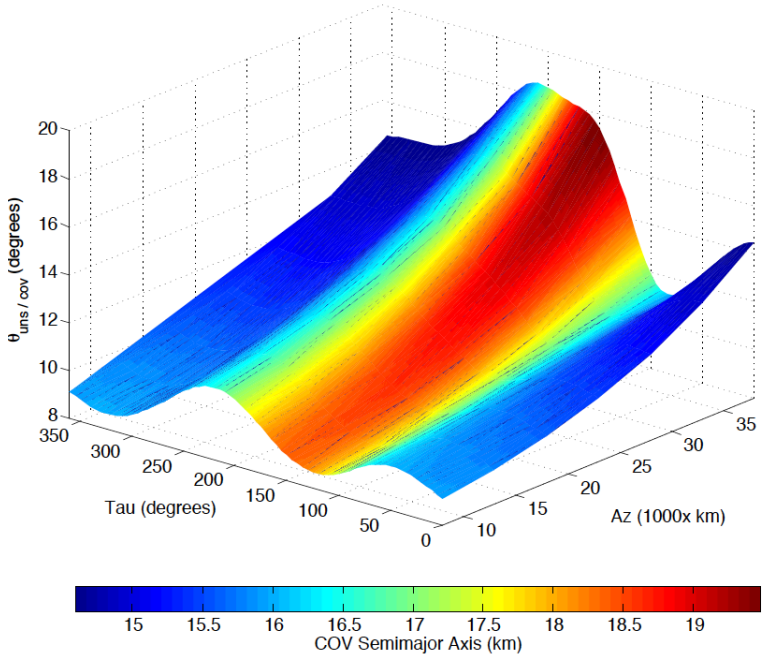

Figure 7.1: Surface comparing the size of the Covariance semi-major axis compared to the size of the Halo orbit, the initial tau angle, and the time it takes for the angle between the unstable manifold direction and the maximum covariance to get to within 10 degrees with discrete Poisson white noise.

In addition to this analysis, it is important to know how long it takes for the uncertainty distribution to align itself with the unstable manifold direction. Similar to before, we will assume that the covariance matrix has aligned itself with the unstable manifold if the angle between the two vectors it within 10 degrees. Figure 7.2 shows that with the addition of Poisson white noise influences the time it takes for the unstable manifold and the maximum uncertainty direction to

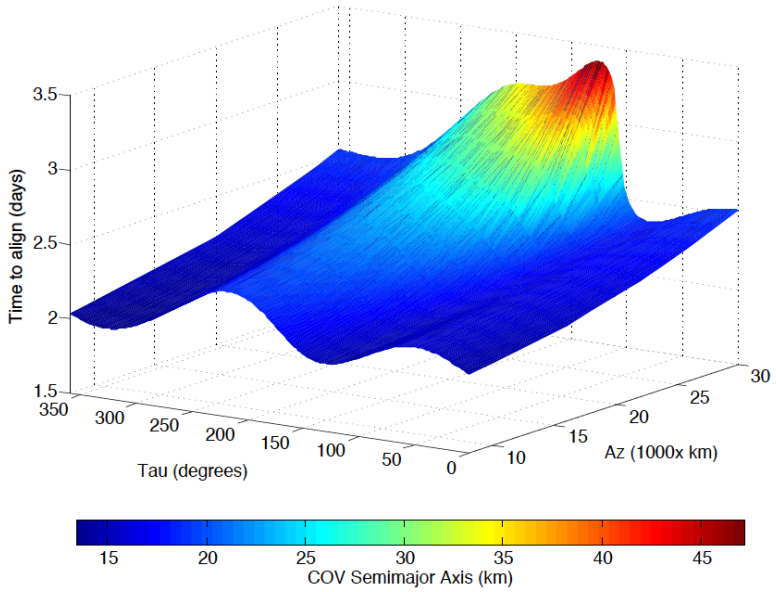

Figure 7.2: Surface comparing the size of the Covariance semi-major axis compared to the size of the Halo orbit, the initial tau angle, and the time it takes for the angle between the unstable manifold direction and the maximum covariance to get to within 10 degrees with discrete Poisson white noise.

align to within 10 degrees. Without the addition of Poisson white noise, it would take a halo orbit with z-axis amplitude of 8,000 km $\sim$ 1.5 days to align its maximum uncertainty direction with the unstable manifold. The addition of process noise has raised this time to $\sim$ 2.0 days for the 8,000 km case.

7.4 Monte Carlo Analysis

Typically, during operations, the timeframe between when tracking data ceases to be processed and when a maneuver is executed is on the order of two to three days. Therefore an investigation of the validity of the linearized propagation assumption of the discrete Poisson FLAK model is necessary. A compound discrete Poisson noise process using the FLAK criterium defined in Table 7.1 was propagated for 5 days. Figures 7.3 and 7.4 show 500 Monte Carlo simulations of the discrete compound Poisson FLAK model for position and velocity (respectively) of an EML-2 halo orbiter. The blue curves are the 500 realizations of a discrete compound Poisson FLAK model,

the dashed black curve is the ensemble 3-sigma of the realizations relative to the mean, and the red curve is the linear propagation of the uncertainty of the discrete compound Poisson process using Eq. 7.16. During the timeframe under consideration, the linearized propagation of the uncertainty for the discrete compound Poisson noise process matches the ensemble uncertainty. This shows that the Kalman filter propagation of the uncertainty is a decent approximation of the uncertainty due to FLAK when using a discrete Poisson model for the propagation and no higher order uncertainty propagation techniques are required for this short timeframe.

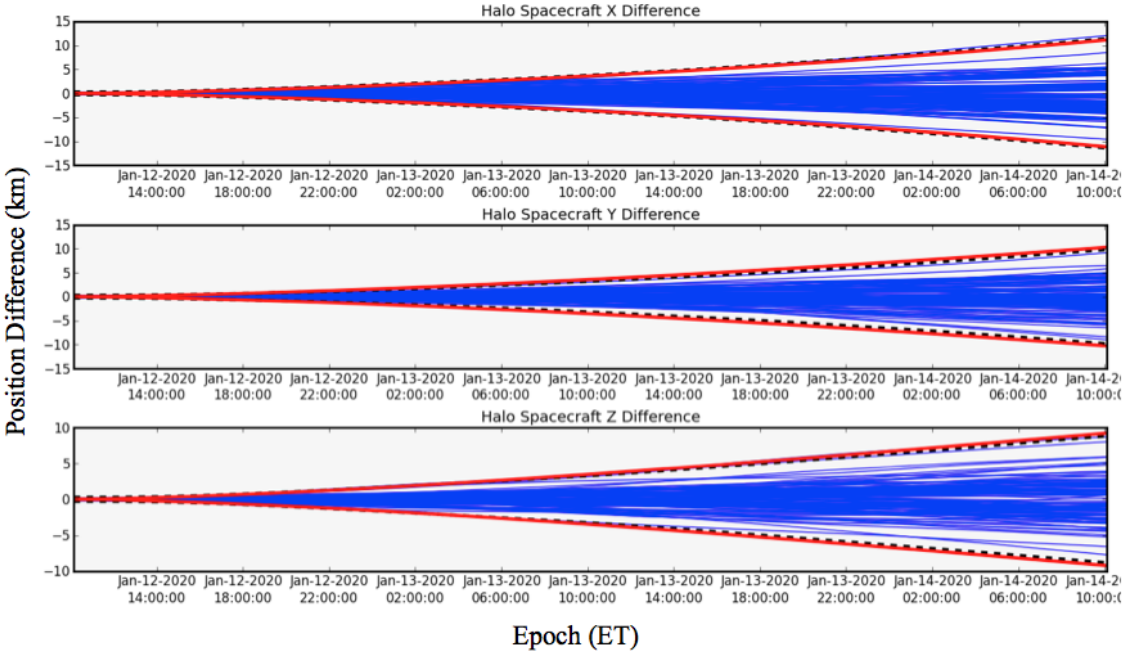

Figure 7.3: Position realizations for 500 Monte Carlo runs of a halo orbit perturbed by FLAK.

7.5 Full Simulation

A high-fidelity navigation simulation for a crewed vehicle being tracked by the IDAC4B ground tracking system is analyzed in this section. The crewed spacecraft is in a halo orbit around the L1 point with a z-axis amplitude of 10,000 km and an initial τ angle of zero degrees. The spacecraft is being tracked with Two-way range and Doppler as well as Three-way Doppler. The Three-way Doppler measurements are from the Usuda, Hartebeesthoek, and Santiago as receive

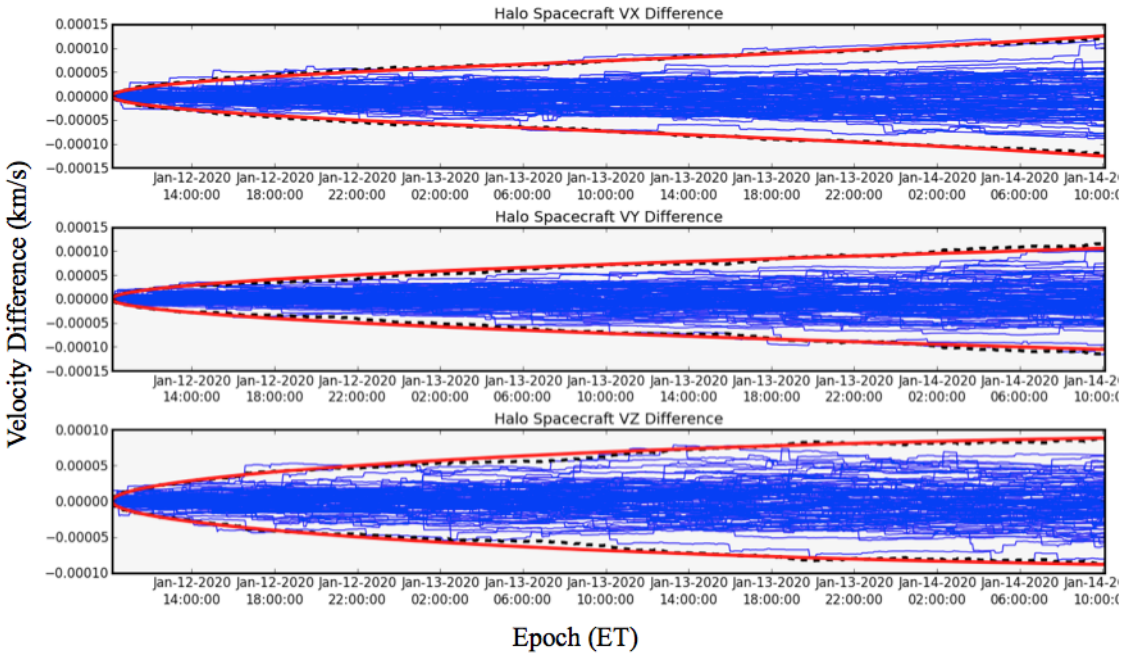

Figure 7.4: Velocity realizations for 500 Monte Carlo runs of a halo orbit perturbed by FLAK.

only stations. The measurement noise is 2 m (every 5 minutes) in range and 0.1 mm/sec in Doppler with a 60 sec count time. The spacecrafts initial state is based on a reference trajectory designed for the 10,000 km amplitude halo orbit. The spacecraft is then integrated forward in time and perturbed by a series of FLAK events defined in Table 7.1. The navigation filter estimates the spacecrafts position, solar radiation pressure coefficient, as well as a time series of stochastic accelerations in order to model the FLAK events. The stochastic accelerations are estimated every every 10 minutes.

Figures 7.5 and 7.6 show the postfit residuals for a filter run that uses stochastic accelerations to estimate the FLAK imparted on the spacecraft. While the range residuals have reached the expected noise value, the Doppler residuals still have some structure due to the FLAK. While the stochastic accelerations have done well to correct the trajectory, there are still several maneuvers that either could not be estimated by the stochastic accelerations or were not accurately estimated. Figure 7.7 shows the estimated stochastic accelerations in the EME2000 reference frame. The Z-component of this reference frame is the least observable while the X is the most observable at

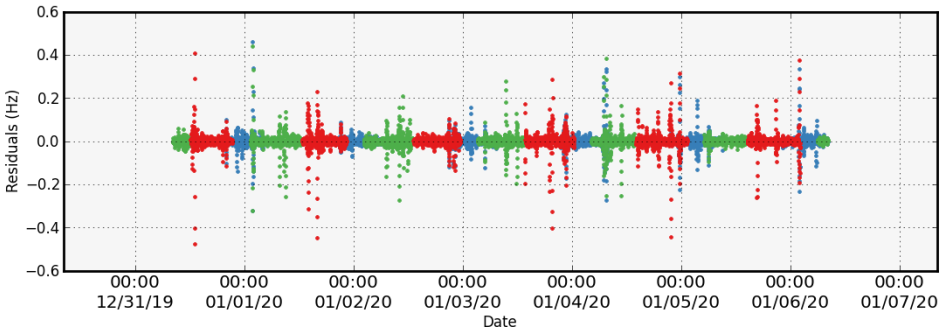

Figure 7.5: Doppler Residuals.

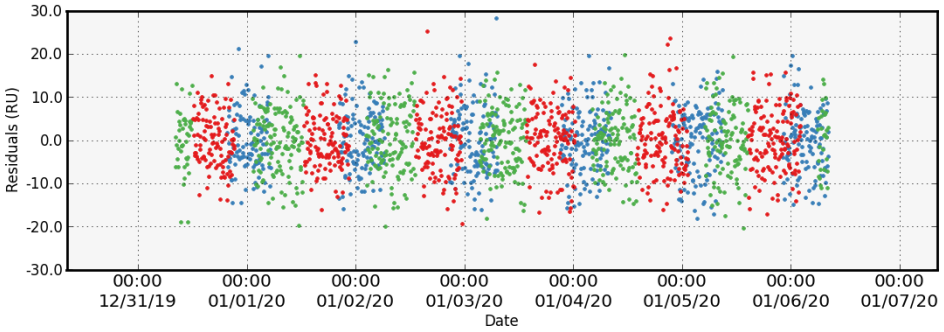

Figure 7.6: Range Residuals.

the beginning which then transitions into the Y-coordinate. Several large outliers exist in order to model some of the larger FLAK events. Overall, the stochastic estimation has done a good job at recovering the unmodeled FLAK events. Figure 7.8 shows how well the estimated trajectory is off from the true trajectory. The final position uncertainty is ~ 200 meters and the final velocity uncertainty is ~ 18 mm/sec. The final estimated trajectory matches the true trajectory to < 100 meters in all coordinates.

This analysis was conducted for a series of initial states ranging form initial τ values of 0 degrees to 360 degrees. Each simulation was able to estimate the trajectory consistently to < 500 meters in all cases. There did not appear to be any relationship between the initial τ angle and the navigation solution accuracy and uncertainty. However, the projected uncertainty mapping to 2 days into the future produced uncertainty evolution similar to Figure 7.1.

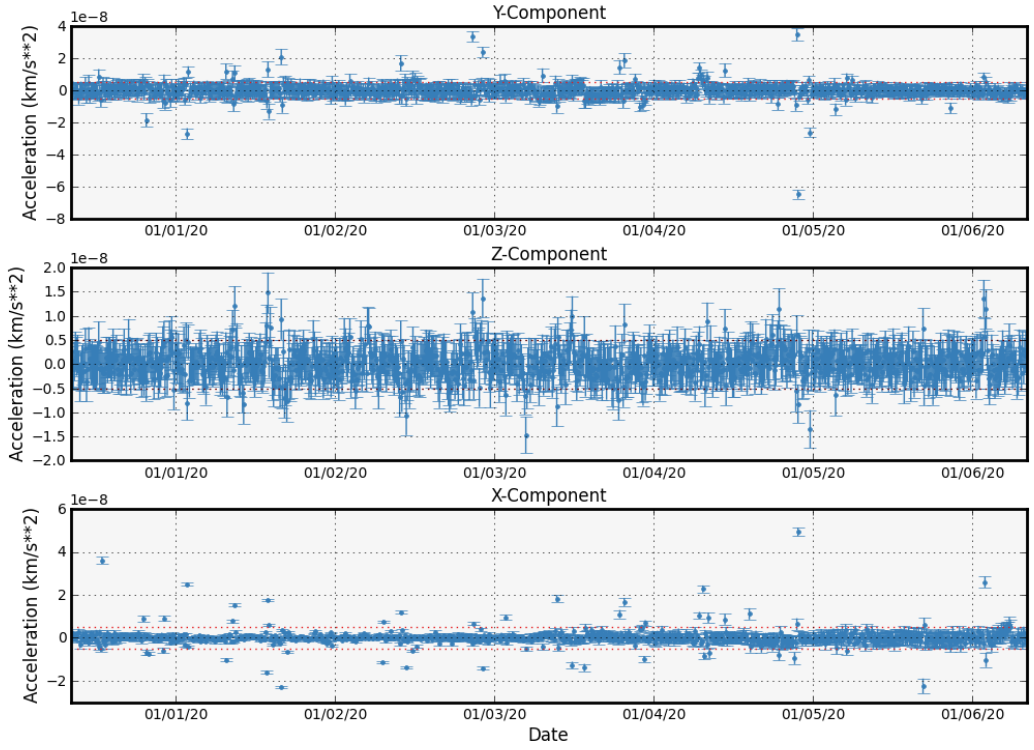

Figure 7.7: Stochastic Accelerations.

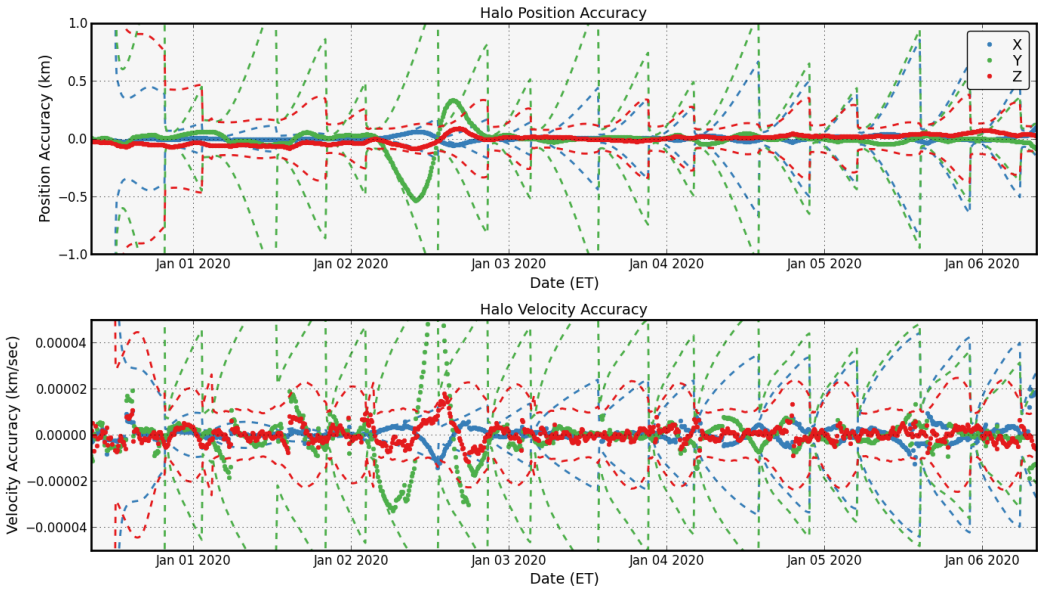

Figure 7.8: Crewed halo orbiter accuracy and uncertainty.

Chapter 8

LiAISON Supporting Lagrange Point Orbits

8.1 GEO Navigation using LiAISON

This work examines a new navigation concept in detail, studying the benefits of supplementing standard ground tracking measurements of two satellites in the Earth-Moon system with relative satellite-to-satellite tracking observations made between these satellites. A concurrent study has demonstrated the viability of the LiAISON technique applied to a constellation of two satellites, where one is in orbit about the lunar L_1 point and the other is at GEO [39, 120]. This paper quantifies the improvement in accuracy that one may expect by supplementing conventional radiometric ground tracking with LiAISON measurements.

This study develops high-fidelity simulations to quantify the benefits of LiAISON applied to tracking GEO and L_1 satellites. The scenario begins with typical ground-only tracking to establish a baseline navigation accuracy of both satellites. This ground-only tracking involves radiometric data to remain consistent throughout the study. LiAISON measurements are then introduced to quickly improve the navigation accuracy of both satellites. The simulations include dynamical modeling errors, measurement errors, and measurement biases. Furthermore, the measurements include large measurement gaps to simulate other activities being performed by each asset. A tracking schedule analysis is performed over a wide range of possible observation pass gaps. The results are compared to both continuous ground-only tracking and LiAISON tracking.

8.1.1 Models and Setup

A truth model simulation of the LiAISON configuration is necessary in order to determine the effectiveness of the proposed filter. In the truth model, a time history of the two satellites states are obtained through numerical integration of the equations of motion previously defined. The simulation then generates SST observations between the two satellites and a fictitious DSN network. The DSN network consists of radiometric tracking from Goldstone, California, Madrid, Spain, and Canberra, Australia. A single ground station tracking the GEO satellite is located in Sky Valley, California. Once the truth simulation is generated with the observations, the filter analysis can be performed. Figure 8.1 shows the LiAISON scenario configuration for this study and the tracking links between the two satellites and the ground.

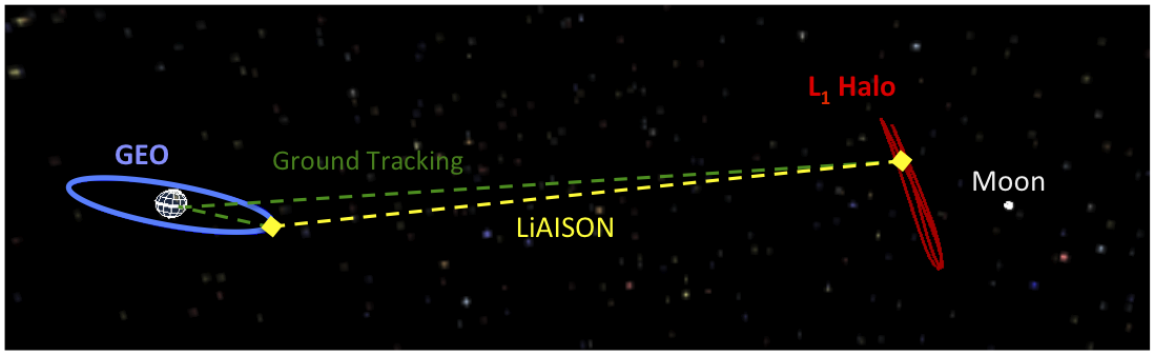

Figure 8.1: Satellite constellation geometry for truth model simulations for LiAISON and ground tracking viewed in the Earth-Moon rotating frame.

The time evolution of the state dynamics are solved using the TurboProp orbit integration package for orbit propagation [59]. The TurboProp software provides the necessary numerical integration capabilities for the generation of the true trajectories and the filter trajectories. The high-fidelity truth model used in this paper is integrated with a DOPRI8(7)13 integrator with variable step size control [125]. A relative tolerance of 10^{-14} was used with an initial step size of 10 seconds.

Table 8.1: L_1 quasi-halo orbit parameters.

Parameter	Value	Comments
A_z	35,500 km	The z-axis amplitude
ϕ	0°	The initial phase angle of the orbit
t_{ref}	1/1/2020 00:00:00 ET	The reference epoch, ephemeris time

8.1.1.1 L_1 Truth Model

The equations of motion for the L_1 truth model have been integrated in the GCRF coordinate system. The L_1 satellite does not use a spherical harmonic model for its representation of Earth's gravitational potential, rather, Earth is assumed to be a point mass. This is considered to be a reasonable estimation since the L_1 orbit is at least 300,000 km from Earth. Third body perturbations are also added to the equations of motion with all of the planets being used as well as the Moon whose states are given by the JPL DE405 ephemeris [141]. A simplified model for SRP given in Eq. 2.31 is used with an area-to-mass ratio of 0.01 m^2/kg and a coefficient of reflectivity, C_R, of 1.0. Table 8.2 gives all of the standard LiAISON simulation models used in this analysis with appropriate references.

The halo reference orbit has been generated using a two-step process. First, a set of states has been generated using an analytical expansion described by Richardson and Cary [131]. The reference epoch for the first state in the series has been set to January 1, 2020 ET (Ephemeris Time), the z-axis amplitude, A_z, has been set to 35,500 km, and the initial phase angle of the orbit, ϕ, has been set to zero degrees. Table 8.1 gives the settings used to generate the halo orbits used in this study. The set includes four states per revolution of the approximate halo orbit and four revolutions about L_1. Ref. [119] describes the benefits gained by adding additional buffer states to this set; hence, an additional revolution of L_1 with four corresponding states is appended to both ends of the set, increasing the number of states in the series to 24.

This set of states is then differentially corrected into the high-fidelity dynamical model previously described with third body perturbations given by the JPL DE405 ephemeris using a multiple

shooting differential corrector [123, 160]. The differential corrector adjusts the position and velocity of each state, such that the integrated trajectory from one state to the next results in position and velocity discontinuities no greater than 10^{-6} km and 10^{-9} km/s, respectively. These discontinuities are far below the level of error typically observed in the navigation of halo orbiters; hence the resulting trajectory is operationally ballistic [38]. Once converged, the first and last revolution about L_1 are then pruned off, as described by Ref. [119], leaving four continuous revolutions about L_1.

8.1.1.2 GEO Truth Model

The GEO satellite used in this study is placed over the western hemisphere to be visible from U.S. ground stations. The initial latitude and longitude of the GEO satellite is 0.10963 deg N and 80.26889 deg W respectively. GEO truth model equations of motion have also been integrated in the GCRF coordinate system. A 20×20 spherical harmonic gravity field representation of Earth given by GRACE Gravity Model 02 (GGM02C) is used [147]. Third body perturbations are also added to the equations of motion with all of the planets being used as well as the Moon whose states are given by the JPL DE405 ephemeris [141]. A simplified model for SRP given in Eq. 2.31 is used with an area-to-mass ratio of 0.01 m^2/kg and a coefficient of reflectivity, C_R, of 1.0. Table 8.2 gives all of the standard LiAISON simulation models used in this analysis with appropriate references.

8.1.1.3 Measurement Generation

LiAISON SST measurements are taken between the GEO satellite and the L_1 satellite during a 9 day period. Both geometric range and range-rate are taken between the two satellites as described in Eq. 3.102 and Eq. 3.109. These measurements are corrupted by zero mean Gaussian white noise with a standard deviation of 1 m and 1 mm/s respectively. Fictitious DSN range and range-rate measurements are also taken during this time frame and corrupted by a zero mean Gaussian white noise with a standard deviation of 100 m and 0.1 mm/s respectively. Figure 8.2 shows the time history of these measurements.

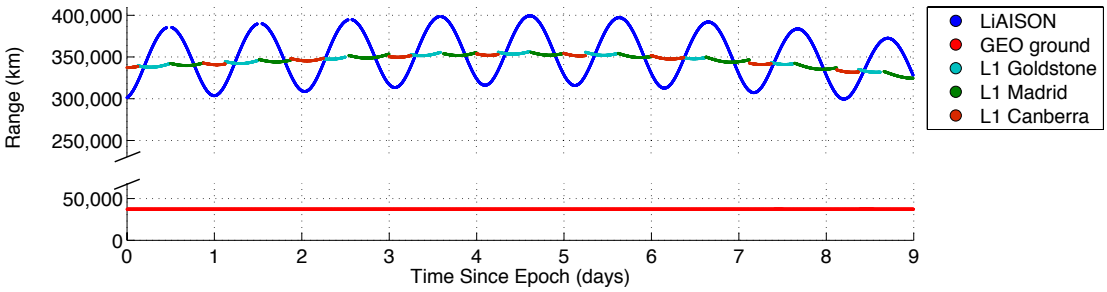

Figure 8.2: Range observations to the GEO and L_1 orbiter from LiAISON and ground station measurements.

Table 8.2: Summary of models used in the LiAISON simulations.

Model	LiAISON Standard			Reference
	Reference Frame			
Conventional inertial system	GCRF			–
Precession	1976 IAU			–
Nutation	1980 IAU			–
Planetary ephemerides	JPL DE405			Ref. [63, 141]
Polar motion	IERS			–
UT1-TAI	IERS			–
JED/TDB/TT	IERS			–
Station coordinates	Lat. (deg)	Lon. (deg)	Alt. (km)	–
Goldstone	35.247	243.205	1.0711	–
Madrid	40.427	4.251	0.834	–
Canberra	-35.398	148.982	0.692	–
Sky Valley	33.930	243.610	0.445	–
Reference ellipsoid	$a_e = 6378136.3$ m			–
	$1/f = 298.257$			–
	Force Models			
GM	398600.4415 km^3/s^2			Ref. [147]
Geopotential	GGM02C & 3–sigma clone 20×20			Ref. [147]
N body	JPL DE405			Ref. [63, 141]
Solar radiation	solar constant $= 4.5298 \times 10^{-6} Pa$ at 1 AU, conical shadow for Earth.			–
	Measurement Models			
Range	Instantaneous			Eq. 3.102
Doppler	Instantaneous			Eq. 3.109

8.1.2 Navigation Simulation Results

The utilization of a truth model simulation allows one to be able to evaluate filter performance under a set of ideal conditions. Since the truth states are known it is easy to investigate filter performance based on initial state perturbations. In order to properly assess filter performance in a real world situation, the filter equations of motion are altered when compared to the truth model simulations. In this section, the proposed filter is tuned in order to obtain reasonable estimates and uncertainties of the state vector given in Eq. 2.27. A trade study of the necessary amount of LiAISON and ground observations is also executed. In addition, an analysis of observation scheduling offset is conducted to determine the benefits of having LiAISON and ground observations at different times.

8.1.2.1 Filter Dynamical Model and Tuning

The reference trajectory used in the filter contains dynamical errors when compared to the truth model. The equations of motion for the GEO satellite in the filter dynamical model consist of a 3-sigma clone of the GGM02C gravity model based on sampling the GGM02C's corresponding error covariance. Third body perturbations for both satellites are reduced to only the Sun and Moon in addition to the Earth central body force. Both satellites are perturbed by SRP, however, the coefficient of reflectivity is initially in error. It is assumed that the ground station locations are known nearly perfectly and are not estimated or perturbed.

Several filter runs were initially executed for a case in which there were constant observations through LiAISON and ground stations in order to determine the necessary stochastic parameters and initial uncertainties. The estimated parameters and *a priori* uncertainties for the filter runs are given in Table 8.3. These values are used consistently throughout the analysis done in this paper for each simulation and filter run that is executed. Initial random perturbations of the states within their 3-sigma uncertainties were used during the filter tuning process. For each of these filter executions, consistency and performance of the filter were checked in order to determine if the filter

Table 8.3: Orbit determination filter uncertainties.

Estimation Parameters	*a priori* uncertainty (1-sigma)	Number of Parameters
Spacecraft position (both)	1,000 m	6
Spacecraft velocity (both)	1 mm/s	6
SRP Coefficient	20%	2
Empirical Accelerations		6
Radial	5×10^{-10} m/s^2	–
Transverse	1×10^{-12} m/s^2	–
Normal	1×10^{-12} m/s^2	–
SST range bias	3 m	1
DSN range bias	6 m	3
GEO-supporting ground station range bias	6 m	1
SST measurements		
range	1 m	–
range-rate	1 mm/s	–
DSN measurements		
range	100 m	–
range-rate	0.1 mm/s	–
GEO-supporting ground station measurements		
range	100 m	–
range-rate	1 mm/s	–

was performing correctly. The total time since epoch that a filter run is executed is 9 days. For each filter run, a comparison to the truth model simulation is used to compare the filter state estimates to the truth states to determine if the estimates are reasonable and within the uncertainty bounds.

8.1.2.2 Example Navigation Scenarios

An example navigation setup is presented here to illustrate the performance of the navigation filters used in this study. The example scenario considers the case of navigating both satellites using only ground-based tracking via the setup summarized in Table 8.3. This is also useful because it may be used to relate the performance of this navigation filter to other similar studies in the literature.

The navigation scenario presented here processes ground-based tracking data that is continuous for a three-hour pass twice per day, i.e., alternating three hours of tracking with nine hours

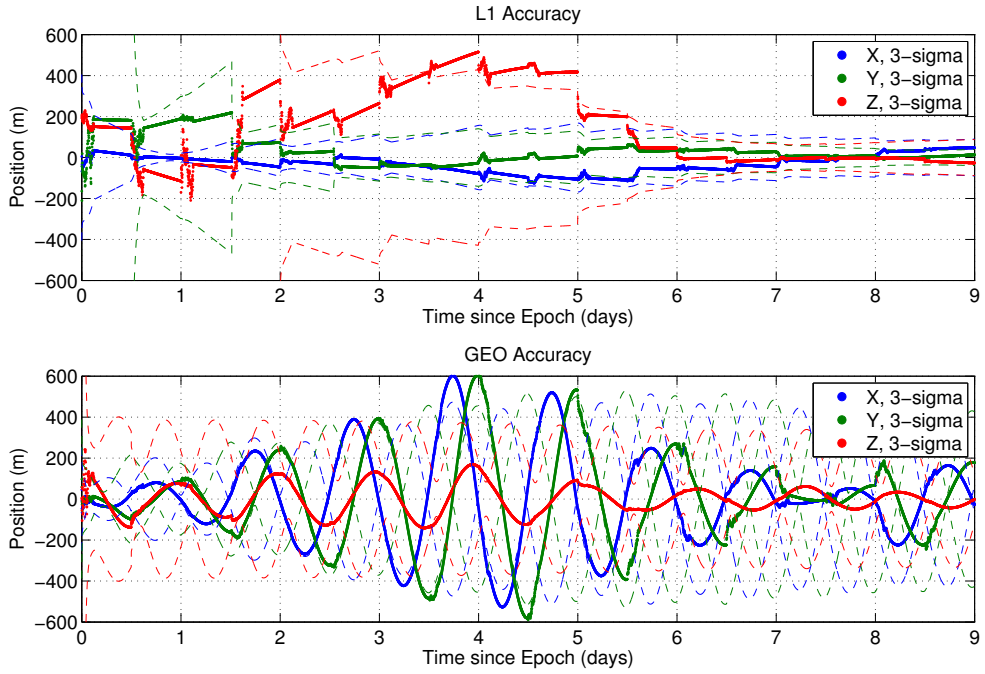

Figure 8.3: Position accuracy and uncertainty for a GEO and L_1 orbiter tracked by ground networks twice a day for 3 hours.

without tracking. Figure 8.3 illustrates the performance of the filter, showing the accuracy of the estimated state over time and the associated 3-sigma uncertainty. One can see that the accuracy of the filter and the corresponding uncertainty in the state estimate of the halo orbit improves as observations are processed until it converges on a solution around Day 6. The uncertainty in the position of the halo orbiter improves in a step-like fashion every time a new measurement pass is processed. The GEO orbiter's state estimate has an oscillating accuracy and uncertainty due to its dynamics; the uncertainty in the estimate of the state is not significantly impacted by the observations taken from the ground station. One can see the estimated state change due to the observations for three hours every 12 hours. Later in the paper one will see that LiAISON observations dramatically improve the uncertainty in the GEO orbiter's state estimates.

In order to relate the results presented in Figure 8.3 with thousands of other results, a cost function is used to evaluate the filter's performance. One notices that the estimated solution's

uncertainty reaches a near-steady state after the 6th day of tracking. The RMS of the data between day 6 and day 9 is used for trade study analyses. The RMS of the data shown in Figure 8.3 results in a filter accuracy of approximately X meters with corresponding RMS uncertainty of approximately X meters (3-sigma). The accuracy and uncertainty of each variable changes quite a lot over time, but the RMS value provides a good metric to evaluate the scenario.

This entire process may be repeated for any combination of ground-based and LiAISON tracking.

8.1.2.3 Trade Study

In this section we investigate the proposed satellite configuration and filter's ability to estimate the parameters listed in Table 8.3. Over 5000 filter runs were executed to determine the accuracy of certain observation schedules for the LiAISON satellite configuration being investigated. For each simulation there is a minimum of 3 hours of continuous observations every 100 seconds from either the ground station or a LiAISON link between the two satellites. After the 3 hours of continuous observations, an observation gap of "X" hours exists. Observation gaps range from 0 hours (continuous observations) to 72 hours (i.e., very sparse data). Both LiAISON and ground station tracking gaps are varied from continuous tracking to very sparse with a resolution of 1 hour to create a mesh of possible tracking schedules. The tracking schedules always start with both LiAISON and ground station tracking to begin simultaneously at epoch. The EML-1 orbiter is tracked by the DSN at the same times as the GEO satellite is tracked by its ground station. The diagonal of the produced mesh will always have LiAISON and ground station tracking for each of the satellites at the exact same time. The tracking schedules are described by the convention (LiAISON Tracking Gap, Ground Tracking Gap). For instance, the schedule (0,0) is continuous LiAISON tracking and ground tracking of both the EML-1 and GEO satellites. A tracking schedule of (28,49) has 3 hours of constant tracking to begin with for both LiAISON and ground tracking, followed by a 28 hour gap for LiAISON and a 49 hour gap for ground tracking. This tracking schedule is then repeated until the final tracking time is reached.

Each of these observation schedules was then used in the processing of tracking data through the Kalman filter previously defined. Figure 8.4 shows a mesh of the resulting accuracies and uncertainties obtained by the filter runs. Figures 8.4(a) and 8.4(b) show the 3-sigma position accuracies determined from the filter runs when compared to the truth model for the EML-1 halo and GEO satellite respectively. Figures 8.4(c) and 8.4(d) show the position uncertainties estimated from the filter runs for the EML-1 halo and GEO satellite respectively. All of the values that are given in the position accuracy and uncertainty meshes are calculated by computing the RMS of the data between the 6^{th} and 9^{th} day past the epoch. The values given in the mesh are determined

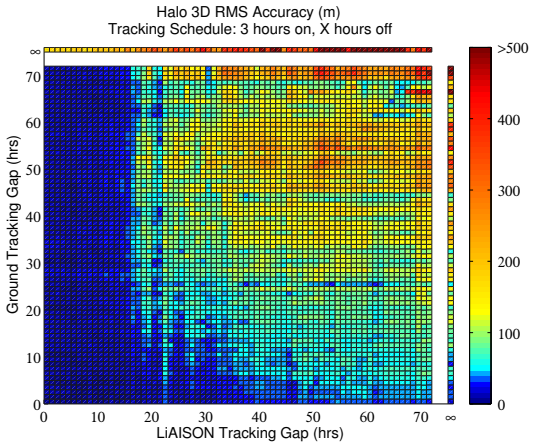

(a) Halo Position Accuracy

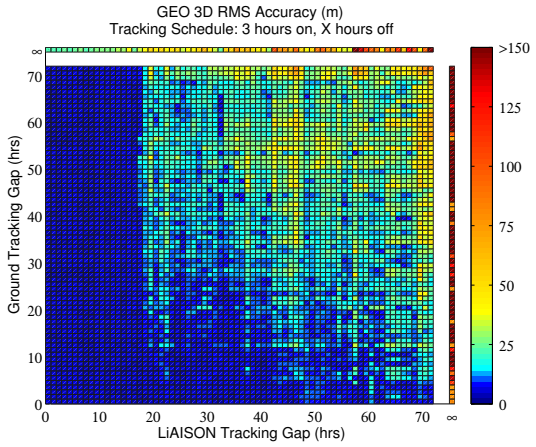

(b) GEO Position Accuracy

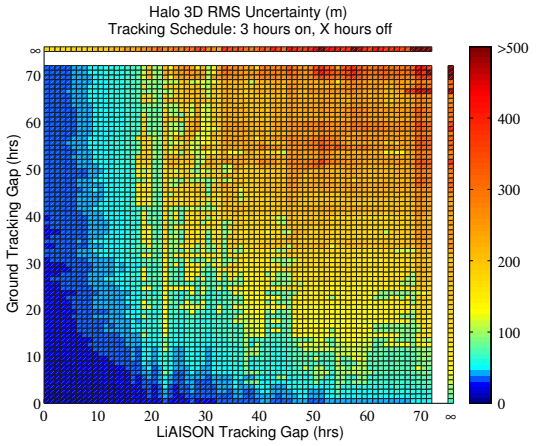

(c) Halo Position 3-sigma Uncertainty

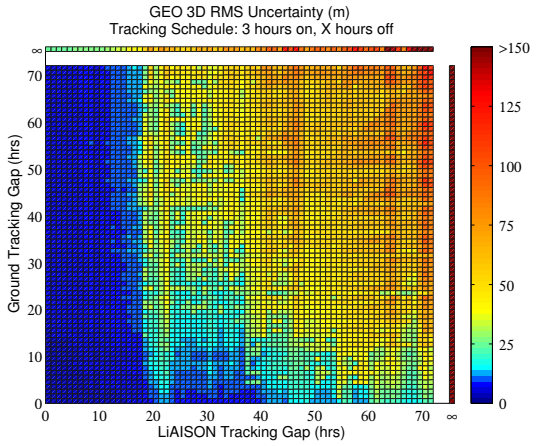

(d) GEO Position 3-sigma Uncertainty

Figure 8.4: Orbit determination accuracy and 3-sigma uncertainty for various amounts of LiAISON and ground station tracking.

from the 3D-RMS of the position accuracy when compared to the truth model simulations and 3D-RMS for the position uncertainties given from the filter runs. The uncertainty values given in the mesh are 3-sigma values. Values with an uncertainty over 500 meters for the halo orbiter and 150 meters for the GEO orbiter are represented by the same color. The far column and row denoted by an observation tracking gap of ∞ corresponds to only LiAISON or ground station tracking data. This is provided as a check to see how accurate one tracking method is completely separate from the other. Tracking of the halo orbiter with continuous ground tracking is the most accurate with an uncertainty of about 70 meters. Continuous ground tracking of the GEO satellite using only radiometric data from one ground station does not reduce the *a priori* uncertainty. Continuous LiAISON only tracking provides reasonable estimates for both the halo and GEO orbiters with an uncertainty of about 160 meters and 24 meters, respectively.

In general, one three-hour LiAISON tracking pass per day (left most side of Figures 8.4(c) and 8.4(d)) or more produces a navigation uncertainty equivalent to or less than four three-hour ground tracking passes per day (bottom of Figures 8.4(c) and 8.4(d)). In order to achieve a position uncertainty of less than 200 m for the halo orbiter, regardless of the amount of LiAISON tracking, a ground track every day is necessary. To achieve the same uncertainty for the halo orbiter using only LiAISON tracking with no ground tracking, only two three-hour tracking passes are necessary per day. This tracking schedule results in the uncertainty of the GEO satellite position being about 30 meters. The addition of a three-hour pass of ground tracking every 3 days to a LiAISON tracking scheme of two passes per day reduces the uncertainty of the halo orbit to about 50 meters and the GEO orbit to about 10 meters. While continuous LiAISON measurements can obtain reasonable position accuracies for both satellites, the addition of relatively few ground tracking passes can greatly improve the solution.

Ideally, one would like to have as few tracking passes from LiAISON and ground tracking as possible to obtain an accurate solution. There exists an area of this analysis from which relatively accurate estimates can be obtained using very few tracking passes. The tracking schedules for this region are 28-30 hour gaps for LiAISON and 48-56 hour gaps for ground tracking. In this region

the halo orbiter's uncertainty is around 110 meters while the GEO accuracy is about 35 meters. With very few measurements from both LiAISON and ground tracking, reasonable estimates of both satellites states are obtained.

Figure 8.5 shows the time history of the position uncertainty for various tracking schedules for a few interesting cases that arise from the trade study analysis. The tracking schedules shown are continuous tracking (0,0), continuous LiAISON and sparse ground tracking (0,72), sparse LiAISON and continuous ground tracking (72,0), and a point from the previously described sparse tracking region that gives reasonable estimates (28,49).

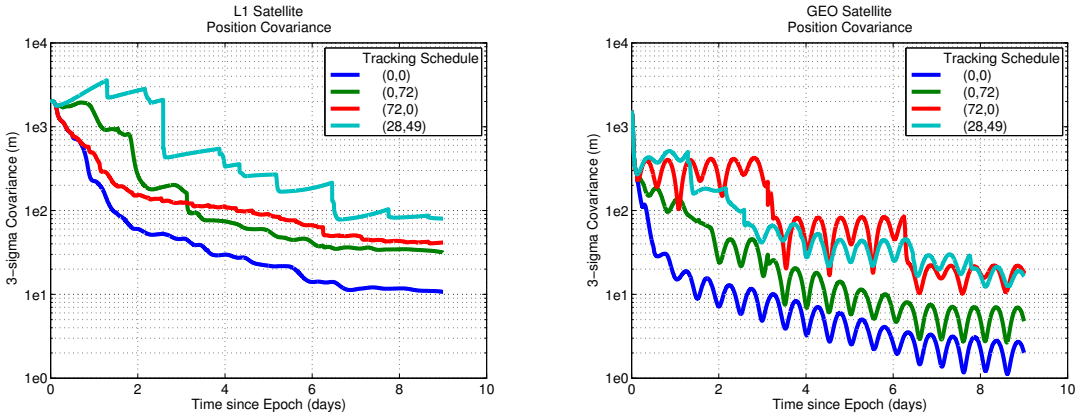

(a) Halo (b) GEO

Figure 8.5: Time history comparison of 3-sigma position uncertainty for various tracking schedules.

The position covariances shown in Figure 8.5 give the filtered updated covariance and filter predicted covariance to make the comparison continuous for all cases. As one would expect, the continuous tracking schedule of (0,0) gives the best results. Here both LiAISON and ground tracking are combined for continuous observation of the two satellites. Final position uncertainties are on the order of 10 meters for the EML-1 orbiter and 3 meters for the GEO satellite.

The next most accurate estimates come from the tracking schedules of (0,72) and (72,0). Both of these tracking schedules produce roughly the same uncertainty for the halo orbiter. Initially, (72,0) has less uncertainty than (0,72), but the second tracking pass from the DSN around 3 days helps lower the uncertainty to less than (72,0). After this second DSN pass, the tracking schedule

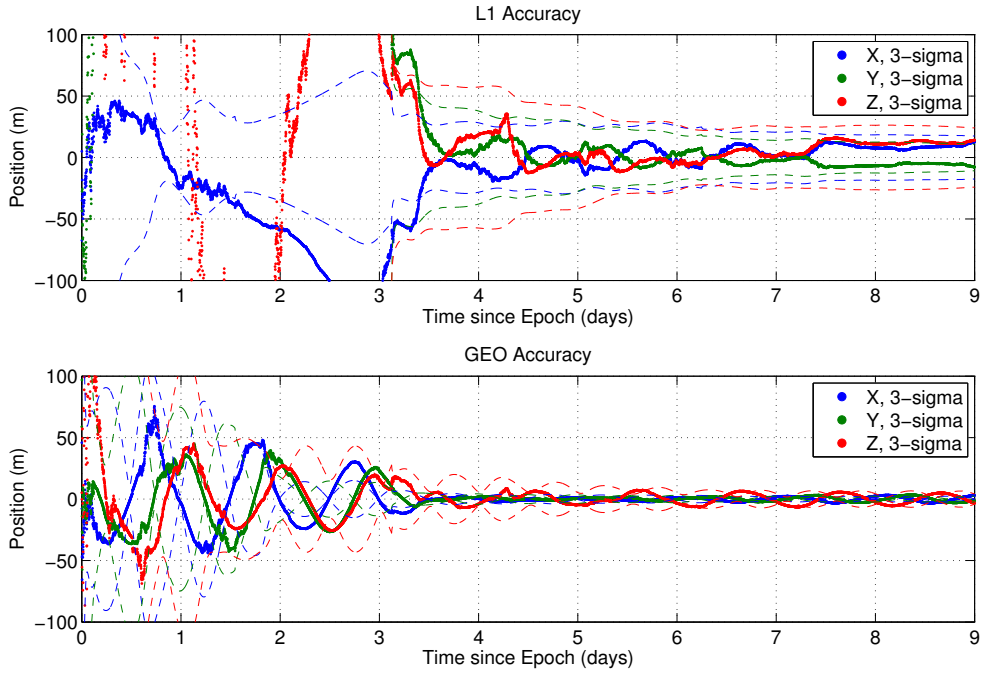

Figure 8.6: Position accuracy and uncertainty for LiAISON constellation for a tracking schedule with continuous LiAISON tracking and 3 hours of ground tracking followed by 72 hour observation gap (0,72).

(0,72) always has less uncertainty than (72,0) but the difference is only 10s of meters. There is a large difference in the uncertainty, however, for the GEO satellite. The tracking schedule (0,72) for the GEO satellite is the most accurate showing that the LiAISON data type defined in this analysis is better suited for estimating the state of the GEO satellite than the radiometric only data from one tracking station. One can notice a large decrease in the uncertainty for the (72,0) case when a LiAISON measurement pass is obtained around day 3. If this LiAISON pass did not exist, the uncertainty in the GEO satellite's position would stay around 500 m instead of reducing to 100 m. The next LiAISON pass for this case occurs at about 6 days, and again, the uncertainty in the GEO satellite is reduced significantly. Figures 8.6 and 8.7 show the position accuracy and 3-sigma uncertainties for a tracking schedule of (0,72) and (72,0). After 3 days of observation processing, the uncertainty of the EML-1 satellite for both tracking schedules is less than 100 m. The GEO satellite's accuracy and uncertainty for the (0,72) schedule is significantly less than

the (72,0) schedule. The (0,72) GEO uncertainty is less than 100 m after 1 day of observation processing while it takes 3 days for the (72,0) schedule. The uncertainty reduction due to the LiAISON measurement updates at 3 and 6 days is clearly visible in Figure 8.7.

The final schedule given in Figure 8.5 is (28,49). This tracking schedule of (28,49) obtains position uncertainties of less than 100 m and 30 m for the halo and GEO satellites respectively after 9 days of tracking. While the uncertainty is higher for the halo orbiter when compared to the other tracking schedules, the uncertainty of the GEO satellite is comparable to constant ground tracking with sparse LiAISON measurements, (72,0). Figure 8.8 shows the time history of the position accuracy and 3-sigma uncertainty for the tracking schedule of (28,49). The reduction in uncertainty for the EML-1 satellite due to measurement updates can clearly be seen. The uncertainty of the EML-1 satellite is well above 1 km for the first 2 days and does not reduce to under 100 m until 6 days of observations. The GEO satellite uncertainty is less than 100 m after 2

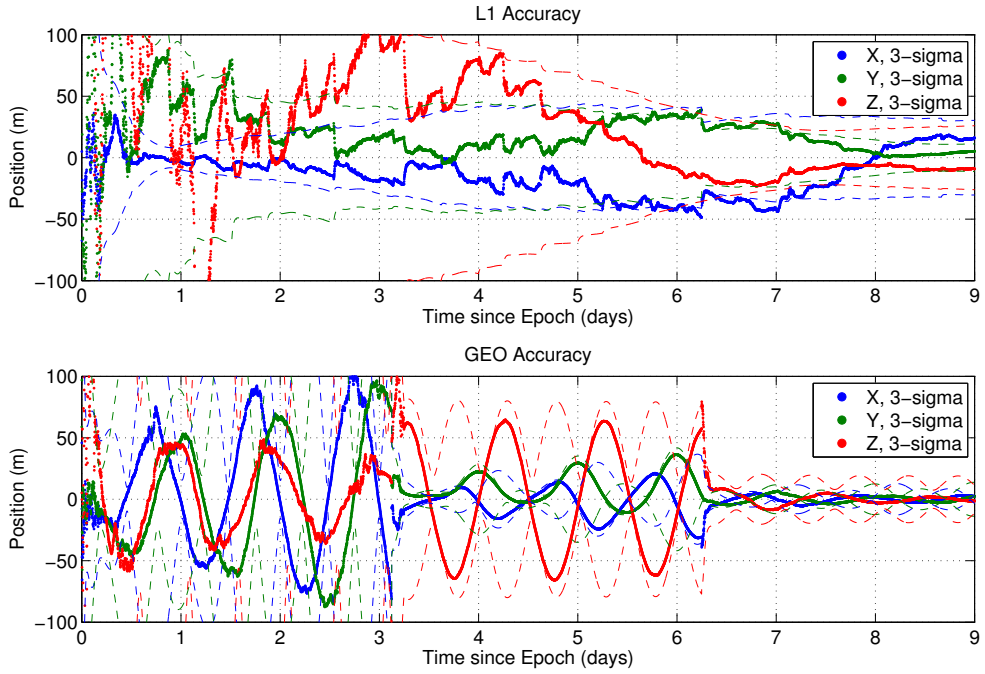

Figure 8.7: Position accuracy and uncertainty for LiAISON constellation for a tracking schedule with 3 hours of LiAISON followed by 72 hour observation gap and continuous ground tracking (72,0).

days of observation processing and reduces down to 30 m after 6 days. The large uncertainties for the first few days are due to the large *a priori* uncertainties in the OD filter's state.

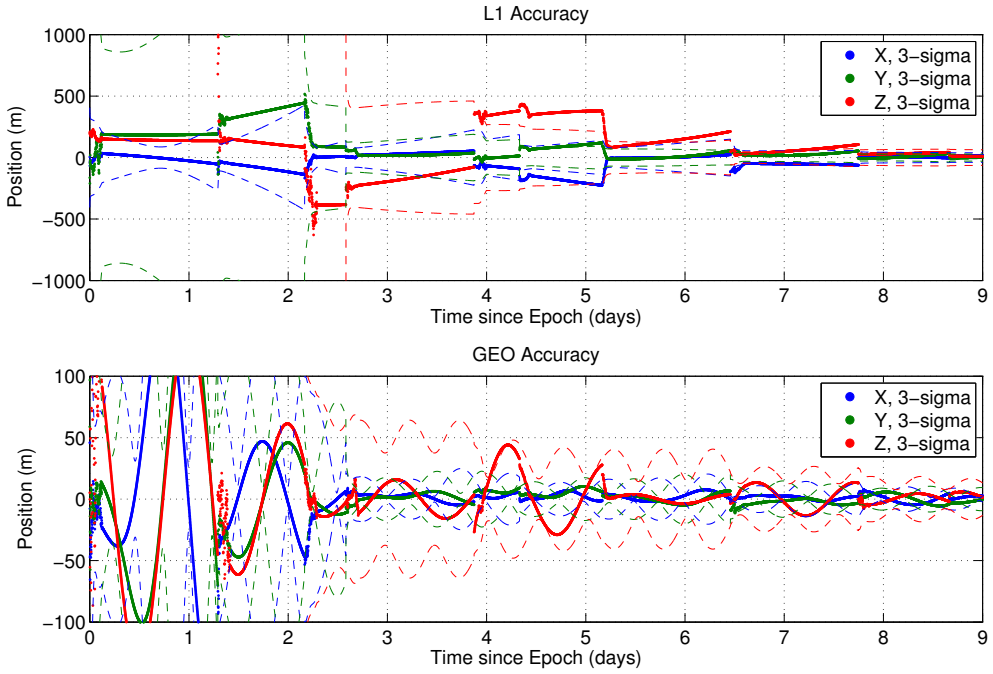

Figure 8.8: Position accuracy and uncertainty for LiAISON constellation for a tracking schedule with 3 hours of LiAISON followed by 28 hour observation gap and 3 hours of ground tracking followed by 49 hour observation gap (28,49).

Another feature that shows up in the trade study analyses is the growth in uncertainty around 22 hours which is a result of a worsening observation geometry. In the trade study analysis, there was a ridge of more inaccurate solutions and uncertainty for tracking schedules that involved a resonance of around 22 hours for both the EML-1 and GEO satellites. Another resonance is noticeable at roughly 44 hours for the GEO satellite. These resonances are caused by a periodic condition in which the LiAISON constellation is observing the GEO satellite at roughly the same geometry as the previous day (i.e. the GEO satellite's orbital period and the Earth's rotational period are nearly equal).

8.1.2.4 Scheduling Offset

In the previous analyses, the diagonal of the produced mesh always had LiAISON and ground station tracking for each of the satellites at the exact same time. Measurements occurring at the exact same time from both LiAISON and ground stations affect the performance of the filter in a certain way. In this section, we investigate filter performance for this diagonal by offsetting the times at which the measurements occur. The times at which these measurements are taken will be offset and compared to when the measurements are taken simultaneously.

The truth simulation used in this study is the same as before with the same dynamical models. The only thing that has changed is the times at which LiAISON observations or ground station measurements are taken of the EML-1 and GEO satellites. Observations generated during this analysis always begin with LiAISON measurements taken for the first three hours followed by a gap of no measurements for "X" hours. Ground station observations are calculated to start exactly half way through the LiAISON observation gap. Three hours of continuous ground station measurements spaced at an interval off 100 seconds are calculated. Preference to the ground station that has the most visibility with an elevation mask of 10 degrees is given as the primary tracker of the satellites. Once the measurements are obtained for that three hour period, the ground station measurements experience a gap of exactly "X" hours (the same gap time as the LiAISON measurements). The process is then repeated to always have ground station measurements to begin at exactly half of the LiAISON observation gap.

Several filter runs were executed to determine the effects of an observation offset for the diagonal elements of the previous trade study mesh. Simulations begin with completely continuous LiAISON and ground station tracking of the EML-1 and GEO satellites. An observation gap of 1 hour is then added until there is a gap of 72 hours. Figure 8.9(a) shows the 3D-RMS position accuracy and uncertainty of the halo orbiter for the offset observation case as well as the no-offset observation case. The GEO satellite's 3D-RMS position accuracy and uncertainty is shown in Figure 8.9(b) for the offset observation case as well as the no-offset observation case.

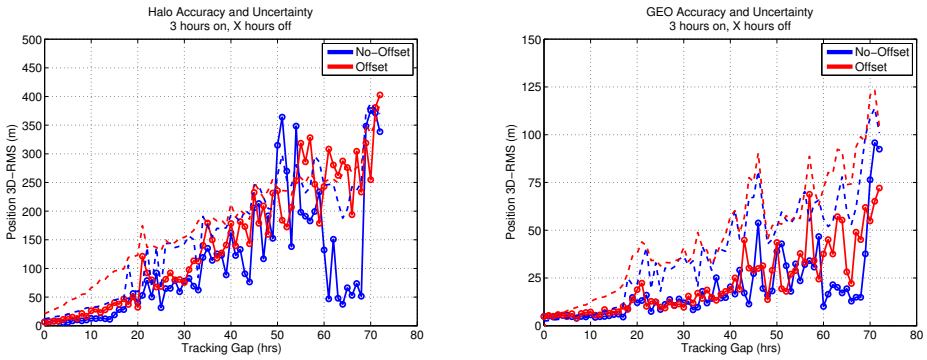

(a) Halo (b) GEO

Figure 8.9: LiAISON L_1 and GEO measurement offset analysis. Solid lines represent 3D-RMS accuracy and dashed lines represent 3-sigma uncertainty.

A few features show up in the offset analysis for this LiAISON constellation. The results show that neither satellite's uncertainty or accuracy is impacted significantly by the scheduling offset. The filter solution accuracy and uncertainty are relatively the same for both cases. Another feature that shows up in both analyses is the growth in uncertainty around 22 hours which is a result of a worsening observation geometry. In the trade study analysis, there was a ridge of more inaccurate solutions and uncertainty for tracking schedules that involved a resonance of around 22 hours for both the EML-1 and GEO satellites. This growth in uncertainty occurs in the offset analysis as well. Another resonance in noticeable at roughly 44 hours for the GEO satellite.

8.1.3 Conclusions

A new LiAISON (Linked Autonomous Interplanetary Satellite Orbit Navigation) constellation configuration involving two satellites, one in orbit about the Earth-Moon L_1 and one in geosynchronous Earth orbit (GEO), has been analyzed. This study demonstrates that the relative and absolute navigation of two satellites at GEO and L_1 is possible through the use of satellite-to-satellite range and range-rate measurements. In addition, this measurement type can supplement and significantly improve radiometric measurements taken from the Deep Space Network for satellite navigation.

A complete study of observation scheduling was done for the GEO and L_1 LiAISON constel-

lation. Filter accuracies and uncertainties obtained through high-fidelity simulations match that of current NASA practices for the ARTEMIS mission. The supplement of LiAISON observations to ground tracking passes can significantly reduce the uncertainty of an orbit determination solution. Several cases have been analyzed and compared. Among these were continuous ground and LiAISON tracking, continuous ground and sparse LiAISON tracking, continuous LiAISON and sparse ground tracking, and relatively sparse tracking for both LiAISON and ground. While continuous tracking of both data types produced the best results, continuous LiAISON with sparse ground tracking produced nearly the same accuracies as continuous ground with sparse LiAISON tracking. This shows that the inclusion of a necessary amount of LiAISON tracking can significantly reduce the number of ground tracks necessary to obtain a given accuracy, which can significantly reduce the costs of ground tracking. It was also shown that there exists a region in which viable tracking schedules with relatively sparse data can produce position uncertainties of about 100 m for the halo orbiter and less than 30 m for the GEO satellite. These types of tracking schedules would allow for a reduction in DSN time with very minimal interaction with the LiAISON constellation while maintaining a given position uncertainty.

A simple study was also conducted to determine if the effect of obtaining observations at the same epoch impacted the solution accuracy and uncertainty. In this study, a tracking schedule that contained the same observation gaps was adjusted to allow for observations to come in at different times but maintain the observation gap duration. There was no significant impact on the accuracy and uncertainty by acquiring observations at different times. During this analysis, interesting features were enhanced for which poor observation geometry on a schedule of roughly 22 hours was experienced. During this timeframe, the geometry of the LiAISON and GEO configuration is such that every observation time the GEO satellite is being sampled in roughly the same position and geometry as it was the previous time. The results of these simulations suggest that navigators avoid an SST schedule that is in resonance with the orbital periods of the satellites

The configuration and simulations studied in this paper are representative of a realistic LiAISON navigation configuration. The analysis has been done in a high-fidelity regime with the

necessary dynamical errors that plague the orbital regime. These dynamical errors were overcome to obtain accurate navigation solutions using only radiometric data from a satellite based at the Earth-Moon libration point L_1. It has been shown that absolute navigation is possible for a GEO satellite and a lunar libration orbiter using minimal ground tracks that have been supplemented with LiAISON observation data. This study has demonstrated LiAISON's potential capability as an addition to the Deep Space Network to help improve navigation solutions for future missions.

8.2 LPO NavSat for Crewed Vehicle at L2

This analysis examines the navigation challenges associated with navigating a crewed vehicle in orbit about the Earth-Moon L_2 point. The crewed disturbance model outline in previous chapters is used in this work to model the associated accelerations and perturbations due to the crew's activities during the mission timeline.

8.2.1 Models and Setup

The scenario studied in this section is for a crewed vehicle in orbit about the EML-2 point in a halo orbit with a z-axis amplitude of 10,000 km. This size halo orbit and orientation has been identified as a suitable candidate for the proposed Orion spacecraft. It has continuous access to the far side of the Moon with beneficial access to the South Pole – Aitken Basin and Schrodinger Crater. Another benefit of this orbit is that it is visible from the Earth and is never occulted by the Moon, allowing for continuous ground tracking for a crewed vehicle if necessary.

In addition to the crewed vehicle, this work explores the use of a navigation satellite located in a LPO around EML-1 and EML-2 for z-axis amplitudes ranging from 10,000 km to 35,500 km. Figure 8.10 illustrates the variety of orbits analyzed in this work and their size and orientation relative to the Earth-Moon rotating frame. The crewed vehicle's orbit is denoted by the solid black line. The navigation satellite's possible orbits are given by the gray lines.

The navigation of a crewed vehicle will near the Moon will undoubtedly require the use of ground-based tracking for state estimation. In addition to radiometric ground tracking, spacecraft

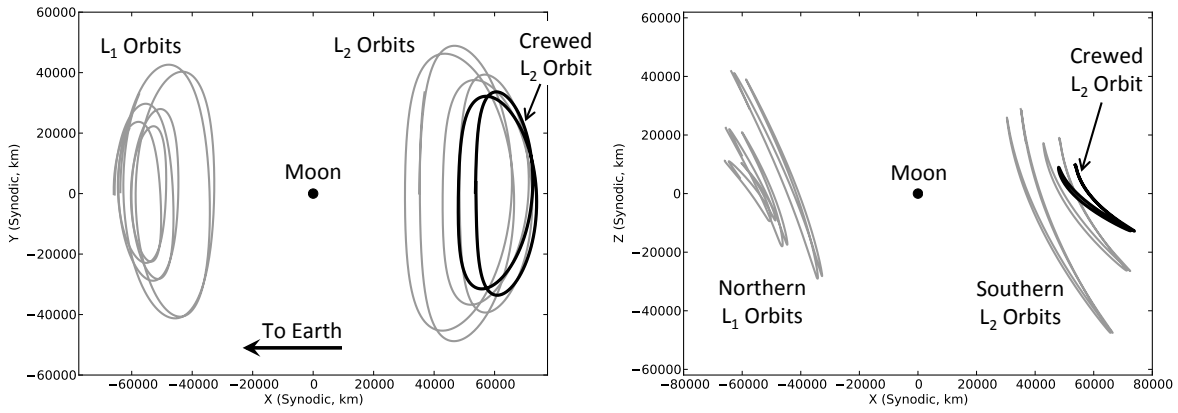

Figure 8.10: An illustration of the orbits studied in this paper, viewed in the Earth-Moon rotating frame from above (left) and from the side (right). The orbits pulsate with the Moon's motion. The NavSat is only located in one orbit per scenario, though each of the locations is visualized.

such as Orion will also use optical tracking of landmarks. Backup navigation and observational data are necessary for contingency plans in the event that one or more sources of tracking are unavailable. This work examines the use of satellite-to-satellite radiometric tracking as a possible supplement to ground based tracking data.

Currently, the exact performance characteristics of a crewed vehicle such as Orion are not well known. As the design improves, FLAK models can be refined to characterize the associated accelerations and perturbations with more detail. The analysis performed in the work uses the CRLB and FLAK models previously defined to model the crews behavior. Several reference trajectories are designed for both the crewed and navigation satellite. Measurements are simulated over the course of the mission for ground based tracking as well as LiAISON between the two spacecraft. The radiometric data in this work contains measurement biases for both range and range-rate. The CRLB analysis is for only the position and velocity states of the two spacecraft being tracked. The *a priori* covariance for the navigation satellite is 100 m in position (1-sigma) and 1 cm/sec (1-sigma) in velocity. This uncertainty is consistent with a spacecraft being tracked by the ground for a period of time before it begins performing LiAISON. The crewed vehicle has a position uncertainty of 1 km (1-sigma) and 1 m/sec (1-sigma) in velocity. FLAK is modeled as

Table 8.4: The parameters used to define the errors in the tracking data. The bias added to each link and the white noise added to each observation are drawn from Gaussian distributions with zero mean and the given standard deviations.

Tracking Link	Const. Bias 1σ	Pass Bias 1σ	White Noise 1σ	Comments
NavSat - Crew 2-way range	1 m	3 m	1 m	LiAISON range SST
NavSat - Crew 2-way range-rate	0.5 mm/s	1 mm/s	1 mm/s	LiAISON range-rate SST
DSN - NavSat 2-way range	10 m	30 m	10 m	DSN ground tracking of
DSN - NavSat 2-way range-rate	0.5 mm/s	1 mm/s	0.5 mm/s	the NavSat halo orbiter
DSN - Crew 2-way range	10 m	30 m	10 m	DSN ground tracking of
DSN - Crew 2-way range-rate	0.5 mm/s	1 mm/s	0.5 mm/s	the crewed vehicle
IDAC4B - Crew 3-way range	10 m	30 m	10 m	IDAC4B ground tracking
IDAC4B - Crew 3-way range-rate	0.5 mm/s	1 mm/s	0.5 mm/s	of the crewed vehicle

outline in previous sections and drops an order of magnitude during crew sleep periods. A 4-day station keeping maneuver period is used in this work as well.

In addition to the three DSN stations, a comparison with the IDAC4B configuration is also analyzed. The three additional stations other than the DSN in the IDAC4B configuration are assumed to be three-way receive only tracking stations. Each of the ground tracking stations are assumed to have a 10 degree elevation mask. If multiple stations are in view of the spacecraft, only one of the stations track the spacecraft at the given time. Tracking data includes 2-way range and range-rate between the DSN and each of the spacecraft. Three-way range and range-rate is processed when the IDAC4B stations are in view. The three-way data is only used for the crewed vehicle. In addition to these ground radiometric tracking sources, a LiAISON link of range and range-rate between the navigation satellite and crewed vehicle is simulated. Each of the radiometric links has a bias associated with it. Table 8.4 summarizes the tracking data simulated in this work.

Figure 8.11 illustrates the tracking data timeline for the simulated crewed vehicle in a 10,000 km EML-2 halo orbit and navigation satellite in a 35,500 km EML-1 halo orbit. This timeline is consistent for any of the other orbits the navigation satellite may be in for these simulations. Figure 8.11 gives the measurement timeline for all measurements simulated, however, not every simulation will utilize all of these measurements at the same time. It is always assumed that the DSN is capable of tracking both the navigation satellite and crewed vehicle at the same time.

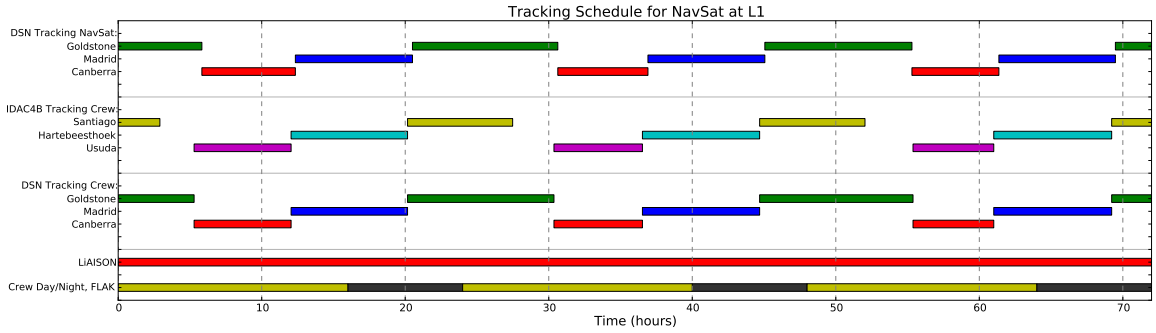

Figure 8.11: An illustration of the schedule of tracking observations for the case of an L_1 halo orbiter. Not all observations are used in all scenarios.

Figure 8.12 gives a time history of the range and range-rate measurements for the crewed vehicle over the course of a halo orbit from the DSN. One can see the white noise applied to the measurements as well as the biases associated with each measurement type. Figure 8.13 gives the time history of LiAISON measurements simulated for this work. It is assumed that the crewed vehicle gets continuous tracking data from the navigation satellite during the course of the mission. However, range biases are added to simulate the crewed vehicle electronics losing lock on the navigation satellite. Range biases are added every two hours to simulate this loss of lock on the signal.

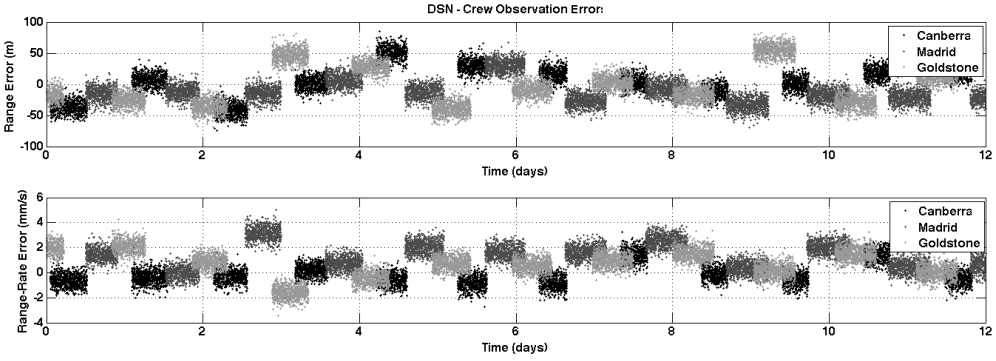

Figure 8.12: Example observation errors applied to the DSN–Crew links.

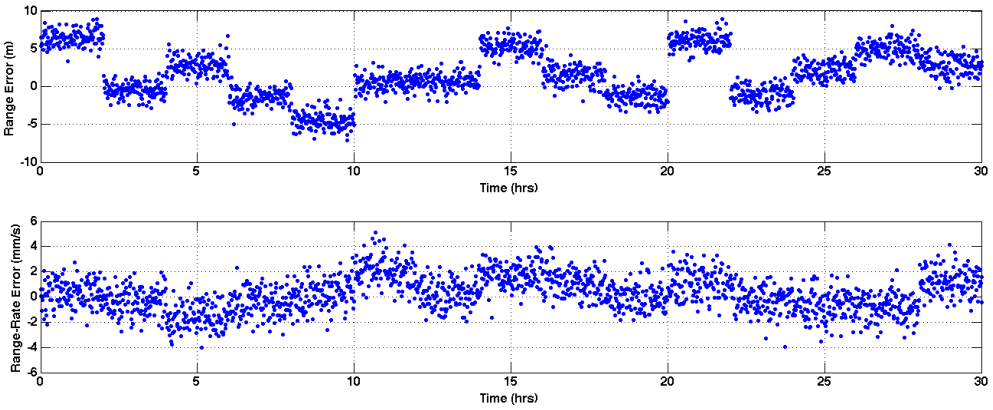

Figure 8.13: The first 30 hours of simulated LiAISON tracking data errors.

8.2.2 Navigation Simulation Results

8.2.2.1 Ground Only

In order to get a baseline navigation uncertainty of the crewed vehicle it is necessary to analyze ground based tracking only. This provides the foundation to compare to when augmenting the system with other measurements and measurement types. In addition, it allows for a comparison with other researchers who use slightly different assumptions for their measurement models, noise values, biases, and other parameters. Each simulation begins with a position uncertainty of 1.0e6 km (1-sigma) and 1.0e6 km/sec (1-sigma) in velocity to simulate an unknown state of the vehicles and to show that the measurement produce an observable system.

Figure 8.14 displays the 3-sigma position uncertainty for the navigation satellite and crewed vehicle tracked by the DSN only. The simulation represented here has no LiAISON or IDAC4B observations and the crewed vehicle has no FLAK modeling. The growth in the uncertainty around days 4 and 8 are due to the station keeping maneuvers. Figures 8.15 and 8.16 illustrate the uncertainty in position and velocity components for each spacecraft over the course of this simulation. The 4-day station keeping maneuver uncertainties are move evident here and can be seen distinctly in Figure 8.16.

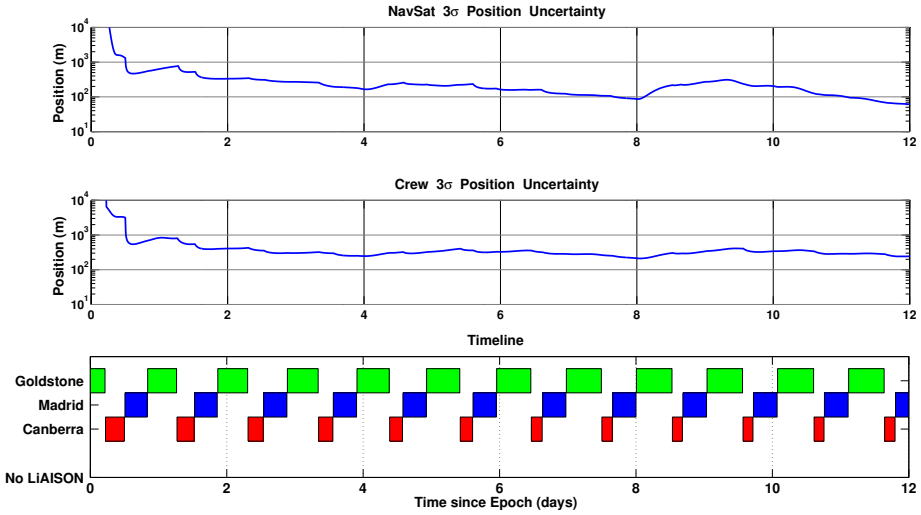

Figure 8.14: The position uncertainty over time of both the NavSat and the crewed vehicle as they are each independently tracked by the three main DSN ground stations. No FLAK or LiAISON observations are included.

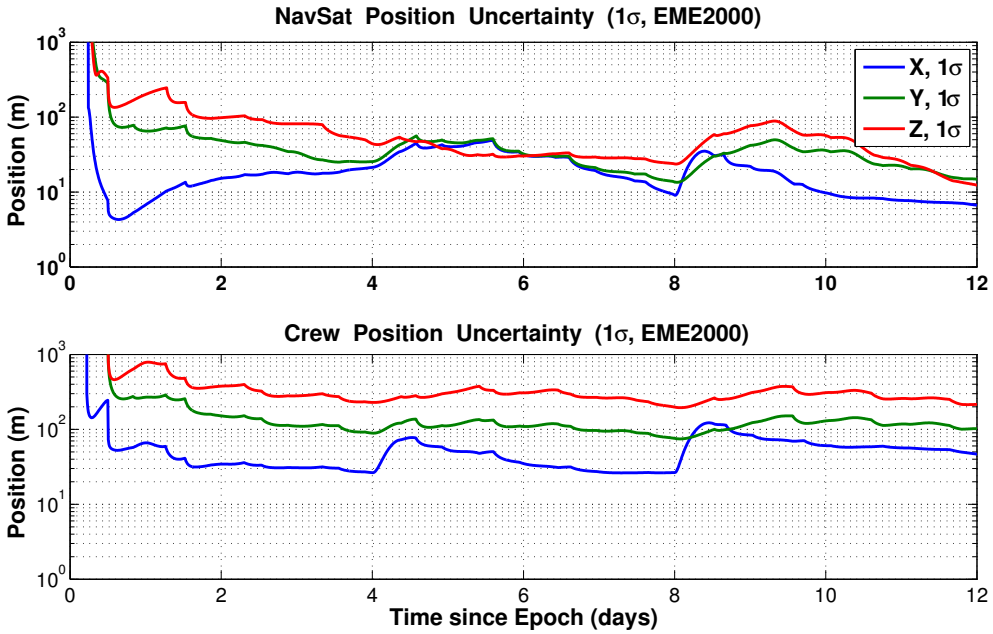

Figure 8.15: The position uncertainty components over time of both the NavSat and the crewed vehicle as they are each independently tracked by the three main DSN ground stations. No FLAK or LiAISON observations are included.

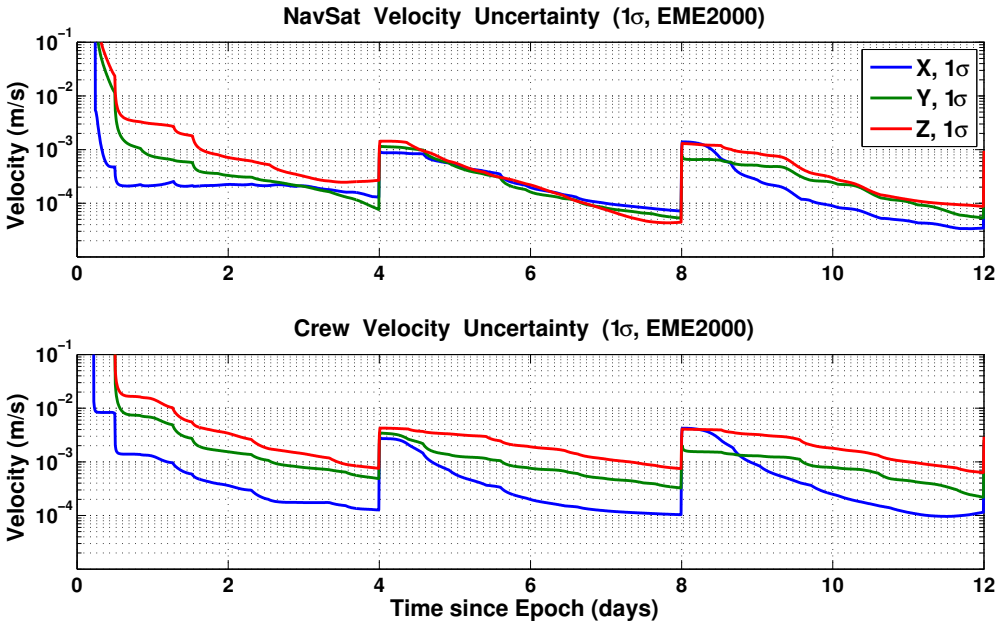

Figure 8.16: The velocity uncertainty components over time of both the NavSat and the crewed vehicle as they are each independently tracked by the three main DSN ground stations. No FLAK or LiAISON observations are included.

Once the baseline navigation uncertainty with no FLAK and DSN only tracking is obtained, a comparison with the addition of the IDAC4B configuration as well as FLAK is possible. One would expect the state uncertainty to decrease due the addition of three-way radiometric observations. However, the addition of FLAK modeling for the crewed vehicle significantly increases the state uncertainty for the crewed vehicle. Figure 8.17 compares four different combinations of tracking and FLAK to illustrate the influence that three-way tracking and FLAK modeling have on the state uncertainty. The navigation satellite state uncertainty does not alter from the previous analysis since the IDAC4B is only used in conjunction with the crewed vehicle and FLAK is only associated with the crewed vehicle.

While the time history of the state uncertainty gives an understanding of the instantaneous uncertainty at any particular time, it does not give any insight into the steady-state uncertainties one should expect. In order to express this, all scenarios use data from day 4 into the simulation through day 12 to compute statistics of the uncertainties. The cost function used to summarize the

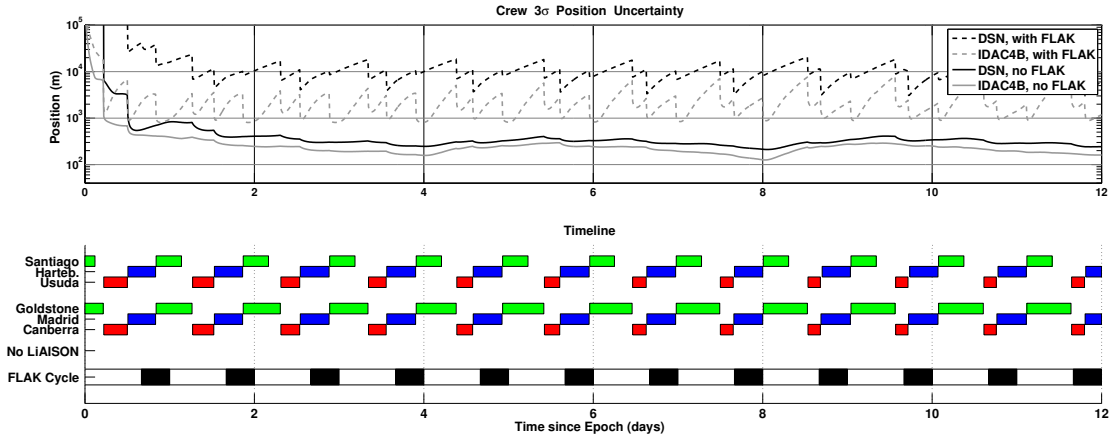

Figure 8.17: A comparison of the position uncertainty over time of the crewed L_2 vehicle as it is tracked by either the DSN or IDAC4B in the presence or not of FLAK.

results of the navigation scenario is quantified using two values based on the position uncertainty throughout the 4-12 day timeframe. This timeframe captures the 24 hour crew activity cycle as well as half of the revolution of the halo orbits. The mean and 99% values of the position uncertainty are used to describe the behavior of the uncertainty time history. The mean is a useful value that describes the expected uncertainty over the course of the simulation. The 99% position uncertainty is useful to describe how uncertain that mean value is. Table 8.5 gives these values for the ground-only simulations described previously. Table 8.5 illustrates the profound influence that FLAK plays on the position uncertainty of the crewed vehicle in these simulations. The IDAC4B configuration does reduce the position mean and 99% uncertainties but not to the level necessary to navigate a crewed vehicle. It would be extremely beneficial to reduce these uncertainties further.

Table 8.5: The mean and 99% position uncertainty 3-σ values for the ground-only simulations of a crewed vehicle in an L_2 halo orbit after the simulation has reached a nearly steady state.

Scenario	Mean Pos Uncertainty (3σ)	99% Pos Uncertainty (3σ)
DSN Tracking, No NavSat, With FLAK	9.850 km	18.501 km
IDAC4B, No NavSat, With FLAK	2.430 km	7.665 km
DSN Tracking, No NavSat, No FLAK	0.308 km	0.409 km
IDAC4B, No NavSat, No FLAK	0.219 km	0.292 km

8.2.3 LiAISON Only

The previous section generated a baseline navigation uncertainty for ground-only tracking. The next set of simulations presented in this section gives a baseline of navigation uncertainties for a LiAISON only tracking configuration. Each set of simulations explores the trade space around EML-1 and EML-2 for the navigation satellite. This is to determine which type or orbit geometry works best for LiAISON navigation.

Previous work looking into LiAISON for spacecraft in LPO about EML-1 and EML-2 showed that LiAISON is capable of reducing each spacecraft's state uncertainty down to acceptable levels for vehicles not experiencing FLAK [56]. However, the timeframe necessary to reduce the position uncertainty from the km level to the m level is on the order of weeks to months. Due to the fact that FLAK is a prominent perturbation to the trajectory, no simulation of LiAISON only tracking reduces the position uncertainty below 100 km. The following work is used to illustrate LiAISON's ability and to examine the trade space for regions where LiAISON provides more information content than others. It is not suggested that LiAISON only observations are capable of navigating a crewed vehicle from an LPO navigation satellite.

The trade space surveyed for the navigation satellite's orbit configuration varies in halo orbit z-axis amplitude, initial τ angle and location about EML-1 or EML-2. For each Lagrange point, EML-1 or EML-2, three different z-axis amplitude halo orbits are generated. A series of halo orbits were generated with z-axis amplitudes of 10,000 km, 20,000 km, and 35,500 km. Also surveyed are differences in the τ angle between the navigation satellite and that of the crewed vehicle at EML-2 which is represented as $\Delta\tau$. The results presented in this section exhaust all possible configurations such that no others exist that are particularly better than the ones presented.

Hill showed that the best symmetry for a LiAISON constellation in a LPO had a $\Delta\tau$ of around 50° to 150° and 210° to 310° [56]. The worst configurations are for those with a $\Delta\tau$ of 0° or 180°. Another feature is that scenarios that are symmetric in $\Delta\tau$, such as $\Delta\tau$ vs. $360° - \Delta\tau$, are expected to produce similar navigation uncertainties. The results presented in this section explore

$\Delta\tau$ values of 0°, 45°, 60°, 90°, and 120°. Only southern L_2 halo orbits and northern L_1 halo orbits are considered. This is due to the fact that southern L_2 halo orbits have communications benefits with the southern lunar hemisphere and northern L_1 halo orbits due to their navigation benefits when doing LiAISON with a crewed vehicle in a southern L_2 orbit.

Table 8.6 presents the results for LiAISON only navigation in the scenarios described above. It is not expected that LiAISON only be the sole navigation source in practicality, however, this trade study is used to determine which LiAISON configuration provides the most information when used in conjunction with ground based tracking. Table 8.6 indicates several important relationships between the two main configurations, a navigation satellite in orbit about L_1 with a crew orbiting L_2. If the navigation satellite is in orbit about L_1, there is little dependence on the size of the halo orbit A_z or the $\Delta\tau$ between the two spacecraft. There is minimal improvement in the navigation for extremely high values of A_z and smaller values of $\Delta\tau$. When the navigation satellite is in orbit about L_2, the results shift. Now the position uncertainty for both satellites benefits significantly when both vehicles have a small A_z and a larger $\Delta\tau$.

Table 8.6: The mean and 99% position uncertainty 3-σ values for the LiAISON-only simulations, where the crewed vehicle is in a 10,000 km L_2 halo orbit and the NavSat is in one of many halo orbits as indicated. The results are shown after each simulation has reached a nearly steady state.

NavSat	A_z	$\Delta\tau$	Crew Pos Uncertainty (3σ)		NavSat Pos Uncertainty (3σ)	
Location	(km)	(deg)	Mean (km)	99% (km)	Mean (km)	99% (km)
L_1	10,000	0	255.615 km	399.072 km	67.568 km	116.154 km
L_1	10,000	45	257.337 km	358.146 km	72.097 km	169.901 km
L_1	10,000	60	264.900 km	362.003 km	75.757 km	190.092 km
L_1	10,000	90	260.768 km	338.923 km	79.653 km	217.581 km
L_1	10,000	120	250.069 km	336.869 km	77.572 km	189.715 km
L_1	20,000	0	210.594 km	270.384 km	80.609 km	149.338 km
L_1	20,000	45	226.625 km	369.461 km	94.249 km	271.130 km
L_1	20,000	60	235.699 km	395.241 km	103.853 km	311.627 km
L_1	20,000	90	238.603 km	386.025 km	108.427 km	316.839 km
L_1	20,000	120	233.942 km	356.510 km	100.781 km	311.439 km
L_1	35,500	0	228.752 km	449.765 km	137.446 km	309.629 km
L_1	35,500	45	265.593 km	638.391 km	176.938 km	535.386 km
L_1	35,500	60	269.041 km	658.821 km	189.755 km	580.990 km
L_1	35,500	90	318.265 km	982.919 km	239.598 km	940.161 km
L_1	35,500	120	310.584 km	719.071 km	228.039 km	710.786 km
L_2	10,000	0	*LiAISON Ineffective: not enough separation*			
L_2	10,000	45	267.862 km	602.170 km	173.665 km	567.057 km
L_2	10,000	60	243.631 km	476.491 km	146.710 km	451.879 km
L_2	10,000	90	212.272 km	344.969 km	120.662 km	304.243 km
L_2	10,000	120	178.914 km	275.691 km	98.739 km	191.683 km
L_2	20,000	0	464.241 km	917.314 km	215.565 km	762.875 km
L_2	20,000	45	316.111 km	592.005 km	169.082 km	559.982 km
L_2	20,000	60	275.637 km	500.623 km	151.460 km	483.095 km
L_2	20,000	90	225.349 km	377.150 km	120.328 km	312.137 km
L_2	20,000	120	185.450 km	309.763 km	104.063 km	211.686 km
L_2	35,500	0	621.691 km	1235.625 km	168.394 km	544.832 km
L_2	35,500	45	471.928 km	1024.344 km	140.630 km	462.895 km
L_2	35,500	60	318.909 km	571.837 km	134.733 km	408.770 km
L_2	35,500	90	227.058 km	440.482 km	103.462 km	265.223 km
L_2	35,500	120	181.372 km	370.286 km	102.552 km	227.899 km

8.2.4 Ground and LiAISON support

Now that a comprehensive analysis of the trade space for ground only and LiAISON only navigation is complete, the combination both data types is examined. Previous analysis gives a general baseline of what to expect for each navigation scenario and the benefits that the scenario's configuration provides for navigation information. The scenarios analyzed in this section are baed on a combination of ground-based and space-based radiometric tracking. The navigation satellite is assumed to be constantly tracked by the DSN. This ensures that the navigation satellite's state is well-known and is behaving as a navigation asset to customers in the Earth-Moon system.

Tables 8.7 through 8.9 summarize results for several different scenario configurations with different tracking data types. The first scenario presented in Table 8.7 is for the situation in which the DSN is tracking only the navigation satellite and there is a LiAISON link between the crewed vehicle and the navigation satellite. The results show that both satellite navigation uncertainties have been reduced however the crewed vehicle uncertainty is still high when compared to the navigation satellite. This is due to the fact that the crewed vehicle is a noisy vehicle and the benefit of knowing exactly where the navigation satellite is does not improve the crewed vehicle position enough, indicating that the LiAISON measurement alone does not contain enough information to reduce the growing uncertainty due to FLAK.

When DSN measurements are added to the crewed vehicle, the position uncertainty is reduced significantly. Table 8.8 summarizes these results. The additional geometry of the ground tracking network combined with LiAISON provides a strong measurement type to reduce the uncertainty on both the crewed vehicle as well as the navigation satellite. These results are comparable to the previous analysis for ground only simulations with either DSN or the IDAC4B configuration. In general, position uncertainties for LiAISON with DSN for both satellites produces a position uncertainty for the crewed vehicle on the order of 2.5 km while the IDAC4B was 2.4 km and DSN only was 9.9 km.

The final configuration examined is that of the crewed vehicle being tracked by the IDAC4B

network while the navigation satellite is tracked by the DSN. Results for this configuration are presented in Table 8.9. There is a LiAISON radiometric link between the navigation satellite and crewed vehicle as well. With this configuration, the mean crewed vehicle position uncertainty is about 1 km or less in several scenarios. The addition of the 3-way tracking from the IDAC4B stations provides a slight geometrical benefit when included with LiAISON measurements. The 99% 3-sigma uncertainty has been reduced significantly from 7.7 km to less than 3 km for most scenarios presented in Table 8.9.

Table 8.7: The navigation performance for the configuration that includes continuous LiAISON tracking between the crew at L_2 and the NavSat, as well as continuous DSN tracking of the NavSat; there is no ground tracking of the crewed vehicle.

Ground	NavSat	A_z	$\Delta\tau$	Crew Pos Uncertainty (3σ)		NavSat Pos Uncertainty (3σ)	
Network	Location	(km)	(deg)	Mean (km)	99% (km)	Mean (km)	99% (km)
LiAISON+	L_1	10,000	0	234.303 km	397.279 km	0.195 km	0.314 km
LiAISON+	L_1	10,000	45	225.342 km	354.658 km	0.188 km	0.316 km
LiAISON+	L_1	10,000	60	226.422 km	357.727 km	0.192 km	0.316 km
LiAISON+	L_1	10,000	90	221.250 km	329.278 km	0.191 km	0.314 km
LiAISON+	L_1	10,000	120	215.562 km	332.095 km	0.193 km	0.317 km
LiAISON+	L_1	20,000	0	182.334 km	257.089 km	0.184 km	0.320 km
LiAISON+	L_1	20,000	45	177.488 km	222.001 km	0.170 km	0.308 km
LiAISON+	L_1	20,000	60	173.766 km	216.644 km	0.172 km	0.309 km
LiAISON+	L_1	20,000	90	175.952 km	205.117 km	0.173 km	0.309 km
LiAISON+	L_1	20,000	120	188.624 km	219.674 km	0.175 km	0.310 km
LiAISON+	L_1	35,500	0	149.344 km	185.203 km	0.186 km	0.379 km
LiAISON+	L_1	35,500	45	135.732 km	151.454 km	0.167 km	0.304 km
LiAISON+	L_1	35,500	60	129.514 km	145.643 km	0.167 km	0.306 km
LiAISON+	L_1	35,500	90	131.470 km	149.936 km	0.167 km	0.310 km
LiAISON+	L_1	35,500	120	143.060 km	161.803 km	0.170 km	0.310 km
LiAISON+	L_2	10,000	0	*LiAISON Ineffective: not enough separation*			
LiAISON+	L_2	10,000	45	146.893 km	320.652 km	0.306 km	0.407 km
LiAISON+	L_2	10,000	60	146.922 km	337.945 km	0.304 km	0.405 km
LiAISON+	L_2	10,000	90	140.042 km	319.765 km	0.290 km	0.400 km
LiAISON+	L_2	10,000	120	129.175 km	274.223 km	0.278 km	0.386 km
LiAISON+	L_2	20,000	0	328.945 km	537.197 km	0.291 km	0.399 km
LiAISON+	L_2	20,000	45	201.478 km	444.084 km	0.298 km	0.411 km
LiAISON+	L_2	20,000	60	176.111 km	425.506 km	0.295 km	0.411 km
LiAISON+	L_2	20,000	90	157.224 km	375.961 km	0.277 km	0.404 km
LiAISON+	L_2	20,000	120	135.738 km	308.594 km	0.263 km	0.395 km
LiAISON+	L_2	35,500	0	496.337 km	927.115 km	0.284 km	0.406 km
LiAISON+	L_2	35,500	45	394.555 km	1022.961 km	0.292 km	0.417 km
LiAISON+	L_2	35,500	60	243.265 km	570.872 km	0.286 km	0.414 km
LiAISON+	L_2	35,500	90	182.272 km	439.300 km	0.267 km	0.406 km
LiAISON+	L_2	35,500	120	142.889 km	369.877 km	0.253 km	0.402 km

Table 8.8: The navigation performance for the configuration that includes continuous LiAISON tracking between the crew at L_2 and the NavSat, as well as continuous DSN tracking of both vehicles.

Ground	NavSat	A_z	$\Delta\tau$	Crew Pos Uncertainty (3σ)		NavSat Pos Uncertainty (3σ)	
Network	Location	(km)	(deg)	Mean (km)	99% (km)	Mean (km)	99% (km)
DSN	None	-	-	9.879 km	18.606 km	-	-
DSN	L_1	10,000	0	2.561 km	7.978 km	0.183 km	0.301 km
DSN	L_1	10,000	45	2.612 km	8.025 km	0.178 km	0.281 km
DSN	L_1	10,000	60	2.654 km	8.157 km	0.182 km	0.282 km
DSN	L_1	10,000	90	2.686 km	8.335 km	0.183 km	0.290 km
DSN	L_1	10,000	120	2.717 km	8.574 km	0.186 km	0.295 km
DSN	L_1	20,000	0	2.333 km	7.604 km	0.173 km	0.304 km
DSN	L_1	20,000	45	2.569 km	7.773 km	0.162 km	0.273 km
DSN	L_1	20,000	60	2.590 km	7.784 km	0.164 km	0.276 km
DSN	L_1	20,000	90	2.670 km	7.990 km	0.165 km	0.284 km
DSN	L_1	20,000	120	2.815 km	10.869 km	0.169 km	0.289 km
DSN	L_1	35,500	0	2.386 km	7.812 km	0.178 km	0.371 km
DSN	L_1	35,500	45	2.553 km	7.779 km	0.159 km	0.271 km
DSN	L_1	35,500	60	2.577 km	7.723 km	0.160 km	0.275 km
DSN	L_1	35,500	90	2.590 km	7.779 km	0.160 km	0.285 km
DSN	L_1	35,500	120	2.635 km	8.071 km	0.163 km	0.289 km
DSN	L_2	10,000	0	*LiAISON Ineffective: not enough separation*			
DSN	L_2	10,000	45	2.715 km	8.289 km	0.291 km	0.396 km
DSN	L_2	10,000	60	2.741 km	8.351 km	0.290 km	0.391 km
DSN	L_2	10,000	90	2.721 km	8.497 km	0.279 km	0.391 km
DSN	L_2	10,000	120	2.834 km	8.546 km	0.269 km	0.384 km
DSN	L_2	20,000	0	2.650 km	7.637 km	0.264 km	0.374 km
DSN	L_2	20,000	45	2.586 km	7.471 km	0.281 km	0.408 km
DSN	L_2	20,000	60	2.600 km	7.843 km	0.280 km	0.406 km
DSN	L_2	20,000	90	2.672 km	7.932 km	0.266 km	0.391 km
DSN	L_2	20,000	120	2.643 km	8.085 km	0.256 km	0.391 km
DSN	L_2	35,500	0	2.649 km	7.751 km	0.260 km	0.382 km
DSN	L_2	35,500	45	2.556 km	7.321 km	0.278 km	0.406 km
DSN	L_2	35,500	60	2.534 km	7.420 km	0.271 km	0.409 km
DSN	L_2	35,500	90	2.632 km	7.713 km	0.253 km	0.395 km
DSN	L_2	35,500	120	2.598 km	7.914 km	0.245 km	0.391 km

Table 8.9: The navigation performance for the configuration that includes continuous LiAISON tracking between the crew at L_2 and the NavSat, as well as continuous ground tracking of both vehicles: DSN for the NavSat and IDAC4B for the crewed vehicle.

Ground	NavSat	A_z	$\Delta\tau$	Crew Pos Uncertainty (3σ)		NavSat Pos Uncertainty (3σ)	
Network	Location	(km)	(deg)	Mean (km)	99% (km)	Mean (km)	99% (km)
IDAC4B	None	-	-	2.449 km	7.695 km	-	-
IDAC4B	L_1	10,000	0	0.971 km	3.852 km	0.167 km	0.279 km
IDAC4B	L_1	10,000	45	0.944 km	3.192 km	0.166 km	0.248 km
IDAC4B	L_1	10,000	60	0.929 km	2.955 km	0.169 km	0.248 km
IDAC4B	L_1	10,000	90	1.007 km	5.018 km	0.168 km	0.272 km
IDAC4B	L_1	10,000	120	0.945 km	2.935 km	0.170 km	0.288 km
IDAC4B	L_1	20,000	0	0.989 km	3.279 km	0.159 km	0.266 km
IDAC4B	L_1	20,000	45	0.979 km	3.569 km	0.152 km	0.246 km
IDAC4B	L_1	20,000	60	0.956 km	3.272 km	0.154 km	0.238 km
IDAC4B	L_1	20,000	90	1.017 km	5.048 km	0.154 km	0.259 km
IDAC4B	L_1	20,000	120	1.142 km	6.124 km	0.156 km	0.280 km
IDAC4B	L_1	35,500	0	1.066 km	3.991 km	0.163 km	0.316 km
IDAC4B	L_1	35,500	45	1.055 km	4.599 km	0.150 km	0.257 km
IDAC4B	L_1	35,500	60	1.008 km	3.654 km	0.151 km	0.237 km
IDAC4B	L_1	35,500	90	1.041 km	5.185 km	0.150 km	0.257 km
IDAC4B	L_1	35,500	120	1.003 km	3.567 km	0.150 km	0.271 km
IDAC4B	L_2	10,000	0	*LiAISON Ineffective: not enough separation*			
IDAC4B	L_2	10,000	45	0.944 km	3.306 km	0.272 km	0.370 km
IDAC4B	L_2	10,000	60	0.919 km	2.933 km	0.273 km	0.377 km
IDAC4B	L_2	10,000	90	0.978 km	4.688 km	0.263 km	0.382 km
IDAC4B	L_2	10,000	120	0.902 km	2.802 km	0.257 km	0.380 km
IDAC4B	L_2	20,000	0	1.212 km	4.327 km	0.234 km	0.330 km
IDAC4B	L_2	20,000	45	0.962 km	3.284 km	0.259 km	0.393 km
IDAC4B	L_2	20,000	60	0.968 km	4.003 km	0.257 km	0.394 km
IDAC4B	L_2	20,000	90	0.959 km	4.181 km	0.245 km	0.367 km
IDAC4B	L_2	20,000	120	0.904 km	2.824 km	0.243 km	0.378 km
IDAC4B	L_2	35,500	0	1.201 km	4.193 km	0.232 km	0.336 km
IDAC4B	L_2	35,500	45	1.021 km	2.992 km	0.251 km	0.367 km
IDAC4B	L_2	35,500	60	1.029 km	4.684 km	0.247 km	0.392 km
IDAC4B	L_2	35,500	90	0.941 km	3.405 km	0.231 km	0.357 km
IDAC4B	L_2	35,500	120	0.908 km	2.854 km	0.230 km	0.369 km

8.2.5 Trade Study

Table 8.10 summarizes the significant findings in the work presented in this section for all of the scenarios discussed. The table gives information on the configuration used, the best mean 3-sigma position uncertainty and the worst-case 99% position 3-sigma uncertainty. One significant finding is that navigating a crewed vehicle undergoing FLAK on an unstable trajectory such as a lunary L_2 halo orbit requires careful navigation planning. This study has demonstrated that LiAISON alone is not sufficient to navigate a noisy spacecraft in this environment under the timeframe considered. It is not capable of achieving meter or even kilometer level of uncertainty. Table 8.10 indicates that LiAISON only with the assumed FLAK model is only capable of achieving position uncertainties on the order of 180 km for the best case and 1,000 km for the worst case scenarios.

Ground only tracking is capable of achieving navigation 3-sigma position uncertainties on the order of 2.4 to 18.5 km. In order to achieve sub km position uncertainty on the crewed vehicle, tracking data must be supplemented with LiAISON. IDAC4B provides the best position uncertainties for both ground only as well as begin supplemented with LiAISON.

Table 8.10 also shows that the IDAC4B-only configuration provides a position uncertainty comparable to the configuration of LiAISON+DSN when the DSN is tracking the crewed vehicle. The navigation satellite alone provides the same geometrical and measurement information as 3 receive only 3-way ground tracking stations specified by the IDAC4B configuration. It is only possible to reach sub km position uncertainty through an architecture that has the IDAC4B configuration supplemented with LiAISON measurements.

Table 8.10: Summary of the approximate position uncertainty levels observed in several different navigation configurations. FLAK and station keeping maneuvers are included.

Scenario	LiAISON Tracking	DSN Tracking		IDAC4B Crew	Expected Position Uncertainty Range (3σ)	
		NavSat	Crew		Crew	NavSat
DSN-only, NavSat	-	Yes	-	-	-	0.17 – 0.42 km
DSN-only, Crew	-	-	Yes	-	9.8 – 18.5 km	-
IDAC4B-only, Crew	-	-	-	Yes	2.4 – 7.7 km	-
LiAISON-only	Yes	-	-	-	180 – 1000 km	70 – 600 km
LiAISON+DSN	Yes	Yes	-	-	140 – 600 km	0.16 – 0.41 km
LiAISON+DSN	Yes	Yes	Yes	-	2.4 – 10.8 km	0.16 – 0.41 km
LiAISON+IDAC4B	Yes	Yes	Yes	Yes	0.9 – 5.1 km	0.15 – 0.39 km

Chapter 9

LiAISON Supporting Low Lunar Orbit

Previous chapters have shown the benefits of having a navigation satellite near the Moon in an LPO at either the Earth-Moon L_1 or L_2 points. This navigation satellite can assist in the navigation of a crewed vehicle traversing this regime. Each of these studies, so far, have shown that LiAISON provides an excellent additional data source to supplement the DSN resulting in precise navigation while reducing the reliance on ground based data types.

Recently, NASA has been considering various mission concepts for the future of lunar exploration. One of those concepts is to fly an Apollo-like mission with humans into low lunar orbit. The previous chapter explored a second concept to send humans on a cruise past the moon and enter into an LPO at the Earth-Moon L_2 point. These options are considered to be a stepping stone to Mars exploration.

Each of these mission concepts require precise navigation in order to perform accurate lunar flybys, maneuvers, and rendezvous throughout the mission sequence. These tight navigation requirements are strained by the fact that a crewed vehicle is typically very noisy. Previous chapters have quantified the sources and strength of these perturbations expected to be generated during a crewed mission. The Apollo ground network compensated for these perturbations through the addition of multiple ground stations. In addition, Constellation proposed the previously introduced IDAC4B six station configuration to reduce navigation uncertainties to acceptable levels for crewed missions.

The work outlined in this chapter examines the benefits of supplementing ground tracking

of a crewed vehicle in low lunar orbit with a LiAISON measurement type for a navigation satellite in either an L_1 or L_2 LPO. The proposed navigation architecture is illustrated in Figure 9.1. The concepts outlined in this chapter will examine the ability for LiAISON to supplement ground tracking and the benefits when compared to a six station configuration.

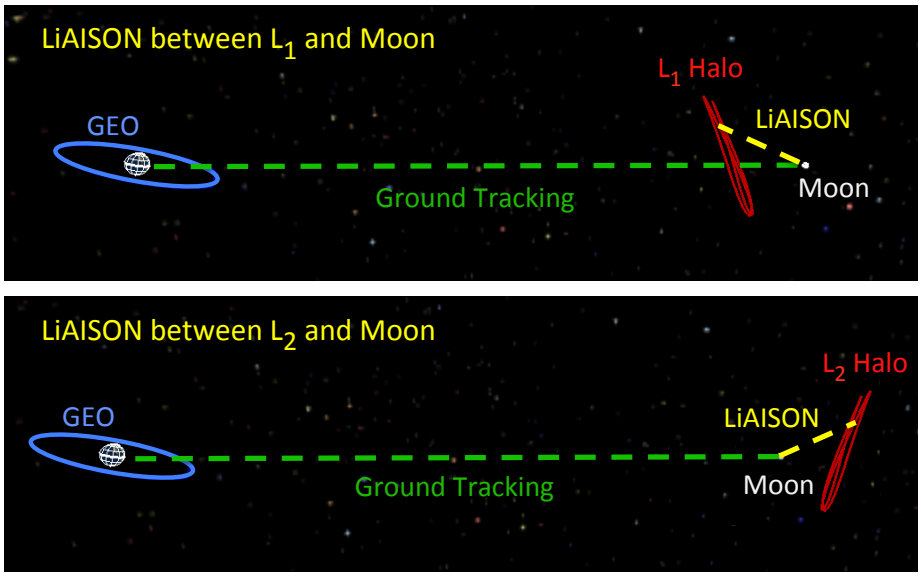

Figure 9.1: The scenarios studied in this paper include a crewed spacecraft in low lunar orbit being tracked by the DSN from the Earth and from a navigation satellite located in orbit about the Earth-Moon L_1 (top) or L_2 (bottom) libration points.

9.1 Mission Concept

The mission outlined in this chapter is where a single crewed vehicle is in orbit about the Moon being tracked by a navigation satellite located in a LPO and ground tracking form the DSN or IDAC4B six station configuration. The SST measurements come from the navigation satellite that may be located at either the Earth-Moon L_1 or L_2 point. The navigation satellite may be tracked by the DSN but it is not necessary. All of these configurations will be considered in the following sections. An outline of the Orbits used and tracking data types used are outlined next.

9.1.1 Orbits

The mission concept for a crewed vehicle in the Earth-Moon regime has a primary interest in the lunar poles and possible landing of a spacecraft or rover near the poles. The crewed spacecraft for this work is located in a 100 km altitude circular orbit with a 90 degree inclination. The longitude of the ascending node is 30 degrees in the Moon oriented coordinate system. The epoch of the trajectories in this study being on January 1, 2020 at 00:00:00 TDB (barycentric dynamical time). The coordinate from of the moon is given by the IAU and in general has it's z-axis aligned with the spin axis.

The Earth-Moon libration orbiter is placed in a halo orbit about the L_1 or L_2 points. A series of halo orbits are examined for each of these Lagrange points. Both orbits have their advantages and disadvantages. The L_1 halo orbiter has been shown to be beneficial for the support of navigating a crewed vehicle during a trans-lunar cruise. The L_2 halo orbiter allows for tracking to occur for assets on the dark side of the Moon. Figure 9.2 illustrates the L_2 halo orbiters geometry relative to tracking an asset at the Moon. The L_1 halo orbiter has a similar geometry but resides on the near side of the Moon relative to Earth. Both orbiters in the study have a z-axis amplitude of 35,500 km with an initial phase angle of zero degrees for the orbit.

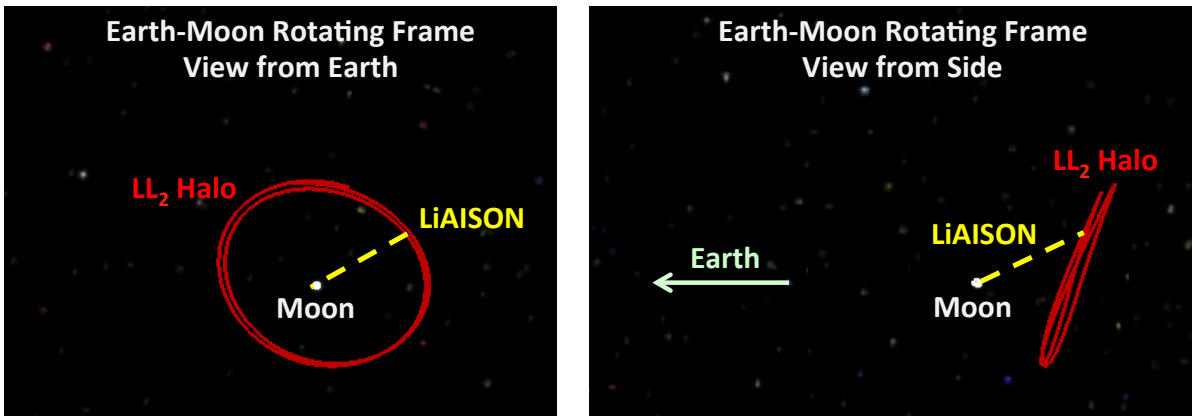

Figure 9.2: LiAISON Configuration.

9.1.2 Tracking Data

The measurements used to model the DSN and SST links are that of the geometric range and range-rate equations introduced in Chapter 3. Each of these measurement types have several sources of errors and noise for each link which can include but are not limited to atmospheric influences for ground based measurements, clock errors, charge particle effects on the signal path, etc. This study simplifies these errors into a systematic bias that occurs for every pass as well as a random white-noise. The bias value is determined by a zero mean Gaussian distribution with a standard deviation given in Table 9.1. The DSN is assumed to be a two-way radiometric link while IDAC4B uses a three-way link for the non-DSN stations. Table 9.1 describes the errors associated with each link and their noise values.

Table 9.1: The parameters used to define the errors in the tracking data. The bias added to each link and the white noise added to each observation are drawn from Gaussian distributions with zero mean and the given standard deviations. The L_1 and L_2 orbiters have the same tracking data characteristics, indicated by **LPO**.

Tracking Link	Bias 1-σ	White Noise 1-σ	Comments
LPO - LLO 2-way range	3 m	1 m	LiAISON range SST
LPO - LLO 2-way range-rate	1 mm/s	1 mm/s	LiAISON range-rate SST
DSN - LPO 2-way range	30 m	10 m	DSN ground tracking of the halo
DSN - LPO 2-way range-rate	1 mm/s	0.5 mm/s	orbiter
DSN - LLO 2-way range	30 m	10 m	DSN ground tracking of the crewed
DSN - LLO 2-way range-rate	1 mm/s	0.5 mm/s	vehicle
IDAC4B - LLO 3-way range	30 m	10 m	IDAC4B ground tracking of the
IDAC4B - LLO 3-way range-rate	1 mm/s	0.5 mm/s	crewed vehicle

As the LLO spacecraft is a crewed vehicle, it is desired to tracking it continuously or as often as possible. The assumption made in this work is that the crewed spacecraft will be tracked by the DSN continuously in a 2-way sense. The IDAC4B will have 3-way receive only tracking data when they are in view of the DSN signals. LiAISON tracking between the LLO crewed vehicle and the navigation spacecraft in a LPO will be tracked continuously except for periods when the Moon is occulting the spacecraft. Figure 9.3 illustrates this tracking schedule for the crewed vehicle in LLO

with a navigation satellite in orbit about the Earth-Moon L_1 point. The timeline for a navigation satellite in orbit about the L_2 point is very similar. Not every scenario in this work will use all of the measurements at the same time, however, each scenario will use a subset if not all of these measurements in this timeline. It is assumed that the DSN is capable of tracking both spacecraft at any given time and that the IDAC4B configuration can only assist in tracking the crewed vehicle in LLO. Figure 9.4 illustrates a compressed timeline to show the similarities and differences between the L_1 and L_2 configurations.

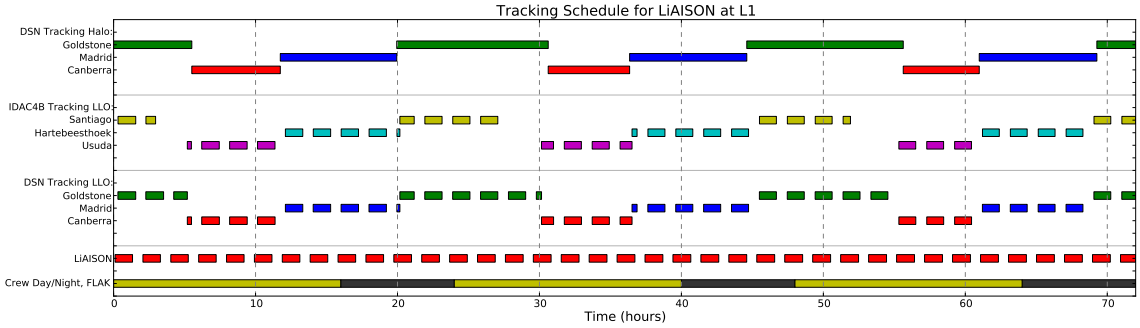

Figure 9.3: An illustration of the schedule of tracking observations for the case of an L_1 halo orbiter. Not all observations are used in all scenarios.

9.2 Simulations

Similar to the previous work, the dynamical models used in this simulation are that of gravity due to the Earth, Moon, Sun, and the rest of the planets given by their values and positions in the JPL DE405 ephemerides. The lunar gravity includes non-spherical terms from the LP150q gravity field for degree and order 20. Each vehicle has an area-to-mass ratio of 0.01 and is under the influence of SRP unless in the Moon's shadow. SRP is modeled as a flat-plate with a C_R value of 1.0 for both vehicles. The FLAK models previously derived are used to model the crew's activity over the course of the mission for the LLO spacecraft only.

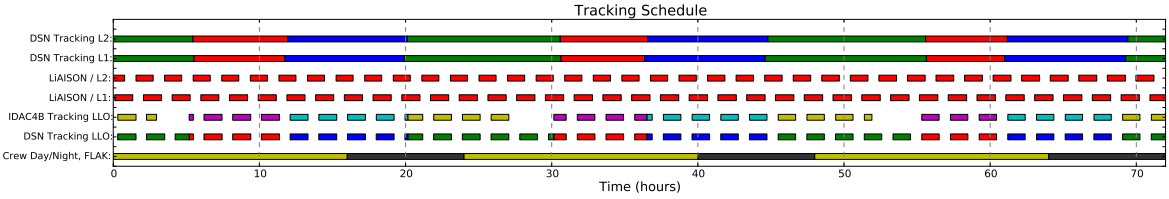

Figure 9.4: A compressed timeline, illustrating when each tracking option is in view.

9.2.1 LiAISON Only

The first simulation in this trade study validates two primary assumptions of this work. The first being that a small *a priori* covariance can be assumed for the navigation satellite in a lunar libration orbit. The second being that LiAISON alone does achieve a reasonable navigation uncertainty without any ground tracking. This scenario simulates the navigation of both the crewed LLO and LPO navigation satellite with large *a priori* covariances which have been set to 100,000 km in position (1-sigma) and 1,000 km/sec (1-sigma) for both spacecraft. Figure 9.5 shows the time history of the position uncertainties for both spacecraft over the course of the simulation timeframe. It also illustrates how the position uncertainty of the LLO reaches steady-state after 2-3 days of LiAISON measurement processing. However, the halo orbiter has not yet reached a steady-state value after 12 days of measurement processing, but it does reach reasonable navigation uncertainties after a week.

An interesting feature of Figure 9.5 is the influence of FLAK over the course of the simulation on the crewed vehicle. During periods of occultation by the Moon, the crewed vehicles uncertainty raises significantly. During constant periods of LiAISON tracking around day 7.5 to 9 one can see the natural variation in the covariance due to the geometry of the problem. A subtle feature is that the navigation uncertainty on the LLO varies due to the procession of the lunar orbiters plane. Around day 8, the plane of the LLO is nearly perpendicular to the halo orbiter, thus less information is gathered in the out of plane directions and the uncertainty rises.

This simulation demonstrates the usefulness of LiAISON as the only measurement type.

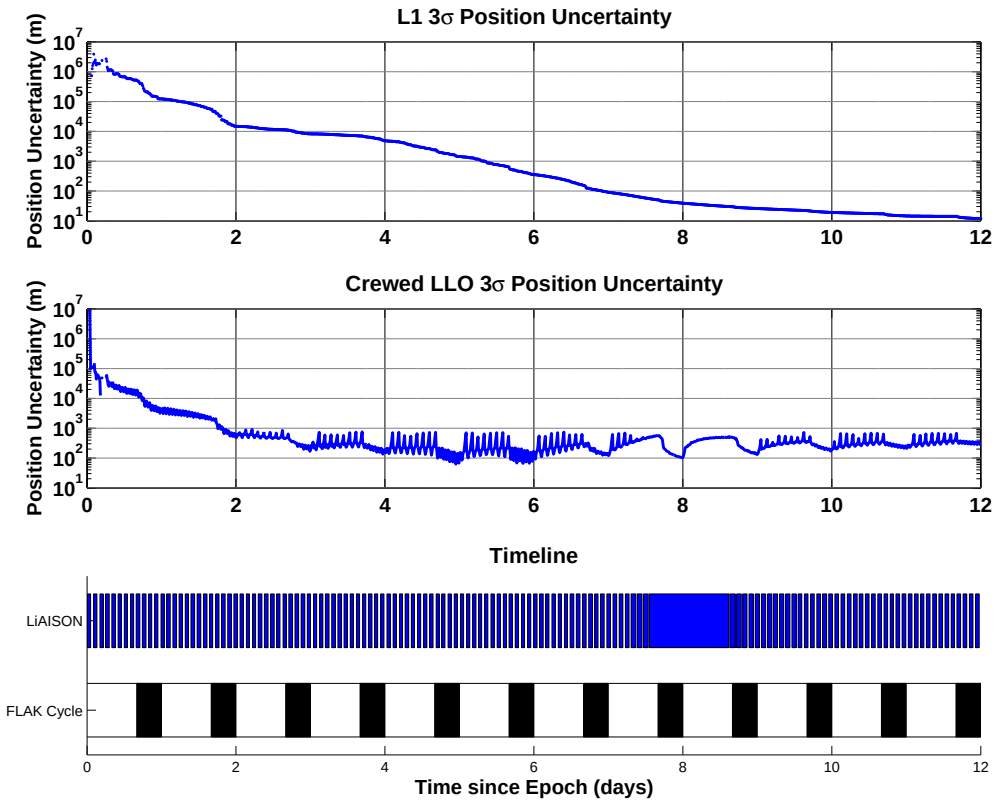

Figure 9.5: The position 3σ uncertainty of the halo orbiter (top) and the crewed lunar orbiter (middle) while processing LiAISON-only observation data using very large *a priori* covariances. The FLAK time profile and availability of LiAISON data is shown at the bottom.

LiAISON alone achieves acceptable levels of uncertainty for both the navigation satellite in a LPO as well as the crewed vehicle in orbit about the moon. This also gives an indication the it is acceptable to choose a smaller *a priori* covariance for the navigation satellite in a LPO. It is a reasonable assumption that prior to this configuration, the navigation satellite as well as the crewed vehicle will be tracked by the DSN thus reducing their *a prior* uncertainty.

9.2.2 Ground Only

It is necessary to determine what the baseline navigation uncertainty is for the currently implementable configuration of the DSN only. This simulation determines the steady-state uncertainties of both spacecraft as if they were tracked by the DSN and no other method. The same

initial large *a priori* covariances of the previous simulation are used for both vehicles again. This is to determine how well each data type is at lower the uncertainty and to what levels are achievable. Using DSN measurements, both satellites reach a steady-state uncertainty quicker than LiAISON only. Figure 9.6 shows the position uncertainty over the course of the simulation for both spacecraft. During the period between day 8 and 12, the LLO is precessing such that it is face-on to the Earth. This limits the information content in the measurements and thus increases the uncertainty for certain periods of its orbit.

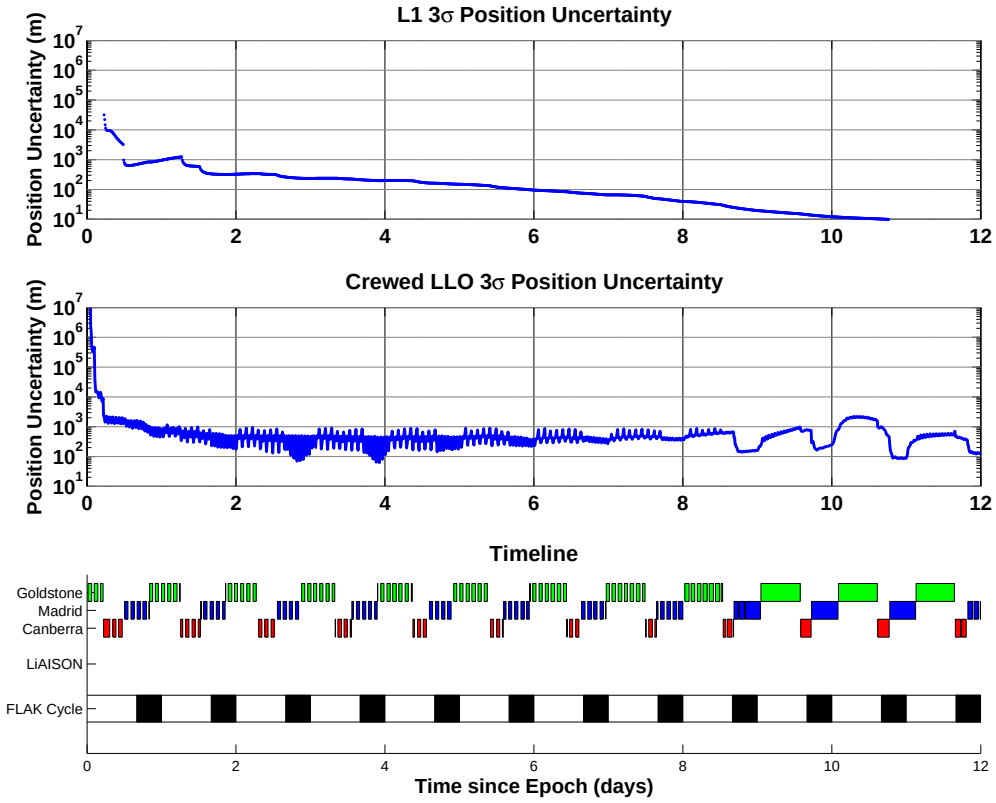

Figure 9.6: The position 3σ uncertainty of the halo orbiter (top) and the crewed lunar orbiter (middle) while processing ground-only observation data from the three DSN sites using very large *a priori* covariances. The FLAK time profile and availability of DSN tracking data is shown at the bottom.

9.2.3 DSN with LiAISON

The previous two sections have show what the achievable steady-state uncertainties are for both configurations. The remainder of the work in this section will use uncertainties of 100 m in position and 1 m/s in velocity for the navigation satellite in a LPO and 10 km in position and 10 m/s in velocity for the crewed vehicle in LLO. The simulation presented in this section covers a brief trade study between a navigation satellite at L_1 versus it being at L_2. In addition, this simulation will use LiAISON and DSN coverage in conjunction.

A brief discussion on the benefits of one geometry versus the other is necessary. Both halo orbits at L_1 and L_2 offer similar geometrical advantages when compared to ground tracking. However, a navigation satellite at L_2 has a significant benefit of one being place at L_1 since it can augment ground tracking when it is being occulted. This allows for continuous tracking of a crewed vehicle at the Moon and thus provides for a more steady navigation performance when compared to its counterpart at L_1. Figure 9.7 illustrates this conclusion for a short period of LiAISON and DSN tracking to compare both L_1 and L_2.

Table 9.2 provides a summary of the navigation performance for the L_1 versus L_2 configura-

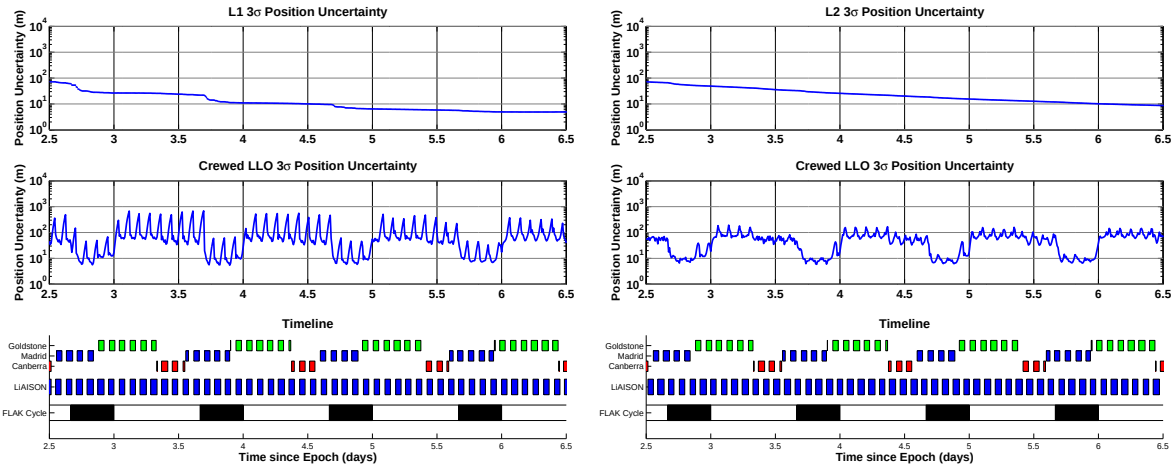

Figure 9.7: The position 3σ uncertainty of the halo orbiter (top) and the crewed lunar orbiter (middle) while processing DSN and L_1 (left) / L_2 (right) LiAISON tracking data.

tions. The table gives three measures of the navigation performance: First is the 3-sigma mean of the position uncertainty; Second is the 99th percentile 3-sigma position uncertainty; and Third is the maximum 3-sigma position uncertainty. The statistics given are generated from data between 3 to 7 days since the epoch of the simulation. It is clear that the navigation satellite at L_2 performs better than the navigation satellite at L_1. It is also clear that the navigation is more consistent for the L_2 spacecraft since the 99th and maximum position uncertainties are reduced significantly when compared to the reduction in the mean uncertainty.

Table 9.2: The 3σ position uncertainties observed in a system that includes the crewed low lunar orbiter and a lunar libration orbiter, being tracked by the three DSN stations and LiAISON.

LiAISON with L_1			
Vehicle	Mean 3σ uncertainty	99% 3σ uncertainty	Max 3σ uncertainty
L_1 Halo	10.3 meters	26.5 meters	26.5 meters
Crewed LLO	92.6 meters	540.9 meters	687.1 meters
LiAISON with L_2			
Vehicle	Mean 3σ uncertainty	99% 3σ uncertainty	Max 3σ uncertainty
L_2 Halo	19.5 meters	47.7 meters	48.6 meters
Crewed LLO	53.7 meters	158.5 meters	192.1 meters

9.3 L1 vs L2 NavSat Trade

The previous sections gave an indication as to the navigation ability of the DSN and LiAISON measurements. While there are an extensive amount of configurations that can be examined, this section attempts to give a survey of some of the main architectures that could contribute to reducing the navigation uncertainties on the crewed vehicle in LLO. This study will compare LiAISON supplemented navigation with traditional ground tracking techniques for both configurations where the navigation satellite is at L_1 or L_2. In addition, a comparison is done to determine the benefits of tracking the navigation satellite with ground tracking and a trade study as to which measurement type or configuration is beneficial.

Each of the following architectures have been simulated for 12 days allowing for each satellite's uncertainty to reach steady-state values and to allow for geometrical variations in both the LLO

and the halo orbiter. The navigation metrics given are computed between days 3 to 12 of the simulation. The 99th percentile of the position uncertainty captures information on the trends and extrema observed in the architecture and is not as sensitive as the maximum uncertainty values. The means give a general indication as to the steady-state performance of the architecture.

The architectures examined in Figure 9.8 are LiAISON-only, LiAISON with DSN for the LLO, DSN only, IDAC4B only, LiAISON plus DSN coverage for both spacecraft, and LiAISON with IDAC4B coverage for the crewed vehicle. Figure 9.8 gives the mean values (bar) and 99th percentile (error bar) for both configurations of the navigation satellite being at L_1 and L_2.

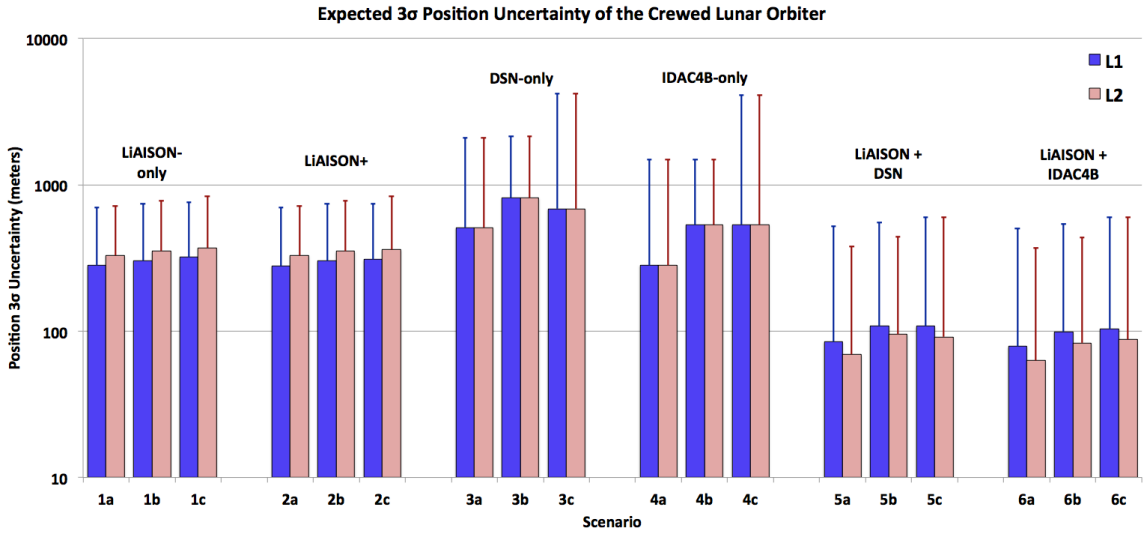

Figure 9.8: The 3σ position uncertainty of the crewed lunar orbiter for a variety of scenarios. The main shaded bars illustrate the mean 3σ position uncertainties over time for each scenario and the thin error bar extensions on top illustrate the 99th percentile of the 3σ position uncertainties over time. The scenarios are defined in Table 9.3.

Table 9.3 provides a survey of the architectures examined in this study. Portions of this survey are shown in Figure 9.8, however, Table 9.3 provides a detailed format of the different scenarios surveyed. Specifically, comparisons of tracking data type is of importance in several scenarios. Each case where both range and range-rate data are processed produce better navigation performance. However, LiAISON-only scenarios perform better with ranging data only compared to range-rate data only. Other scenarios, such as DSN-only, provide better performance with range-rate only data when compared to range only data.

Continuous LiAISON-only tracking performs at roughly the same navigation accuracy as IDAC4B and slightly better than DSN-only. Combining LiAISON tracking data with ground tracking data only improves the navigation as seen in Figure 9.8 and Table 9.3. If DSN does need to be supplemented, this work shows that the addition of a LiAISON data type outperforms the inclusion of 3 additional ground tracking sites.

Table 9.3: Survey of LLO scenarios, including their definitions and resulting performance.

Scenario	Halo Orbit	LiAISON included	Halo Tracked by DSN	Crew Tracked by DSN	Crew Tracked by IDAC4B	Range Data	Range-Rate Data	3σ Pos Uncertainty of LLO (m) Mean	99%	Max
1a-1	L_1	1	0	0	0	1	1	281.6	698.5	742.7
1a-2	L_2	1	0	0	0	1	1	329.5	712.7	832.9
1b-1	L_1	1	0	0	0	1	0	303.9	744.2	787.1
1b-2	L_2	1	0	0	0	1	0	353.7	776.4	844.0
1c-1	L_1	1	0	0	0	0	1	319.6	757.3	897.6
1c-2	L_2	1	0	0	0	0	1	371.5	831.4	979.8
2a-1	L_1	1	1	0	0	1	1	279.9	696.8	741.3
2a-2	L_2	1	1	0	0	1	1	328.5	712.4	832.5
2b-1	L_1	1	1	0	0	1	0	301.3	743.9	786.5
2b-2	L_2	1	1	0	0	1	0	351.8	774.4	842.7
2c-1	L_1	1	1	0	0	0	1	310.0	745.4	895.9
2c-2	L_2	1	1	0	0	0	1	361.0	831.0	979.4
3a-1	L_1	0	0	1	0	1	1	511.4	2087.9	2223.3
3a-2	L_2	0	0	1	0	1	1	511.4	2087.9	2223.3
3b-1	L_1	0	0	1	0	1	0	812.1	2156.0	2276.4
3b-2	L_2	0	0	1	0	1	0	812.1	2156.0	2276.4
3c-1	L_1	0	0	1	0	0	1	687.2	4209.0	6528.5
3c-2	L_2	0	0	1	0	0	1	687.2	4209.0	6528.5
4a-1	L_1	0	0	1	1	1	1	282.7	1494.4	1653.4
4a-2	L_2	0	0	1	1	1	1	282.7	1494.4	1653.4
4b-1	L_1	0	0	1	1	1	0	532.2	1495.0	1653.8
4b-2	L_2	0	0	1	1	1	0	532.2	1495.0	1653.8
4c-1	L_1	0	0	1	1	0	1	535.9	4116.6	6180.8
4c-2	L_2	0	0	1	1	0	1	535.9	4116.6	6180.8
5a-1	L_1	1	1	1	0	1	1	84.7	518.5	687.1
5a-2	L_2	1	1	1	0	1	1	69.4	379.4	636.8
5b-1	L_1	1	1	1	0	1	0	109.0	553.8	716.1
5b-2	L_2	1	1	1	0	1	0	94.9	442.1	641.8
5c-1	L_1	1	1	1	0	0	1	108.4	602.4	855.7
5c-2	L_2	1	1	1	0	0	1	91.5	603.7	723.4
6a-1	L_1	1	1	1	1	1	1	78.7	501.0	650.7
6a-2	L_2	1	1	1	1	1	1	63.0	372.1	601.7
6b-1	L_1	1	1	1	1	1	0	99.2	541.9	710.9
6b-2	L_2	1	1	1	1	1	0	83.2	435.9	606.5
6c-1	L_1	1	1	1	1	0	1	104.0	602.3	855.7
6c-2	L_2	1	1	1	1	0	1	87.7	603.7	723.4

9.4 Variations in FLAK Level

The assumption thus far is that the FLAK level chosen in this work is constant throughout the mission timeframe and that the level chosen represents the actual characteristics of the spacecraft. This assumption may be invalid depending on the type of spacecraft being flow since the FLAK level was derived from experiences during the Apollo era. It is thus necessary to investigate the effect that the FLAK level has on the navigation performance. Figure 9.9 illustrates how the variation in FLAK level influences the navigation performance. The figure represents the navigation performance behavior for Scenario 5a-1 (LiAISON and DSN tracking both vehicles) and their 3-sigma position uncertainties and their corresponding 99th percentile. FLAK levels are varied between $10 - 150\%$ of the nominal value. Within this regime, the effect that FLAK has on the position uncertainty is fairly linear, meaning that an increase in FLAK by a certain factor will also scale the position uncertainty by that factor. This is useful since the exact FLAK level is not perfectly known.

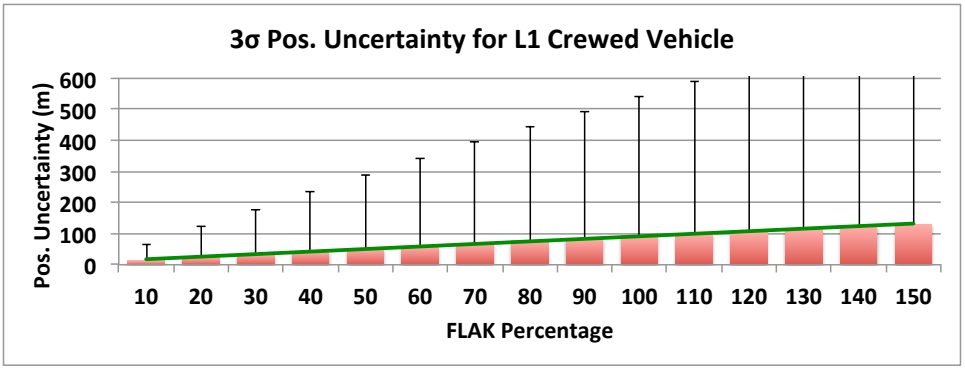

Figure 9.9: The effect of changing the level of FLAK in the simulation.

9.5 Conclusions

The benefit of navigating a crewed vehicle in LLO with a navigation satellite in an Earth-Moon libration point orbit and ground tracking data was analyzed. A trade space analysis was conducted in which the navigation satellite location as well as tracking data types were varied.

Tracking data consisted of DSN, IDAC4B, and LiAISON measurements with range and range-rate measurements. The crewed behavior is assumed to impart a 500 meter position uncertainty increase over the course of an hour due to unknown accelerations, known as FLAK.

The results presented in this section demonstrate that LiAISON alone can provide enough navigation information to track both the crewed vehicle and navigation satellite to a few hundred meters. The mean 3-sigma position uncertainty for a crewed vehicle in LLO being tracked by the DSN is approximately 500-800 meters. The inclusion of the IDAC4B ground station configuration reduces this position uncertainty to approximately 280-530 meters 3-sigma. If LiAISON tracking data is included with the DSN tracking data, then the position uncertainty is reduced to 85-109 meters 3-sigma. Finally, if the IDAC4B configuration is used in conjunction with LiAISON tracking, the crewed vehicle position uncertainty is reduced to 63-104 meters 3-sigma. A navigation satellite in a lunar halo orbit provides significant information and navigation benefits to a crewed vehicle in LLO, whether as a stand-alone tracking data source, or a supplement to current and future ground station tracking networks.

Chapter 10

LiAISON Supporting Trans-lunar Cruise

This chapter examines a LiAISON constellation with an EML-1 halo satellite and a crewed spacecraft during a trans-lunar cruise to the Moon. This is an initial study into the benefits of adding LiAISON measurements to the DSN and IDAC4B for crewed navigation. Simplifying assumptions are made to the strength and characteristics of FLAK to assess the improvement in OD by adding LiAISON.

A LiAISON constellation configuration involving two satellites, one in a halo orbit about EML-1 and one in geosynchronous Earth orbit, was analyzed in the previous chapter. References [120] and [85] demonstrated that the relative and absolute navigation of two satellites at GEO and EML-1 is possible through the use of satellite-to-satellite range and range-rate measurements. In addition, this measurement type can supplement and significantly improve radiometric measurements taken from the DSN for satellite navigation.

This chapter examines various navigation architectures, including ground-based and LiAISON-supplemented configurations, for a crewed mission to the Moon. A crewed trans-lunar cruise (TLC) mission is designed with a navigation satellite located at EML-1. Both ground-based tracking and LiAISON tracking support the crewed mission. An acceleration uncertainty model is developed based on Apollo era uncertainties to reflect a noisy crewed vehicle. Several tracking architectures are then compared. Finally, the sensitivity of navigation uncertainty due to the strength of the acceleration uncertainty is determined.

10.1 Mission Design

The reference mission designed for this study involves two spacecraft: one is a navigation satellite in a halo orbit about EML-1 and the other is a crewed spacecraft on a TLC. Figure 10.1 illustrates the tracking network used in this study that helps support a crewed spacecraft traveling form the Earth to the Moon that includes ground observations from the DSN as well as SST measurements obtained from a LiAISON navigation satellite near EML-1.

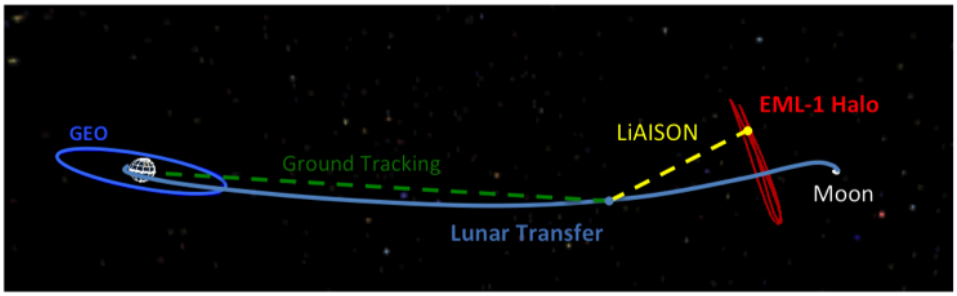

Figure 10.1: LiAISON constellation for an EML-1 navigation satellite and a crewed spacecraft on TLC. The plots are visualized in the Earth-Moon rotating frame.

There are several potential benefits of this LiAISON configuration. First, the EML-1 navigation satellite would have near-continuous communication with the spacecraft in TLC. The variation in geometry of the EML-1 navigation satellite and the TLC spacecraft provides significant information for tracking when compared to ground tracking. This variation in geometry allows for more information in the radial, in-track, and cross-track directions when compared to conventional DSN radiometric data.

10.1.1 Lunar L1 Halo Orbit

This work assumes that there is already a dedicated navigation satellite in a halo orbit located at EML-1. The orbit is similar to that of the ARTEMIS mission that traversed the EML-1 point in 2010 and 2011 [5, 145]. The halo reference orbit used in this study was generated using a two-step process. First, the analytical expansion described by Richardson and Cary was used to generate a set of initial states [131]. The reference epoch for the initial state is defined as January 1, 2020

ET (Ephemeris Time). The amplitude of the z-axis for the halo orbiter, A_z, has been set to 35,500 km. The initial phase angle of the orbit, Φ, has been set to zero degrees. The parameters used to generate the reference trajectory are given in Table 10.1.

10.1.2 Trans-lunar Cruise

The trans-lunar cruise designed for this study is based on a possible crewed mission traversing EML-1 and EML-2. The trajectory involves a direct transfer to the Moon from a LEO parking orbit from a trans-lunar injection maneuver (TLI), followed by a powered lunar flyby, resulting in a direct transfer to an EML-2 halo orbit. This work only utilizes the first phase of the TLC from LEO to the powered lunar flyby. The full TLC to EML-2 is described since the trajectory is constrained to enter a 29.5 day (one synodic month) EML-2 halo orbit. This orbital period was chosen such that any crewed mission can launch a month late and have the same exact repeating geometry.

Table 10.1: Initial LEO parking orbit conditions for TLI.

		Orbital Parameters				
Epoch	Alt.	Ecc.	Inc.	RAAN	Arg. Per.	True Anom.
1/14/2020 00:00:00 ET	185 km	0.000	28.5 deg	223.144 deg	0 deg	-191.756 deg

The TLC begins from a LEO parking orbit with the orbital parameters given in Table 10.1. The transfer duration from LEO to the Moon is approximately 3.7 days. A delta-v of approximately 3.134 km/s in the along-track direction is used to insert into the TLC trajectory. A lunar flyby occurs at 1/17/2020 16:28:1.9163 ET. The lunar flyby occurs at an altitude of 100 km with a delta-v of approximately 213.56 m/s, performed at the periapse of the flyby. After the lunar flyby, the transfer to the EML-2 halo orbit is approximately 3.3 days. The crewed spacecraft reaches that halo insertion maneuver at 1/21/2020 00:00:00 ET with a delta-v of approximately 138.28 m/s.

10.1.3 Ground Tracking Networks

During the Apollo era there existed 12 land-based and sea-based tracking stations that made up the Manned Space Flight Network. These stations were necessary in order to obtain reasonably accurate navigation estimates for early spaceflight. A subset of the Manned Space Flight Network was the DSN. The DSN is still operated today supporting various deep space missions that require accurate radiometric observations and communications. The DSN has three locations: Goldstone in California, Canberra in Australia, and Madrid in Spain. Another tracking network was defined during the Constellation programs 4B integrated design and analysis cycle (IDAC4B). This network is denoted as IDAC4B and utilizes the DSN and three additional tracking stations located at Santiago, Chile; Hartebeesthoek, South Africa; and Usuda, Japan. The location of these three tracking networks is shown in Figure 10.2. The IDAC4B stations are located in the opposite hemisphere of their corresponding DSN stations by a significant difference in latitude. This difference in latitude provides a significant geometrical advantage when using radiometric data yielding better navigation solutions using a smaller number of stations when compared to the Apollo tracking network.

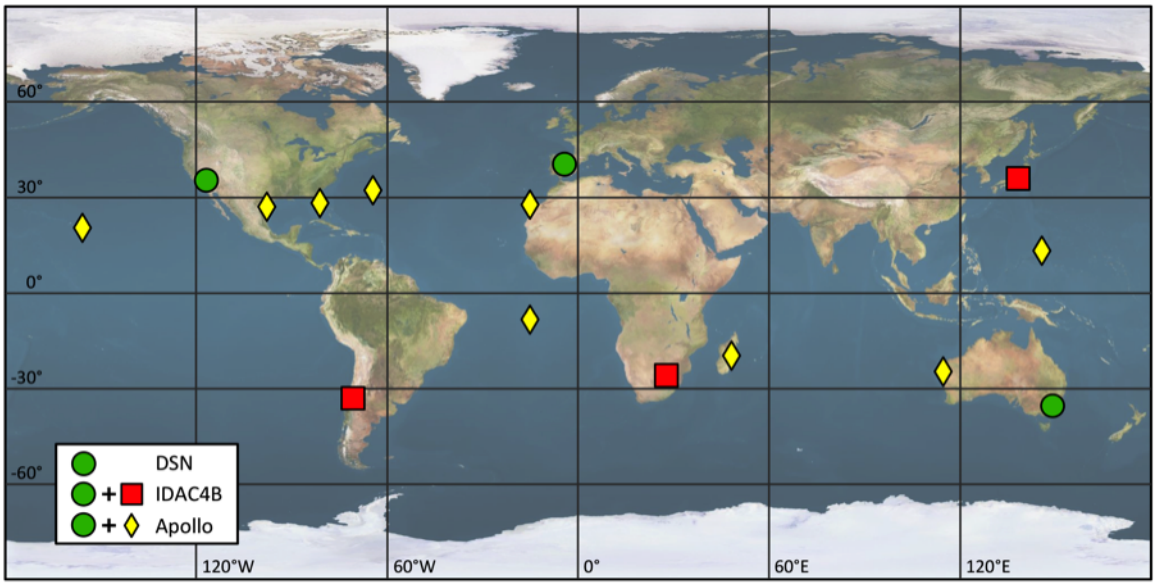

Figure 10.2: Locations of the DSN, IDAC4B, and Apollo tracking networks. The DSN network is common for all of the tracking networks and is denoted by green circles; the IDAC4B network is denoted by red squares, and the Apollo stations are given by yellow diamonds.

For this study, only the DSN and the IDAC4B tracking networks are used. It has previously been shown that the IDAC4B configuration is sufficient enough to obtain navigation uncertainties necessary for crewed spaceflight to the Moon [26, 29]. The DSN stations continuously collect two-way range and range-rate measurements with a 10 deg elevation mask on a 100 s observation interval. The additional IDAC4B stations continuously collect three-way range and range-rate data with a 10 deg elevation mask on a 100 s observation interval. For this study, it is assumed that the crewed TLC spacecraft has access to the observations at all times for use in the onboard navigation.

10.2 Navigation Performance Methods

10.2.1 FLAK Model Used

This section describes nongravitational disturbances in the trajectory that are commonly caused by environmental venting and frequent attitude adjustments that are common to crewed vehicles. It is assumed that these disturbances are primarily due to: 1) wastewater dumps, 2) momentum desaturation maneuvers, 3) attitude control burns, 4) CO2 venting, 5) thermal venting, and 6) water sublimation. These disturbances are increased during active crew cycles and are reduced during crew rest periods. These disturbances have been referred to as FLAK (un**F**ortunate **L**ack of **A**cceleration **K**nowledge) [29].

The term FLAK appeared during the Apollo program when it was determined that significant deviations in the trajectory occurred due to the activity of the crew and certain outgassing or maneuver events [25, 29, 161]. The current model used to estimate these disturbances is a simple state noise compensation method [29]. Until a better model is developed, this simplistic FLAK model will be used to determine the necessary disturbance level. For the purpose of this work, a stochastic acceleration process is used to create a spherical position dispersion of 500 m (1-σ) every hour.

A discrete white noise process is used to drive the acceleration of the system that in turn induces errors in the position and velocity of the spacecraft. A linear discrete model for this system

in one dimension is given by

$$\begin{bmatrix} x_{k+1} \\ v_{k+1} \\ a_{k+1} \end{bmatrix} = \begin{bmatrix} 1 & \Delta t & \Delta t^2/2 \\ 0 & 1 & \Delta t \\ 0 & 0 & 0 \end{bmatrix} \begin{bmatrix} x_k \\ v_k \\ a_k \end{bmatrix} + \begin{bmatrix} 0 \\ 0 \\ 1 \end{bmatrix} u_k \tag{10.1}$$

where $\Delta t = t_{k+1} - t_k$ and u_k is the discrete Gaussian white noise process such that the statistics are $E[u_k] = 0$ and $E[u_i u_k] = q\delta_{i,k}$ where $\delta_{i,k}$ is the Kronecker delta function. For the dynamic model and linearization used in this study, the state transition matrix and the process noise mapping matrix for one dimension of this system is defined as

$$\Phi(t_{k+1}, t_k) = \begin{bmatrix} 1 & \Delta t \\ 0 & 1 \end{bmatrix}, \quad \text{and} \quad \Gamma(t_{k+1}, t_k) = \begin{bmatrix} \frac{\Delta t^2}{2} \\ \Delta t \end{bmatrix} \tag{10.2}$$

This method can be assumed if the dynamics do not change significantly over a short duration of time. In order to determine the strength of the process noise q one needs to know the covariance $\mathbf{P}_k$. Reference [29] shows that if one assumes that the initial covariance $\mathbf{P}_0$ is zero such that only the process noise used, the covariance $\mathbf{P}_k$ can be calculated as

$$\mathbf{P}_k = q \begin{bmatrix} \frac{4n^3 - 3n^2 + 2n}{12}\Delta t^4 & \frac{n^2}{2}\Delta t^3 \\ \frac{n^2}{2}\Delta t^3 & n\Delta t^2 \end{bmatrix} \tag{10.3}$$

This derivation allows for more than one variation while achieving the same results such that the total propagation time $T = n\Delta t$. This shows that the same propagation time can result in different step sizes Δt and produce different values for $\mathbf{P}_k$. Thus, the process noise strength q must be computed in conjunction with the selection of a step size Δt.

If one assumes that Δt is small and thus n is very large, the covariance can be simplified and approximated by

$$\mathbf{P}_k \approx q \begin{bmatrix} \frac{n^3}{3}\Delta t^4 & \frac{n^2}{2}\Delta t^3 \\ \frac{n^2}{2}\Delta t^3 & n\Delta t^2 \end{bmatrix} \tag{10.4}$$

This result is the same as that found in Reference [29] and similar to that in Reference [19].

The only information concerning the strength of the process noise comes from the Apollo era. From the navigation solutions for Apollo missions, a trajectory deviation of several hundred

meters was experienced over an hour in lunar orbit [25, 29, 161]. For this study, it is assumed that the uncertainty due to FLAK during TLC has a spherical position dispersion equivalent to 500 m (1-σ) over one hour. In order to determine the strength of the process noise in a single dimension, the position dispersion is equivalent to 288.6751 m. With a step size Δt of 100 s and a propagation time of 1 hour ($n = 36$), the process noise strength is $\sqrt{q}$ = 2.3148e-7 km/s^2. This process noise strength is used for active periods when the crew is awake and moving around. For quiet periods when the crew is asleep, the amount of FLAK is 10 times less ($\sqrt{q}$ = 2.3148e-8 km/s^2).

10.3 Trans-lunar Cruise Navigation Performance

The results obtained in this section are for the TLC mission previously presented. Four tracking architecture types are analyzed: 1) DSN only, 2) IDAC4B only, 3) DSN and LiAISON, and 4) IDAC4B and LiAISON. Each simulation utilizes the same force models and measurement models. Both spacecraft are propagated using the GCRF coordinate system and are integrated using a point mass representation of Earth with third body perturbations due to the Sun and Moon using the JPL DE405 ephemeris. The TLC spacecraft uses a 20x20 spherical harmonic representation of the gravity field for both the Earth and Moon given by the GGM02C and LP150Q models respectively [77, 147]. The C_R values for the TLC and EML-1 halo orbiter are 1.5 and 1.2 respectively. FLAK levels vary based on crew activity levels where there are 16 hours of active periods followed by 8 hours of quiet periods. The time evolution of the state dynamics is solved using the TurboProp orbit integration package for orbit propagation [59]. Initial state and measurement uncertainties are given in Table 10.2.

10.3.1 TLC with Standard FLAK Level

The best possible navigation uncertainties obtained in this study for a crewed vehicle using four different tracking architectures is shown in Figure 10.3. The results in Figure 10.3 show navigation uncertainties from just after TLI to just prior to the lunar flyby. Continuous range and range-rate measurements from each tracking source are taken every 100 s over the 3.7 day TLC.

Table 10.2: Navigation performance initial uncertainties.

Estimation Parameters	*a priori* uncertainty (1-sigma)	Number of Parameters
TLC spacecraft position	1,000 m	3
TLC spacecraft velocity	500 m/s	3
EML-1 spacecraft position	100 m	3
EML-2 spacecraft velocity	1 m/s	3
SRP Coefficient	20%	2
Active FLAK	2.3148e-7 km/s^2	–
Quiet FLAK	2.3148e-8 km/s^2	–
LiAISON measurements		
range	1 m	–
range-rate	1 mm/s	–
Ground measurements		
range	2 m	–
range-rate	0.5 mm/s	–

The navigation results show that all navigation architectures approach steady state after 12 hours of tracking. DSN only tracking has the worst navigation uncertainty of all tracking architectures. When using the IDAC4B configuration only, navigation accuracies are reduced significantly from that of DSN only. When LiAISON measurements are introduced to the DSN only measurements, the navigation uncertainty is reduced to that of using only the IDAC4B configuration. The best possible navigation solution is achieved using the IDAC4B configuration with LiAISON mea-

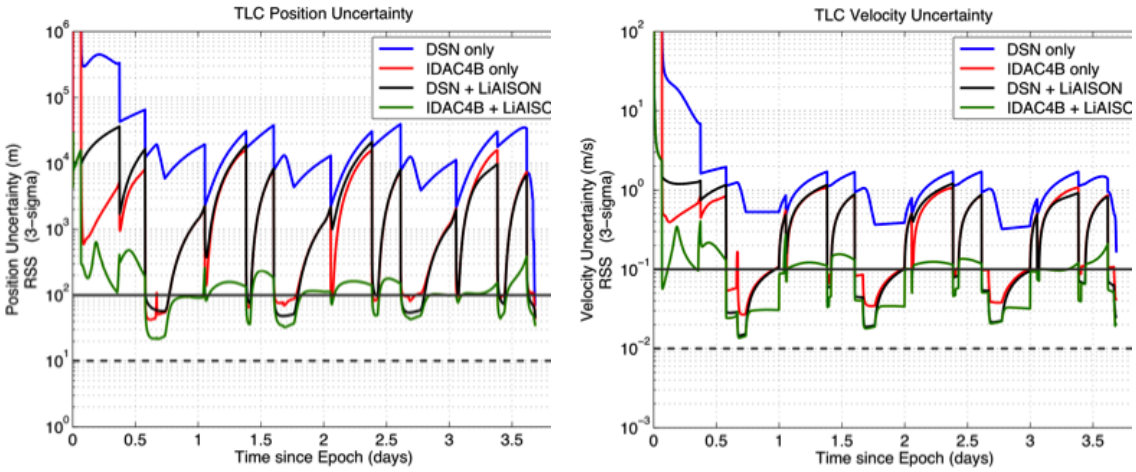

Figure 10.3: Time history of the position and velocity RSS navigation uncertainty for four different tracking architectures. 1) DSN only (blue), 2) IDAC4B only (red), 3) DSN and LiAISON (black), and 4) IDAC4B and LiAISON (green).

surements. The 3D-RMS position and velocity uncertainties are given in Table 10.3. The 3D-RMS values are calculated after steady state is reached at 12 hours until the lunar flyby occurs.

Table 10.3: TLC navigation uncertainties.

Architecture	3D-RMS Position Uncertainty (m)	3D-RMS Position Uncertainty (m/s)
DSN only	18,113.7	1.1028
IDAC4B only	5,467.3	0.5645
DSN + LiAISON	5,772.0	0.5713
IDAC4B + LiAISON	130.4	0.0996

10.3.2 Navigation Sensitivity to FLAK Level

The Apollo era acceleration uncertainties due to FLAK events may not correspond directly to future crewed missions to the Moon. This analysis varies the strength of the FLAK events to determine the navigation sensitivities due to the FLAK levels. Five different FLAK levels are chosen for this study. Each simulation uses the exact same observation measurements and uncertainties given in Table 3. FLAK levels are varied by 0.1, 0.5, 1, 2, and 5 times the acceleration uncertainty determined from the Apollo era assumption that the acceleration uncertainties due to FLAK events creates a 500 m dispersion in 1 hour.

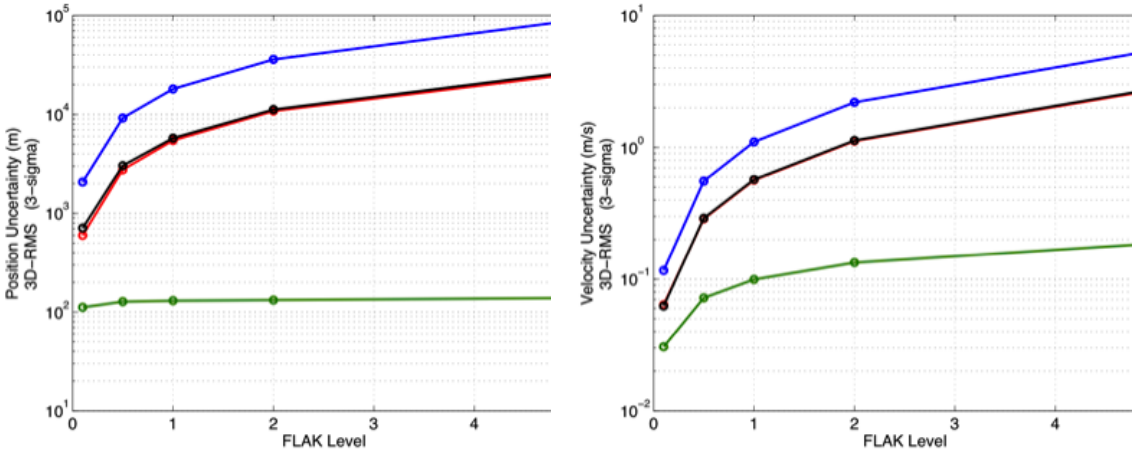

Figure 10.4: Navigation sensitivities due to FLAK levels. 1) DSN only (blue), 2) IDAC4B only (red), 3) DSN and LiAISON (black), and 4) IDAC4B and LiAISON (green).

The navigation sensitivities to the several different FLAK levels are shown in Figure 10.4 for both position and velocity. Similar to the previous analysis, the 3D-RMS values are calculated after steady state is reached at 12 hours until the lunar flyby occurs. FLAK levels are more sensitive to the DSN only, IDAC4B only, and DSN and LiAISON tracking architectures. The IDAC4B and LiAISON navigation architecture is the least sensitive to various FLAK levels. The navigation uncertainties are similar to the previous analysis such that DSN has the largest 3D-RMS uncertainty while IDAC4B has the smallest uncertainty. IDAC4B only and DSN and LiAISON have nearly identical navigation uncertainties.

10.4 Conclusions

The benefit of navigating a crewed vehicle between the Earth and the Moon using both ground tracking and satellite-to-satellite tracking was analyzed. Various navigation architectures, including ground-based and LiAISON supplemented configurations of a crewed mission to the Moon, were examined. A crewed trans-lunar cruise mission was designed with a navigation satellite located at EML-1. An acceleration uncertainty model based on historical Apollo data was derived to quantify the level of activity expected on a crewed vehicle. It was shown that a DSN only based tracking method has the worst position navigation uncertainty of about 18 km (3-σ) for a standard FLAK level. The best navigation uncertainty was achieved using the six station IDAC4B configuration with a LiAISON based navigation satellite producing a position uncertainty of about 130 m (3-σ). Navigation uncertainties were about the same for the IDAC4B only case and the DSN with LiAISON tracking case and resulted in position uncertainties of about 5.5 km (3-σ). Various FLAK levels were also examined to determine the sensitivity of the navigation uncertainties due to unmodeled stochastic acceleration intensity. The least sensitive configuration to FLAK levels was determined to be the IDAC4B with LiAISON architecture. If the IDAC4B only tracking architecture can produce sufficient navigation uncertainty for crewed missions to the moon, then it could be substituted for three ground stations and one LiAISON satellite significantly reducing the cost of navigation for the crewed vehicle.

Chapter 11

Conclusions and Future Work

The research presented in this dissertation has explored the use of LiAISON navigation as a supplemental navigation data type to existing and proposed ground tracking networks for future crewed missions in the Earth-Moon system. This final chapter summarizes the research presented and provides recommendations for future work.

11.1 Conclusions

The main contribution of this dissertation has been to advance the understanding of LiAISON navigation and its application for increased spacecraft autonomy for crewed missions in the Earth-Moon system while evaluating its costs (e.g., dedicated navigation satellite, additional hardware, etc.) and benefits (e.g. improved navigation accuracy, fewer DSN tracks, etc.) ultimately providing information for future mission planners to determine its applicability. A baseline navigation capability utilizing ARTEMIS tracking data was conducted for use in subsequent simulations. A large trade space was explored analyzing the navigation capabilities of LiAISON supplemented tracking data for crewed mission in Earth-Moon halo orbits, low lunar orbit, and trans-lunar cruise.

An analysis of raw tracking data for the ARTEMIS mission was conducted to establish a baseline for navigation performance capabilities with current ground station configurations. Since ARTEMIS was the first mission to fly an Earth-Moon libration point orbit, it's navigation capabilities and operations experiences provide an invaluable measure of what is to be expected. The work performed in this thesis systematically investigated techniques not used in operations to obtain

the best navigation performance capabilities attainable. Significant findings include the necessity of a more complex solar radiation pressure shape model of the spacecraft, sequential estimation as opposed to batch processing, estimation of maneuvers and extended tracking data arc lengths. By properly editing tracking data residuals and extending the data arc length, it was shown that overlap precisions on the order of 150 m or less in position was possible. The most important aspect of longer data arcs is the reduction of uncertainty or increased precision in the velocity estimates of the spacecraft. With a longer data arc it is possible to achieve velocity uncertainties less than 1 mm/sec, whereas a shorter data arc as used in operations only provides uncertainties on the order of 5 mm/sec.

Initial observability work discussing the capabilities of LiAISON data types was limited in scope however it did explore some features relating to the environment that allows LiAISON to use relative radiometric data to obtain absolute state estimates. An extension to this work is covered in this dissertation in which an exploration of the information content of range and Doppler using simplified first-order models was conducted. The Earth-Moon system was mapped out using partial derivatives of the relative acceleration between a spacecraft and the libration points to define regions where LiAISON Doppler data provides limited ranging information necessary to obtain full estimates of the spacecrafts state.

An extension of the local stability characteristics of halo orbits and how they related to the uncertainty propagation was examined. It was shown that the stability is directly related to the stretching and alignment of the uncertainty propagated along a halo orbit. A crewed vehicle disturbance and environment model (FLAK) was derived using data describing the expected crew ECLSS system. An introduction to a Poisson counting process for use with FLAK uncertainty propagation was derived using linearized assumptions. A Monte Carlo analysis of a trajectory undergoing FLAK showed that a linearized assumption of the uncertainty propagation was valid over the timeframe of concern between the end of a tracking data arc and the next performed maneuver. The inclusion of a Poisson noise model intuitively makes sense for modeling FLAK and requires minimal modifications to current navigation software to implement.

Surveys of the trade space concerning LiAISON supplemented navigation for Earth-Moon halo orbiters, low lunar orbiters, and trans-lunar cruise trajectories was conducted. For lunar halo orbiters, TDRSS/GEO type LiAISON measurements can significantly improve the navigation capabilities of both the TDRSS/GEO satellite and a spacecraft in orbit about one of the Earth-Moon Lagrange points. There exists regions where the observability and information content of the data is reduced to due repetitious sampling of the same regions, specifically with a periodicity of 22 hours. An extension to LiAISON navigation of two spacecraft in lunar halo orbits, where one is a crewed vehicle, was conducted. It was shown that LiAISON alone is not sufficient to accurately determine the trajectories of both the navigation satellite and crewed vehicle. However, the addition of a dedicated LiAISON navigation satellite supplementing existing ground tracking networks significantly improves the navigation performance of a crewed vehicle. LiAISON supplementing the DSN produces similar navigation uncertainties as the proposed six station IDAC4B configuration. Similar results were seen for both a crewed vehicle in low lunar orbit and a crewed vehicle on a trans-lunar cruise trajectory. DSN and LiAISON performs on par with the IDAC4B configuration, while LiAISON supplementing the IDAC4B configuration produces the best navigation performance typically invariant of the level of FLAK experienced by the crewed vehicle.

11.2 Future Work

Additional analysis of the ARTEMIS tracking data is necessary to reduce the effects of spacecraft spin on the Doppler residuals. In the analysis presented in this thesis, the spin signature was ignored due to the fact that the amplitude of the spin signature was near expected the noise level of the Doppler residuals. Further work is necessary to fully characterize the navigation precision and uncertainties for both spacecraft, P1 and P2. This analysis only focused on a few months of P2s early orbits in the Earth-Moon system. However, an extension of this to the full mission timeframe for both spacecraft could yield more insight into the challenges navigating a spacecraft in this dynamical environment. During the early processing phase of the ARTEMIS data, an unmodeled acceleration was detected for every data arc as the spacecraft was at lunar closest approach. This

anomaly needs to be investigated in more detail to determine the cause. Finally, the use of a nonlinear filter or extended Kalman filter may be necessary for data arcs longer than 14 days as analyzed in this thesis. The unstable environment severely limits the capabilities of a linearized Kalman filter for long data arcs.

Bibliography

[1] The Astronomical Almanac for the Year 2003. United States Naval Observatory/Nautical Almanac Office, 2002.

[2] The Astronomical Almanac for the Year 2015. United States Naval Observatory/Nautical Almanac Office, 2014.

[3] Rodney L Anderson, Martin W Lo, and George H Born. Application of local lyapunov exponents to maneuver design and navigation in the three-body problem. In AAS/AIAA Astrodynamics Specialist Conference, AAS 03–549, Big Sky, Montana, August 3–7 2003.

[4] Juan Andrade-Cetto and Alberto Sanfeliu. The effects of partial observability when building fully correlated maps. Robotics, IEEE Transactions on, 21(4):771–777, 2005.

[5] V. Angelopoulos. The artemis mission. Space science reviews, 165(1-4):3–25, 2011.

[6] M. Athans, R. Wishner, and A. Bertolini. Suboptimal state estimation for continuous-time nonlinear systems from discrete noisy measurements. Automatic Control, IEEE Transactions on, 13(5):504–514, 1968.

[7] M. Beckman. Orbit determination issues for libration point orbits. In G. Gómez, M. W. Lo, and J. J. Masdemont, editors, Libration Point Orbits and Applications: Proceedings of the Conference, Aiguablava, Spain, June 2003. World Scientific Publishing Company.

[8] Mike Georg Bernhardt, Werner Becker, Tobias Prinz, Ferdinand Maximilian Breithuth, and Ulrich Walter. Autonomous spacecraft navigation based on pulsar timing information. In 2011 2nd International Conference on Space Technology (ICST), 2011.

[9] G. Beutler, A. Jäggi, L. Mervart, and U. Meyer. The celestial mechanics approach: application to data of the grace mission. Journal of Geodesy, pages 1–21, 2010.

[10] G.J. Bierman. Factorization methods for discrete sequential estimation, volume 128. Academic Press, 1977.

[11] Philippe Bonnifait and Gaëtan Garcia. Design and experimental validation of an odometric and goniometric localization system for outdoor robot vehicles. Robotics and Automation, IEEE Transactions on, 14(4):541–548, 1998.

[12] S. B. Broschart, M. J. Chung, S. J. Hatch, J. H. Ma, T. H. Sweetser, S. S. Weinstein-Weiss, and V. Angelopoulos. Preliminary trajectory design for the ARTEMIS lunar mission. In A. V. Rao, T. A. Lovell, F. K. Chan, and L. A. Cangahuala, editors, Proceedings of the AAS/AIAA Astrodynamics Specialist Conference held 9-13 August 2009, Pittsburgh, Pennsylvania, volume 134 of Advances in Astronautical Sciences, San Diego, CA, 2009. AAS/AIAA, Univelt Inc.

[13] R. A. Broucke. Periodic orbits in the restricted three-body problem with Earth-Moon masses. Technical Report 32-1168, Jet Propulsion Laboratory, California Institute of Technology, 1968.

[14] A. Bryson and Y.C. Ho. Applied Optimal Control: Optimization, Estimation, and Control. Hemisphere Pub, 1975.

[15] Caltech. Advanced composition explorer (ace). `http://www.srl.caltech.edu/ACE/newhome/ace\_mission.html`.

[16] Lamberto Cesari. Asymptotic behavior and stability problems in ordinary differential equations. Springer, 2nd edition, 1963.

[17] Y. Cheng and J. K. Miller. Autonomous landmark based spacecraft navigation system. In 13th AAS/AIAA Astrodynamics Specialist Conference, Ponce, Puerto Rico, February 9–13 2003.

[18] MA Chory, DP Hoffman, and JL LeMay. Satellite autonomous navigation - status and history. In IEEE Position, Location, and Navigation Symposium, volume 1, pages 110–121, Las Vegas, NV, 1986.

[19] J. Crassidis and J. Junkins. Optimal Estimation of Dynamic Systems. Chapman & Hall, 2004.

[20] D. W. Curkendal and S. R. McReynolds. A simplified approach for determining the information content of radio tracking data. Journal of Spacecraft and Rockets, 6(5):520–525, 1969.

[21] M Di Paola. Linear systems excited by polynomials of filtered poission pulses. Journal of applied mechanics, 64(3):712–717, 1997.

[22] M Di Paola and G Falsone. Higher order statistics of the response of linear systems excited by polynomials of filtered poisson pulses. Probabilistic engineering mechanics, 14(1):55–62, 1999.

[23] Mario Di Paola and Isaac Elishakoff. Non-stationary response of linear systems under stochastic gaussian and non-gaussian excitation: a brief overview of recent results. Chaos, Solitons & Fractals, 7(7):961–971, 1996.

[24] Mario Di Paola and Giovanni Falsone. Stochastic dynamics of nonlinear systems driven by non-normal delta-correlated processes. Journal of Applied Mechanics, 60(1):141–148, 1993.

[25] C. D'Souza. Process noise for lunar missions. NASA Johnson Space Center EG-CX-06-03, 2006.

[26] C. D'Souza, J. Getchius, G. Holt, and M. Moreau. Lunar navigation architecture design considerations. In AAS Guidance and Control Conference. Univelt Inc., 2009.

[27] C. D'Souza, G. Holt, R. Gay, and R. Zanetti. Navigation design and analysis for the orion cislunar exploration missions. In 37th Annual AAS Guidance and Control Conference, Breckenridge, CO, January 31 – February 5 2014.

[28] C. D'Souza and R. Zanetti. Navigation design and analysis for the orion earth-moon mission. In 24th AAS/AIAA Space Flight Mechanics Conference, Santa Fe, NM, 2014.

[29] T. Ely, M. Heyne, and J. E. Riedel. Altair navigation during trans-lunar cruise, lunar orbit, descent, and landing. In Proceedings of the AIAA Guidance, Navigation, and Control Conference, and Exhibit, Toronto, Ontario, Canada, 2010.

[30] ESA. `http://www.esa.int/Our\_Activities/Space\_Science/Herschel/Operating\_Herschel`.

[31] JA Estefan and OJ Sovers. A comparative survey of current and proposed tropospheric refraction-delay models for dsn radio metric data calibration. Jet Propulsion Lab. Report, 1, 1994.

[32] R. W. Farquhar and A. A. Kamel. Quasi-periodic orbits about the translunar libration point. Celestial Mechanics, 7(4):458–473, June 1973.

[33] Robert W Farquhar and David W Dunham. Use of libration-point orbits for space observatories. In Observatories in Earth Orbit and Beyond, pages 391–395. Springer, 1991.

[34] Robert W Farquhar, Daniel P Muhonen, Charles R Newman, and Howard S . Heubergerg. Trajectories and orbital maneuvers for the first libration-point satellite. Journal of Guidance, Control, and Dynamics, 3(6):549–554, 1980.

[35] Uwe Feucht and Gottlob Gienger. Launch and early operations of herschel and planck. Acta Astronautica, 68(7):1283–1291, 2011.

[36] W. M. Folkner, J. G. Williams, and D. H. Boggs. The planetary and lunar ephemeris DE 421. Technical Report IOM 343R–08–003, Jet Propulsion Laboratory, California Institute of Technology, March 2008. ftp://naif.jpl.nasa.gov/pub/naif/generic_kernels/spk/planets/de421_announcement.pdf.

[37] D Folta and F. Vaughn. A survey of Earth-Moon libration orbits: Stationkeeping strategies and intra-orbit transfers. In AIAA/AAS Astrodynamics Specialist Conference and Exhibit, number AIAA 2004-4741, Providence, Rhode Island, August 16–19, 2004. AIAA/AAS.

[38] D. Folta, M. Woodard, and D. Cosgrove. Stationkeeping of the first earth-moon libration orbiters: The artemis mission. In AAS/AIAA Astrodynamics Specialist Conference, Girdwood, Alaska, 2011.

[39] K. Fujimoto, J. M. Leonard, R. M. McGranaghan, J. S. Parker, R. L. Anderson, and G. H. Born. Simulating the liaison navigation concept in a geo + earth-moon halo constellation. In Accepted to 23rd International Symposium on Space Flight Dynamics, Pasadena, California, October 29 – November 2 2012.

[40] K. Fujimoto and D. J. Scheeres. Analytical nonlinear propagation of uncertainty in the two-body problem. Journal of Guidance, Control and Dynamics, 35(2):498–509, 2012.

[41] A. Gelb. Applied Optimal Estimation. MIT press, 1974.

[42] J. Getchius, D. Kukitschek, and T. Crain. Orion navigation sensitivities to ground station infrastructure for lunar missions. In AAS Guidance and Control Conference. Univelt Inc., 2008.

[43] R. Ghanem and PD Spanos. Polynomial chaos in stochastic finite element. Journal of Applied Mechanics, 57(1):197–202, 1990.

[44] R. Ghanem and PD Spanos. A stochastic galerkin expansion for nonlinear random vibration analysis. Probabilistic Engineering Mechanics, 8(3):255–264, 1993.

[45] Bruce P Gibbs. Advanced Kalman filtering, least-squares and modeling: a practical handbook. John Wiley & Sons, 2011.

[46] D. Giza, P. Singla, and M. Jah. An approach for nonlinear uncertainty propagation: Application to orbital mechanics. In AIAA Guidance, Navigation, and Control Conference, Chicago IL, 2009.

[47] B. Godard, M. Croon, F. Budnik, and T Morley. Orbit determination of the planck satellite. In 21st International Symposium on Space Flight Dynamics, Toulouse, France, Sept. 28–Oct. 2, 2009.

[48] R. G. Gottlieb. Fast gravity, gravity partials, normalized gravity, gravity gradient torque and magnetic field: Derivation, code and data. Tech. Rep. NASA Contractor Report 188243, 1993.

[49] P Graven, J Collins, S Sheikh, J Hanson, P Ray, and K Wood. Xnav for deep space navigation. In 31st Annual AAS Guidance and Control Conference, 2008.

[50] Mircea Grigoriu. Response of dynamic systems to poisson white noise. Journal of Sound and Vibration, 195(3):375–389, 1996.

[51] Mircea Grigoriu and Eric Harper. Applied non-Gaussian processes: Examples, theory, simulation, linear random vibration, and MATLAB solutions. PTR Prentice Hall Upper Saddle River, NJ, 1995.

[52] K. Hamera, T. Mosher, M. Gefreh, R. Paul, L. Slavkin, and J. Trojan. An evolvable lunar communication and navigation constellation concept. In IEEE Aerospace Conference, number IEEE 1491, Big Sky, Montana, 28 April–1 May 2008. IEEE.

[53] T. W. Hamilton and W. G. Melbourne. Information content of a single pass of doppler data from a distant spacecraft. JPL Space Programs Summary, 3(37–39):18–23, 1966.

[54] Joseph A Hashmall, Denis Felikson, and Joseph E Sedlak. Use of fuzzycones for sun-only attitude determination: Themis becomes artemis. In 21st International Symposium on Spaceflight Dynamics, Toulouse, 2009.

[55] Robert Hermann and Arthur Krener. Nonlinear controlability and observability. Automatic Control, IEEE Transactions on, 22(5):728–740, 1977.

[56] K. Hill. Autonomous Navigation in Libration Point Orbits. PhD thesis, University of Colorado, Boulder, Colorado, 2007.

[57] K. Hill and G. H. Born. Autonomous interplanetary orbit determination using satellite-to-satellite tracking. AIAA Journal of Guidance, Control, and Dynamics, 30(3), May–June 2007.

[58] K. Hill, G. H. Born, and M. W. Lo. Linked, autonomous, interplanetary satellite orbit navigation (liaison) in lunar halo orbits. In AAS/AIAA Astrodynamics Specialist Conference, number AAS 05-400, Lake Tahoe, CA, August 7–11, 2005. AAS/AIAA.

[59] K. Hill and B. A. Jones. TurboProp Version 4.0. Colorado Center for Astrodynamics Research, May 2009.

[60] K. Hill, M. W. Lo, and G. H. Born. Linked, autonomous, interplanetary satellite orbit navigation (liaison). In AAS/AIAA Astrodynamics Specialist Conference, number AAS 05-399, Lake Tahoe, CA, August 7–11, 2005. AAS/AIAA.

[61] K. Hill, J. S. Parker, G. H. Born, and N. Demandante. A lunar L2 navigation, communication, and gravity mission. In AIAA/AAS Astrodynamics Specialist Conference, number AIAA 2006-6662, Keystone, Colorado, August 2006. AIAA/AAS.

[62] Keric Hill, Martin W Lo, and George H Born. Liaison navigation in the Sun-Earth-Moon four-body problem. In AAS/AIAA Spaceflight Dynamics Conference, number AAS 06-221, Tampa, FL, January 22–26, 2006. AAS/AIAA.

[63] D. Hoffman. A Set of C Utility Programs for Processing JPL Ephemeris Data. Johnson Space Center, 1998.

[64] J.T. Horwood, N.D. Aragon, and A.B. Poore. Gaussian sum filters for space surveillance: theory and simulations. Journal of guidance, control, and dynamics, 34(6):1839–1851, 2011.

[65] K. C. Howell. Three-dimensional, periodic, 'Halo' orbits. Celes. Mech., 32(1):53–71, 1984.

[66] K. C. Howell and H. J. Pernicka. Numerical determination of lissajous trajectories in the restricted three-body problem. Celes. Mech., 41:107–124, 1988.

[67] Radoslaw Iwankiewicz and Søren RK Nielsen. Dynamic response of hysteretic systems to poisson-distributed pulse trains. Journal of Sound and Vibration, 156:407–423, 1992.

[68] A. H. Jazwinski. Stochastic processes and filtering theory, volume 63. Academic Press, 1970.

[69] B. A. Jones, A. Doostan, and G. H. Born. Nonlinear propagation of orbit uncertainty using non-intrusive polynomial chaos. Journal of Guidance, Control and Dynamics, 2012.

[70] P. Jordan and et al. Solar and heliospheric observatory (soho) mission description and flight dynamics analysis reports, revision 2. Technical report, CSC/TM-91/6030ROUDO, 1993.

[71] JB Joyce and AF Schanzle. Trajectory determination support and analysis for isee-3 from halo orbit to escape from the earth/moon system. In AIAA/AAS Astrodynamics Conference, Seattle, WA, Aug. 20–22 1985.

[72] Hee Jung and Mark L Psiaki. Tests of magnetometer/sun-sensor orbit determination using flight data. Journal of Guidance, Control, and Dynamics, 25(3):582–590, 2002.

[73] J.L. Junkins, M.R. Akella, and K.T. Alfrined. Non-gaussian error propagation in orbital mechanics. Journal of Astronautical Sciences, 44(4):541–563, October – December 1996.

[74] Steven M Kay. Fundamentals of statistical signal processing, volume I: Estimation theory. Prentice Hall, 1993.

[75] T. H. Kerr. Status of cr-like lower bounds for nonlinear filtering. IEEE Transactions on Aerospace and Electronic Systems, 25(5):590–601, 1989.

[76] A. S. Konopliv, R. S. Park, D. Yuan, S. W. Asmar, M. M. Watkins, James G Williams, Eugene Fahnestock, Gerhard Kruizinga, Meegyeong Paik, D. Strekalov, et al. The jpl lunar gravity field to spherical harmonic degree 660 from the grail primary mission. Journal of Geophysical Research: Planets, 118(7):1415–1434, 2013.

[77] AS Konopliv, SW Asmar, E. Carranza, WL Sjogren, and DN Yuan. Recent gravity models as a result of the lunar prospector mission. Icarus, 150(1):1–18, 2001.

[78] Hasan Ugur Köylüoglu, Søren RK Nielsen, and Radoslaw Iwankiewicz. Response and reliability of poisson-driven systems by path integration. Journal of engineering mechanics, 121(1):117–130, 1995.

[79] HU Köylüoğlu, Søren RK Nielsen, and Radoslaw Iwankiewicz. Reliability of non-linear oscillators subject to poisson driven impulses. Journal of sound and vibration, 176(1):19–33, 1994.

[80] Arthur J Krener and Witold Respondek. Nonlinear observers with linearizable error dynamics. SIAM Journal on Control and Optimization, 23(2):197–216, 1985.

[81] Daniel G Kubitschek, Nickolaos Mastrodemos, Robert A Werner, Brian M Kennedy, Stephen P Synnott, George W Null, Shyam Bhaskaran, Joseph E Riedel, and Andrew T Vaughan. Deep impact autonomous navigation: the trials of targeting the unknown. In 29th Annual AAS Guidance and Control Conference, Breckenridge, CO, Feb. 4–8 2006.

[82] Kwang Wee Lee, W Sardha Wijesoma, and Ibanez Guzman Javier. On the observability and observability analysis of slam. In Intelligent Robots and Systems, 2006 IEEE/RSJ International Conference on, pages 3569–3574, 2006.

[83] Jason Leonard, Brandon Jones, Eduardo Villalba, and George Born. Absolute orbit determination and gravity field recovery for 433 eros using satellite-to-satellite tracking. In AIAA/AAS Astrodynamics Specialist Conference, 2012.

[84] Jason M Leonard, B. W. Cheetham, and G. H. Born. Preliminary evaluation of earth-moon libration point orbit navigation with post-processed artemis data. In 24th International Symposium on Space Flight Dynamics, Laurel, Maryland, May 5–9, 2014.

[85] Jason M Leonard, Ryan M McGranaghan, Kohei Fujimoto, George H Born, Jeffrey S Parker, and Rodney L Anderson. Liaison-supplemented navigation for geosynchronous and lunar l1 orbiters. In AAS/AIAA Astrodynamics Specialist Conference, number AIAA-2012-4664, Minneapolis, MN, August 13–16 2012.

[86] Jason M Leonard, Felipe G Nievinski, and George H Born. Gravity error compensation using second-order gauss-markov processes. Journal of Spacecraft and Rockets, 50(1):217–229, 2013.

[87] Jason M Leonard, Jeffrey S Parker, Rodney L Anderson, Ryan M McGranaghan, Kohei Fujimoto, and George H Born. Supporting crewed lunar exploration with liaison navigation. In 2013 Guidance, Navigation, and Control Conference, number 13-053, Breckenridge, CO, Feb. 1–6 2013.

[88] Jason M Leonard, Jeffrey S Parker, and George H Born. Uncertainty mapping and navigation techniques for crewed missions in libration orbits. In AIAA/AAS Astrodynamics Specialist Conference, San Diego, CA, August 4–7, 2014.

[89] J. O. Light. An investigation of the orbit redetermination process following the first midcourse maneuver. Space Programs Summary 37–33, IV, June 30 1965.

[90] S. Luthcke, N. Zelensky, D. Rowlands, F. Lemoine, and T. Williams. The 1-centimeter orbit: Jason-1 precision orbit determination using gps, slr, doris, and altimeter data special issue: Jason-1 calibration/validation. Marine Geodesy, 26(3):399–421, 2003.

[91] Jeffrey E Marchese, Brandon D Owens, Daniel Cosgrove, Sabine Frey, and Manfred Bester. Calibration of in-flight maneuver performance for the themis and artemis mission spacecraft. In Proceedings of the AIAA 2010 SpaceOps Conference, pages 25–30, 2010.

[92] F Landis Markley and Joseph E Sedlak. Kalman filter for spinning spacecraft attitude estimation. Journal of guidance, control, and dynamics, 31(6):1750–1760, 2008.

[93] J. Marshall, N. Zelensky, S. Klosko, D. Chinn, S. Luthcke, K. Rachlin, and R. Williamson. The temporal and spatial characteristics of topex/poseidon radial orbit error. Journal of Geophysical Research, 100(C12), 1995.

[94] Agostino Martinelli and Roland Siegwart. Observability analysis for mobile robot localization. In Intelligent Robots and Systems, 2005.(IROS 2005). 2005 IEEE/RSJ International Conference on, pages 1471–1476, 2005.

[95] Nikos Mastrodemos, Daniel G Kubitschek, and Stephen P Synnott. Autonomous navigation for the deep impact mission encounter with comet tempel 1. Space Science Reviews, 117(1-2):95–121, 2005.

[96] P. Maybeck. Stochastic Models, Estimation and Control, volume 141-1. Academic press, 1979.

[97] Joseph J Michalsky. The astronomical almanac's algorithm for approximate solar position (1950–2050). Solar Energy, 40(3):227–235, 1988.

[98] J. Miller, L. Wood, and C. Week. Orbit determination strategy and accuracy for a comet rendezvous mission. Journal of Guidance, Control, and Dynamics, 13:775–784, 1990.

[99] J. K. Miller. A continuous square root in formation filter-swoother with discrete data update. In AAS/AIAA Spaceflight Mechanics Meeting, 1994.

[100] J.K. Miller and Y. Cheng. Autonomous landmark tracking orbit determination strategy. In 13th AAS/AIAA Space Flight Mechanics Conference, Ponce, Puerto Rico, February 9–13 2003.

[101] O. Montenbruck and E. Gill. Satellite Orbits: Models, Methods and Applications. Springer-Verlag, Netherlands, corrected 3rd printing 2005 edition, 2000.

[102] O. Montenbruck, T. Van Helleputte, R. Kroes, and E. Gill. Reduced dynamic orbit determination using gps code and carrier measurements. Aerospace Science and Technology, 9(3):261–271, 2005.

[103] M. C. Moreau, P. Axelrad, J. L. Garrison, and A. Long. GPS receiver architecture and expected performance for autonomous navigation in high earth orbits. Navigation, 47(3):191–204, 2000.

[104] K. Myers and B. Tapley. Dynamical model compensation for near-earth satellite orbit determination. AIAA Journal, 13:343–349, 1975.

[105] H.N. Najm. Uncertainty quantification and polynomial chaos techniques in computational fluid dynamics. Annual Review of Fluid Mechanics, 41:35–52, 2009.

[106] NASA. `http://www.nasa.gov/mission\_pages/artemis/multimedia/image-gallery.html`.

[107] NASA. National space science data center. `http://nssdc.gsfc.nasa.gov/space/image/isee3\_traj.jpg`.

[108] NASA. Solar and heliospheric observatory. `http://soho.nascom.nasa.gov/about/images/halo\_orbit.gif`.

[109] NASA. Wilkinson microwave anisotropy probe. `http://map.gsfc.nasa.gov/mission/observatory\_orbit.html`.

[110] A. I. Nazarenko and K. T. Alfriend. Development of the technique for covariance prediction using the gravity color noise. In AAS/AIAA Space Flight Mechanics Conference, Savannah, Georgia, February 8 – 12 2009.

[111] Isaac Newton. Philosophiae Naturalis Principia Mathematica. Londoni, 1687.

[112] A. E. Niell. Global mapping functions for the atmosphere delay at radio wavelengths. Journal of Geophysical Research: Solid Earth (1978–2012), 101(B1):3227–3246, 1996.

[113] F. G. Nievinski, B. Yonko, and G. H. Born. Improved orbit determination using second-order gauss-markov processes. In AAS/AAIA Space Flight Mechanics Meeting, number AAS 11–119, New Orleans, Louisiana, February 13–17 2011.

[114] V. J. Ondrasik and D. W. Curkendall. A first-order theory for use in investigating the information content conatined in a few days of radio tracking data. JPL Technical Report 32-1526, III:77–93, 1971.

[115] Valery Iustinovich Oseledec. A multiplicative ergodic theorem. lyapunov characteristic numbers for dynamical systems. Trans. Moscow Math. Soc, 19(2):197–231, 1968.

[116] WM Owen Jr, N Mastrodemos, BP Rush, TCM Wang, SD Gillam, and S Bhaskaran. Optical navigation for deep impact. In 16th Annual AAS/AIAA Space Flight Mechanics Meeting, pages 1231–1250, 2006.

[117] Brandon D Owens, Jeffrey E Marchese, Daniel P Cosgrove, Sabine Frey, and Manfred G Bester. Optimizing artemis libration point orbit stationkeeping costs through maneuver performance calibration. In Proceedings of the 22nd AAS/AIAA Space Flight Mechanics Meeting, 2012.

[118] R.S. Park and D.J. Scheeres. Nonlinear mapping of gaussian statistics: theory and applications to spacecraft trajectory design. Journal of Guidance, Control, and Dynamics, 29(6):1367–1375, 2006.

[119] J. S. Parker. Low-Energy Ballistic Lunar Transfers. PhD thesis, University of Colorado, Boulder, Colorado, 2007.

[120] J. S. Parker, R. L. Anderson, G. H. Born, K. Fujimoto, J. M. Leonard, and R. M. McGranaghan. Navigation between geosynchronous and lunar l1 orbiters. In AAS/AIAA Astrodynamics Specialist Conference, number AIAA-2012-4878, Minneapolis, MN, August 13–16, 2012. AAS/AIAA.

[121] Jeffrey S Parker, Jason M Leonard, Rodney L Anderson, and George H Born. Liaison-supplemented navigation for a crewed vehicle in a lunar halo orbit. In AAS/AIAA Astrodynamics Specialist Conference, Hilton Head, South Carolina, August 11–15 2013.

[122] Jeffrey S Parker, Jason M Leonard, Kohei Fujimoto, Ryan M McGranaghan, George H Born, and Rodney L Anderson. Navigating a crewed lunar vehicle using liaison. In Proceedings of the 23rd AAS/AIAA Spaceflight Mechanics Meeting, number AAS 13–330, Kauai, HW, Feb. 10–14 2013.

[123] H. J. Pernicka. The numerical determination of Lissajous orbits in the circular restricted three-body problem. Master's thesis, Purdue University, December 1986.

[124] Gérard Petit and Brian Luzum. Iers conventions (2010). Technical report, DTIC Document, 2010.

[125] P. J. Prince and J. R. Dormand. High order embedded runge-kutta formulae. Journal of Computational and Applied Mathematics, 7:67–75, 1981.

[126] M. L. Psiaki. Absolute orbit and gravity determination using relative position measurements between two satellites. Journal of Guidance, Control and Dynamics, 34(5):1285–1297, September–October 2011.

[127] Mark L Psiaki. Autonomous low-earth-orbit determination from magnetometer and sun sensor data. Journal of Guidance, Control, and Dynamics, 22(2):296–304, 1999.

[128] Mark L Psiaki, Lejin Huang, and Stephen M Fox. Ground tests of magnetometer-based autonomous navigation (magnav) for low-earth-orbiting spacecraft. Journal of Guidance, Control, and Dynamics, 16(1):206–214, 1993.

[129] Yingjing Qian, Chaoyong Li, Wuxing Jing, Inseok Hwang, and Jian Wei. Sun–earth–moon autonomous orbit determination for quasi-periodic orbit about the translunar libration point and its observability analysis. Aerospace Science and Technology, 2012.

[130] D. L. Richardson. Analytical construction of periodic orbits about the collinear points. Celestial Mechanics, 22:241–253, 1980.

[131] D. L. Richardson and N. D. Cary. A uniformly valid solution for motion of the interior libration point for the perturbed elliptic-restricted problem. In AAS/AIAA Astrodynamics Specialist Conference, number AAS 75-021. AAS/AIAA, July 1975.

[132] Wilson J Rugh. Linear system theory. Prentice-Hall, 1996.

[133] C. Sabol, C. Binz, A. Segerman, K. Roe, and P. Schumacher. Probability of collision with special perturbations dynamics using the monte carlo method. In AAS/AIAA Astrodynamics Specialist Conference, Girdwood, AK, July 31 – Aug 4, 2011.

[134] C. Sabol, T. Sukut, K. Hill, K.T. Alfriend, B. Wright, Y. Li, and P. Schumacher. Linearized orbit covariance generation and propagation analysis via simple monte carlo simulations. In Annual AAS/AIAA Space Flight Mechanics Conference, San Diego, CA, AAS 10-134, February 15–17 2010.

[135] C. A. Sabol. A role for Improved Angular Observations in Geosynchronous Orbit Determination. PhD thesis, University of Colorado, Boulder, Colorado, 1998.

[136] Stefan Schaer, Werner Gurtner, and Joachim Feltens. Ionex: The ionosphere map exchange format version 1. In Proceedings of the IGS AC Workshop, Darmstadt, Germany, volume 9, 1998.

[137] DJ Scheeres, D Han, and Y Hou. Influence of unstable manifolds on orbit uncertainty. Journal of Guidance, Control, and Dynamics, 24(3):573–585, 2001.

[138] Suneel I Sheikh, Darryll J Pines, Paul S Ray, Kent S Wood, Michael N Lovellette, and Michael T Wolff. Spacecraft navigation using x-ray pulsars. Journal of Guidance, Control, and Dynamics, 29(1):49–63, 2006.

[139] Gil Shorshi and Itzhack Y Bar-Itzhack. Satellite autonomous navigation based on magnetic field measurements. Journal of Guidance, Control, and Dynamics, 18(4):843–850, 1995.

[140] Aurore E Sibois. GPS-based Sub-Hourly Polar Motion Estimates: Strategies and Applications. PhD thesis, University of Colorado Boulder, 2011.

[141] E. M. Standish. Jpl planetary and lunar ephemerides, de405/le405. Jet Propulsion Laboratory Interoffice Memorandum IOM 312F-98-048, Aug. 26 1998.

[142] EM Standish Jr. The observational basis for jpl's de 200, the planetary ephemerides of the astronomical almanac. Astronomy and Astrophysics, 233(252–271), 1990.

[143] Debo Sun and John L Crassidis. Observability analysis of six-degree-of-freedom configuration determination using vector observations. Journal of Guidance, Control, and Dynamics, 25(6):1149–1157, 2002.

[144] Richard F Sunseri, Hsi-Cheng Wu, Scott E Evans, James R Evans, Theodore R Drain, and Michelle M Guevara. Mission analysis, operations, and navigation toolkit environment (monte) version 040. In NASA Tech Briefs, volume 45, September 2012.

[145] Theodore H Sweetser, Stephen B Broschart, Vassilis Angelopoulos, Gregory J Whiffen, David C Folta, Min-Kun Chung, Sara J Hatch, and Mark A Woodard. Artemis mission design. Space science reviews, 165(1-4):27–57, 2011.

[146] V. Szebehely. Theory of Orbits: The Restricted Problem of Three Bodies. Academic Press, New York, 1967.

[147] B. Tapley, J. Ries, S. Bettadpur, D. Chambers, M. Cheng, F. Condi, B. Gunter, Z. Kang, P. Nagel, R. Pastor, T. Pekker, S. Poole, and F. Wang. Ggm02 - an improved earth gravity field model from grace. Journal of Geodesy, 79(8):467–478, 2005.

[148] B. D. Tapley, B. E. Schutz, and G. H. Born. Statistical Orbit Determination. Elsevier Academic Press, Burlington, MA, 2004.

[149] J. Taylor. The cramer-rao estimation error lower bound computation for deterministic nonlinear systems. IEEE Transactions on Automatic Control, 24(2):343–344, 1979.

[150] Catherine Lee Thornton. Triangular covariance factorizations for kalman filtering. PhD thesis, University of California at Los Angeles, School of Engineering, 1976.

[151] J. Tombasco. Orbit Estimation of Geosynchronous Objects via Ground-Based and Space-Based Optical Tracking. PhD thesis, University of Colorado, Boulder, Colorado, 2011.

[152] Chi Chao Tung. Random response of highway bridges to vehicle loads. Journal of engineering mechanics, 1967.

[153] George E Uhlenbeck and Leonard Salomon Ornstein. On the theory of the brownian motion. Physical review, 36(5):823, 1930.

[154] D. A. Vallado. Fundamentals of Astrodynamics and Applications, Second Edition. Microcosm Press, El Segundo, CA, and Kluwer Academic Publishers, Dordrecht/Boston/London, 2001.

[155] B. Villac, C. Chow, M. Lo, G. Hintz, and Z. Nazari. Dynamic optimization of multi-spacecraft relative navigation configurations in the Earth-Moon system. In George H. Born Symposium, Boulder, Colorado, 13–14 May 2010. AAS.

[156] S. Wallace, C. Sabol, and S. Carter. Optical sensor calibration using GPS reference orbits. In MIT/Lincoln Lab Space Control Workshop, Lexington, MA, March 1997.

[157] M. Wang and G. Uhlenbeck. On the theory of the brownian motion ii. Reviews of Modern Physics, 17(2–3):323–342, 1945.

[158] D.M. Wiberg. The mimo wiberg estimator. In Decision and Control, 1989., Proceedings of the 28th IEEE Conference on, pages 2590–2594. IEEE, 1989.

[159] N. Wiener. The homogeneous chaos. American Journal of Mathematics, 60(4):897–936, 1938.

[160] R. Wilson. Derivation of differential correctors used in GENESIS mission design. Technical Report JPL IOM 312.I-03-002, Jet Propulsion Laboratory, California Institute of Technology, 2003.

[161] W. R. Wollenhaupt. Apollo orbit determination and navigation. 8th AIAA Aerospace Sciences Meeting, 1970.

[162] M. Woodard, D. Cosgrove, P. Morinelli, J. Marchese, B. Owens, and D. Folta. Orbit determination of spacecraft in earth-moon l1 and l2 libration point orbits. In Proceedings of the 2011 AAS/AIAA Astrodynamics Specialists Conference, AAS 11–514, July 31 – August 4, 2011, Girdwood, Alaska 2011.

[163] M. Woodard, D. Folta, and D. Woodfork. ARTEMIS: The first mission to the lunar libration orbits. In 21st International Symposium on Space Flight Dynamics, Toulouse, France, September 28 – October 2, 2009. Centre National d'Études Spatiales.

[164] M. Woodard, D. Folta, and D. Woodfork. Artemis: the first mission to the lunar libration orbits. In 21st International Symposium on Space Flight Dynamics. Centre National d'Études Spatiales, Toulouse, France, 2009.

[165] J.R. Wright. Sequential orbit determination with auto-correlated gravity modeling errors. Journal of Guidance, Control, and Dynamics, 4(3):304–309, 1980.

[166] J.R. Wright, J. Woodburn, S. Truong, and W. Chuba. Orbit covariance inner orbit covariance inner integrals with polynomials. In 18th AAS/AIAA Space Flight Mechanics Meeting, AAS 08–161, Galveston, TX, January 2008.

[167] J.R. Wright, J. Woodburn, S. Truong, and W. Chuba. Oribt gravity error covariance. In 18th AAS/AIAA Space Flight Mechanics Meeting, AAS 08–157, Galveston, TX, January 2008.

[168] J.R. Wright, J. Woodburn, S. Truong, and W. Chuba. Sample orbit covariance function and filter–smoother consistency tests. In 18th AAS/AIAA Space Flight Mechanics Meeting, AAS 08–159, Galveston, TX, January 2008.

[169] S. Wu, T. Yunck, and C. Thornton. Reduced-dynamic technique for precise orbit determination of low earth satellites. Astrodynamics 1987, 1:101–113, 1988.

[170] D. Xiu and G. Em Karniadakis. Modeling uncertainty in steady-state diffusion problems via generalized polynomial chaos. Computer Methods in Applied Mechanics and Engineering, 191(43):4927–4948, 2002.

[171] D. Xiu, D. Lucor, C.H. Su, and G.E. Karniadakis. Stochastic modeling of flow-structure interactions using generalized polynomial chaos. Journal of Fluids Engineering, 124:51–59, 2002.

[172] Jo Ryeong Yim. Autonomous Spacecraft Orbit Navigation. PhD thesis, Texas A & M University, 2002.

[173] Jo Ryeong Yim, John L Crassidis, and John L Junkins. Autonomous orbit navigation of interplanetary spacecraft. In AIAA/AAS Astrodynamics Specialist Conference, number AIAA 2000–3936, Denver, CO, Aug. 14–17 2000.

[174] Jo Ryeong Yim, John L Crassidis, and John L Junkins. Autonomous orbit navigation of two spacecraft system using relative line of sight vector measurements. In AAS/AIAA Astrodynamics Specialist Conference, number AAS 04–257, Maui, Hawaii, Feb. 8–12 2004.